PHYSIK DEPARTMENT

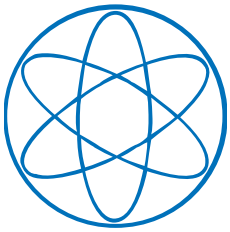

# Dynamic Structure Formation in Active Cytoskeletal Systems

Dissertation
von

Volker Schaller

TECHNISCHE UNIVERSITÄT MÜNCHEN

TECHNISCHE UNIVERSITÄT MÜNCHEN
Lehrstuhl für Zellbiophysik E27

# Dynamic Structure Formation in Active Cytoskeletal Systems

**Volker W. Schaller**

Vollständiger Abdruck der von der Fakultät für Physik der Technischen Universität München zur Erlangung des akademischen Grades eines

Doktors der Naturwissenschaften (Dr. rer. nat.)

genehmigten Dissertation.

Vorsitzender: Univ.-Prof. Dr. M. Zacharias

Prüfer der Dissertation: 1. Univ.-Prof. Dr. A. Bausch

2. Univ.-Prof. Dr. E. Frey,
Ludwig-Maximilians-Universität München

Die Dissertation wurde am 10.09.2012 bei der Technischen Universität München eingereicht und durch die Fakultät für Physik am 04.10.2012 angenommen.

# Summary

The emergence of collective motion in non-equilibrium systems is an ubiquitous and fascinating phenomenon. Prime examples of this complex self-organization process are the flocking motion of birds and schools of fish as well as collective motion patterns in bacterial colonies – but also the complex dynamics inside the cytoskeleton of living cells. Although the composition of collectively moving systems is generically simple – they consist of a sufficiently dense ensemble of (self-)propelled particles – the dynamical properties of this class of materials are very complex. They range from the spontaneous transition to collective dynamics and swirling motion to persistent density inhomogeneities. To elucidate the physical principles that underly collective motion, numerous theoretical studies have been devoted to model self-propelled particle systems at high particle densities. They approach the problem on all levels of description, ranging from agent-based simulations to mean field models in the hydrodynamic limit. The dynamics of all these models are strikingly similar to the phenomena observed in experimental systems. Moreover, the theoretic concepts provide some key predictions for the statistical properties of collectively moving particles that sharply discriminate them from systems in thermal equilibrium. However, a detailed one-to-one comparison and thus an experimental verification of the theoretic predictions is still hampered by the lack of well defined and well controllable experimental systems.

In this thesis, I established and analyzed a set of reconstituted model systems that confirm the theoretic predictions and allow for a quantitative comparison between theory and experiment. The experimental systems are based on biological proteins; actin filaments, molecular motor, and crosslinking proteins. The motor proteins are the active component. They constantly consume energy and are able to move on the filaments in a directed manner. Thereby they can build up stresses or generate motion. The molecular nature of these experiments provides truly large system sizes in a well controlled environment with system parameters that can be adjusted to a high precision.

The first part of the thesis focuses on high density motility assay experiments where highly concentrated actin filaments are propelled by immobilized motor proteins in a planar geometry. Above a critical density, the filaments self-organize to form coherently moving structures with persistent density modulations such as clusters, swirls and interconnected bands – structures that have been theoretically predicted but were not experimentally verified so far. These polar structures are long-lived and can span length scales orders of magnitudes larger than their constituents. The reconstituted experimental approach complemented by agent-based simulations enables a backtracking of the assembly and disassembly pathways to the underlying local interactions. I identify weak and local alignment interactions to be essential for the observed dynamic pattern formation. Furthermore, the ordered state is shown to have remarkable statistical properties: the fluctuations in the particle density are abnormally large compared to systems in thermal equilib-

rium, density- and velocity-correlations are anisotropic with respect to the direction of motion, and the individual filaments perform a superdiffusive motion transversal to the mean direction of motion. All these findings confirm the theoretical picture – both qualitatively and quantitatively. It is shown that these generic features of collective motion arise from the coupling between the particle density and velocity field of the collectively moving filaments. In turn, the collective motion of millions of filaments drags the surrounding fluid and induces a fluid flow that considerably extends the size of the collective motion patterns. By analyzing the interaction between colliding patterns and the dynamics of clusters within confinements, it is shown that both the stability and the size of the patterns depend on long ranged hydrodynamic interactions that are self induced by the coherently moving filaments.

The second part of the thesis addresses the question how actin crosslinking proteins modify and alter the pattern formation in the high density motility assay. By adding the crosslinking protein fascin, it is shown that the interplay of only three components is sufficient for the emergence of a "frozen" active steady state, where fluctuations on the single filament level are successively eliminated during a coarsening process while keeping the system in an active state. The emergent structures are highly symmetric and consist of rings and elongated fibers that are actively assembled and propelled by the motor proteins. The symmetry of the frozen steady state structures reflects the binding properties of fascin that only crosslinks filaments that are aligned in a polar conformation. By complementing the experimental findings with an agent-based simulation, I correlate the formation of a frozen steady state with the mechanical properties of the emergent structures and identify the crosslinker mediated growth processes as driving mechanism for the emergence of frozen active steady states. While frozen active states were reported for externally driven systems through macroscopic shear or agitation, this is the first example for a frozen active state in inherently active systems like cytoskeletal suspensions or active gels.

In a next step, I compare the pattern formation induced by fascin to the behavior of other crosslinking proteins. In general, the pattern formation in the motility assay depends sensitively on the specific properties of the crosslinking protein. Even if crosslinking proteins behave similarly in passive systems, they may display a surprisingly different behavior once they are set under stress in active systems. For instance, $\alpha$-actinin and filamin, two crosslinking proteins that crosslink actin filaments with comparable *on* and *off* rates and that *a priori* form similar passive networks, yield a completely different kind of pattern formation: while the addition of $\alpha$-actinin leads to an actively contracting network, filamin promotes a highly resilient network that cannot be deformed by the motor proteins. These results not only provide insight into the microscopic binding properties of crosslinking proteins under load, but also show that the high variability in the behavior of different crosslinking proteins in active systems adds a new degree of freedom to the physics of active gels. By varying the specific abundances of crosslinking proteins, not only can active networks tune their mechanical properties, but can also "shift gears" between different mechanisms and regimes of self-organization.

In the last part of the thesis, these principles are transferred to the pattern formation of three-dimensional active gels that consist of actin, the crosslinking protein fascin and oligomeric motor filaments that induce relative displacements between neighboring filaments. The intricate interplay between active force generation and passive crosslinking in active gels leads to a highly dynamic structure formation process similar to the cytoskeletal dynamics. Again, the reconstituted experimental system allows to model the experimentally observed pattern formation with an agent based simulation. Here, the simulation is based on the competitive interaction of crosslink-

ers and motor proteins. Despite its minimal nature, it retrieves the main experimental findings: like the experiment it shows a dynamic coarsening with a characteristic structure size distribution that is set by the actin, fascin and motor concentrations. In the simulation, as well as in the experiments, the motility of these structures generically depends on the structure size and the competition between active transport and passive binding. Moreover, this results in anomalous transport dynamics, that is similar to those observed in cells. The thesis closes with an investigation of collective modes in active gels that are characterized by the correlated movement of remote structures. It is shown that these collective modes rely on the connectivity within the active gel and a sufficient binding strength of the myosin-II filaments to the actin filaments.

The results of this thesis exemplify the importance of reconstituted systems for advancing our understanding of active matter. Only with a bottom up approach to the physics of collective motion, it is possible to compare experimental results to the minimal theoretic models in the field and to substantiate serveral theroretic key predictions. Moreover, the minimal nature of the experimental systems allows to systematically accompany the experimental findings with agent-based simulations, mapping the microscopic interactions on the molecular level. Thus, the physical principles and effects described in this thesis help to establish a microscopic understanding of the structure formation and collective motion in active systems.

# Contents

# 1 Motivation and Introduction

How order can emerge spontaneously by means of simple local interactions among constituent components of a system has always fascinated scientists from numerous disciplines. It is by now well known that maintaining a system far from thermal equilibrium by external constraints induces a plethora of different spatio-temporal patterns. Generically, upon increasing the strength of the constraint, patterns change through a succession of instabilities, with the Rayleigh-Benard instability being a prototype [43]. In chemically active and some biological systems, patterns arise through the competition between nonlinear catalytic or regulatory processes and transport phenomena. Turing' s pattern is one of the paradigms for self-organization in this field of reaction-diffusion processes [214].

Active systems, like flocks of animals, self-propelled microorganisms or the cytoskeleton constitute yet another intriguing class of non-equilibrium systems. Here, locally generated internal forces together with interactions between the constituents are the cause for remarkable self-organization processes, which lead to structures as diverse as cohesive flocks of vertebrates [11, 38, 231], swarming microorganisms [31, 33, 44, 53, 168, 239], collective motion patterns in confluent cell layers [1, 2, 86, 210], embryogenesis [141, 165], or intracellular dynamics [116, 122, 131, 134, 137, 138, 160, 182, 229]. At first glance, these examples may seem very diverse but by taking a closer examination, all these systems share some mutual similarities, including the inherent polarity of the constituents that breaks the symmetry in the systems, a density-dependent transition to ordered phases, collective dynamics, or huge fluctuations in the particle density in the ordered phase.

These similarities suggest universal organizing principles underlying the pattern formation in these systems; an idea followed by theoretical models on all levels of description. Microscopic models directly map local forces and interactions via only a few and preferably simple interaction rules [3, 9, 29, 30, 72, 108, 157, 162, 163, 199, 222, 232, 241], while more macroscopic approaches map microscopic interactions and coarse-grain them to obtain a mean field description [13, 14, 17, 19, 71, 111–113, 128, 164, 240, 242]. Finally, theories in the hydrodynamic limit are based on the generic symmetries of the system [73, 78, 94–96, 114, 148, 186, 207, 208, 213]. All these approaches contribute to the general physical framework for this material class of active matter that has emerged in the past decade.

However, all these models characteristically have a broad, partially empirically chosen parameter space and show a manifold of possible patterns comprising the coexistence of ordered and disordered phases, spiraling movements and propagating wave-like structures – most of which are not experimentally verified so far. Moreover, experimental systems studied to date either exhibit static steady states or are likely to rely on higher ordering principles like chemical signaling cascades or even cognitive processes. It is thus indeed justified to say that in the field of active soft matter, the theory currently is ahead of the experiments [49, 208]. This hampers any further progress in our physical understanding of the self-organization processes in active matter, as the detailed comparison of theoretical predictions to experimental observations is indispensable to narrow down the parameter space and to decide which of the manifold of conceivable theoretic terms are the most important contributions.

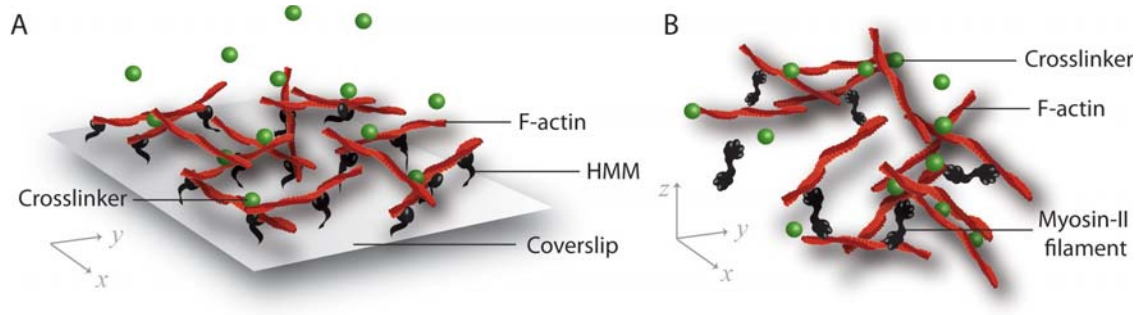


**Figure 1.1: Schematic representation of the reconstituted setups used in this thesis.** In the motility assay displayed in **A**, the molecular motor HMM is immobilized on a cover slip. In the presence of ATP, they propel the filaments in a directed manner. The structure formation takes place in a quasi two-dimensional geometry. In contrast, the structure formation in the active gel displayed in **B** takes place in three dimensions. Here, the structure formation arises from the interplay between passive crosslinking and active transport induced by oligomeric myosin-II filaments.

To overcome these limitations, well-controlled and quantifiable experimental systems are urgently needed. Generically, such reconstituted systems consist of a minimal set of purified components with precisely adjustable interactions. One class of these reconstituted systems uses ensembles of macroscopic granular particles that are actively agitated by vibrating the arena they are embedded in [6,49,50,115,154,158,211,216]. So far, these systems have successfully verified the theoretically predicted transition to collective behavior above a certain critical particle density [49,158,211]. Using macroscopic particles, these systems allow for a precise quantification of the particle-particle interactions in dense granular monolayers and thus provide a very complete picture of the emergence of order in these systems [50, 154]. Moreover, these systems could provide the first qualitative evidence for several theoretic key predictions such as the existence of abnormally large particle fluctuations in the ordered phase [50,154] or the existence of anisotropic correlations with respect to the broken symmetry mode [154]. The main disadvantage of these granular systems is their limited system size. Characteristically consisting of up to several ten thousands of particles with an arena only two orders of magnitude larger than the particle diameter, they defy a rigorous quantitative comparison with theoretical predictions which are based on infinitely large systems in the mean field limit.

Another class of reconstituted systems consists of purified cytoskeletal components [15], filamentous proteins, crosslinking proteins, and associated motor proteins that, under constant energy consumption, can exert forces by "walking" on the filaments. Such model systems have established a physical understanding for the self-organization of quasi-static patterns, such as aster-like structures [156, 199] or local accumulations of material [10, 185, 188]. Furthermore, it was possible to relate the inherent activity stemming from the molecular motors to the bulk properties of the active network or gel [18, 89, 102, 121, 150] and to induce the large scale contraction of the active gel at high material concentrations [93, 97]. The molecular nature of these systems permits truly large system sizes with millions of individual proteins. This, together with the detailed parameter control and the wealth of knowledge about passive crosslinked filament networks [123–125, 175, 176, 192, 228] makes these systems ideally suited to accompany theoretic efforts in the field. Yet, the statistical properties and the emergence of collective behavior so far remain to be systematically addressed – despite that the investigation of these aspects is crucial for a more thorough understanding of this material class.

To this end, in this thesis I introduce and analyze a set of reconstituted systems that are based on cytoskeletal actin filaments and associated myosin-II motor proteins. Thereby two setups are used: the motility assay setup and the reconstituted active gel (Figure 1.1). The motility assay displayed in Figure 1.1 A, consists of actin filaments that are propelled by a myosin-II fragment (HMM) in a planar geometry [55, 110, 183]. The reconstituted active gel (Figure 1.1 B) consists of actin filaments, crosslinking proteins, and oligomeric myosin-II filaments that induce relative displacements between actin filaments and crosslinked structures. Apart from the excellent accessibility of all relevant system parameters, the minimal nature of the systems introduced here is another major advantage. This made it possible to systematically complement the experimental results by simple agent based simulations. The experimental procedures and the subsequent analysis follow certain key aspects and guidelines that most concisely can be summed up in the following **main questions of the thesis**:

1. *Is it possible to induce a transition to collective motion by increasing the filament density in motility assay experiments? If so: what are the statistical properties of this ordered state and how do they compare to theoretic predictions? Is it possible to map the transition to collective motion by a simple simulation that is solely based on short range interactions?*

2. *What happens if the active transport in the motility assay is complemented by a defined growth process induced by crosslinking proteins? How do the mechanical properties of the emergent structures affect the pattern formation?*

3. *How do different crosslinking proteins behave in active systems? Can the motility assay be used as a tool to investigate and pinpoint the non-equlibrium properties of crosslinking proteins?*

4. *What are the dynamic properties of an active actin network that is set under stress by molecular motors? Can these properties be retrieved in a simple simulation that models the interplay between passive crosslinking and active driving based on interaction rates? Do active gels also display collective modes?*

The first set of questions is addressed in chapter 2. Here it is shown that above a critical filament density the high density motility assay indeed undergoes a transition to collective motion. Subsequently, the statistical properties of the collectively moving phase are quantified. By means of such quantification, it is possible to confirm several theoretic predictions and to relate them to the coupling between the density and velocity fields of the moving particles. Introducing a minimal agent-based simulation, it is shown that the emergence of collective motion can indeed be traced back to local interactions – although the collective behavior on large length and time scales is modulated by long-range hydrodynamic interactions.

Chapter 3 is devoted to the second set of questions. By adding the crosslinker protein fascin, I show that the pattern formation is substantially altered if the active transport is complemented by a growth process. In the case of fascin, this leads to the emergence of highly symmetric structures that gradually absorb all individual filaments – until all fluctuations on the single filament level have literally frozen.

By comparing various crosslinking proteins, in chapter 4, it is shown that the pattern formation in the motility assay indeed depends sensitively on the specific crosslinking protein – thereby adressing the third set of questions. The observed patterns turn out to be highly diverse. They range from the self-organization of the driven filaments to form actively compacting structures to the formation of highly stable networks.

This lays the basis for the last part (chapter 5) of this thesis that is devoted to the analysis of three-dimensional active gels. The chapter starts with a detailed analysis of the pattern formation in active gels crosslinked by fascin. On this basis, I develop a simple agent-based simulation for the dynamics inside the active gel. Although it is solely based on the interplay of binding and unbinding rates of crosslinkers and motor proteins, the simulation is able to retrieve the main experimental findings, such as the dynamic structure size distribution, the superdiffusive transport properties inside the gel, and the phase behavior. Finally, answering the last and final question of the thesis, it is shown that active gels can indeed exhibit collective modes, provided that the connectivity and the crossbridge strength of the acto-myosin interaction are sufficiently high.

# 2 Polar Patterns of Driven Filaments

*The emergence of collective motion such as exhibited by systems ranging from flocks of animals, self-propelled microorganisms or the cytoskeleton is an ubiquitous and fascinating self-organization phenomenon. Similarities between these systems suggest universal organizing principles underlying pattern formation. This idea is followed by theoretical models that provide a general framework for the understanding of this material class of active fluids. However, further progress in the field is hampered by the lack of adequate model systems that allow for a precise quantification of the statistics of collective motion and that help to pin down the relevant parameter regime.*
*In this chapter I demonstrate the emergence of collective motion in a high density motility assay, which consists of highly concentrated actin filaments propelled by immobilized molecular motors in a planar geometry. After the setup and the basic properties of the filament motion have been introduced (section 2.1), the basic phenomenology of the system is examined in section 2.2. There I show that above a critical density, the filaments self-organize to form coherently moving structures with persistent density modulations such as clusters, swirls and interconnected bands. As illustrated in section 2.3, these polar structures are long-lived and can span length scales orders of magnitudes larger than their constituents.*
*The detailed parameter control and the excellent accessibility of all relevant observables enables a detailed quantification of the statistical properties of collective motion in section 2.4. There it is shown that the collectively moving phase is characterized by unique statistical properties, comprising the occurrence of (i) anomalously large fluctuation in the filament density, (ii) velocity and density correlations that are anisotropic with respect to the direction of motion, and (iii) a superdiffusive particle movement perpendicular to the mean direction of motion, properties that were predicted to be key signatures of collective motion. With the results obtained in section 2.4 these predictions cannot only be confirmed, but their emergence can be traced back to the complex interplay between the density and velocity fields of the collectively moving particles.*
*Further, the reconstituted approach enables a backtracking of the assembly and disassembly pathways to the underlying local interactions. With an agent based simulation that is introduced in section 2.5, weak and local alignment interactions are identified to be essential for the observed emergence of the patterns. While these local interactions are sufficient to explain the emergence of collective motion, the dynamic properties of the system are modulated by long-range hydrodynamic interactions. This is shown in section 2.6 by analyzing the interactions between colliding patterns and the dynamics of clusters within confinement.* [1]

## 2.1 The disordered phase: persistent random walk of driven filaments

The molecular system investigated here, consists of only a few components: actin filaments and fluorescently labelled reporter filaments that are propelled by heavy mero myosin (HMM) motor proteins in the planar geometry of a standard motility assay [110, 198, 209, 217] (Figure 2.1 A). In eukaryotic cells, the globular $42\,\mathrm{kDa}$ protein actin is highly abundant and fulfills numerous tasks and is one of the three main scaffold polymers of the cytoskeleton. In this study actin is used in its polymerized form with contour lengths ranging from $1$ to $10\,\mu\mathrm{m}$, with a persistence length of $17\,\mu\mathrm{m}$ [121].
The molecular motor HMM is a myosin-II fragment with a molecular weight of $350\,\mathrm{kDa}$ [132]. It is obtained by enzymatically cleaving myosin-II with chymotrypsine and retains the two actin binding domains of myosin II and the ATP binding site. However, it has lost its tail with which myosin-II can either attach to cargo or polymerize to form oligomeric motor filaments. This makes HMM ideally suited for motility assay experiments, as it still readily attaches to the coverslip, but

[1] The main results of this chapter are published in References [171] and [172].

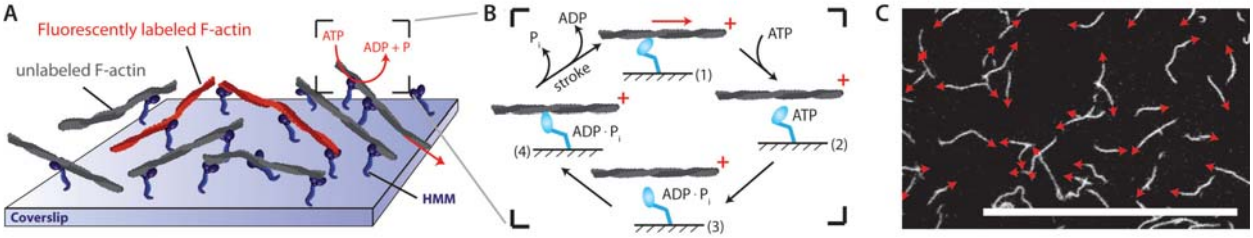


**Figure 2.1: Schematic representation of the high density motility assay and systems behaviour at low filament densities.** (**A**): the molecular motor HMM is immobilized on a cover slip. The filament motion is visualized by the use of fluorescently labelled reporter filaments with a ratio of labelled to unlabelled filaments adjusted to $\approx$ 1:50 - 1:320. The motor proteins propel the filaments in a succession of conformational changes in a mechanochemical cycle that is depicted in (**B**). In step (1), displayed at the top, a nucleotide-free motor head is bound to actin. This attachment is released upon binding of ATP (2). Hydrolyisis of ATP leads to a conformational change (3) and rebinding to actin (4). The release of the ionic phosphate between step (4) and (1) results in a strained conformation which is relaxed by the power stroke that propels the filament. For low filament densities, the action of the motor proteins leads to a disordered phase (**C**). The individual filaments perform a persistent random walk without any specific directional preference. Encounters between filaments lead to crossing events with only slight reorientations. The scale bar is $30\,\mu\mathrm{m}$.

in a more controlled manner than myosin-II and without extended tail regions that interfere with the active transport.

Myosin-II is an actin-based non-processive motor protein that by hydrolyzing ATP induces a sliding movement of the actin filament and the myosin-II motor protein against each other [87, 88]. The chemomechanical cycle of the acto-myosin crossbridge involves a succession of conformational changes of the motor protein that are illustrated in Figure 2.1 B). In its nucleotide-free state the myosin-II head is bound to actin. Upon binding of ATP, the motor head detaches and ATP is hydrolyzed. This triggers a conformational change and myosin in its $\mathrm{ADP} \cdot \mathrm{P_i}$ state rebinds to actin at a position $5\,\mathrm{nm}$ closer to the plus end of the filament. The phosphate release leads to a conformational strain which is released through a conformational change back to the initial configuration. This switch back is called power stroke and leads to a sliding motion of the actin filaments in the motility assay.

The duty ratio, i.e. the fraction of time myosin-II is bound to actin during the mechanochemical cycle, is of the order of $1/100$, making myosin-II a highly non-processive motor protein [87, 166]. This opens up the possibility for many motor proteins to simultaneously move a single filament in the motility assay. Although the frequency of the power stroke is limited to up to $100\,/\mathrm{sec}$, the concerted action of multiple motor proteins thus can lead to maximal actin gliding speeds in the order of $5\,\mu\mathrm{m/sec}$. In general, the gliding speed depends on both, the filament lengths and the motor density at the surface. With decreasing motor concentration the maximal gliding speed is declining. Further, this saturation level in velocity requires increasingly higher filament lengths [217]. To avoid these effects, the experiments presented here were performed at high motor densities at the surface in the order of $5000\,\mu\mathrm{m}^{-2}$, close to the saturation density [198, 209].[2]

At low actin concentrations, the filaments, with a length of about $10\,\mu\mathrm{m}$, perform persistent random walks without any specific directional preference and a dynamic persistence length of approximately $5\,\mu\mathrm{m}$ (Figures 2.1 C and 2.2 A). On long time and length scales, the filament motion

[2]For details please see the materials and methods section.

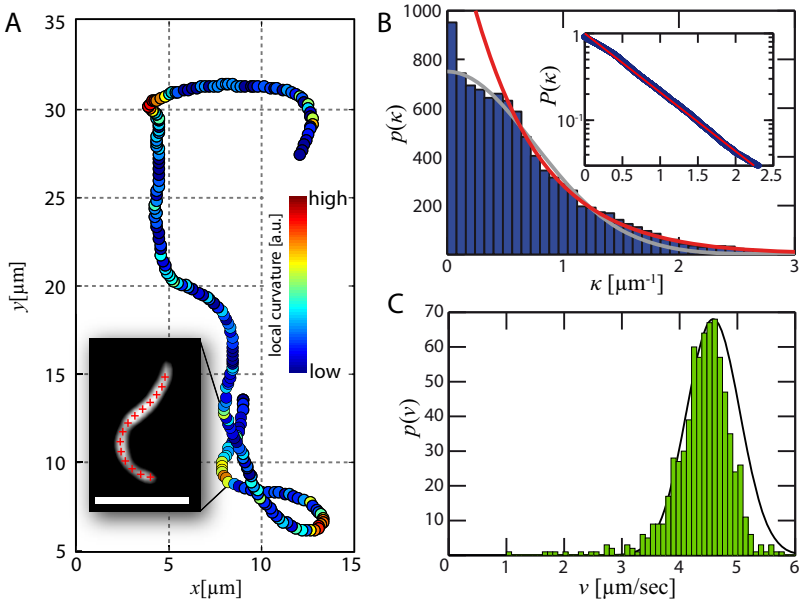


**Figure 2.2: Origin of noise in motility assay experiments.** (**A**) shows a typical trajectory of an approximately $10\,\mu$m long filament. The filament performs a persistent random walk with frequent alternations of its curvature. The inset shows a micrograph of the filament together with the detected contour points. The detected contour is used to calculate the curvature distribution $p(\kappa)$ of the persistent random walk of driven filaments (**B**). For small curvatures, $p(\kappa)$ can be described by a gaussian distribution: $p(\kappa) \propto \exp(-\kappa^2/0.14)$. In contrast to freely fluctuating semiflexible polymers, the distributions shows an exponential tail decaying according to $p(\kappa) \propto \exp(-\kappa/1.71)$. The inset shows the cummulative distribution $P(\kappa)$ that also follows an exponential decay. The random curvatures of the persistent random walk are not the only source of noise in the motility assay: besides, the velocities, though sharply peaked around $4.54\,\mu$m/sec, are broadly distributed. Compared to a gaussian distribution (grey curve), the distribution of velocities shows a pronounced skewness of the order of $1.4$. The scale bar is $5\,\mu$m.

is diffusive with an effective diffusion coefficient in the order of $50\,\mu\mathrm{m}^2/\mathrm{sec}$ [225]. The observed directional randomness is thermal in nature, but also reflects the motor distribution on the surface and the stochasticity of the acto-myosin interaction. The resulting curvature distribution $p(\kappa)$ shown in Figure 2.2 B deviates from the gaussian distribution one would expect for a freely fluctuating semi-flexible polymer according to the worm-like chain model [83]. While $p(\kappa)$ for small curvatures $\kappa$ indeed can be described by a gaussian distribution, it shows an exponential decay for large curvatures.

The velocities of the filaments is set by the motor proteins at the surface and ATP concentration ($c_{\mathrm{ATP}} = 2\,\mathrm{mM}$). The velocities are broadly distributed with a pronounced peak at $4.5\,\mu$m/sec with variance of $0.9\,\mu$m/sec. The distribution itself is asymmetric (skewness $\approx 1.4$) with an approximately gaussian decay towards small velocities and a faster decay towards large velocities (Figure 2.2 C).

The random curvature changes during the persistent random walk and the broad velocity distribution are the main origins of noise in the movement of single filaments. Theoretically, the random curvature changes can readily be modeled by an angular noise [30, 222], whereas the broad velocity distribution can be accounted for by a vectorial noise [30]. The random perturbations oppose the emergence of order in the system at low filament densities. Even if encounters between filaments lead to the alignment of two filaments, they are quickly transported away from one another again. Increasing the filament density, however, it can be expected that the steric constraints be-

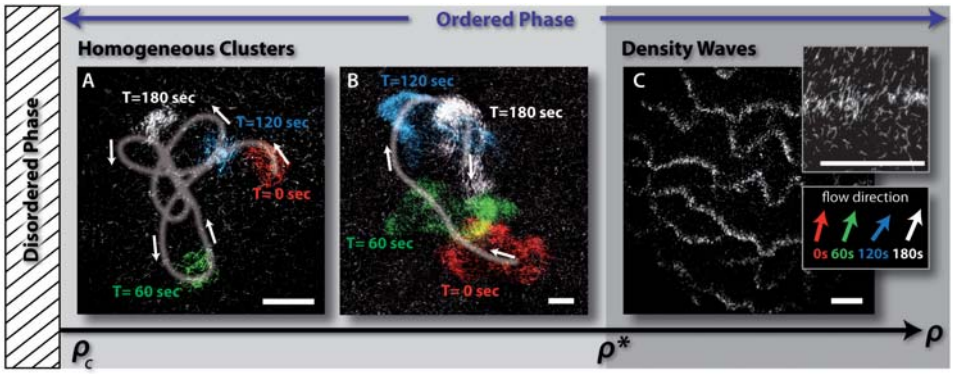


**Figure 2.3: Systems behaviour dependent on the filament density $\rho$.** For low densities a disordered phase is found. Above a certain critical density $\rho_c$, in an intermediate concentration regime, the disordered phase is unstable and small polar-nematic clusters of coherently moving filaments start to form (**A**). At higher densities these clusters become larger but remain homogeneous (**B**). Above a threshold density $\rho*$, in the high density regime, persistent density fluctuations lead to the formation of wave like structures (**C**). In addition, an enhanced directional persistence is observed with increasing filament density. The trajectory of the clusters is shown by a colour coded time overlay of their movements in time (white line) (**A** and **B**). The movement of the small cluster in (**A**) has a low persistence length $L_P \approx 65\,\mu m$. The cluster in (**B**) is larger, less prone to reorientations and exhibits a considerably higher persistence length $L_P \approx 65\,\mu m$. In the inset of (**C**) a zoom in and a local analysis of the average flow direction is shown. The density waves show only minor reorientations in the time period of several minutes. All scale bars are $50\,\mu m$.

tween the elongated filaments limit the noise in the system. In principle this should induce a transition to an ordered state – just like it is the case in passive systems in thermal equilibrium [68,159]. This transition and the properties of the ordered state are examined in the subsequent chapters.

## 2.2 Transition to collective motion

To investigate the stability and dynamics of an active ordered phase, the filament density $\rho$ is chosen as control parameter and is systematically varied. Dependent on the density $\rho$ two phases are discernable: a disordered phase below a critical density $\rho_c$ of $\approx 5$ filaments per $\mu m^2$ and an ordered phase above $\rho_c$. Increasing the filament density above $\rho_c$, results in a transition to an ordered phase which is characterized by a polymorphism of different polar-nematic patterns, coherently moving with the speed $v_0$ (Figure 2.3 A – C).

These patterns can be further classified according to their size, orientational persistence, overall life time and assembly/disassembly mechanisms: in an intermediate density regime above $\rho_c$ moving clusters (swarms) of filaments appear; in the high density regime starting at a threshold density of $\rho*$ ($\approx 20$ filaments per $\mu m^2$) propagating waves start to form. As common feature both patterns are characterized by persistent density modulations.

The clusters encountered in the intermediate state move independently and exhibit cluster sizes ranging from about $20\,\mu m$ to more than $500\,\mu m$ in diameter (Figure 2.3 A and B). In general, clusters exhibit an erratic motion with frequent reorientations of low directional persistence (Figure 2.3 A and B). This low directional persistence affects the clusters' shape but barely influences its temporal stability. The cluster integrity is only affected, if collisions with boundaries or other clusters are encountered. Increasing the filament density in this intermediate regime not only yields larger clusters, but also a more persistent cluster movement. Individual clusters spontaneously emerge

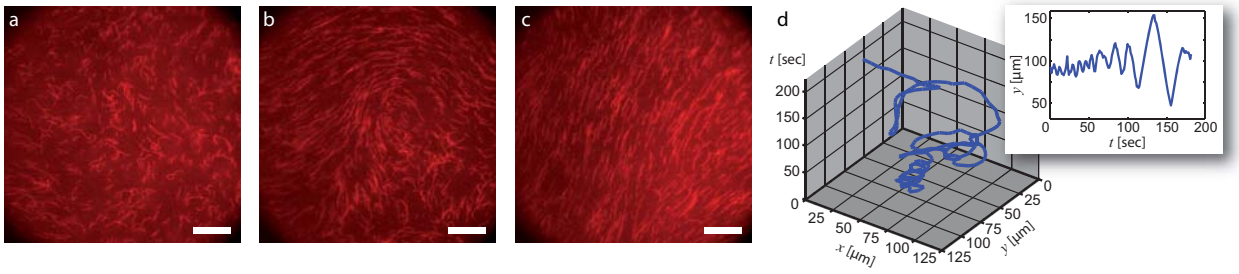


**Figure 2.4: Emergence of ordered structures.** Images (**A**) – (**C**) illustrate the gradual formation of ordered structures starting from an apolar and homogeneous basic state. After the addition of ATP, the filaments move in an oscillatory manner on circular trajectories with a growing radius as can be seen in (**D**), where the trajectory of an individual filament is shown. The orientational instability results in the gradual emergence of ordered zones that successively coarsen. The further the ordering has progressed, the more space is cleared for further binding of filaments to the motor proteins at the surface and initially only partly bound filaments can bind fully. Consequently, the apparent filament length at the surface increases concomitantly with increasing order. The filament density amounts to $\rho = 21\,\mu\mathrm{m}^2$ and the scale bar is $20\,\mu\mathrm{m}$.

from the dilute and disordered background and continuously loose and recruit filaments. As long as single clusters move embedded in this homogeneous disordered background, this uptake and loss dynamics is balanced and leads to cluster sizes stable for several minutes.

A further increase of filament concentration above $\rho*$ results in density waves characterized by correlated movement of high density regions. In this high density regime, the filaments move predominantly in bands which are stable throughout the observation time (up to $30\,\mathrm{min}$). They exceed the size of their constituent filaments by up to three orders of magnitude, almost spanning the entire system and comprising a crescent-shaped substructure. The appearance of the bands is a generic feature of the high-density motility assay. While filaments in the high density regions move collectively with a high orientational persistence, filaments lying outside the bands perform persistent random walks.

## 2.3 Properties of the ordered state

### 2.3.1 Emergence of collective motion

One key aspect in understanding the structure formation in the system lies in the observation of their emergence. In order to visualize the emergence of the density waves, samples were prepared in the absence of ATP at filament densities above $\rho_c$. On that condition, the filaments bind to the motors in the rigor state in an isotropic and homogenous manner, where no orientational preference of the filaments is observable. Upon addition of ATP, molecular motors are activated and filaments start to move in an uncoordinated fashion. Local interactions result in the emergence of small polar zones that span the width of a few filaments only and exhibit small wavelength oscillations (Figure 2.4). This is similar to theoretical model systems where the constituents interact through inelastic collisions [72]. The successive coordination and synchronization of extended coherently moving areas results in the formation of domains which grow larger and move with increasingly greater persistence (Figure 2.4).

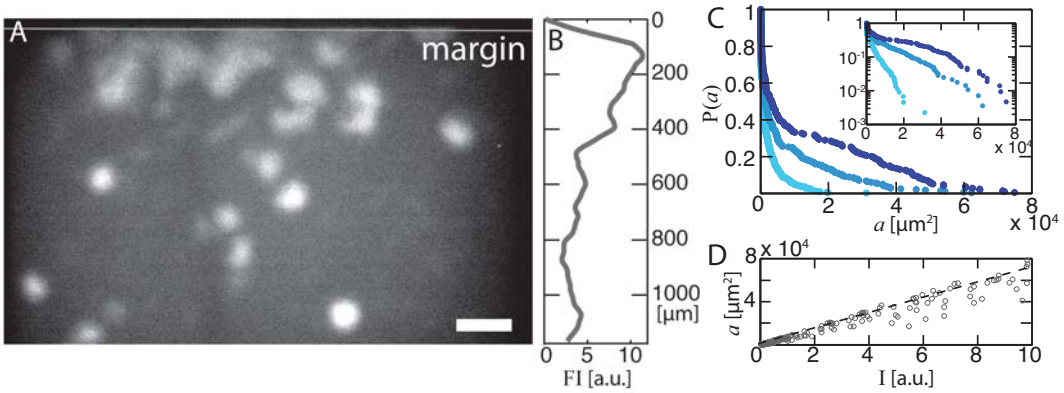


**Figure 2.5: Large scale density inhomogeneities and cluster size distributions in high density motility assay experiments.** Characteristically, the filament density close to the margin of the active region is much higher than in the center (**A**). Despite the individual filament is only several $\mu m$ long, the collective motion leads to phase separation on macroscopic length scales. This also becomes manifest in the line-averaged fluorescence intensity shown in **B** that is three times higher close to the margin of the flow chamber than in the center. The filament density was adjusted to $\rho = 7 \pm 2\,\mu\mathrm{m}^{-2}$. In **C**, the cumulative cluster size distribution $P(a)$ is plotted as a function of the area of the cluster for three different filament densities (dark blue: $\rho \approx 17\,\mu\mathrm{m}^{-2}$; light blue $\rho \approx 9\,\mu\mathrm{m}^{-2}$; cyan $\rho \approx 6\,\mu\mathrm{m}^{-2}$). For low densities (cyan), the cluster sizes are approximately exponentially distributed. For higher filament densities (dark and light blue), the probability to find large clusters increases compared to the exponential distribution. In **C**, the area $a$ of the identified cluster is chosen as measure for the cluster size. The fluorescence intensity $I$ of an identified cluster provides an equivalent measure for the cluster size, as exemplified in **D**, where the area is plotted as function of the fluorescence intensity. The scale bar is $200\,\mu\mathrm{m}$.

### 2.3.2 Large scale density inhomgeneities and clusters of collectively moving filaments

Motility assay experiments at high filament densities are characterized by huge density inhomogeneities. They do not only become manifest in the self-organized formation of coherently moving structures such as density waves and clusters, but also in large scale density inhomogeneities throughout the entire flow chamber. This becomes most evident for small filament densities, where the systems self-organizes into clusters of collectively moving filaments (Figure 2.5). The better part of the clusters is located close to the margin of the chamber, whereas the density in the middle of the flow chamber is depleted (Figure 2.5 A). This is retrieved in the line-averaged fluorescence intensity throughout the flow chamber (Figure 2.5 B) which is three times higher close to the margin than in the center of the flow chamber.

It is this local filament density that sets the size of the collectively moving structures. This is demonstrated in Figure 2.5 C, where the area of the identified clusters is shown for different filament densities. For small filament densities close to the onset of collective motion, the cluster sizes are exponentially distributed. For higher filament densities, the probability of finding larger clusters is considerably higher, visible in a pronounced peak for large clusters (Figure 2.5 C, dark blue curve).

Importantly, the filament packing inside the clusters is independent of the cluster size or the filament density. Consequently, plotting the area $a$ as function of the fluorescence intensity $I$ yields a linear relationship (Figure 2.5 D). This is equivalent to a maximal packing fraction that apparently is independent of the structure size and the filament density.

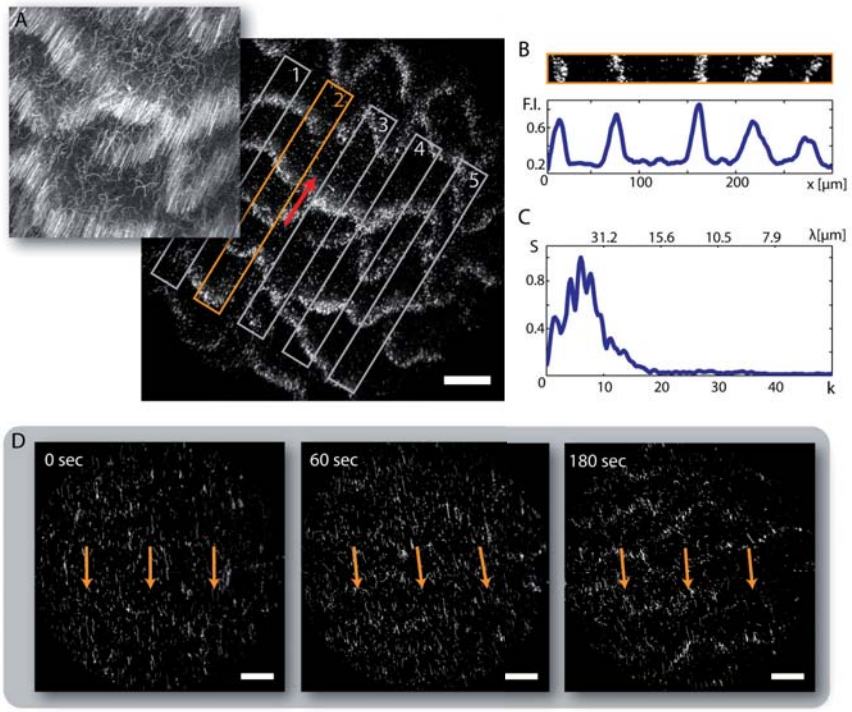


**Figure 2.6: Characteristics and emergence of density waves.** Within the bands, filaments move in straight trajectories parallel to the mean direction of the traveling density wave (red arrow). This can be seen from the time overlay in **A**, where 10 consecutive images in a time period of $T = 11.7\,\mathrm{sec}$ were projected on the underlying image. To extract the fluorescence intensity profiles and the associated power spectra, images were subdivided into five equally spaced reference frames, each with a length of $\approx 300\,\mu\mathrm{m}$ and a width of $\approx 30\,\mu\mathrm{m}$ that co-rotate with the mean direction of motion (**A** and **B**). To obtain an averaged power spectrum this procedure was carried out for three time points in three independent samples respectively. This spectrum that is shown in **C**, is peaked at a wavenumber of $k = 6$ corresponding to a band spacing of $\approx 50\,\mu\mathrm{m}$. Image **D** shows the gradual emergence of density waves, which occurs at sufficiently high densities. Well defined density waves only develop after a transient in the order of several minutes. The scale bars are $50\,\mu\mathrm{m}$.

### 2.3.3 Density waves

The formation of density waves relies on the amplification of density fluctuations on the single filament level. Individual filaments do not always perfectly follow the mean direction of motion inside a collectively moving cluster, but deviate from it. As a consequence, they get run over by the other filaments – and get relocated to a different position inside the cluster, when they realign their direction of motion. This realignment is due to collisions with other filaments. Consequently, realignment-events are more likely to occur in zones where the density is already enhanced, amplifying density inhomogeneities even more. Inside small clusters these density inhomogeneities get annihilated by large scale directional rearrangements that homogenize the particle density again. For large structures above $\rho*$, however, the directional persistence is so high that the density inhomogeneities are not smoothed out anymore. Gradually this leads to the formation of dense bands of collectively moving filaments above for filament densities $\rho*$.

This can be demonstrated, by observing the temporal evolution of the underlying density instability (Figure 2.6). An isotropic and homogenous state, prepared in the absence of ATP, is rapidly evolving into a homogeneously moving polar state upon addition of ATP. The subsequent emer-

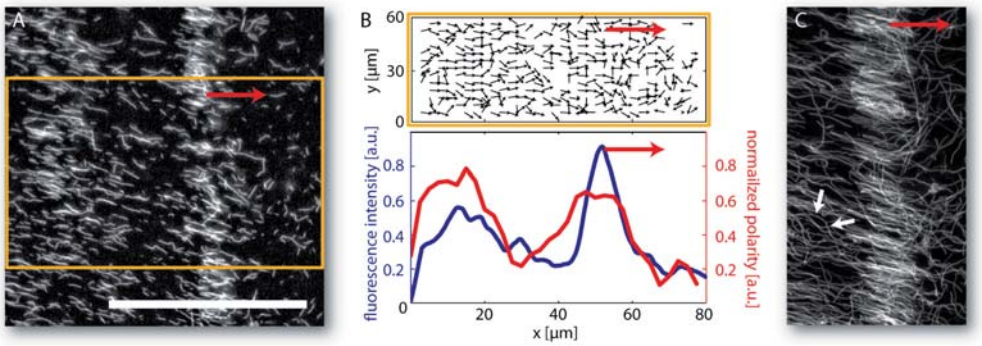


**Figure 2.7: Density and polarity profiles along a traveling wave band.** Filament density and polarity are calculated in a reference frame (yellow box), co-rotating with the average direction of motion (red arrow) (**A**). The filament density along the direction of motion is proportional to the fluorescence intensity shown in blue (**B**). The polarity shown in red, is calculated by evaluating the velocity profile obtained by particle image velocimetry (**B**, upper picture; every $4^{th}$ vector displayed). While the filament density is clearly peaked, exhibiting a symmetric profile across the high density band, the polarity is asymmetric with a decaying tail. This tail is due to a lateral memory effect stemming from the persistence of the single filament motion. Since individual filaments cannot immediately adopt the direction imposed by the high density band, they perform straight trajectories in the dense band and curved shaped paths after leaving the band. This can be seen in the time overlay of 10 consecutive images depicted in (**C**, white arrows). The scale bar is $50\,\mu$m.

gence of density waves requires a minimal orientational persistence which is only provided by the high densities above $\rho*$. In this regime, local de-correlation mechanism are not effective enough to result in the immediate destruction or reorientation of the polarity of the entire transient homogenous state. Yet, they induce persistent density fluctuations which grow gradually in time to form the characteristic density waves (Figure 2.6 D). This can be seen in a dynamic Fourier analysis of the density profile in a reference frame along the mean direction of motion. Initially, there is a wide band of wavelengths, but after several minutes the power spectrum is peaked at about three times the persistence length of individual filaments at approximately $50\,\mu$m (Figure 2.6 C).

Along the direction of movement, the density waves are characterized by an abrupt change of the filament density (Figure 2.7 A). While the density profile is symmetric, the orientational order exhibits a rather asymmetric shape with a sharp front edge and a decaying tail (Figure 2.7 B). This is due to the fact that the randomly moving filaments are oriented by the moving bands, but cannot immediately adopt to this imposed reorientation. As a consequence they follow a circular-shaped trajectory and eventually get run over by a high density band (Figure 2.7 C). In the low density zone, they gradually loose this directional bias due to the randomized movement at low filament densities.

This lateral memory effect is intimately related to the persistence of the single filament motion, as well as to microscopic interactions between individual filaments which are short-ranged in nature. It is best seen in low density motility assays, where encounters between filaments most frequently lead to crossing events with only slight reorientations. Rarely, a steric repulsion with an instantaneous and significant directional change of the filaments is observed.

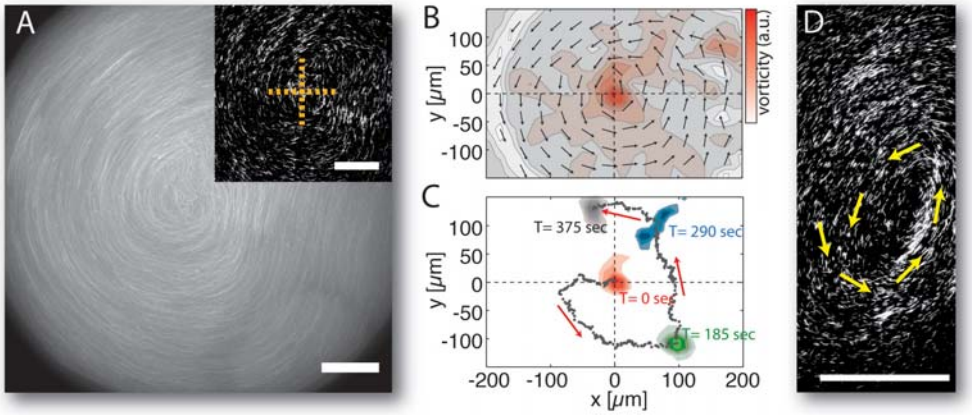


**Figure 2.8: Swirling Pattern of coherently moving filaments.** In (**A**) the swirling motion is visualized by a time overlay of $1.17\,\mathrm{sec}$ (10 consecutive images) starting from the image depicted in the inset. Since all filaments move with the same velocity $v_0$, swirls are characterized by huge angular velocity gradients leading to an inherent destabilization of the pattern. The resulting unsteady movement can be studied by evaluating the velocity fields and the corresponding vorticity profile as shown in (**B**). The maximum of the vorticity profile, marking the center of the counter clockwise rotating swirls, performs a counter clockwise trajectory, as can be seen in (**C**). In the course of this movement, a deformation of the initially well defined swirl develops ($T = 290\,\mathrm{sec}$) eventually leading to disintegration of the swirling pattern. The limited stability of swirling motions is visible in the vicinity of the center region, where crushing events of the filament currents are likely to develop (**D**). All scale bars are $50\,\mu\mathrm{m}$.

### 2.3.4 Swirling motion

In all states above $\rho_c$ also swirls or spirals of actin filaments can be observed, reminiscent of spiraling patterns predicted by active gel theory [96]. They form spontaneously either from the random movement of bands or individual clusters or upon the collision of different actin bands or clusters (Figure 2.8 A, B and D). These rotating structures are visible for up to ten minutes, before they dissolve or merge with adjacent and interfering structures. Since all filaments move at the same speed $v_0$, huge gradients of angular velocity are generated throughout a swirl, leading to an inherently metastable structure most often with an unsteady and even moving centre (Figure 2.8 C).

## 2.4 Statistical properties of collective motion

To elucidate the physical principles that underly collective motion, numerous theoretical studies have been devoted to model self-propelled particle systems at high particle densities. They approach the problem on all levels of description ranging from agent-based simulations [29, 30, 38, 71, 213] and mesoscopic models coarse-graining microscopic interaction rules [3, 5, 13, 14, 17] to mean field models in the hydrodynamic limit [114, 186, 207]. The dynamic properties of all these models are strikingly similar to the phenomena observed in experimental systems. Yet, all these models naturally rely on different, partly empirically chosen parameters, hampering a one-to-one quantitative comparison between different models and related experiments.

Instead, it proved favourable to identify and compare key properties that characterize collective motion independent of the exact parameter values. These hallmarks of collective motility include the occurrence of abnormally large fluctuations in the particle density, the so called giant number

fluctuations [30, 49, 50, 154, 186, 207, 239] and correlations that are anisotropic with respect to the direction of collective motion [148, 207, 213].

Despite the utmost importance of these unifying observables for the comparison between theoretic approaches and experiments, most experimental systems studied to date defy their unambiguous measurement. Neither it was possible to pinpoint the underlying microscopic mechanisms, nor to elucidate how the coupling between order and particle density can give rise to these phenomena. On the one hand, this can be attributed to the limited system size of most experimental setups, whereas theoretic predictions are based on infinitely large system sizes in the mean field limit. On the other hand, many experimental systems are prone to rely on higher ordering principles such as the exchange of signals or even cognitive processes.

In this context, the motility assay is ideally suited to bridge between theory and experiments. The molecular nature of the system allows us to access and control the mean field properties of collectively moving driven filaments with only a few and easily adjustable key parameters and at the same time permits large system sizes and high particle densities. In the subsequent section it is shown that the dynamical, statistical, and morphological properties of collectively moving propelled particle suspensions result from a close coupling between the density and the velocity field of the propelled particles. The emergence of collective motion is always accompanied by anomalously large and long-lived fluctuations in the filament density that emanate from directional fluctuations in the velocity field. These directional fluctuations are anisotropic and decorrelate faster longitudinal to the direction of motion than perpendicular to it. As the density field is coupled to the velocity field, this results in anisotropic density fluctuations that also become manifest in the morphology of the collectively moving structures.

### 2.4.1 Giant density fluctuations

Above a critical filament density of $\rho_c \approx 5\,\mu\mathrm{m}^{-2}$, the driven filaments form an ordered phase of polar aligned and collectively moving filaments. The ordered phase is characterized by persistent density inhomogeneities as the filaments self-organize to form coherently moving structures such as homogenous clusters and density waves [24, 171]. However, already in a regime where the overall filament density is still homogeneous (Figure 2.9 A and B) and where large-scale density currents are absent, the filament density shows anomalously large fluctuations. These temporal fluctuations of the filament density can be quantified by evaluating the fluorescence intensity $I$ of the filaments (Figure 2.9 C) that is directly proportional to the number of particles [3]. Instead of growing proportional to $\langle I\rangle^{0.5}$, as one would expect from systems in thermal equilibrium obeying the central limit theorem, the fluctuations of the fluorescence intensity $\Delta I$ grow far more rapidly proportional to $\langle I\rangle^{0.81\pm0.03}$. $\langle I\rangle$ denotes the mean intensity. Importantly, these giant number fluctuations only occur when the filaments have self-organized in collective motion patterns: below the onset of collective motion, where the filament density is not sufficient for collective motion to evolve, the filament density shows only normal random fluctuations, with $\Delta I$ scaling according to $\langle I\rangle^{0.5}$ (Figure 2.9 C). The occurrence of these anomalously large fluctuations in the ordered phase is intimately related to the lifetime of local density fluctuations $\delta I$ that can be quantified by their autocorrelation function[4]

$$G_{\delta I}(t) \;\propto\; \langle \delta I(T+t)\cdot \delta I(T)\rangle\,. \tag{2.1}$$

[3] For details see materials and methods section (A.2.2).

[4] Details of the calculation can be found in the materials and methods section (A.2.6)

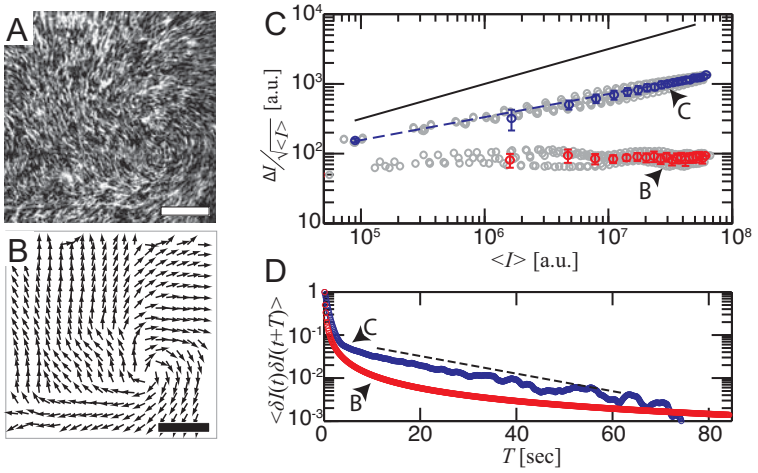


**Figure 2.9: Collectively moving filaments show anomalously huge fluctuations in the particle density.** At high F-actin concentrations the driven filaments form a polar phase of collectively moving particles (**A** and **B**). Besides the emergence of coherent particle currents, this phase is characterized by anomalously high fluctuations in the particle density. These fluctuations can be quantified by recording the temporal fluctuations of the fluorescence intensity $\Delta I$ for various subsystems of different sizes. (**C**) shows $\Delta I$ normalized by $I^{0.5}$ as a function of the mean intensity $\langle I \rangle$. For systems obeying the central limit theorem, these fluctuations should scale according to $\Delta I \propto \langle I \rangle^{0.5}$ – and in the absence of collective motion this is exactly the case (**C**, red data points). Above the critical density, where the individual filaments move collectively, these fluctuations become anomalously large and scale according to $\Delta I \propto \langle I \rangle^{0.81 \pm 0.03}$ (**C**, blue data points). These fluctuations are not only anomalously large in magnitude, but also very long lived, as can be seen from the auto-correlation $C(t) = \langle \delta I(T) \cdot \delta I(T+t) \rangle$ of the local density fluctuations $\delta I$ that denote local deviations from the overall mean density (**D**). While in the absence of collective motion density fluctuations decorrelate diffusively according to $C(t) \propto t^{-1}$ (**D**, red data points), fluctuations in the collectively moving phase show a pronounced exponential contribution for long time scales (**D**, blue data points). The filament density was adjusted to $\rho = 12 \pm 2\,\mu\mathrm{m}^{-2}$ and the average filament length was $6.8\,\mu\mathrm{m}$. All scale bars are $50\,\mu\mathrm{m}$.

In the ordered phase, $G_{\delta I}(t)$ decays according to $G_{\delta I}(t) \propto t^{-1}$ on short time scales. For longer time scales, however, $G_{\delta I}(t)$ shows a pronounced exponential contribution (Figure 2.9 D). It is this exponential contribution that discriminates the ordered state from the disordered state, where $G_{\delta I}(t)$ decays according to $G_{\delta I}(t) \approx t^{-1}$ for all times. Thus, the fluctuations in the ordered phase are not only anomalously large in magnitude, they are also very persistent.

But what exactly is responsible for these intriguing statistical properties that sharply discriminate the ordered from the disordered phase? Plainly, the main difference between the two phases is the emergence of coherent currents of collectively moving filaments (Figure 2.10 A). To investigate this coupling, we calculate the coarse grained velocity field $\mathbf{v}(\mathbf{r}, t)$ of the collectively moving particles with a particle image velocimetry scheme [53, 171]. Indeed, the dynamic properties of the velocity field and the density field are closely related: qualitatively, at points where the velocity field converges and has a sink, material is accumulated and the density increases, while at points where the velocity field has a source, material is transported away and the density locally decreases (Figure 2.10 B and C). The change in density as a response to local defects ($\mathrm{div}(\mathbf{v} \neq 0)$) is only one part of the coupling between the density and the velocity field. The sinks and sources in the velocity field are not stationary either. They constantly dissolve and emerge, but are also advected within the velocity field. This dynamics of the distorsions is closely related to the local filament density: defects emerge predominately at spots with a low filament density and are advected from high to low filament densities. Physically, this happens because the filaments are less ordered and thus

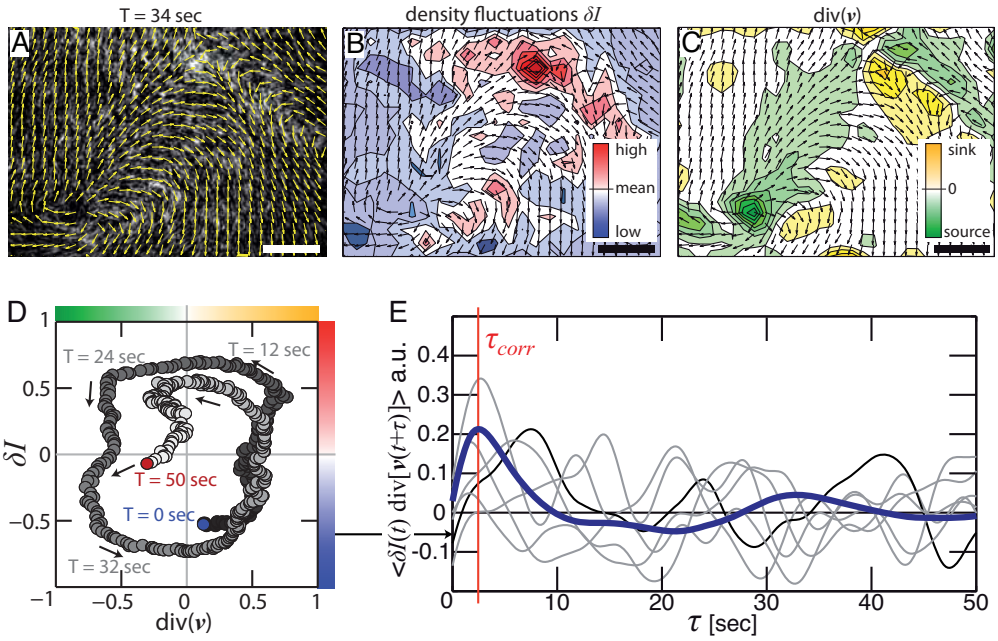


**Figure 2.10: Fluctuations in the particle density arise from the coupling between density and velocity field.** (**A**) shows a typical velocity profile of collectively moving filaments. The phase of collectively moving filaments is always characterized by local density fluctuations that can be quantified by the local deviation $\delta I$ from the mean fluorescence intensity, as shown in (**B**). These density fluctuations naturally coincide with local defects in the velocity field. At spots where material moves away from, i.e. where the velocity field has a source ($\mathrm{div}(v) < 0$), the local density is reduced; at sinks in the velocity field ($\mathrm{div}(v) > 0$), the local density is increased (**C**). Both, the local density fluctuations and the defects in the velocity field are highly dynamic: they constantly form and dissolve and are advected with the fluid. This is exemplified in (**D**), where the temporal evolution of $\delta I$ and $\mathrm{div}(v)$ for a local spot is shown. Starting at $T = 0\,\mathrm{sec}$ a sink in the velocity field develops and the local density rises until the packing of the filaments is maximal and no more material can accumulate ($T \approx 12\,\mathrm{sec}$). Consequently, the sink has to either dissolve or move to a different spot. A source develops that reduces the material density again ($T \approx 12\,\mathrm{sec}$ – $24\,\mathrm{sec}$). Low densities are not stable either: due to the sparse packing, individual filaments fluctuate more, thereby generating new defects. A sink emerges and the cycle starts over. The coupling between the morphology of the velocity field, quantified by $\mathrm{div}(v)$ and the density fluctuations $\delta I$ is a general signature of the dynamics in the system. This can be seen from the temporal correlations between $\mathrm{div}(v)$ and $\delta I$ depicted in (**E**). Light gray curves denote sample correlation functions for different local spots; the black curve illustrates the correlation for the spot shown in (**D**) and the blue curve is the ensemble average over 768 independent spots. The correlation function is maximal for a finite correlation time $\tau$, illustrating the delayed coupling between $\mathrm{div}(v)$ and $\delta I$. The filament density was adjusted to $\rho = 12 \pm 2\,\mu\mathrm{m}^{-2}$ and the average filament length was $6.8\,\mu\mathrm{m}$. All scale bars are $50\,\mu\mathrm{m}$ and the local spot size for the data shown in D and E was set to $10\,\mu\mathrm{m}$ x $10\,\mu\mathrm{m}$.

exhibit stronger directional fluctuations at spots with low filament densities. Moreover, local sinks in the velocity field are not stable either: they only persist as long as the further accumulation of material is not limited by a too high local material density due to excluded volume effects.

Thus, the density not only follows the flow field, but the dynamic transport of defects within the flow field is also tightly coupled to the filament density. This bidirectional coupling between density and velocity can even lead to persistent local oscillations of the filament density and the velocity field (Figure 2.10 D): conceptually, a sink $(\mathrm{div}(\mathbf{v}) > 0)$ in the velocity field locally causes a rise in density until the local density is so high that no more filaments can be accumulated. At this point, the sink either has to dissolve or move to lower densities. This in turn causes a density outflux in the respective region and a source develops $(\mathrm{div}(\mathbf{v}) < 0)$. The decreased density leads

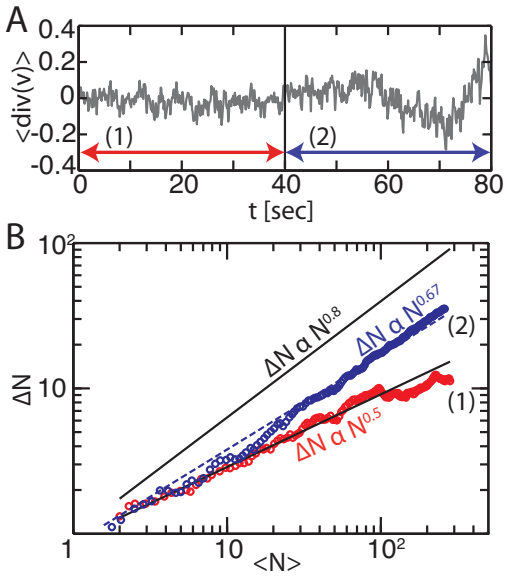


**Figure 2.11: Steady currents without defects lead to normal fluctuations.** (**A**) shows the overall divergence of the velocity profile of a filament current. Within the first $40\,\mathrm{sec}$ (stage 1), the current is extremely steady and lacks any defects like splay and especially sinks and sources. The fluctuations that are visible are due to uncertainities stemming from the particle image velocimetry analysis. After $40\,\mathrm{sec}$ (stage 2), the filament current performs a slight and gradual turn, visible in a non-vanishing contribution in the divergence of the velocity field (**A**). In the first $40\,\mathrm{sec}$, where the current is perfectly steady the particle fluctuations are normal and scale according to $\Delta N \propto N^{0.5}$ (**B**, red data points). Although the turning event that sets in after $40\,\mathrm{sec}$ is only slight and evolves very gradually, it still leads to transient local density inhomogeneities. These inhomogeneities directly become visible in the fluctuations in the particle density: compared to the first time period, the fluctuations are considerably higher and scale according to $\Delta N \propto N^{0.67}$ (**B**, blue data points). The filament density was adjusted to $\rho = 12 \pm 2\,\mu\mathrm{m}^{-2}$ and the average filament length was $1.1\,\mu\mathrm{m}$.

to stronger fluctuations in the velocity, until the density rises again. A sink emerges and the cycle starts over. The region of these local oscillations can extend up to $200\,\mu\mathrm{m}$ in diameter with a corresponding oscillation period of up to $30\,\mathrm{sec}$ (Figure 2.10 D).

The bidirectional coupling between local defects in the velocity field and the density can further be quantified by introducing the averaged local temporal correlation function

$$\Gamma(t) \;=\; \langle \delta I(T) \cdot \mathrm{div}(v)(T+t) \rangle \tag{2.2}$$

between the density fluctuations $\delta I$ and the divergence of the velocity field $\mathrm{div}(v)$ measuring the strength of the sinks and sources in the velocity field (Figure 2.10 E). Remarkably, the correlation between density fluctuations and the divergence of the velocity field is maximal for a finite time $t = \tau = 2.4\,\mathrm{sec}$, before it decays. The maximum at $\tau$ indicates that the coupling between density and velocity is characterized by a delay-time of the order of $\tau$. This implies that the density follows distortions in the flow field only with a certain retardation and that density changes result from local defects in the velocity field and *vice versa*. By contrast, in the absence of local defects, for a perfectly homogenous and steady current with $\mathrm{div}(v) = 0$ no anomalously large fluctuations do emerge (Figure 2.11).

### 2.4.2 Anisotropic spatial correlations

The directional fluctuations that underlie the formation of distortions in the velocity field are strongly anisotropic with respect to the direction of motion, as can be seen from the angle dependent two-point velocity correlation function[5]

$$P_v(\mathbf{r},\alpha) \propto \langle v(\mathbf{R}+\mathbf{r},\alpha)\cdot v(\mathbf{R})\rangle\,, \tag{2.3}$$

with $\alpha$ being the angle between $v(\mathbf{R})$ and $\mathbf{r}$ (Figure 2.12). While the velocity field is highly correlated transversal to the direction of movement ($\alpha = 90°$, $270°$), $P(\mathbf{r},\alpha)$ decays faster along the direction of motion ($\alpha = 0°$) (Figure 2.12 A). Both, longitudinal and transversal to the direction of motion, velocity correlations can be described by stretched exponential according to

$$P_v(\mathbf{r},\alpha) \propto \exp(-\Gamma/x)^{-\beta} \tag{2.4}$$

with a stretching exponent of $\beta = 1.2$ and a correlation length of $\Gamma = 197.4\,\mu\mathrm{m}$ transversal (averaged over $\alpha = 90°$ and $\alpha = 270°$) and $\Gamma = 149.7\,\mu\mathrm{m}$ longitudinal ($\alpha = 0°$) to the direction of motion, respectively (Figure 2.12 B). Apart from the pronounced anisotropy, the correlation function shows a pronounced asymmetry along the direction of motion (Figure 2.12 B). While the correlation length ahead of the direction of motion ($\alpha = 0°$) averages to $\Gamma = 149.7\,\mu\mathrm{m}$, it is considerably enhanced behind the direction of motion ($\alpha = 180°$) where $\Gamma = 168.6\,\mu\mathrm{m}$. This asymmetry can be attributed to a lateral memory effect within the collectively moving flock: succeeding filaments that lie in an angular sector of around $\alpha = 180°$ cannot immediately loose the orientational bias of the leading filaments, naturally enhancing the correlation in this direction.

Microscopically, the anisotropy that characterizes the collective motion of driven filaments stems from the extreme aspect ratio of the individual filaments. With a length in the order of $10\,\mu\mathrm{m}$ and a thickness of $7.5\,\mathrm{nm}$ the filaments have an aspect ratio of around $1,000$. It is this extreme aspect ratio that allows for an efficient alignment and a swift information transfer transversal to the direction of motion. Conceptually, any change in this aspect ratio should become manifest in both, the overall correlation length and the anisotropy of the velocity field. This is indeed the case: While the shortening of the filaments[6] only barely affects the phase behavior of the system, the correlation length of the velocity field drastically decreases (Figure 2.12 C). With a correlation length in the order of $100\,\mu\mathrm{m}$, velocity correlations decay two fold faster for short, on average $0.8\,\mu\mathrm{m}$ long filaments, than for filaments with an average length of $6.8\,\mu\mathrm{m}$. The decrease in the overall correlation is accompanied by a concomitant decrease in the anisotropy of the velocity field (Figure 2.12 C), illustrating that shorter filaments provide a less effective information transfer transversal to the direction of motion.

According to the identified coupling between density and velocity, this anisotropy should also become manifest in the dynamical properties of the density field. As can be inferred from the correlation map of the density fluctuations

$$P_{\delta I}(\mathbf{r},\alpha) = \langle \delta\mathrm{I}(\mathbf{R}+\mathbf{r},\alpha)\cdot \delta\mathrm{I}(\mathbf{R})\rangle\,, \tag{2.5}$$

this is indeed the case (Figure 2.13 A). Just like the velocity, the density fluctuations are anisotropic and decay faster along the direction of motion than perpendicular to it (Figure 2.13 B). The observed anisotropy in both, the density fluctuations and the velocity field, has severe consequences

[5] Details of the calculation can be found in section A.2.5 in the materials and methods chapter.

[6] A detailed description of the procedure including the corresponding filament length distributions can be found in the materials and methods section A.1.1.

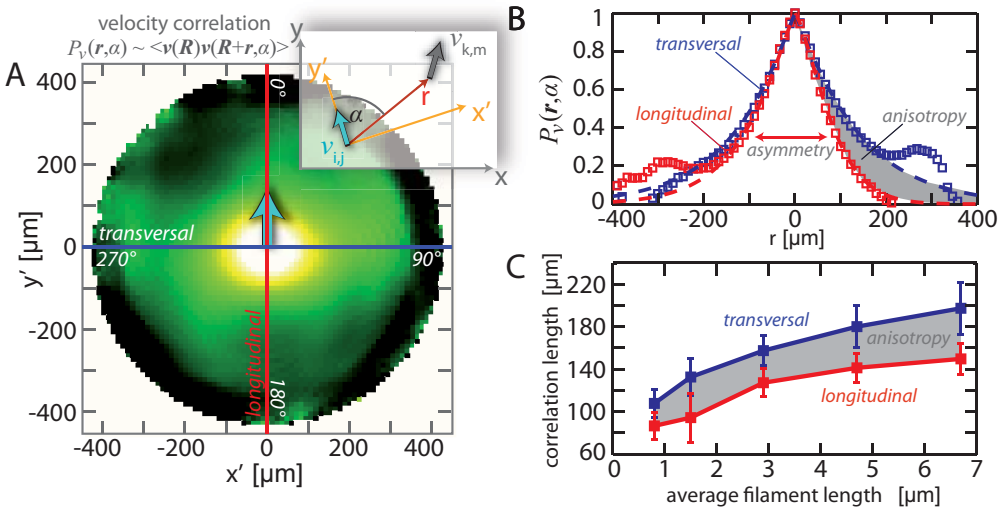


**Figure 2.12: The correlation of the flow profile is anisotropic.** (**A**) shows the correlation map of the velocity field of coherently moving filaments. To quantify the angle dependent correlation in the system, the correlation function is evaluated in a coordinate system that co-rotates with the local direction of motion (inset). The resulting correlation of the velocity field is anisotropic with respect to the direction of motion and shows a pronounced asymmetry in the transversal direction (**B**). In all cases, the correlation functions can be described by stretched exponentials according to $\exp(-\Gamma/x)^{-\beta}$ with a stretching exponent of $\beta = 1.2$ (dashed lines). Both, the anisotropy and the correlation length $\Gamma$, are a function of average filament length (**C**). In general, shorter average filament lengths lead to smaller correlation lengths with a concomitantly decreasing anisotropy. The filament concentration was adjusted to a monomeric concentration of $18\,\mu$M.

for the dynamic structure formation of the driven filaments. Practically, the enhanced correlation transversal to the direction of motion means that density accumulations transversal to the direction of motion are more stable than along the direction of motion and by consequence they get amplified. This explains the formation of traveling bands of propagating filaments at high filament densities above 20 filaments per $\mu m^2$ [171]. Besides, the anisotropy in both the velocity and density correlations also becomes manifest in the cluster phase at lower filament concentrations. While the cluster sizes are a function of the filament density, the morphology of the clusters is determined by the collective dynamics of the coherently moving filaments: on average clusters are predominately oblate with their long axis pointing perpendicular to the direction of motion – independent of the cluster sizes (Figure 2.13 C) [7].

### 2.4.3 Temporal correlations of the particle velocity

A key characteristic of pattern forming systems is their dynamics and stability far away from thermal equilibrium. While some systems result in stationary patterns, which do not change their form and structure in time, others may show highly dynamic spatio-temporal patterns. The latter rely on a constant reorganization governed by distinct assembly and disassembly pathways visible in the behavior of the order parameter. In the high density motility assay described here, these reassembly processes result in a characteristic orientational persistence, which increases with in-

[7] The data analysis tool that is used to extract the cluster sizes and the cluster morphologies is introduced in the materials and methods section A.2.1.

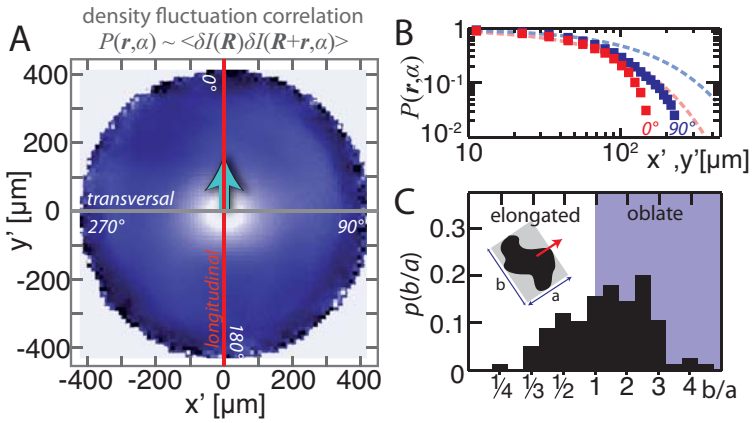


**Figure 2.13: The anisotropy in the correlation of the density fluctuations affects the morphology of clusters of collectively moving filaments.** Like in the case of the velocity (Figure 2.12), correlations $P_{\delta I}(\mathbf{r}, \alpha)$ among intensity fluctuations $\delta I$ are anisotropic (**A**). Compared to correlations of the velocity field, the correlation length is approximately a factor of two smaller and the anisotropy is less pronounced (**B**). The dashed lines denote the corresponding velocity correlation functions (c.f. Figure 2.12 B). The anisotropy of the density correlations with respect to the direction of motion also becomes manifest in the morphology of the collectively moving clusters. **C** shows the distribution of the main axes a and b of a moving cluster (**C**, inset). $b$ denotes the axes length perpendicular to the direction of motion (red arrow); $a$ is the length of the main axes alongside the mean direction of motion. While a ratio of $b/a = 1$ is equivalent with a spherical cluster, $b/a > 1$ denotes an oblate cluster that is stretched out perpendicular to the direction of motion and $b/a < 1$ results from an elongated cluster. As can be seen from the distribution of $b/a$-values in (**C**), clusters are predominantly oblate, once again exemplifying the close coupling between density, velocity and morphology of the structures. The filament density was adjusted to $\rho = 12 \pm 2\,\mu\mathrm{m}^{-2}$ and the average filament length was $6.8\,\mu\mathrm{m}$.

creasing filament density. Introducing the velocity autocorrelation function[8]

$$G(\tau) = \frac{\langle v(t+\tau) \cdot v(t) \rangle - \langle v(t) \rangle^2}{\langle v(t)^2 \rangle - \langle v(t) \rangle^2}, \tag{2.6}$$

the orientational persistence can directly be related to the underlying disassembly mechanisms. The velocity is calculated using a particle image velocimetry scheme (PIV). For each grid point of a PIV sampling grid $G(\tau)$ reflects local de-correlations assigned to local orientational fluctuations. Averaging over PIV grid points for a large sample area results in a spatially averaged autocorrelation function $\langle G(\tau) \rangle$, which characterizes global de-correlations resulting from correlated reorientations of larger areas or destructions of entire clusters or patterns.

All decorrelation mechanisms are governed by the persistence of the underlying random walk of the individual filaments and filament-filament interactions. Both processes prevent any instantaneous destruction of patterns. Right above $\rho_c$, in the intermediate concentration regime, the averaged autocorrelation function $\langle G(\tau) \rangle$ decays within seconds (Figure 2.14 A). The gradual increase of $\rho$ within this regime results in higher decorrelation times. Small clusters loose their global correlation either due to their limited overall orientational persistence or through large scale directional changes, such as bending. Bigger clusters frequently show an internal loss of polar order due to gradually developing splay patterns (Figure 2.14). While such internal cluster dynamics lead to a characteristic gradual change of $G(\tau)$, spontaneous bending predominantly observed for small clusters, shows rapid and large decorrelations (Figure 2.14 A).

[8] A detailed description of the calculation of $G(\tau)$ can be found in the materials and methods section A.2.5.

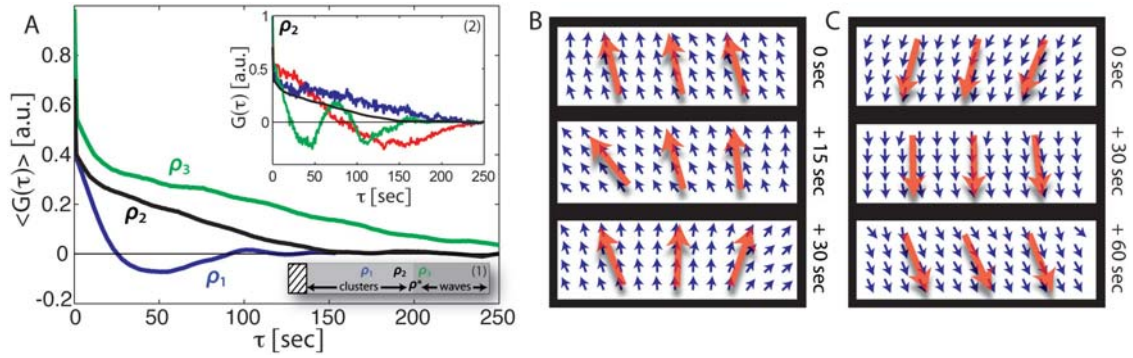


**Figure 2.14: Temporal correlations of the velocity field.** In (**A**) spatially averaged autocorrelation functions $\langle G(\tau) \rangle$ for three different densities $\rho_1 = 10\,\mu\mathrm{m}^{-2}$, $\rho_2 = 18\,\mu\mathrm{m}^{-2}$, $\rho_3 = 21\,\mu\mathrm{m}^{-2}$ are depicted. For the intermediate densities $\rho_1$ and $\rho_2$, homogenous structures are observed; $\rho_3$ is in the high density regime right above the transition to density waves $\rho*$ (see inset 1). With increasing filament density, the directional persistence of the polar current increases, visible in an enhanced correlation time from $\rho_1$ to $\rho_2$. The anticorrelation in the curve for $\rho_1$ reflects the systematic $180^\circ$ turns observed at small densities. Above $\rho*$, the correlation time is of the order of several minutes. Since the emergence of density waves requires a transient in the order of minutes and since reorientations annihilate density fluctuations, the high directional steadiness found in the high density regime is the precondition for the emergence of density waves. The local autocorrelation functions $G(\tau)$ depict the underlying decorrelation mechanisms (**B** and **C**). The anticorrelation as observed in the red curve, reflects a large scale reorientation of the entire structure. A splay like pattern (**B**) results in a local decorrleation shown in the blue curve, while oscillatory bending movement (**C**) results in a local decorrelation shown in green.

Since these directional instabilities are prone to develop at the margin of moving clusters, the enhanced stability of larger clusters, exhibiting a better area-to-boundary ratio is intuitive. Consequently, clusters below a diameter of $50\,\mu\mathrm{m}$ are rather unstable, as they tend to disintegrate from their margins, while the larger the clusters the longer lived they are. At the same time, larger cluster do show a less erratic motion with less frequent reorientations.

In the high density regime above $\rho*$, the decorrelation time averages up to several minutes, which implies ordered structures spanning length scales of the order of several millimeters. These density waves are only destroyed by global decorrelation mechanism, such as large scale reorientations. Provided that structures are more likely to disintegrate from their margins, and due to the closer packing within the highly ordered and interconnected bands, density waves are inherently more stable and less prone to bend and splay instabilities or the formation of swirls. Thus, the system self-stabilizes the coherently moving state and in turn, the slow decorrelation time is a prerequisite for the emergence of the density wave.

### 2.4.4 Transverse superdiffusion

The collective motion of driven filaments is highly correlated both in space and time. Despite this highly correlated collective motion, individual filaments still have remarkable degrees of freedom: generically, individual filaments considerably deviate from the mean direction of motion of the flock. This is illustrated in Figures 2.15 A and B, where an ensemble of filaments is tracked and followed over time. At $T = 0\,\mathrm{sec}$, a compact filament package is located in the center of the field of view. After $32\,\mathrm{sec}$, the filaments have considerably dispersed transversal to the mean direction of motion. This can also be seen from the trajectories of individual filaments that considerably deviate from the mean direction of motion (Figure 2.15 C).

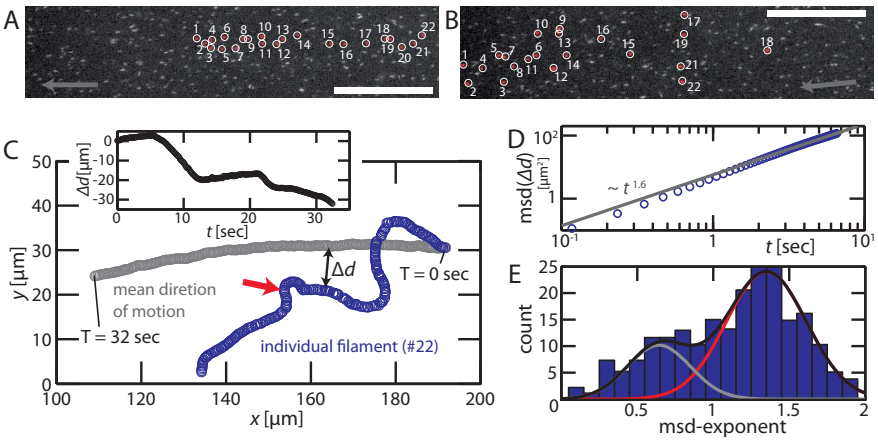


**Figure 2.15: Superdiffusive particle transport transversal to the mean direction of motion.** Image (**A**) shows a representative ensemble of filaments that are compactly located in the center of the field of view. The filaments collectively move to the left, in the direction of the white arrow. After 32 sec the filaments that initially were located close to each other have considerably dispersed (**B**). This is due to the fact that individual filaments can deviate considerably form the mean direction of motion, as can be seen in (**C**), where the trajectory of the mean direction of motion is compared to the trajectory of an individual filament. The distance $\Delta d$ between the mean direction of motion and the trajectory of individual filaments grows in time (inset) and individual filaments can even move in opposition of the mean direction of motion for short periods of time (red arrow). The mean squared displacement of the distance msd($\Delta d$) shown in (**D**), can be described by a power law $\propto t^{\alpha}$ with an appropriate diffusion exponent $\alpha$. Characteristically, for finite observation times, one finds two population, a superdiffusive population with $\alpha > 1$ where the filaments considerably deviate from the mean direction of motion, and a subdiffusive population with $\alpha < 1$ where the filaments more closely follow the mean direction of motion (**E**). Both populations can be described by a gaussian distribution (red and grey lines). The filament density was adjusted to $\rho = 12 \pm 2\,\mu\mathrm{m}^{-2}$ and the average filament length was $1.1\,\mu$m.

The dispersion of the filaments can be quantified by calculating the mean squared displacement of the relative motion $x_\perp$ perpendicular to the mean direction of motion:

$$\Delta x_\perp = \langle x_\perp(t) x_\perp(0) \rangle_t, \tag{2.7}$$

whereby $\langle . \rangle_t$ denotes the time average that is limited by the maximal observation time until the filaments have either left the field of view or the tracking algorithm has lost them. For normal diffusion, the mean squared displacement, $\Delta x \propto \tau^{\alpha}$, is expected to increase with time $\tau$ with a power law exponent $\alpha = 1$, while $0 \leq \alpha < 1$ or $1 < \alpha \leq 2$ are indicative of sub- or superdiffusion, respectively [22, 146, 147]. Figure 2.15 D shows a sample mean squared displacement that is superdiffusive with an exponent of $\alpha = 1.6$. For finite observation times, generically two populations of mean squared displacement exponents are found (Figure 2.15 D). While one part of the filaments shows a clear superdiffusive behavior with a pronounced maximum in the occurrence probability at $\alpha = 1.45$, the other part of the filaments is trapped in a subdiffusive state with an occurrence probability peaked at $\alpha = 0.62$. Both subpopulations can be described by gaussian distributions according to $\propto \exp[(\alpha/\sigma)^2]$. For the superdiffusive population, the variance is in the order of $\sigma = 0.5$ and for the subdiffusive population $\sigma = 0.3$.

While the occurrence of relatively broad distributions in the diffusive exponent $\alpha$ reflects the intrinsic degree of heterogeneity in the system, the existence of the two populations directly relates to the transport dynamics of the individual filaments. Generically, there are two states: inside a coherently moving flock a filament can either more or less strictly follow the mean direction of motion or it can deviate considerably from it. The former becomes manifest in subdiffusive expo-

nents and the latter leads to superdiffusive exponents. Moreover, the filaments can readily switch between these state: within fractions of seconds the filaments can change their motion pattern form superdiffusive to subdiffusive and *vice versa*.

The fact that the filaments can get reversibly trapped in a subdiffusive state can possibly be explained by the molecular conformation of the actin filaments. Actin filaments are semi-flexible; they can readily get entangled with each other all while being transported by the motor proteins. However, if the filaments are entangled with each other, the diffusion perpendicular to the mean direction of motion is restricted, leading to the occurence of the subdiffusive population. By contrast filaments that are not entangled have more degrees of freedom, which leads to the superdiffusive population. As the entanglement is reversible, the hypothesis of entangled filaments not only could provide an explanation for the occurrence of two populations, but also for the observed switching between the subdiffusive and the superdiffusive state.

### 2.4.5 Comparison to theoretic results

The ordered phase of collectively moving filaments shows some remarkable statistical properties: the fluctuations in the particle density are abnormally large (*i*), density and velocity correlations are anisotropic with respect to the direction of motion (*ii*), and the individual filaments perform a superdiffusive motion transversal to the mean direction of motion (*iii*). All these properties were predicted by generic theories in the mean field limit [206, 207, 213]. Meanwhile, they could be substantiated by agent based simulations [30, 71] and qualitatively verified in experiments on swarming bacteria colonies [239] and vibrated granular media [154], indicating that the statistical properties of collective motion are largely independent of the microscopic details of the system. The results obtained in this chapter now allow for an even more thorough and quantitative comparison to the theoretic predictions:

(*i*) **Particle fluctuations:** The scaling exponent of roughly $0.8$ that characterizes the particle fluctuations in the motility assay is in excellent quantitative agreement with the theoretic predictions and provides the first quantitative proof of this key signature of collective motion. It was first predicted by applying a dynamic renormalization group analysis to the coarse grained equations of motion of a flock of active polar particles [206, 207][9]. Moreover, the exponent of $0.8$ could be verified in agent based simulations [30]. The emergence of abnormally large fluctuations is intimately related to the occurrence of long lived density fluctuations. In the experiment, this can be seen in a pronounced exponential tail in the autocorrelation function of the density fluctuations defined in Equation 2.1. While the exact functional dependence is different from the theoretical prediction that foresees a logarithmic decay, the occurrence of long-time tails is in agreement with the theoretic predictions [207].

(*ii*) **Anisotropic correlations:** Even in the homogeneous regime, the correlations of the particle velocities and the density fluctuations are predicted to be highly anisotropic with respect to the direction of motion [207]. Recently, these results that are obtained form a dynamic renormalization group analysis, could be retrieved in agent based simulations [30] and by numerically solving the underlying equations of motion in the nonlinear regime [148]. Thus the theoretic predictions are in qualitative accordance with the results presented here. Yet,

[9] Initially, Toner and Tu calculated a value of $0.58$ for the scaling exponent of the particle fluctuations. The authors meanwhile recognize that they made a mistake and that the correct value is $0.8$. For further details I would like to refer to Reference [49] and there in particular to Reference [19].

the exact shape of the decaying correlation functions is still the matter of ongoing discussions: While the analytical results suggest a power law decay with different power law exponents characterizing the decay along and orthogonal to the direction of motion [207], the numerically obtained correlation functions [148] and the correlation functions observed in the motility assay suggest that the decay can rather be described by an exponential or stretched exponential.

(*iii*) **Transversal superdiffusion:** According to the predictions of Toner and Tu [206, 207, 213], the dynamics of the ordered phase of polar active particles should be characterized by a superdiffusive mean squared displacement transversal to the direction of motion. In particular, in two dimensions one has $\Delta x_\perp \propto t^\alpha$ with $\alpha = 4/3$. While this analytical result has successfully been tested by agent based simulations with [71, 213] and without cohesive interactions [30], the experimental verification of so far proved difficult. The results presented here provide the first experimental test for the theoretic predictions. However, the exact value of $\alpha = 1.45 \pm 0.5$ for the superdiffusive exponent slightly deviates from the theoretic predictions.

The experimental system studied here allowed to test three key predictions based on theoretic models for collectively moving particles: the occurrence of giant fluctuations, anisotropic correlations, and superdiffusive particle trajectories. In all cases, we found at least a qualitative agreement with the theoretic predictions. The slight discrepancies that were found concerning the exact scaling exponent for the superdiffusive particle currents and decay of the correlation function, are mainly attributed to two factors. First, most theoretic predictions are based on a one loop dynamic renormalization group analysis for a homogeneous and fully polarized basic state [206, 207, 213]. The analysis neither applies for intermittent, finite patterns like waves or clusters, nor for the emergence of topological defects like the sinks and sources that were identified to be crucial for the occurrence of large particle fluctuations. Second, the discrepancy may be attributed to the fact that the particle-particle interactions in the experiment are far more complex than in the simulations and the generic theories. In contrast to the model systems investigated so far, the filaments in the experiment are semi-flexible polymers. They interact by a weak excluded volume potential that is likely to be modified by entanglement effects between adjacent filaments, while the interactions rules in microscopic and mesoscopic theories are based on collisions of hard particles.

## 2.5 Agent based simulations

Despite the fact that the collectively moving structures are highly stable and very persistent, they still consist of millions of individual filaments. By consequence, the properties of the collective phase reflect the properties of the motion of individual filaments. This becomes evident from the erratic motion of small clusters that is determined by the probabilistic motion of individual filaments (Figure 2.3) and the superdiffusive particle transport transversal to the mean direction of motion (Figure 2.15). Moreover, the motion of individual filaments is responsible for a lateral memory effect that has been observed in the motion of density waves (Figure 2.7) and the asymmetry in the spatial correlations of the velocity (Figure 2.12). By consequence, an agent based simulation is desired that is based on the dynamics of individual filaments.

To investigate how the persistent random walk of individual filaments can lead to highly ordered collective motion, we developed a minimal agent based simulation that is motivated by the dy-

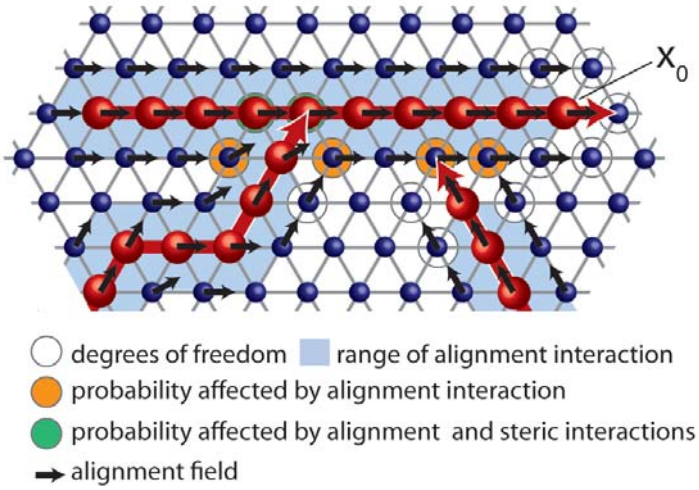


**Figure 2.16: Schematic representation of the cellular automaton simulations.** On the hexagonal lattice, the filament's head at $x_0$ has 5 degrees of freedom. The probability to move from $x_0$ to $x$ depends on whether or not a designated lattice site is occupied. The probability to advance to occupied lattice sites (yellow) is reduced by the the steric repulsion parameter $\zeta$. Moving filaments are influenced by an alignment interaction which is calculated as follows: Each filament carries a vector field. The projection of the normalized distance $x-x_0$ onto the local alignment field is taken as exponent of a power law to the basis of $\alpha$. The resulting factor reflects the change of the probability induced by the alignment interaction.

namics of single filaments. The agents are finite length filaments (length $L$) moving with a velocity $v$, each performing a persistent random walk and interacting with other filaments through steric repulsion, parameterized by $\zeta$, and weak local alignment interactions, parameterized by a parameter $\alpha$ (Figure 2.16). The simulation is implemented on a hexagonal lattice structure with reflective boundary conditions; all length are measured in units of the lattice constant. The velocity and thus the time scale is fixed by allowing each filament's head to move one lattice unit per time step. The particles' dynamics is assumed to be fully determined by its head, while the tail strictly follows the head's trail.

### 2.5.1 Details of the simulation

#### Persistent random walk

The persistent random walk is implemented by a stochastic process, where each filament's head at $x_0$ moves to one of its five neighboring sites $x$ according to a fixed set of conditional probabilities $\mathbf{P}$. The set of probabilities is given by a noise vector:

$$\mathbf{P} = (P_\mathrm{s};\ P_\mathrm{r};\ P_\mathrm{l};\ P_\mathrm{br};\ P_\mathrm{bl}), \tag{2.8}$$

where the indices s,r,l,br and bl mark the respective probabilities to move straight, right, left, back-right or back-left, respectively. For a fixed filament length $L = 10$ we choose the conditional probabilities such that each filament performs a persistent random walk with constant unit speed and a kinetic persistence length $l_\mathrm{kp} = 8.7$ lattice sites. The model includes an effective excluded volume interaction and a local alignment field. Both enter the model as multiplictative factors for the directional probabilities $\mathbf{P}$.

**Excluded volume**

For a lattice site that is already $k$-times occupied, the probability for further occupation is reduced by a Boltzmann factor $\exp(-k\zeta)$, where $\zeta$ characterizes the penalty for multiple occupations. Formally, for $\zeta \to \infty$, the limit of strict excluded volume is obtained [13, 148]. Analyzing weak penalties for multiple occupations (low $\zeta$) is appropriate for propelled particles that move in a quasi two dimensional thin-films, where crossings in the two dimensional plane of projection frequently occur [171, 172].

**Alignment interaction**

Motility assay experiments show that there is a local alignment interaction between filaments [171, 197]. Physically, such alignment can be explained by the asymmetric micro-structure of actin filaments that can work as a barb for filaments roughly moving in the same direction [120]. To model such an interaction, each particle is assigned an alignment field $u(x,t)$ at its occupied and neighboring lattice sites (Figure 2.16); overlapping alignment fields of different filaments are averaged. In a collision event with another filament, the alignment field modifies the transition probability to move from $x_0$ to $x$ by the factor $\alpha^{\cos\phi}$, where $\phi$ is the relative angle between the alignment field and the direction of motion of the respective collision partner: $\phi = \measuredangle(u, x - x_0)$. The parameter $\alpha$ characterizes the strength of the polar alignment; higher values of $\alpha$ correspond to an increasingly strong alignment.

In summary, assuming that the different contributions are statistically independent, we arrive at the updating rule

$$\mathbf{P}' = \mathbf{P} \cdot \alpha^{\cos\phi} \cdot \exp(-k\zeta), \tag{2.9}$$

with random sequential updating.

### 2.5.2 Results of the simulation

Like in the experiment, the pattern formation is determined by the density. For low filament densities no collective motion develops. The filaments move randomly; the overall filament density stays homogeneous and the directions of motion are isotropically distributed. For densities above a threshold, an ordered phase develops. It is characterized by small coherently moving clusters that spread perpendicular to their direction of motion and form bands (Figure 2.17 A and B). In accordance with the experiment, the clusters move embedded in an isotropic background of randomly moving filaments. These observations resemble similar simulation results found previously in Vicsek-like models [30] and other agent-based lattice gas models [23, 163].

The pattern formation process can further be quantified by introducing the time-dependent mean polarity $P$, i.e. the magnitude of the polarization, averaged over the directions of movement of all filaments in a region of interest in the middle of the simulation box (ROI) or the entire simulation box (SIM), respectively. These two measures of polarity provide complementary information about the pattern forming process. $P_{\mathrm{ROI}}$ illustrates the formation of small polarized clusters that develop into bands: the sequence of spikes in the time traces indicate clusters passing through the ROI in the center of the simulation box (Figure 2.17 D). In contrast, $P_{\mathrm{SIM}}$ characterizes the evolution of global order in the system: the mean value slowly grows in time and fluctuations are much less pronounced (Figure 2.17 C).

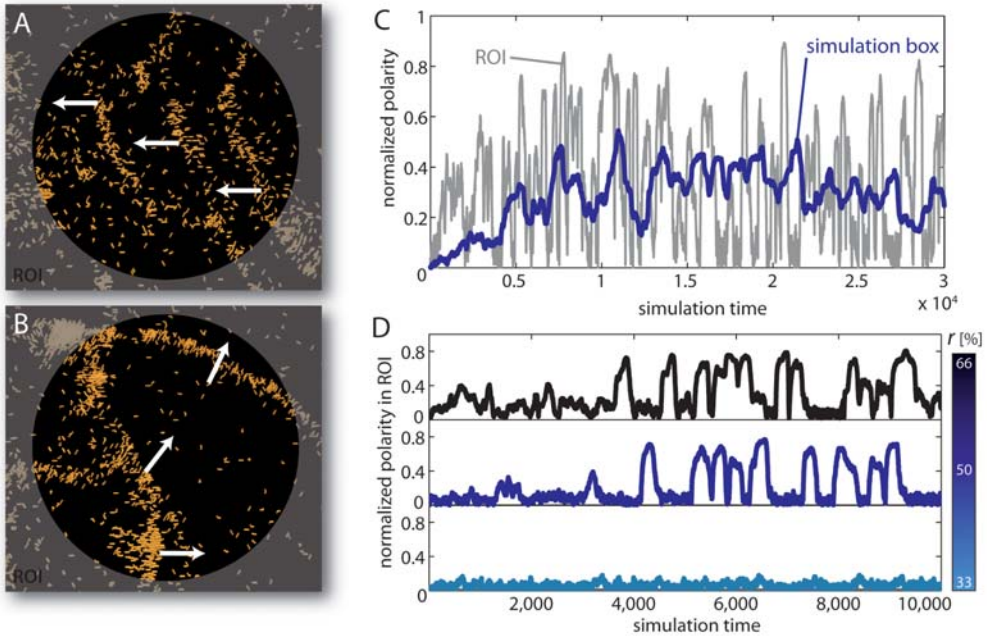


**Figure 2.17: Polar order and collective motion in the agent based simulations.** Images (**A**) and (**B**) show typical snapshots of the agent based simulation. Above a critical density the driven filaments self-organize to form collectively moving structures. They are either wave-like (**A**) or aggregated (**B**). Like in the experiment, the structures are characterized by huge density inhomgeneities as the ordered structures coexist with a dilute and disordered background. (**C**) shows the temporal evolution of the polarization in the ROI (grey line) in comparison to the polarization in entire simulation box (blue curve). Distinct peaks reflects the passage of collectively moving particles. As the blue curve shows, the overall polarization saturates. In (**D**) the temporal evolution of the mean polarization in the ROI for different densities ($r = 33\%$, $r = 50\%$, $r = 66\%$, measured in percentage of occupied lattice sites) is shown. As can be seen, a minimal density is required for the emergence of large-scale coherent motion. The total system has typical length $L$ of 1000 lattice sites. Filament length is set to 10 lattice sites. Parameters were set to $\zeta = 10$, $\alpha = 10$ and $r = 83\%$, if not indicated otherwise.

For the emergence of collective motion, the symmetry breaking nature of the local alignment interactions is crucial: without it, filaments interact only sterically and do not show collective motion at all (Figure 2.18 A). At a fixed parameter set, a small increase of the alignment parameter ($\alpha > 3.5$) drastically changes the outcome and polar-nematic structures developing to wave-like patterns are observed (Figure 2.18 A). In contrast, increasing the strength of the steric repulsion $\zeta$ suppresses the formation of collectively moving polar patterns (Figure 2.18 B). Thus, it is the cooperative effect of many interacting filaments together with the weak alignment interactions, which leads to the collective order phenomena based on the balanced uptake and loss dynamics of the individual constituents. Purely steric repulsion together with high densities suffice not to induce any order in this system entirely driven by the input of mechanical energy at the smallest scales.

Importantly, the cellular automaton barely finds spontaneous swirling motion. This can be attributed to the lack of weak long-range interactions, such as hydrodynamics, which may be self-induced by the moving clusters. This contribution may turn out to be an important ingredient for the enormous stability observed in the high density wave regime. Theoretical approaches best suited for a description of such phenomena seem to be generic hydrodynamic approaches taking into account the coupling of density fluctuations with solvent dynamics [14, 114, 208].

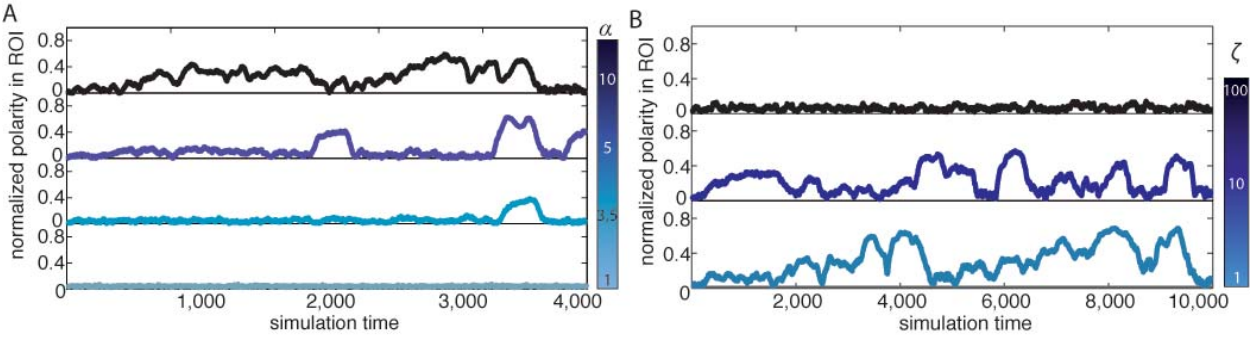


**Figure 2.18: Collective motion relies on weak excluded volume and weak alignment effects.** In (**A**) the mean polarity in a region of observation (ROI) is shown for different weightings of the alignment interaction $\alpha$. For small $\alpha$, no polar structures evolve (lowermost curve). Starting from $\alpha = 3.5$ polar ordered structures start to evolve, visible in a clearly peaked time course of the polarity ($r = 83\%$, $\zeta = 10$) (upper curves). Distinct peaks reflect the passage of polar structures, either wave-like or aggregated. With increasing $\alpha$, an increasing fraction of filaments is recruited to the polar structures, visible in an higher overall polarity at earlier simulation times (upper curves) Parameters were set to $\zeta = \alpha = 10$. In (**B**) the normalized polarity in the ROI for three different values of the weighting of the steric repulsion $\zeta$ is shown. While for $\zeta = 1$ crossing events between filaments can readily occur, they are suppressed nearly completely for $\zeta = 100$, in the case of which no coherent motion occurs. The alignment parameter was adjusted to $\alpha = 10$ at a density of $r = 83\%$.

## 2.6 Hydrodynamic coupling of driven filaments

Motility assay experiments at high filament densities show a plethora of competing spatio-temporal patterns. This comprises persistent swirling motions and traveling density inhomogeneities like clusters and density waves. While the formation of collective motion in such experiments can in principle be explained by purely short-range interactions, the long term stability of these patterns may be modulated by long ranging interactions.

This becomes evident during the emergence of collective motion that relies on the successive synchronization of ordered patches that are much more than an average filament length apart (Figure 2.4). Neither this synchronization process nor the remarkable stability of the evolving structures can be explained by purely short ranged interactions alone. Rather, this suggests the presence of a medium to long ranged interaction. While electrostatic interactions are effectively screened in the electrolyte solutions, hydrodynamic interactions are the most promising candidate.

In this section we take a closer look on how the patterns formed in the high density motility assay depend on long ranged hydrodynamic interactions that are self induced by the coherently moving filaments. To investigate this aspect we observe (1) the behavior under external flow, (2) the interaction between colliding clusters, and (3) the dynamics of clusters within confinements.

### 2.6.1 Sensibility against external fluid flow

Despite being crafted to the surface by molecular motors, actin filaments in a motility assay are highly sensible to external fluid flow. If subjected to a laminar shear flow with a flow velocity in the order of the filament velocity, the filaments orient and move alongside the fluid flow (Figure 2.19 A and B). After the cessation of the flow, filaments gradually loose their orientation and resume their persistent random walk (Figure 2.19 C).

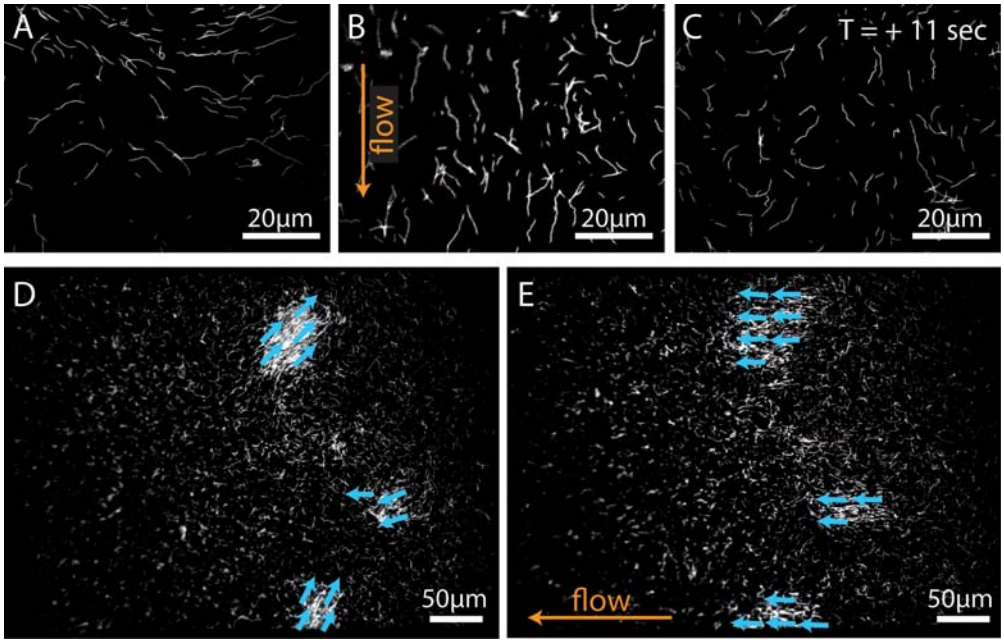


**Figure 2.19: Orientation alongside external flow fields.** A motility assay experiment is subjected to a hydrodynamic flow field directed along the arrow in images (**B**) and (**E**). In the low density phase (images **A**–**C**), before being subjected to an external flow field, individual filaments perform random walks with only a minor directional preference (**A**). When the external flow is applied, the filaments get oriented alongside the flow (**B**). After the cessation of the flow and a certain relaxation time $T$ in the order of 10 sec, the filaments resume their random walk and the directional bias due to the flow alignment gradually vanishes (**C**). In the cluster phase individual clusters move uncorrelated (**D**). When subjected to a flow field, the clusters orient alongside the flow (**E**). The filament density for (**A**)-(**C**) was set to $\rho = 2\,\mu\mathrm{m}^{-2}$ and to $7\,\mu\mathrm{m}^{-2}$ for (**D**) and (**E**).

Clusters of coherently moving filaments are even more sensible to externally imposed flow fields: They already reorient alongside the flow if subjected to flow velocities that are not sufficient to turn individual filaments (Figure 2.19 D and E). Similar to individual filaments, they gradually loose the directional bias once the flow was stopped. The time after which the clusters have lost the directional bias due to the external flow depends on the magnitude of the flow velocity: The higher the velocity of the external fluid flow the better the alignment alongside the flow and the longer it takes the clusters to loose the externally imposed direction.

In the high density motility assay flow fields are self-induced by the coherently moving structures. Despite the hydrodynamic drag individual filaments can generate is limited in reach to several $\mathrm{nm}$ [90], large coherently moving structures like density waves generate a stable fluid flow that lately extends throughout the entire flow chamber.

### 2.6.2 Hydrodynamic interactions between clusters

These flow fields naturally influence the dynamics in the high density motility assay, as it becomes manifest if coherently moving structures interact with adjacent patterns. A gradual increase of the filament density not only results in an increased average size of the clusters, but also in their more frequent occurrence. The enhanced cluster density leads to more frequent collisions between clusters, in the course of which the clusters reorient and reorganize their shape.

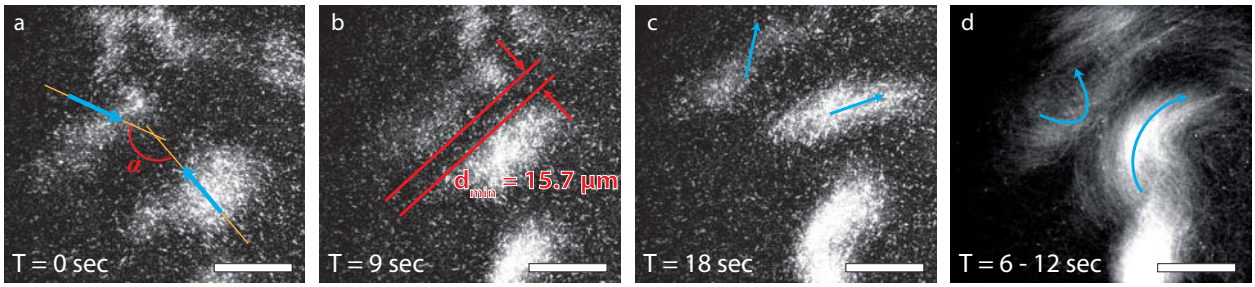


**Figure 2.20: Dynamics of interacting clusters.** Images (**A**) – (**C**) show a typical scattering process of two interacting clusters. The blue arrows denote the direction of motion of the clusters. Even for scatter events with an interaction angle close to $\alpha = 180°$, the formation of a depletion layer with a thickness of $d_{\min}$ in between the interacting clusters is observed (**B**). This can also be seen in the time overlay in image (**D**) where the trajectories of the interacting clusters are visualized (blue arrows). The filament density was adjusted to $\rho = 14\,\mu\mathrm{m}^{-2}$ and the scale bar is $50\,\mu\mathrm{m}$.

During collisions, clusters approach each other only up to a minimal distance $d_{\min}$, which is of the order of a filament length. Reorganization and reorientation of the clusters during collisions take place before the cluster's margins physically touch. As a consequence, a depletion zone with a thickness of $d_{\min}$ forms that is given by the minimal distance between two colliding clusters (Figure 2.20). Being short range in nature, simple hard core repulsion does not suffice to describe this scattering behavior; rather, it can be attributed to the hydrodynamic coupling of the flow fields of interacting clusters. The existence of the depletion zone prevents colliding clusters from merging with one another in a coarsening process and thus adds to the enormous stability of individual clusters.

### 2.6.3 Impact of a boundary on the pattern formation

It can be expected that interactions with solid walls lead to similar behavior: if a cluster scatters at a solid wall, it should only approach the wall up to a minimal distance $d_{\min}$ and a depletion layer should form. To address this, the diameter of active regions was systematically reduced down to $50\,\mu\mathrm{m}$ with the help of micropatterning techniques (Figure 2.21 A).

The boundary between the active and passive region is characterized by a sharp margin (Figure 2.21 C). Filaments are only propelled within the active region and are repelled and have to turn around at the boundaries. Provided that the active region is sufficiently large, the confinement does not change the overall behavior of the system and the same density dependent phenomenology is observed. Above the critical density $\rho_c$, clusters evolve inside the active region (Figure 2.21 B) and similar to the case without confinement, clusters grow larger with increasing density. If the clusters are large enough, their directional persistence gets higher than the diameter of the confinement. Unavoidably, this leads to multiple scattering events of the coherently moving structure with the boundary, in the course of which the cluster successively explores the entire active region.

The interference with the confinement has severe consequences on the emergence of density waves: in contrast to the case without confinement, no density waves could be found below a confinement diameter of $550 \pm 25\,\mu\mathrm{m}$ (Figure 2.22). This is consistent with the observation of the emergence of density waves in the high density motility assay without confinement: The density fluctuations need a minimal orientational persistence and hence a minimal mean free path to evolve into stable density modulations (Figure 2.6). In confinement, the mean free path is set

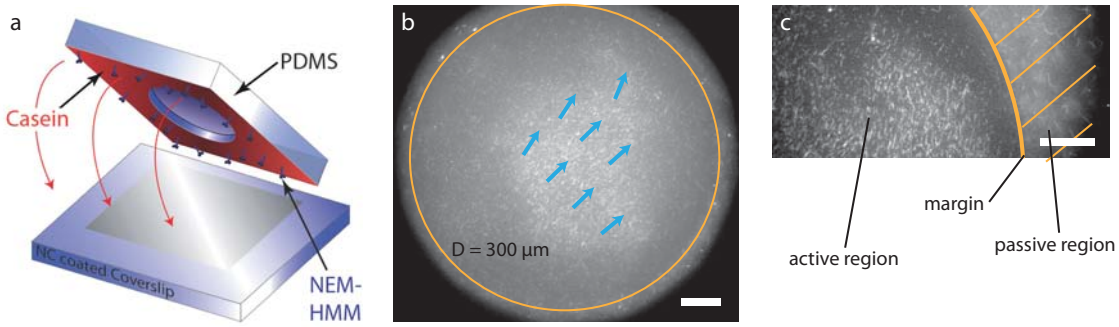


**Figure 2.21: Microcontact imprinting technique.** Image (**A**) shows a schematic representation of the used microcontact imprinting technique, with the help of which arbitrary boundaries with a diameter down to $50\,\mu\mathrm{m}$ can be designed. To selectively passivate distinct regions, a PDMS stamp treated with Casein and HMM motor proteins in the rigor state (NEM-HMM) is placed on the coverslip. This procedure results in an active region and a passive region made up of filamentous actin bound to rigor HMM (**C**). The boundary of the two regions is characterized by a sharp margin. In (**B**) a cluster moving in a circular boundary is shown. The filament density was adjusted to $\rho = 14\,\mu\mathrm{m}^{-2}$ and the scale bar is $50\,\mu\mathrm{m}$.

by the dimensions of the active regions, as density modulations are destroyed during interactions with the boundary (Figure 2.23). Below a confinement diameter of $550 \pm 25\,\mu\mathrm{m}$ scattering events occur too often for stable density modulations to evolve.

Importantly, if geometry confines the high density motility assay into structures smaller than $75 \pm 25\,\mu\mathrm{m}$, no coherently moving patterns evolve at all. Already small clusters cannot evolve in such confining geometries, since even the persistence length of their movement is too large. Only in a sufficiently large active region enough maneuvering space is given to allow for the synchronization process and hence the formation of stable patterns. This is equivalent with the notion that the hydrodynamic interactions need to be fully developed to stabilize the emerging structures.

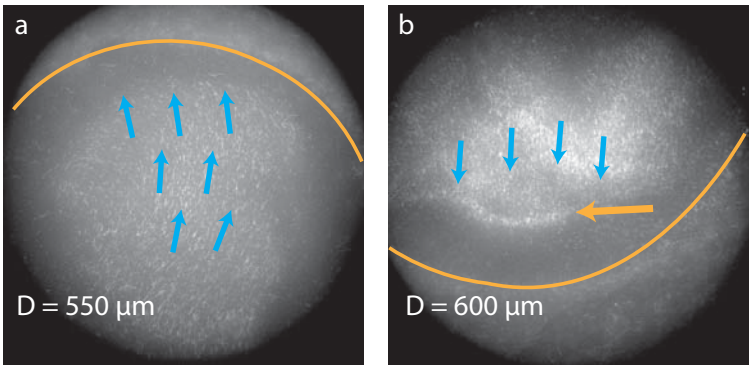


**Figure 2.22: Boundaries suppress the formation of density waves.** For too small active regions, the mean free path between boundary encounters is not sufficient for the density waves to evolve. In this case, the filaments move in homogenous clusters as can be seen in (**A**) for a circular active region with a diameter of $D = 550\,\mu\mathrm{m}$. Above a diameter of $600\,\mu\mathrm{m}$ enough maneuvering space is given and density inhomogeneities (yellow arrow) can develop, before they get destroyed by collisions with the boundary. In (**A**) and (**B**) the direction of motion is visualized by blue arrows and the boundary of the active region is marked by a yellow line. The filament density is $\rho = 18\,\mu\mathrm{m}^{-2}$.

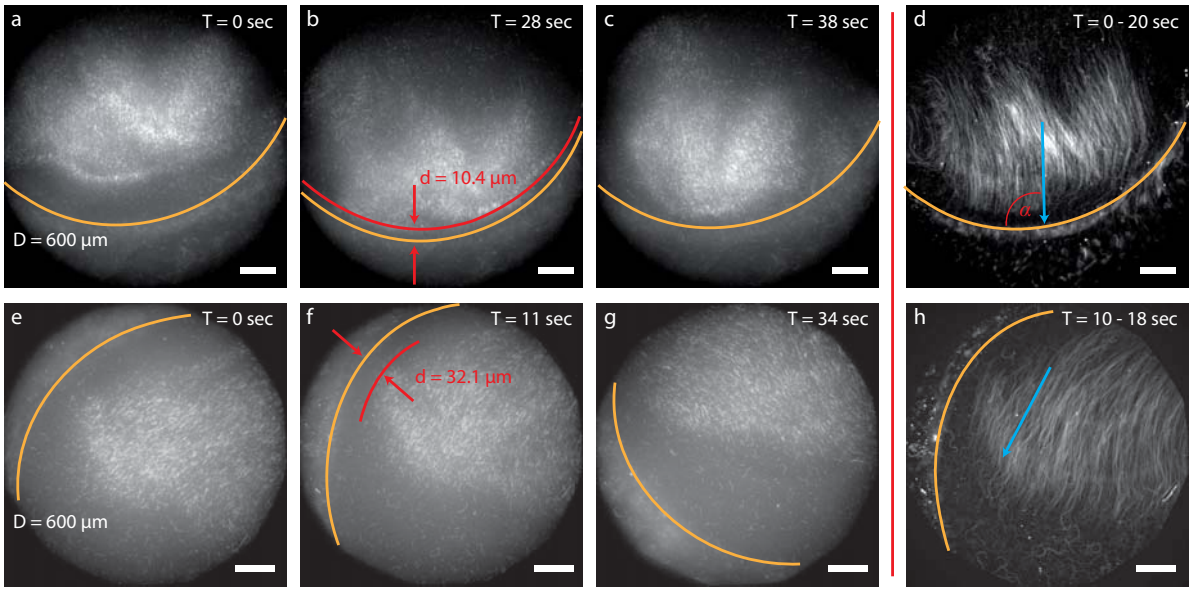


**Figure 2.23: Formation of a depletion layer during interactions with boundaries.** The images (**A**) – (**C**) and (**E**) – (**G**) illustrate a sequence of snapshots for two scattering events of clusters with the boundary (yellow line); (**D**) and (**H**) are the corresponding time overlays and the blue arrows denote the direction of motion. Whereas in (**A**) – (**D**) the intersection angle is close to $\alpha = 90°$ (**D**), the image series (**E**) – (**H**) shows the cluster-wall interaction for an interaction angle close to $\alpha = 0°$. In both cases a depletion layer is formed and the clusters already turn before physically touching the boundary (**B** and **F**). The thickness of the depletion layer and the change in the cluster morphology depends on the angle of intersection: angles close to $\alpha = 90°$ lead to a minimal depletion layer of $\approx 10\,\mu$m and a complete reorganization of the clusters; small angles yield larger depletion layers in the order of $30\,\mu$m. The filament density is set to $\rho = 20\,\mu\text{m}^{-2}$ and the scale bar is $50\,\mu$m.

### 2.6.4 Hydrodynamic interactions with confining boundaries

The usage of boundaries on the $\mu$m scale allows for a systematic investigation of the influence of hydrodynamic interactions. Similar to the occurrence of a depletion zone during two-cluster interactions, clusters turn around already before reaching the boundary, while individual filaments do this at the very boundary. Depending on the intersection angle, clusters are repelled at distances up to $30\,\mu$m from the wall. Angles close to $90°$ result in shallow depletion zones and major changes in the cluster morphology (Figure 2.23), while small angles lead to larger depletion zones with minor reorientations of the clusters (Figure 2.23 E – H). Still, the overall cluster integrity is not disturbed – demonstrating once again the enormous stability of the cluster, which is attributed to the shielding through a self induced flow field since other long-ranged cohesive interactions are assuredly absent.

For high filament densities, $90°$ collisions are unlikely to develop, since the mean free path for individual structures is too small and interactions with boundaries predominantly occur at shallow interaction angles. This "guiding effect" of the wall can be utilized to tune the movement of the structures, as can be seen in Figure 2.24, where circular boundaries induce persistent swirling motions. In this case the confinement reduces the movement of the swirls' centers that limits the stability of swirling motion without confining boundaries.

The occurrence of an angle dependent minimal cluster-to-wall distance $d_{\text{min}}$ during such scattering events is a proof for the existence of long ranged interactions in the system. Purely short

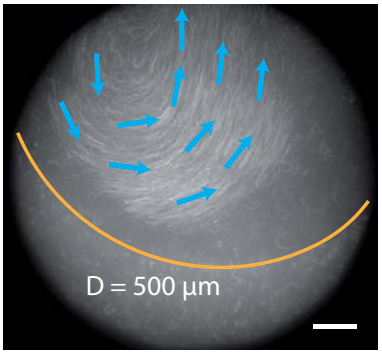


**Figure 2.24: Guidance of molecular motion by micro-patterned surfaces.** With circular boundaries (yellow line) persistent swirling motions can be induced, as exemplified with a time overlay of 10 consecutive images. The blue arrows mark the margin of the active region. The scale bar is $50\,\mu$m and the density is set to $\rho = 18\,\mu\text{m}^{-2}$.

ranged interaction can neither account for the occurrence of a depletion zone nor for the observed angular dependence. This is reminiscent of theoretical work on solid objects moving parallel near a wall [70]. Here, the objects are likewise subjected to a torque that increases with decreasing distance from the wall. In the motility assay, this torque leads to a rotation of the direction of movement of the clusters and their deflection from the wall.

In theoretic models for suspensions of collectively moving particles, mid- to long-ranged hydrodynamic interactions have been used as the main ordering principle [14, 148]. The flow fields of individual particles like bacteria couple, leading to an alignment between the directions of motions on length scales much longer than the size of the individual particles. This long range coupling is possible because the individual bacteria are modeled as pushers or pullers, thus force dipoles, with a flow field decaying according to $r^{-2}$. However, in recent experiments on bacteria swarms [54] it was shown that the flow field of self propelled bacteria resembles a higher order flow profile with a much faster decay proportional to $r^{-3}$. At least for bacteria colonies, this suggests that hydrodynamic interactions are not the main ordering principle leading to collective motion.

For the motility assay the situation is different. In contrast to bacteria swarms, the filament clusters in the high density motility assay do not move through the fluid but are propelled by the motor proteins. Conceptually this yields a force monopole flow field that is much longer ranged than the flow fields for low-Reynolds swimmers [54]. Thus, while the emergence of collective motion can be explained by predominately short ranged interactions [72,171], long ranged hydrodynamic interactions contribute to the long-term stability of the patterns and the dynamics of the ordered phase.

## 2.7 Discussion

The reconstituted system introduced and analyzed here, provides a bottom-up approach to the physics of active fluids. Despite its minimal nature, it shows a plethora of spatio-temporal patterns that generically show persistent density inhomogeneities. The patterns include clusters, density waves, and swirls of collectively moving filaments that were theoretically predicted but not experimentally verified so far. While the recently introduced paradigm of active fluids provides a general framework for the investigation of non-equilibrium dynamics driven by local internal forces,

a thorough understanding of the underlying mechanism for the emergence of highly ordered structures is still at large. The here described combined approach of well controlled experimental and theoretical model systems, is ideally suited to identify the lynchpin between microscopic interactions, density and macroscopic structures. The minimal approach and detailed control of all relevant system parameters enables the identification of an astonishing variety of spatiotemporal patterns, still allowing the backtracking of the assembly and disassembly pathways to the underlying local interactions.

The unique properties and accessibility of the high density motility assay further allowed to verify the existence of three key signatures of collective motion: the anisotropy of of the collective motion, the emergence of anomalously large fluctuations in the particle density, and superdiffusive particle motion transversal to the mean direction of motion. All these properties agree qualitatively with generic theories [148,206,207,213] and agent based simulations [30,71,213]. Moreover, we could relate the emergence of the anomalous statistical properties to the coupling of the particle density to the velocity field of the collectively moving particles. Thereby we are able to show that the statistical properties arise from fluctuations in the velocity field that can evolve into topological defects like local sinks and sources. While these defects are explicitly allowed in generic theories, their role for the dynamic structure formation remains to be systematically addressed in the full non-linear regime. The further investigation of this interplay will not only contribute to a better understanding of the unique statistical properties of active systems, but will pave the way for a further understanding of the complex physics of flocking, swarming, and collective motion.

By extending the experimental system to more complex interactions, confined geometries and external stimuli [219], we showed that pattern formation in the high density motility assay is modulated by long ranged hydrodynamic interactions. While the emergence of collective motion can be explained by predominately short ranged interactions [72,171], short ranged interactions alone can neither account for the long-term stability of the patterns, nor for the intriguing behavior when collectively moving structures interact with their environment. Moreover, this opens the door to steer the pattern formation in the system and to control the time and length-scale of the collective motion. Thus, the findings presented here not only will stimulate new theoretic approaches but also pave the way for the tailored design of reconstituted active systems for various purposes that range from bottom-up approaches to cell mechanics to technological applications.

# 3 Frozen Steady States in Active Systems

*In the previous chapter we saw that a simple active systems like the high density motility assay, can show an extremely rich phase behavior. It is a general signature of active systems that even simple systems can show a plethora of intriguing phenomena and often we find complexity were we would have expected simplicity. One striking example is the occurrence of a quiescent or absorbing state with frozen fluctuations that at first sight seems to be impossible for active matter driven by the incessant input of energy. Using high density motility assay experiments, we demonstrate that frozen steady states can arise in active systems if active transport is coupled to growth processes.*
*In section 3.2 we show that the interplay of only three components, actin filaments, HMM motor proteins, and fascin crosslinkers is sufficient for the emergence of a frozen active steady state. It consists of highly symmetric structures, rings and elongated fibres, that are actively assembled and propelled by the motor proteins. The emerging structures have characteristic structure size distributions that reflect the transient structure formation process (3.3). Using an agent based simulation, we relate the steady state properties to the transient structure formation process and show that the frozen steady state in the system sharply documents the history of the pattern formation instabilty (3.4). Thus, the noise level in the system during the emergence of the patterns proves to be the major control parameter for the sizes and the morphology of the structures in the frozen steady state (3.5). In the last section (3.6) I discuss whether the transition to a frozen steady observed here can be conceived as an absorbing transition.*[1]

## 3.1 Frozen steady states: competition between transport and growth

How does a dynamic system approach its steady state and what is the nature of it? For a thermodynamic system Onsagers regression hypothesis [159] asserts that the relaxation is governed by the same laws as the fluctuations in thermal equilibrium, and Boltzmann-Gibbs theory defines the nature of all steady states. For active systems like vibrated granules [115, 154], animal swarms [11, 38, 231], microorganisms [33, 53, 168] and cytoskeletal systems [10, 24, 103, 104, 156, 171, 172] there are no such general laws. Instead, one finds a plethora of spatio-temporal patterns including swarming [11,33,38,53], density inhomogeneities [24,103,171], and swirling patterns [168,171]. A common feature of these patterns is that they are all fluid-like [3, 5, 13, 14, 186]. One might ask whether there is something like the analog of a solid-like or frozen state in active systems. At first sight this seems to be impossible for active matter driven by the incessant input of energy which is expected to cause highly dynamic states through a perpetual balance between assembly and disassembly processes [103]. Yet, there are examples where the constituents of active systems self-organize into non-equilibrium steady states with slowed dynamics or regular spatial patterns. Activity has been found to give rise to a diverging viscosity at the isotropic-nematic transition of active gels [27,78,129], and glassy behavior has recently been observed for confluent cell layers [2]. Systems that are externally driven, like agitated granular media, exhibit a plethora of regular static patterns [4,158,216] and rotating assemblies [211]. While in all these non-equilibrium systems degrees of freedom are slowed down or frozen out, the very existence of a pattern or the anomalous rheological properties is only made possible by the activity in the system. This has to be contrasted with non-equilibrium systems, where the system ends up in a set of configurations from which it cannot escape. Once such an absorbing state is reached, the dynamics ceases and the ensuing pattern is frozen in [80,85]. Particularly illustrative examples are growing bacterial colonies

[1] The main results of this chapter are published in Reference [173].

showing natural selection [76] or periodically sheared colloidal suspensions which self-organize into an absorbing state [36].

Here, we ask for the existence of steady states which carry the hallmarks of both an active system and a frozen absorbing state, i.e. where fluctuations are successively eliminated during a coarsening process, while keeping the system in an active state. In driven systems, frozen steady states can arise when particles are not only actively transported, but also integrated into new self-assembled higher-order structures where single particle fluctuations are arrested. A frozen active state combines the rapid self-organization characteristics of driven systems with the robustness, stability and reproducibility of growth and self-assembly processes. Thus, the combination of self-organization and growth that characterizes frozen active states may turn out to be important for many systems in biology and materials science. However, the complexity of most experimental systems defies the thorough identification and analysis of the intricate balance of the underlying principles that lead to a frozen active state.

To shed light on the mechanisms that govern the emergence of such states, we modify the high density motility assay setup introduced in the preceding chapters by adding the crosslinker protein fascin. The addition of fascin leads to the emergence of a frozen steady state consisting of highly symmetric structures, rings and elongated fibres that are actively assembled and propelled by the motor proteins. The phase behavior of the frozen steady state depends on the fascin concentration: For high fascin concentrations highly ordered polar streaks are formed that span the whole flow chamber; for an intermediate fascin concentration regime a frozen steady state is formed in which polar actin-fascin-strings are moving on stable non-interfering circular trajectories. For even lower fascin concentrations the phenomenology of the standard high density assay is retreived. The reconstitued approach complemented by an agent based simulation allows us to identify the three main factors controlling the pattern formation: directional fluctuations due to the active transport by the motor proteins, merging of adjacent strings and the uptake of individual filaments perpendicular to the direction of motion.

## 3.2 Emergence of actin-fascin rings

To investigate how the dynamic structure formation in high density motility assay experiments is affected by a defined growth process, the crosslinker protein fascin is added and its concentration systematically varied. In this context, fascin is ideally suited as it assembles polar filament structures and thus does not obstruct the material transport by the molecular motors. Fascin is a relatively small crosslinking protein with amolecular weight of $55\,\mathrm{kDa}$ [237] that crosslinks filaments only in a parallel or polar orientation [37]. *In vivo* fascin is predominately responsible for the fortification of cellular protrusions like filopodia where it organizes filaments into thick bundles [224].

### 3.2.1 Basic phenomenology

The addition of trace amounts of fascin does not suffice to change the pattern formation mechanisms in the high density motility assay. Even at high filament densities the individual filaments display directional fluctuations that stem from the persistent random walk of single filaments in the motility assay. These fluctuations are responsible for the formation of density inhomogeneities that accumulate to form coherently moving structures such as clusters and density waves (Figure

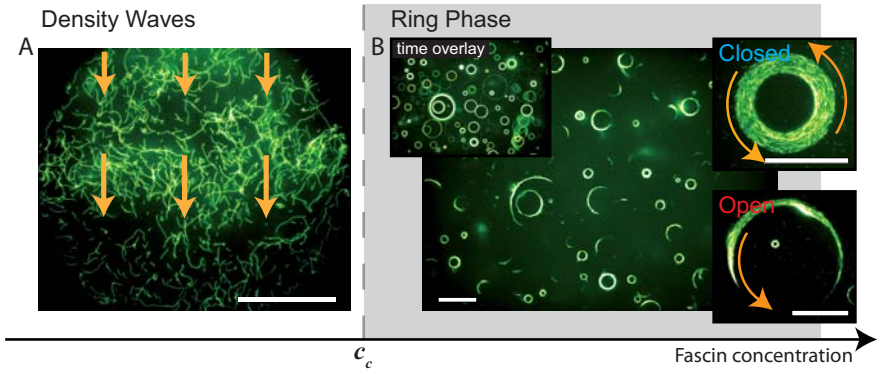


**Figure 3.1: Phase behaviour as a function of the fascin concentration.** Low fascin concentrations are not sufficient to fundamentally alter the pattern formation in the high density motility assay and at an actin concentration of $\rho = 10\,\mu$M the characteristic travelling density waves evolve (**A**). Compared to the case without crosslinkers they are less pronounced, as the crosslinker slightly hinders the formation of density inhomogeneities. Above a critical fascin concentration of $c_c = 0.075 \pm 0.025\,\mu$M, the pattern formation drastically changes as constantly rotating rings evolve that are either closed or open (**B**). In the steady state all actin filaments are incorporated in rotating rings and fluctuations on the single filament level are entirely absent. All scale bars are $50\,\mu$m.

3.1A). Low fascin concentrations dampen these fluctuations by crosslinking events but are not sufficient to completely inhibit them. As a consequence structures like density waves are less pronounced (Figure 3.1A). This drastically changes, if the added fascin concentration exceeds a critical concentration: Now the crosslinker leads to the emergence of rotating polar actin-fascin structures, which are effectively planar. The rotating speed of the rings corresponds to the single filament speeds and is about $3\,\mu\mathrm{m/sec}$.

While the structure formation in the high density motility assay relies on the balance between assembly and disassembly processes, the addition of crosslinker molecules promotes defined assembly processes and at the same time inhibits the disassembly of the emergent structures. This finally leads to a quiescent steady state where all filaments are firmly incorporated in constantly rotating rings (Figure 3.1B); fluctuations on the single filament level are completely arrested. The absence of disassembly pathways renders the structure formation mechanism reminiscent to a coarsening process into an absorbing state [80] and the conditions during the pattern formation are directly reflected and frozen-in in the steady state.

In the frozen steady state, constantly rotating rings are homogeneously distributed throughout the motility assay (Figure 3.1B). No preferred direction of rotation is observable. Rings occur in two distinct conformations, which are equally abundant: open and closed (Figure 3.1 B). Closed rings consist of self-contained and constantly rotating actin-fascin fibres. Open rings also move on a stable circular trajectory with a uniform curvature radius, as can be seen in the time overlay shown in Figure 3.1 B.

### 3.2.2 Ring radii distributions

A characteristic distribution of ring curvature radii $p(r)$ in the steady state is observed (Figure 3.2).[2] The radii are broadly distributed, with a decay towards large radii $r$. $p(r)$ shows a pro-

[2] A detailed description of the numeric procedure to extract the radii distribution from the microscopy images can be found in the appendix A.2.8

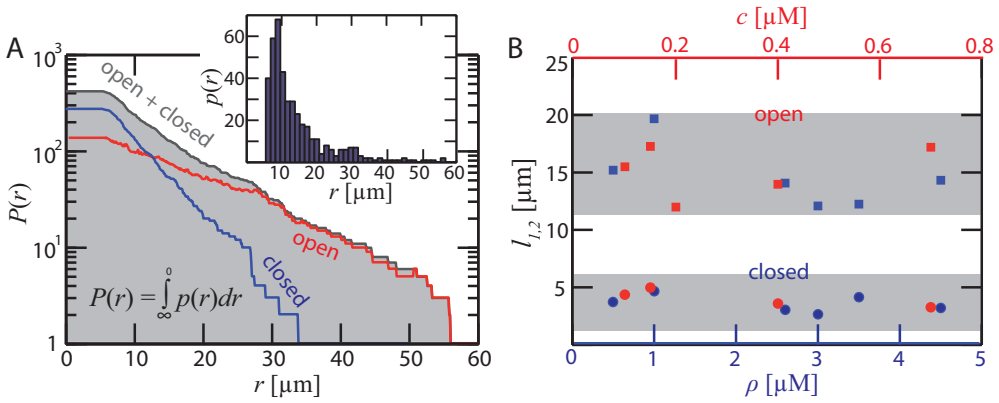


**Figure 3.2: Ring radii distributions for open and closed rings. A** shows the cumulative curvature radii distribution $P(r)$ in the frozen steady state; the inset depicts the non-cumulative distribution $p(r)$. The distribution can be described by a double exponential decay according to $P(r) \propto A_1 \cdot \exp(r/l_1) + A_2 \cdot \exp(r/l_2)$ with decay lengths of $l_1 = 3.3\,\mu$m and $l_1 = 10.1\,\mu$m. This double exponential shape reflects the occurrence of two different ring morphologies: open and closed rings. Open rings are considerably bigger than closed rings and have an approximately three fold bigger decay length. The double exponential decay and the decay lengths $l_1$ and $l_2$ are independent of the actin and fascin concentration. This is shown in **B** where the decay lengths are plotted for various actin and fascin concentrations. For all concentrations the decay of the closed rings is of the order of $l_1 = 3 - 6\,\mu$m and the decay of the closed rings lies in an interval of $l_2 = 12 - 20\,\mu$m. For the actin-concentration series the fascin concentration was set to $c = 0.2\,\mu$M; for the fascin-concentration series the actin concentration was adjusted to $\rho = 3\,\mu$M.

nounced maximum at around $10\,\mu$m. Towards small curvature radii, the distribution is characterized by a cut-off radius in the order $r_c \approx 5\,\mu$m, below which no rings are found. The decay of the distribution for large radii is of double exponential shape and can be described by

$$p(r) = a_1 \cdot \exp\left(\frac{r}{l_1}\right) + a_2 \cdot \exp\left(\frac{r}{l_2}\right), \tag{3.1}$$

with two independent decay lengths in the order of $l_1 = 3 - 6\,\mu$m and $l_2$ ranging from $12 - 20\,\mu$m. The double exponential nature of the curvature radii distribution is highly robust upon parameter variation and is conserved throughout variations of the fascin and actin concentrations (Figure 3.2 B), making this to a generic feature of the system.

The double exponential shape directly relates to the two distinct ring populations found in the system. This can best be seen by investigating the cumulative radii distributions defined by

$$P(r) = \int_{\infty}^{0} p(r)\, dr\,, \tag{3.2}$$

separately for both ring populations. From the cumulative distributions shown in Figure 3.2, it can be infered that closed rings in general are smaller than open rings: While closed rings do not exceed a maximal ring radius of $30\,\mu$m open rings can reach radii in the order of $100\,\mu$m. Likewise the maximum of the distributions is shifted to higher radii for open rings: The distribution of the open rings is peaked around $30\,\mu$m whereas the distribution for closed rings has its maximum at around $10\,\mu$m, which is of the order of the persistence length of individual filaments. The distribution of both open and closed rings decay exponentially – adding up to a double exponential for the overall ring radii distribution.

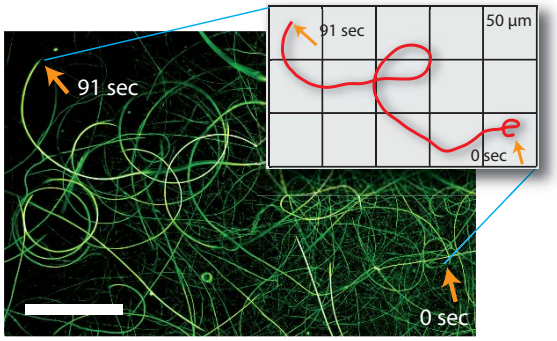


**Figure 3.3: Time overlay of a moving actin-fascin string.** Actin-fascin strings move on circular trajectories. The thicker the strings get, the higher their directional persistence. As a consequence variations of a given curvature happen increasingly less frequent and have less effect. The motor density was adjusted to $\sigma_m = 90\,\mathrm{nM}$, the actin concentration was set to $\rho = 3\,\mu\mathrm{M}$ and the fascin concentration was $c = 0.5\,\mu\mathrm{M}$. The scale bar is $50\,\mu\mathrm{m}$.

## 3.3 Pattern formation mechanisms

Since frozen steady states directly reflect the history of the pattern formation, the occurrence of the two distinct ring populations can directly be related to transient dynamics during the pattern forming instability. Indeed, the ring curvatures reflect the balance between aggregation processes and active transport during the ring formation: Polar actin-fascin strings nucleate from individual actin filaments crosslinked by fascin. While being transported, the actin strings grow larger by two competing mechanisms, either by taking up individual filaments alongside the bundle, or by merging with adjacent structures, leading predominantly to an increased length. These growth processes in turn affect the mechanical properties of the structures. A growth in length results in long and thin strings with relatively low persistence lengths. The continuous growth alongside the strings, yields shorter and thicker structures with a higher persistence length. It is the resulting increased stiffness of the individual strings which determines the susceptibility towards directional changes in the motility assay. Directional changes that alter a given curvature happen more seldom and have less effect for thicker and thus stiffer strings. This can be seen in the trajectory of individual fibres that is composed of circular segments (Figure 3.3).

The interplay between active transport and the mechanical properties of the emergent structures determines the actual ring formation processes, and leads to two generic ring formation mechanisms: Once strings have grown enough in length, they may close on themselves (Figure 3.4 A). Alternatively, lateral growth may increase the string's stiffness to such an extent that their current curvature freezes in without a ring closure and open rings result (Figure 3.4 B). While the ring closure leads to predominantly small ring diameters, the frozen-in curvature process naturally yields rings with larger curvature radii. This is reflected in cumulative curvature radii distributions $P(r)$, which are different for closed and open rings. Both are exponentially distributed, yet their decay lengths differ by a factor of 3 (Figure 3.2 B).

Thus, we are able to identify three mechanisms that govern the pattern formation in the system: The directional fluctuations stemming from the active transport and the two aggregation processes induced by fascin: the continuous growth in thickness and the merging of adjacent strings. Growth and merging compete with each other for the available material in the system and seemingly their balance is set by level of the directional fluctuations in the system. However, with the experimental data only, the question how exactly the directional fluctuations govern the balance

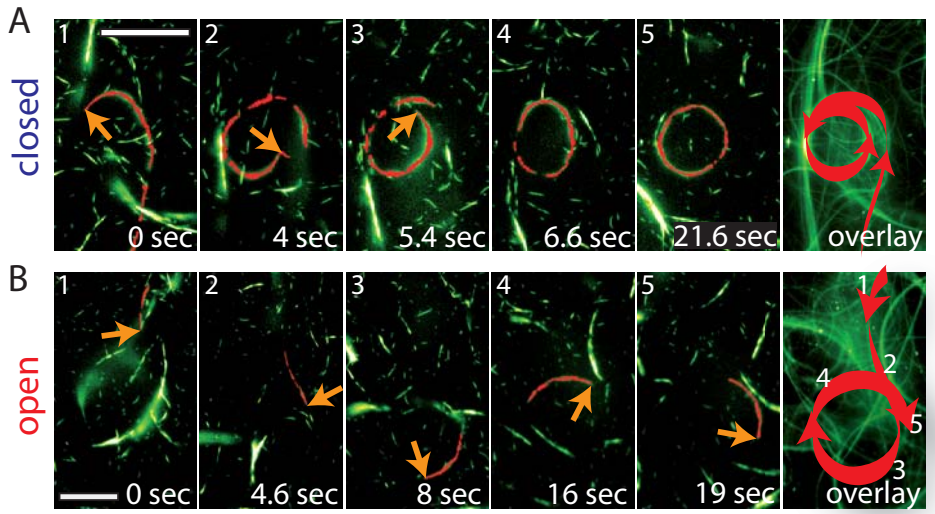


**Figure 3.4: Ring formation mechanisms.** The two different ring populations, open and closed rings, rely on distinct ring formation mechanisms that are related to the growth mechanisms in the system. While being transported, moving actin-fascin strings grow by merging with other strings of similar size. This leads to elongated but still flexible strings that predominantly form closed ring if they cross their own tail (**A**). Open rings form upon a different mechanism (**B**): While moving, actin fascin strings continuously pick up material – individual filaments or smaller actin fascin strings. Thereby, they grow predominately in width and get thicker and stiffer. If they are stiff enough, the curvature freezes and the forces and fluctuations in the motility assay are not sufficient anymore to induce any change in curvature. While closed rings characteristically are small in size with radii of up to $30\,\mu$m, open rings are considerably broader and can have radii of up to $100\,\mu$m. In (**A**) and (**B**) the investigated actin-fascin string is shown in red and its tip is marked by a yellow arrow. The motor density was adjusted to $\sigma_m = 90\,$nM, the actin concentration was set to $\rho = 3\,\mu$M and the fascin concentration was $c = 0.2\,\mu$M. The scale bars are $50\,\mu$m.

between merging and growth remains difficult to address. To take a closer look on this interplay, we devised a minimal agent based simulation that incorporates these three processes: continuous growth, merging and directional fluctuations.

## 3.4 Simulation of the pattern formation mechanisms

The experimental system consists of actin filaments that are propelled and crosslinked in the quasi two dimensional geometry of a motility assay. The presence of the crosslinker protein fascin leads to the gradual emergence of actin fascin-bundles in the course of a coarsening process. Initially, these bundles are still quite flexible and meander on trails that locally can be described as circular orbits with varying curvatures (Figure 3.3). Subsequently, these actin-fascin bundles aggregate further into thicker and longer structures which finally freeze into what we have termed open and closed rings. The objective of the agent-based simulations is to model and analyze the mechanisms underlying this freezing process that leads to the assembly of rings with frozen-in curvature radii.

To this end, the experimentally observed actin-fascin bundles are modeled as finite objects that consist of $N$ beads and that move with a constant velocity $v$. Like in the experiment, these strings pursue circular trajectories with stochastically varying curvatures and the tail strictly following the head's trajectory. Further, the strings are subjected to aggregation processes which result in a

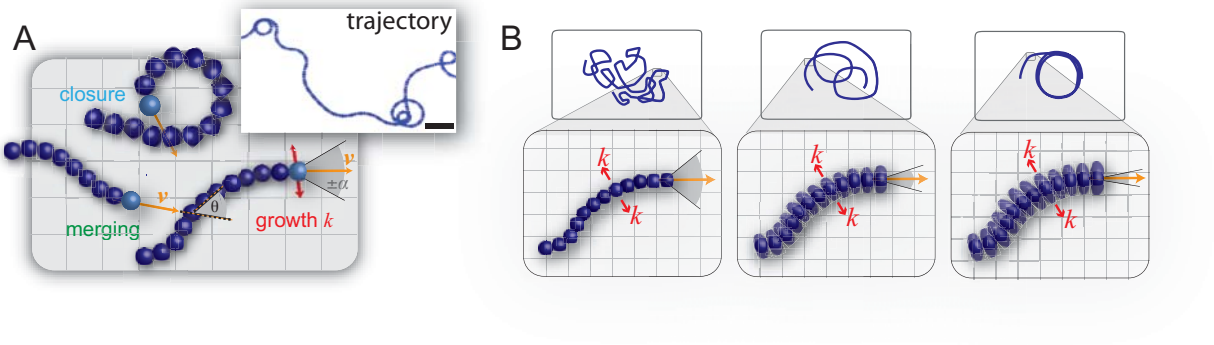


**Figure 3.5: Cellular automaton simulations.** Image (**A** and **B**) illustrate the three microscopic process included in the simulation: the two competing growth processes (continuous growth and merging) and the noise scaling as a function of the thickness. The actin fascin strings are modelled as polar elongated strings that move with with a velocity $v$ on meandering trails. The tip is subjected to curvature changes of rate $\omega$ and a noise level $\alpha$, resulting in a meandering trajectory (inset A). While being actively transported, the strings merge with adjacent strings, if their relative angle $|\Theta|$ is smaller than a certain critical angle $\Theta_c$ – this naturally includes ring closure events (**A**). Besides, the strings continuously take up material, predominately leading to a growth in width and a stiffness increase. The growth in width is modeled by a homogeneous growth rate $\lambda$ and the increase in stiffness is accounted for by scaling the angular noise as a function of the thickness (**B**): while the strings grow in thickness, the effect of the angular noise is gradual lowered and the trajectory stabilizes more and more.

continuous string thickening and merging processes between adjacent strings. In the following, these basic ingredients of the simulations – the computation of the random trajectories and the incorporation of the aggregation mechanisms – are described in detail.

### 3.4.1 Simulation of the string trajectories

In the absence of aggregation processes, the trajectory of the strings is determined by stochastic forces stemming from the HMM motor proteins at the surface. Similar to worm-like bundles [83], it can be expected that the curvature distribution is of approximately Gaussian shape with a width inversely proportional to the bundle's stiffness and proportional to the "activity" of the molecular motors. Mathematically, such a distribution can be generated by a stochastic process defined by the following update rule for the curvature $\kappa$

$$\kappa(t_{n+1}) = 0.5 \cdot (\kappa(t_n) + \eta), \tag{3.3}$$

whereby $n$ denotes the time step and $\eta$ represents a random variable that is uniformly distributed over the interval $[-\alpha, \alpha]$. Stochastic changes of a given curvature occur with a rate $\omega$, with equally spaced time intervals, $t_{n+1} - t_n = \omega - 1$. The updating rule (3.3) leads to a distribution for the curvatures $p(\kappa)$, that resembles a Gaussian with a width proportional to the noise level $\alpha$ (Figure 3.6). The corresponding cumulative radii distribution $P(r)$ follows a power law with an exponent $-1$ (Figure 3.6).

### 3.4.2 Modeling of the aggregation mechanisms

Aggregation of the strings into longer and thicker bundles affects the strings' trajectories in a twofold way: While elongation of strings changes their probability to collide and form even longer

strings or closed loops, thicker bundles that are the result of transverse aggregation, are less susceptible to curvature changes. The elongation of strings is mainly based on merging events between adjacent strings, which occurs only for certain collision parameters: The colliding beads, say bead 1 and 2, have to be within a capture distance $R_1 + R_2$, where $R_1$ and $R_2$ denote the radii of the particular beads. The bead's radius $R_i$ mainly depends on the excluded volume of the strings and scales with the number of already merged strings $M$ according to $R_i = M \cdot R_i^0 \cdot L_0/L$, where $R_i^0$ denotes the initial radius and $L$ being the length of the structure. Further, strings only merge if the collision angles $|\Theta|$ are smaller than a critical merging angle $\Theta_c$. This accounts for the binding properties of fascin, which is only able to link approximately parallel orientated filaments [37]. The merging naturally includes ring closure events, when the head of a string interacts with its own tail. The transversal aggregation is based on the continuous uptake of individual filaments and small strings, leading predominantly to a growth in thickness. The growth in thickness results in an increased stiffness of the strings that is modeled by a linear increase of the tenacity parameter $b(t)$

$$b(\tau_{n+1}) = b(\tau_n) + \beta b_0, \tag{3.4}$$

with $b_0$ being the initial tenacity $b(\tau = 0)$ and $\beta$ determining the thickening speed. The time intervals are equally spaced and $\tau_{n+1} - \tau_n = \lambda - 1$ defines the thickening rate. The linear tenacity increase modeled in Equation(3.4) is motivated by a linear increase of the thickness of the strings. This implicitly implies an infinite filament reservoir. Since the experimentally observed ring formation is completed long before the filament reservoir is depleted, this is in good agreement with the experimental observations.

Thicker strings have a higher tenacity and are thus less susceptible to curvature changes. This can readily be modelled by modifying the update rule of Equation(3.3) with a weight factor $w[b(t)]$ that depends on the tenacity

$$\kappa(t_{n+1}) = (w[b(t_n)] \cdot \kappa(t_n) + \eta)/(w[b(t_n)] + 1). \tag{3.5}$$

The functional dependence of the weight factor $w$ on the tenacity b is given by

$$w[b(t)] = exp([b(t) - b_0]/b_0). \tag{3.6}$$

### 3.4.3 Parameters

In all simulations, the initial bead radius was set to half of the unit length, and initially each string consisted of $N = 10$ beads, implying an initial string length of $L_0 = 10$. The velocity was set to $v = 1.0$, i.e. a string covers its own length in a simulation time of 10. All rates are measured in units of $v/L_0$. Thus a rate of $0.1$ means that the corresponding stochastic process occurs on the time scale a string needs to cover its own length. For all simulations the thickening speed $\beta$ was chosen to $\beta = 0.2$. For every simulation run, we started with $1500$ strings distributed randomly in space and orientation in a cubic simulation box of size $L_{box} = 50 \cdot L_0$ with periodic boundary conditions. The time discretization $\Delta t$ is $0.1$.

### 3.4.4 Results of the simulation

The key ingredient of the agent based simulation is the competition between continuous growth and merging processes of actively transported strings. These two competing aggregation processes already suffice to retrieve the coexistence of open and closed rings (Figure 3.7A). Omission

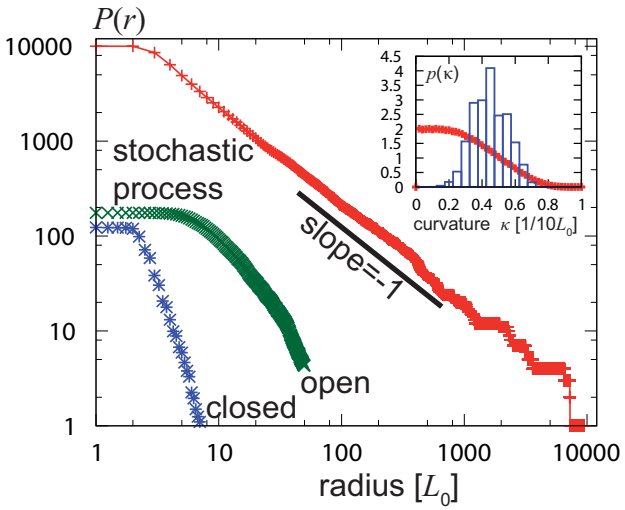


**Figure 3.6: Cumulative radii distribution $P(r)$ with and without aggregation.** The stochastic process determined by equation (3.3) leads to a power-law of slope $-1$ (black line) in the cumulative radii distribution $P(r)$ (red curve). In contrast, simulations that include growth stiffening according to equations (3.5) and (3.5), as well as the possibility of merging events, exhibit a different shape (green and blue curve). Inset: Normalized non-cumulative curvature distribution $p(\kappa)$ for stochastic processes according to equation (3.3) (red curve) and for the aggregation process according to equation (3.4) (blue boxes correspond to closed). In all simulation runs $\alpha$ was set to $\alpha = 1.0$. The parameters that determine the aggregation processes were set to: $\lambda = 0.1$, $\omega = 0.4$, $\Theta_c = 100$ (blue and green curve).

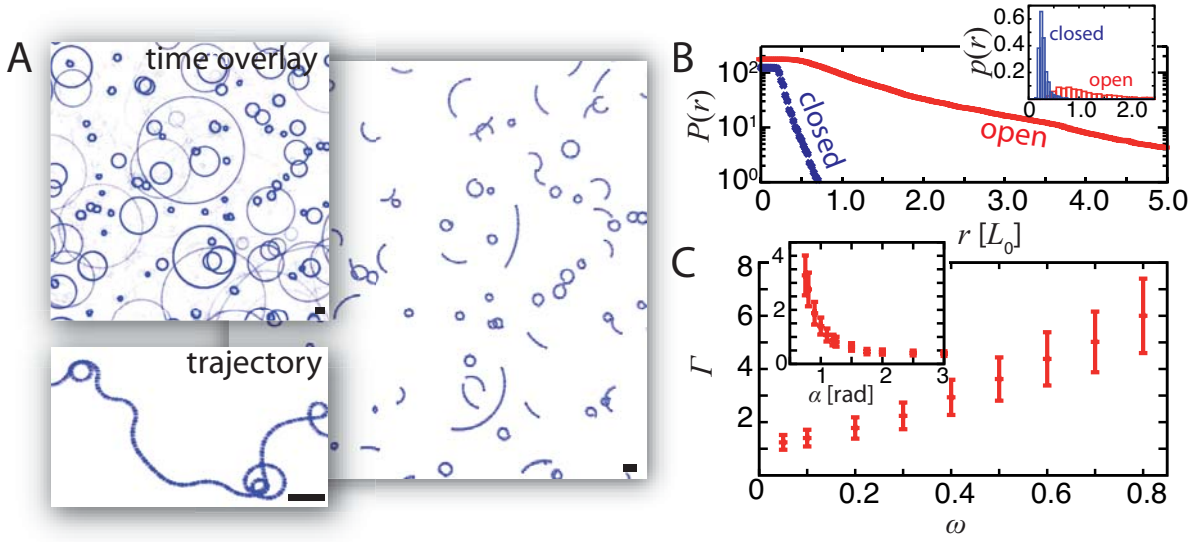


**Figure 3.7: Simulation results.** The incorporation of the two competing growth mechanisms together with the noise scaling as a function of the thickness is indeed sufficient to retrieve the experimental findings: like in the experiment two distinct ring configurations emerge: open and closed (**A**). This is reflected in the ring radii distribution $p(r)$ and the corresponding cumulative distribution $P(r)$ that can be separated in open and closed contributions (**B**). Both distributions decay approximately exponentially. The noise level in the system determines the balance between the two competing growth mechanisms and thus controls the properties of the frozen steady state: The ratio of open to closed rings $\Gamma$ increases with the rate of the random turns $\omega$, while it decreases with the noise level $\alpha$ (**C**). If not indicated otherwise the parameters are $\omega$ = 0.1, $lambda$ = 0.4, $\alpha$ = 1.0 and $\theta_c$ = 1. All scale bars are one string length $L_0$.

of one of these processes leads to the formation of either closed or open rings only. The cumulative radii distributions $P(r)$ for open and closed rings decay exponentially in accordance with experimental observations (Figure 3.7B).

Moreover, the simulations allow for a backtracking of the steady state properties to the inherent noise in the active system which determines the stochasticity of each string's trajectory: increasing the noise level by increasing the noise-amplitude or decreasing the rate of curvature changes, leads to a decrease in the fraction of open to closed rings $\Gamma$ (Figure 3.5C). An increase in the noise level increases the mean time until curvature freezing can take place. Strings can sweep a larger area leading to a higher amount of merging events. These merging events lead to a length increase that in turn favors ring closure events.

## 3.5 The noise level controls the assembly mechanisms

According to the simulation, it is the noise level in the system that sets the balance between the two growth processes competing for material in the system. High noise levels lead to predominately closed rings and *vice versa*. This can directly be tested in the experiment as the noise level in the system can be addressed by varying the motor density on the cover slip $\sigma_m$. A decreased number of motor proteins on the surface leads to more rugged trajectories of the strings and hence to smaller curvature radii (Figure3.8 A and B). In accordance with the simulations, a gradual decrease of the motor density shifts the fraction $\Gamma$ from open to closed rings: Small motor densities

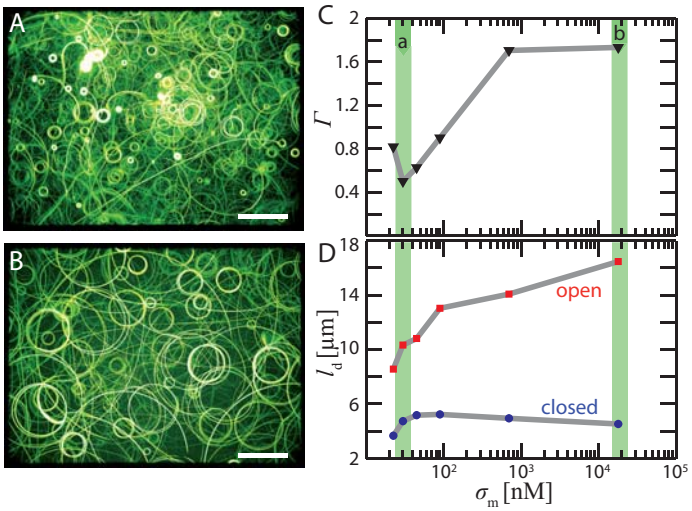


**Figure 3.8: The noise level controls the assembly mechanisms** By varying the motor density $\sigma_m$ on the surface, the feedback between growth, and the fluctuations that arise in the motility assay can be examined. In general, high motor densities lead to less fluctuations and a more persistent movement as can be seen in the time overlay image in (**B**), $\sigma_m = 700\,\mathrm{nM}$, while low motor densities lead to a more fluctuations (**A**), $\sigma_m = 30\,\mathrm{nM}$. The higher the noise level (i.e. the lower $\sigma_m$), the higher is the chance for individual strings to cross their own tail and to form closed rings. This is directly reflected in the higher abundance of closed rings at low motor densities, quantified by the ratio of open to closed rings $\Gamma$ (**C**). The radial distribution of closed rings itself is unaffected, as can be seen in the decay lengths $l_d$ of the exponentially decaying distributions (**D**). This is different for open rings, where the frozen-in curvature of the open rings directly reflects the fluctuations and the persistence of the movement in the motility assay: here, $l_d$ monotonically increases with increasing motor concentration $\sigma_m$. The actin concentration was set to $\rho = 3\,\mu\mathrm{M}$ and the fascin concentration was $c = 0.2\,\mu\mathrm{M}$. All scale bars are $50\,\mu\mathrm{m}$.

favor the emergence of closed rings with a $\Gamma$ of $0.5$, while high motor densities lead to predominately open rings with $\Gamma = 2$ (Figure 3.8 C). Importantly, upon changing the motor density, the conformational statistics of closed rings remains invariant, while the distribution of open rings is shifted to smaller radii with smaller decay lengths (Figure 3.8 D). This is attributed to the underlying coupling of growth and active transport through the mechanical properties of the emergent structures and the freezing mechanism that reflects the conditions during the assembly process. At low motor densities, the less persistent movement (Figure 3.8 A) implies smaller frozen-in radii of the open rings. The ring closure process, on the other hand, is triggered by stochastic changes in a string's trajectory, yet, the radius is determined by the stiffness of each individual structure. As a consequence, closed rings get only more abundant, but the ensuing distribution of curvature radii remains independent of the motor density $\sigma_m$.

## 3.6 Competition between rings and streaks

Frozen-in structures directly document the conditions during the coarsening process, and thus are expected to strongly depend on the nucleation and growth mechanisms. In the present system these are governed by the filament and the crosslinker concentration. Increasing these concentrations not only leads to more nucleation seeds and thus actin-fascin strings, but also to a more rapid growth process yielding stiffer strings. Above a critical material density at the surface, the strings are unable to pursue curved trajectories anymore and they are forced to align. They get increasingly interconnected and crosslinked to form frozen elongated and straight polar actin-fascin streaks with a thickness of up to $50\,\mu\mathrm{m}$ and a length in the order of centimetres (Figure. 3.9).

The emergence of elongated structures following straight trajectories has severe consequences for the further growth process in the system. Compared to the rings, the straight-moving streaks cover a large area. This not only leads to a more effective growth process and larger structures but also gives way to coarsening and subsequent merging processes. While neighbouring fibres initially tend to move in opposite directions, they gradually synchronize their directions of motions

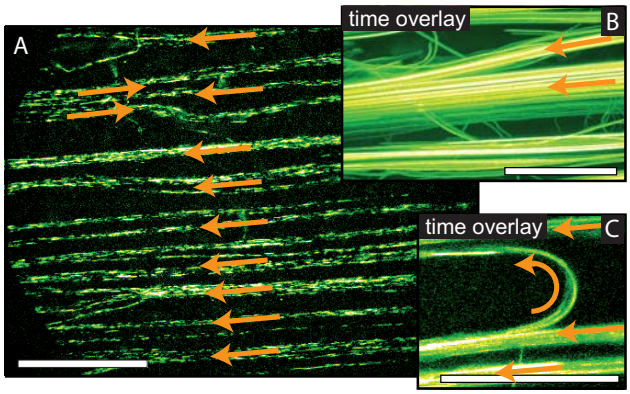


**Figure 3.9: Collectively moving streaks.** Above a certain material density, the ring formation processes are hindered and elongated actin fascin streaks emerge that are aligned alongside the long axis of the flow chamber. Like in the ring phase, all individual filaments gradually get incorporated in large-scale, polar structures and fluctuations on the single filament level cease. Initially, the streaks move in opposition to the mean direction of motion. With time, a major direction of motion develops that is adopted by all streaks in the course of turning events (**C**). This is accompanied by a coarsening process, where polarly aligned fibres gradually merge to larger ones (**B**). The actin concentration was set to $\rho = 10\,\mu\mathrm{M}$ and the fascin concentration was $c = 0.5\,\mu\mathrm{M}$. All scale bars are $50\,\mu\mathrm{m}$.

by merging (Figure. 3.9 B). This is accompanied by a coarsening process, in the course of which fibres of the same polarity gradually merge to larger ones (Figure. 3.9 C) which finally leads to large-scale symmetry breaking and a preferred direction of motion develops. After a time period of 10 min, extended fibre structures uniformly move in the same direction, imposing a polarity in the entire flow chamber on the centimetre scale.

The phase boundary determining the transition from ring formation to fibres depends on both the actin and the fascin concentration (Figure. 3.10). Consequently, the critical material density is not related to the critical filament densities in the ordinary high density motility assay without crosslinkers.

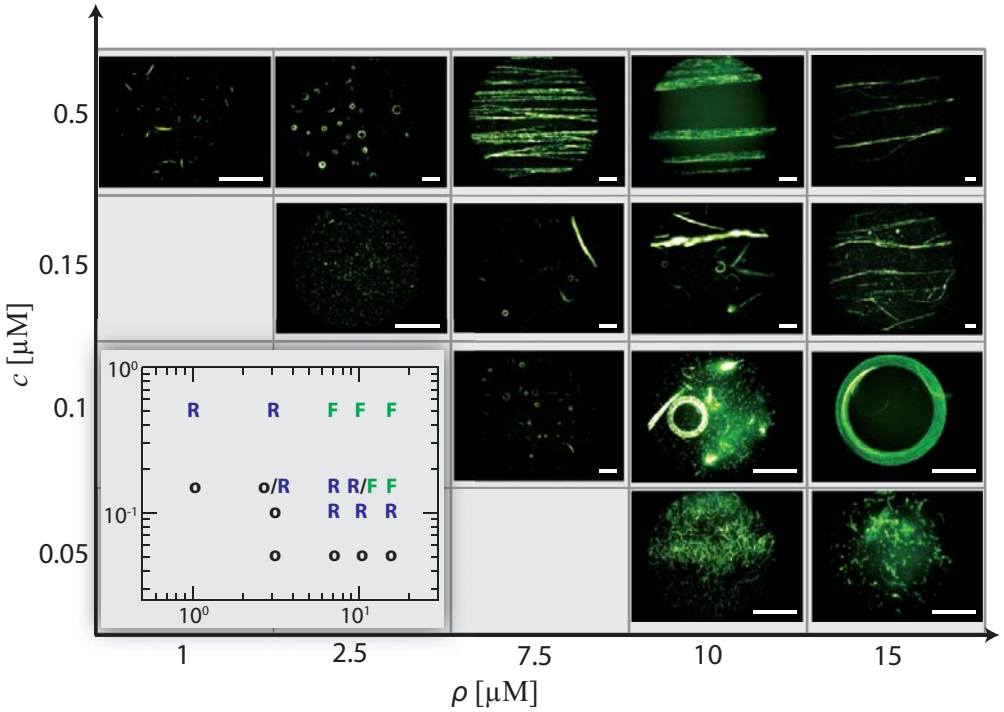


**Figure 3.10: Phase diagram as a function of the actin ($\rho$) and fascin concentration ($c$).** For high actin and fascin concentrations, the systems evolves into a frozen steady state that is characterized by coherently moving streaks or fibres (**F**). For intermediate concentrations of actin and fascin, the frozen active state is given by the ring phase (**R**). At low fascin concentrations, the steady state is characterized by persistent fluctuations on the single filament level and no frozen steady state emerges (**o**). All scale bars are $50\,\mu$m and the motor density was adjusted to $90\,$nM.

## 3.7 Discussion – a model system for absorbing transitions

The minimal system presented here allows a systematic parameter control through the variation of motor, crosslinker and actin concentrations. This is mandatory for the robust and reproducible assembly of frozen steady states with structures of defined size and morphology. It opens the door for various applications with the nanopattering of surfaces being a prime example, as suggested in motility assay experiments with microtubules [81, 127]. At the same time, the high-density motility assay can serve as a versatile model system to explore the full breath of non-equilibrium steady states in active systems. In previous investigations, it was shown that the interplay between

assembly and disassembly of driven filaments leads to dynamic patterns like swirls, clusters and density waves [171]. These non-equilibrium steady states are characterized by the perpetual built-up and destruction of structures driven by the incessant input of energy at the scale of an individual fibre. Upon adding a single new ingredient, namely passive crosslinking molecules, we have found here that the nature of the non-equilibrium steady state changes fundamentally; the presence of crosslinking molecules facilitates permanent filament aggregation and thereby switches off the disassembly pathway. As a consequence, the system's dynamics drives the filament assembly into an absorbing state where the structures arrest while the filaments still move. The coarsening process towards this absorbing state combines active driving with filament aggregation. Once reached, this state is stable and independent of the activity of the system, yet, it directly maps the assembly pathway. This "structural memory" relies on the intricate mechanical coupling between active transport and aggregation processes. This coupling and the ensuing aggregation mechanisms fully determine the statistical properties of the absorbing state.

From the experimental point of view, it remains a great challenge to unambiguously pinpoint the nature of the non-equilibrium phase transition. There exist only very few experimental systems that show clear evidence for an absorbing phase transition – with turbulent liquid crystals being probably the first example [201]. The main difficulty lies in the quantitative measurement of the transition over long time and length scales in the absence of interfering long-range interactions or boundary effects [201]. In this context, the system introduced here could provide a versatile tool towards the investigation of absorbing transitions. Consisting of only a few purified components, it allows for a precise investigation of the statistic properties of the phase transition. Future investigations might also want to explore analogies and differences between these active systems and externally driven systems showing shear-induced gelation [126] or aggregation [177]. In general, the further investigation of active systems complemented by an assembly process that in turn affects the mechanical properties, may set a new paradigm of frozen active states and seems to be an attractive route of explanation for many examples from cytoskeletal to colloidal systems.

# 4 Crosslinker Sensitive Structure Formation in Active Fluids

*In the previous chapter we investigated how the pattern formation in the high density motility assay is affected by the addition of the crosslinking protein fascin. There, we saw that in the presence of fascin, the system evolved into a frozen steady state where all the fluctuations on the single filament level had ceased. The unique patterns of this frozen steady state, rings and fibers, were the result of the microscopic binding properties of fascin that only crosslinks polar aligned filaments. In this chapter we will now address how the binding properties of different crosslinking proteins will affect the pattern formation in the system.*
*The chapter starts with a brief introduction of the investigated crosslinking proteins, $\alpha$-actinin, filamin, mini-FlnA, eplin, cortexillin and anillin (section 4.1). Subsequently, it is shown that the motor proteins in the motility assay drive the phase separation of $\alpha$-actinin/actin networks resulting in the actively compacting fibers consisting of actin filaments crosslinked by $\alpha$-actinin (section 4.2). The size of these fibers, that exceeds the size of individual actin filaments by two orders of magnitude results form the interplay of active driving and passive binding and can be adjusted by controlling the motor activity in the system. By contrast the addition of filamin and its truncation mutant mini-FlnA largely supresses any structure formation in the system (section 4.3). The characterization of the behavior of $\alpha$-actinin and filamin provides the benchmark for the investigation of eplin, cortexillin and anillin (section 4.4). While eplin and cortexillin in principle behave similar to $\alpha$-actinin, the concentration regimes and the time scale where the active compaction are considerably different. The addition of anillin, by contrast, results in the formation of static fiber-like structures.*
*Altogether, the results of this chapter demonstrate that the pattern formation in the motility assay sensitively depends on the properties of the individual crosslinking protein. The addition of different crosslinking proteins not only lead to a polymorphism of different steady state structures, but also to a self-organization dynamics that is highly specific for the individual crosslinking protein. This illustrates that motility assay experiments can provide a first readout for the behavior of crosslinkers in an active environment.*[1]

## 4.1 Crosslinking proteins in active systems

### 4.1.1 Contractile systems: force generating vs. force bearing structures

The functionality of most biological systems relies on the self organization of their constituents into higher order structures. By the cost of constant dissipation of energy, complex structures on various length-scales self-organize, ranging from macroscopic self-organization phenomena in animal groups to the molecular scale in intracellular structures. One of these self-organized structures is the contractile machinery of eukaryotic cells that is essential for numerous cellular processes ranging from the formation of stress fibers [99, 109] and contractile rings during cytokinesis [134, 170], to cell migration [144, 220] and intracellular transport processes [122]. Conceptually, those active materials owe their unique dynamic properties to the competition between force exerting components like molecular motors and force dissipating structures in the viscoelastic environment [73, 114, 130, 150]. Microscopically, the contractile machinery is made up of two key components: actin and myosin II [64]. The contractile ability of the actin-myosin complex arises from crosslinked actin networks that canalize and transmit motor mediated forces and translate them into contractile activity [41, 151]. To identify the role of myosin in the self organization processes, various studies have been devoted to simplified systems of purified cytoskeletal components [10, 18, 102, 103, 185, 203, 205]. In most of these reconstituted systems it was possible to relate

[1] The main results of this chapter are published in Reference [174].

the macro- or mesoscopic structure formation processes to the simultaneous action of myosin and crosslinking molecules and the competition between active driving and passive crosslinking. Recently, the reconstitution of contractile bundles in the presence of only myosin II filaments was achieved using a pre-patterning approach with functionalized colloidal beads [205].

However, the direct reorganization processes of the individual components were rarely accessible and the self-organization principles and the mechanisms setting the size in these structures remain unresolved. This can certainly be attributed to the inherent complexity of such model systems, but also to the commonly used approach of the simultaneous action of molecular motors and crosslinking proteins. In three dimensional systems, the myosin II filaments do not only provide the active driving, but they, themselves, are simultaneously reorganized in the course of the structure formation process [103, 185]. Only by a complete decoupling of the active driving from the actual structure formation process, it is possible to elucidate the underlying microscopic mechanisms and to specifically assess the behaviour of crosslinkers in an active environment.

To this end, we introduce high density motility assay experiments, where highly concentrated actin filaments, in the presence of crosslinking proteins, are propelled by motor proteins that are immobilized on a surface. This allows us to selectively investigate the behavior of crosslinking proteins in active systems. By using high density motility assay experiments, we show that already the interplay of only three components – molecular motors, filamentous actin and crosslinking proteins – is sufficient for an extremely broad range of self-organization phenomena. The morphology and the dynamic properties of the emerging patterns sensitively depend on the microscopic properties of the specific crosslinking proteins, such as the binding affinity, size and structure of the crosslinker, the behavior under load or the number nad type of the binding sites.

### 4.1.2 Introduction of the investigated crosslinking proteins

To assess to what extent crosslinking proteins can affect the behavior of active systems, a variety of crosslinking proteins was investigated. Subsequently, these crosslinking proteins and their basic properties are introduced.

**$\alpha$-actinin:** $\alpha$-actinin is a large homodimeric protein of the spectrin superfamily with a molecular weight of 215 kDa [40]. $\alpha$-actinin belongs to a highly conserved family of ABPs; its different isoforms are ubiquitous in muscle as well as in non-muscle cells [187]. It is a flexible crosslinker that crosslinks filaments regardless of their polarity [37]. $\alpha$-actinin is abundant in many cytoskeleton assemblies of the contractile machinery like myofibrils, stress fibres and contractile rings [56, 57, 170, 238]. *In vitro*, experiments have shown that $\alpha$-actinin is able to form homogenous actin-networks, tight bundles or mixtures of both [124, 125, 161, 226, 227, 235].

**Filamin and Mini-Filamin A:** Filamin is a large homodimer with a contour length of 160nm and a molecular weight of 560kD that has a spectrin-type actin binding domain at the N-termini [152]. Unlike $\alpha$-actinin, the crosslinking protein filamin is not predominantly assigned to contractile cytoskeletal assemblies. Filamins crosslink and bundle actin filaments, but also play an important role as signaling proteins *in vivo* [62]. Recent single molecule [169] and *in vitro* bulk experiments [58] have shown that filamin has mechanosensing abilities. Compared to $\alpha$-actinin, filamin forms morphological similar networks that are characterized by

a coexistence of bundles and clusters at high crosslinker concentrations [125, 176]. Mini-filamin A (Mini-FlnA) is a synthetic derivative of filamin that only consists of the actin-binding-domain and the domain 23 and 24 [84]. The long repetitive neck regions are lost and thus Mini-FlnA has a much smaller contour length than filamin. Thus, the usage of this mutant is promising for the selective investigation of how the crosslinker size and geometry affect the pattern formation in motility assay experiments.

**Eplin:** Eplin is a cytoskeleton-associated protein with a molecular weigth of $67\,\mathrm{kDa}$ [140]. It localizes to focal adhesions and regulates the dynamics of actin stress fibres [200]. Further, it inhibits actin filament depolymerization and the branching nucleation of actin filaments by the Arp2/3 complex. Eplin has at least two actin binding sites and crosslinks filaments in bundles [140].

**Cortexillin:** Cortexillin-I is an actin-binding protein which dimerizes via its central coiled-coil region. At their N-termini the monomers have actin binding domains of the spectrin-type, while the C-terminal domains are regulated by PIP(2). *In vivo*, cortexillins are enriched in the cortex of locomoting cells and play a crucial role in cytokinesis [61,191]. *In vitro*, it forms antiparallel bundle networks [107].

**Anillin:** Like $\alpha$-actinin and filamin, anillin forms bundle-cluster in *in vitro* networks. *In vivo*, however, it serves as a scaffold protein that is able to link myosin and actin [193], resulting in an even more complex interplay between active force exertion and passive crosslinking.

## 4.2 $\alpha$-actinin: Active compaction of driven filament networks

By adding $\alpha$-actinin to high density motility assay experiments, we show that a homogeneous $\alpha$-actinin/actin network that is set under stress by molecular motors is intrinsically unstable. It disintegrates and forms actively compacting patches that finally evolve into highly compact $\alpha$-actinin/actin fibres that exceed the length of individual filaments by two orders of magnitude. The structure formation is determined by the initial phase, where the reorganization of individual filaments leads to a phase separation between dense and dilute regions. The efficiency of this reorganization process and hence the length scale of the phase separation directly depend on the motor activity. This allows us to control the size and morphology of the $\alpha$-actinin/actin fibres: high motor activities lead to fibres of up to $100\,\mu\mathrm{m}$ in length whereas low motor activities result in only $5\,\mu\mathrm{m}$ long fibres.

### 4.2.1 Basic phase behavior and active compaction

In the regime of high actin densities and without crosslinking proteins, the filaments self-organize to form coherently moving structures, clusters and density waves [171]. This drastically changes if the crosslinking protein $\alpha$-actinin is added to the motility assay. As $\alpha$-actinin crosslinks filaments regardless of their orientation and leads to the formation of predominately apolar structures [37], it directly opposes the active transport in the motility assay that relies on the structural polarity of the filaments. Initially, this leads to a homogeneous distribution of actin filaments that are firmly incorporated in a two dimensional $\alpha$-actinin/actin network (Figure 4.1). This elastic network is actively set under stress by the underlying motor proteins. The interplay of $\alpha$-actinin crosslinkers and the motor activity determines the further dynamic development of this initial basic state.

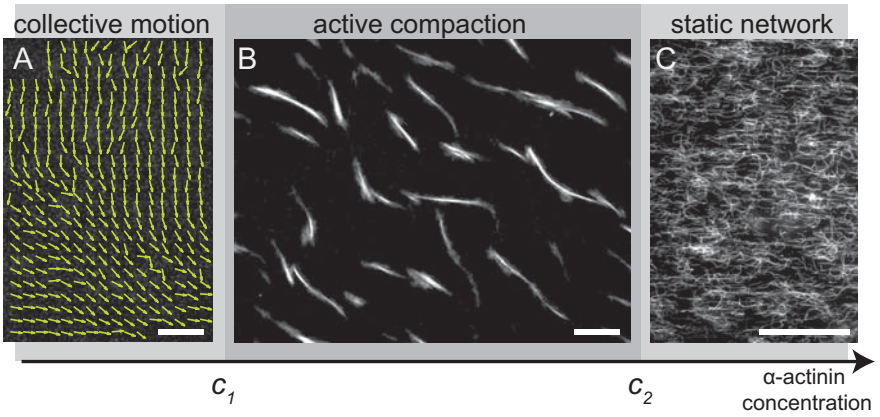


**Figure 4.1: Phase behaviour as a function of the $\alpha$-actinin concentration.** For low crosslinker concentrations below $c_1 = 0.05\,\mu$M, the steady state of the system is characterized by the collective movement of driven filaments, similar to the high density motility assay without crosslinking proteins (**A**). Compared to the case without crosslinkers, the structures are less pronounced, as the crosslinking proteins dampen the formation of density inhomogeneities. Moreover, due to the competition between active driving and passive crosslinking, the filaments get actively ruptured. Increasing the crosslinker concentration above a threshold concentration of $c_1 = 0.05\,\mu$M, leads to a fundamentally different behavior: instead of collectively moving structures, the system actively compacts and forms highly condensed $\alpha$-actinin/actin fibres (**B**). These fibres consist of millions of individual filaments and exceed the size of the individual filament by two orders of magnitude. The active compaction is only possible in an intermediate concentration regime: at high crosslinker concentrations above $c_2 = 0.23\,\mu$M, the motor activity is not sufficient to disintegrate the network and the isotropic initial state is preserved (**C**). For (**A**) the $\alpha$-actinin-concentration was adjusted to $c_{cl} = 0.005\,\mu$M, for (**B**) to $c_{cl} = 0.17\,\mu$M and for (**C**) to $c_{cl} = 0.46\,\mu$M. The actin concentration was set to $7.6\,\mu$M. All scalebars are $25\,\mu$m.

Consequently, the phase behavior of the system depends on the $\alpha$-actinin concentration $c_{cl}$ (Figure 4.1).

For a given actin concentration, high $\alpha$-actinin concentrations effectively prevent any further reorganization and the homogeneous basic state is frozen in (Figure 4.1 C). In this regime of high crosslinker concentrations, the motor proteins are not able to induce large-scale rearrangements in the network.

On the other extreme, in the regime of low $\alpha$-actinin concentrations, the amount of crosslinking proteins in the network is too small to sustain the integrity of the network. The motor proteins drive the active fluidization of the network and the initial basic state disintegrates (Figure 4.1 A). Subsequently, the system self-organizes into coherently moving structures reminiscent to the collective motion observed in the motility assay without crosslinks. Yet, even in this concentration regime the influence of crosslinkers is still visible, as the competition between motor induced active transport and passive crosslinking leads to a shortening of the filaments. Moreover, the density inhomogeneities that characterize the high density motility assay without crosslinkers are less pronounced. Only for trace amounts of $\alpha$-actinin, the phase behaviour of the high density motility assay without crosslinkers can be retrieved – exemplifying the high sensibility of the setup with respect to the addition of crosslinking proteins.

For any given actin concentration, an intermediate $\alpha$-actinin concentration can be found, where the motor activity and the influence of the crosslinkers are relatively balanced (Figure 4.2). This enables the active reorganization of the initial basic state and at the same time ensures the integrity of the network. This is mandatory for the subsequent dynamic structure formation that leads to the self-organized formation of highly compact $\alpha$-actinin/actin fibres (Figure 4.1 B).

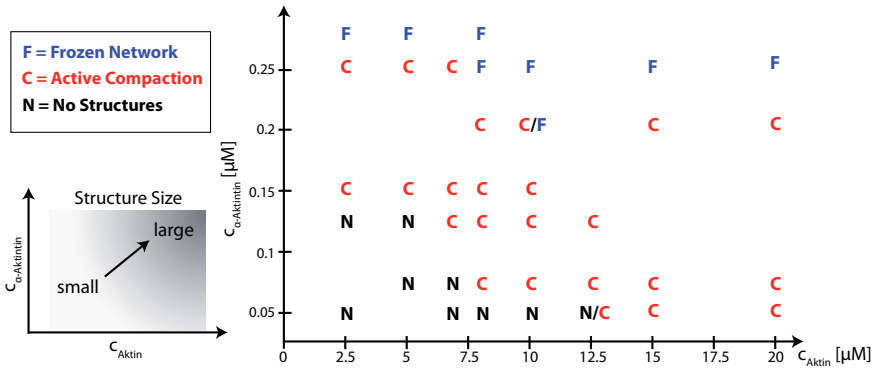


**Figure 4.2: Schematic phase behavior as a function of the $\alpha$-actinin and actin concentrations.** For low crosslinker and actin concentrations no stable structures evolve, as the motor proteins drive the disintegration of the network (**N**). In a regime where active driving and crosslinking are balanced, the system actively compacts (**C**). In this intermediate regime the steady state is characterized by compact fibers. The size of these structure depends on the actin and $\alpha$-actinin concentrations. In general, high material densities lead to larger steady-state structures. At high crosslinker concentrations, the network is tightly crosslinked. The motor proteins cannot compromise its overall stability and the initial basic state is frozen (**F**).

This self-organization process can be conceived as a phase separation between patches that are densely packed with material and depleted regions that appear as holes in the $\alpha$-actinin/actin microstructure (Figure 4.3). While filaments in the dense regions are firmly crosslinked and barely move, individual filaments in the depleted regions can move freely and perform persistent random walks before they get crosslinked again. Successively, the dense patches contract and eventually evolve into compact $\alpha$-actinin/actin-fibres, reflecting the tendency of $\alpha$-actinin to form bundles in passive in vitro networks [124].

The self-organization takes place on the timescale of several tens of minutes in a multistage coarsening process (Figure 4.3 B-E). As can be inferred from the area fraction covered by the dense patches (Figure 4.4), the process of active compaction is continuous, until a steady state of maximal compaction is reached after approximately $30\,\mathrm{min}$. In contrast to other reconstituted systems, the observed active compaction neither relies on the formation of contractile foci of aggregating motor proteins, nor on the pre-assembly of F-actin bundles. The isotropic active driving of immobilized motor proteins is sufficient to destabilize the crosslinked F-actin network and to trigger the self-organized formation of compact fibers.

### 4.2.2 The multiple stages of active compaction

The active compaction in the system can be further quantified by introducing the average mesh size $\Phi$ of the densely packed regions as order parameter[2]. Starting from the initial, homogeneously distributed state with a mesh size of $\Phi = 8\,\mu\mathrm{m}$, $\Phi$ increases monotonically with time until a steady state is reached that averages a meshsize of $\Phi \approx 50\,\mu\mathrm{m}$ (Figure 4.4). The overall temporal evolution of the order parameter is characterized by subtle variations in the rate of change of $\Phi$: in the early stage of the pattern formation, a linear rise in the mesh size occurs, followed by a plateau, where the mesh size stays almost constant. In the late stages of the pattern formation, the coarsening process gets increasingly slower, before it finally levels of again in the steady state. These

[2]Details of the calculation of the meshsize can be found in the appendix A.2.9.

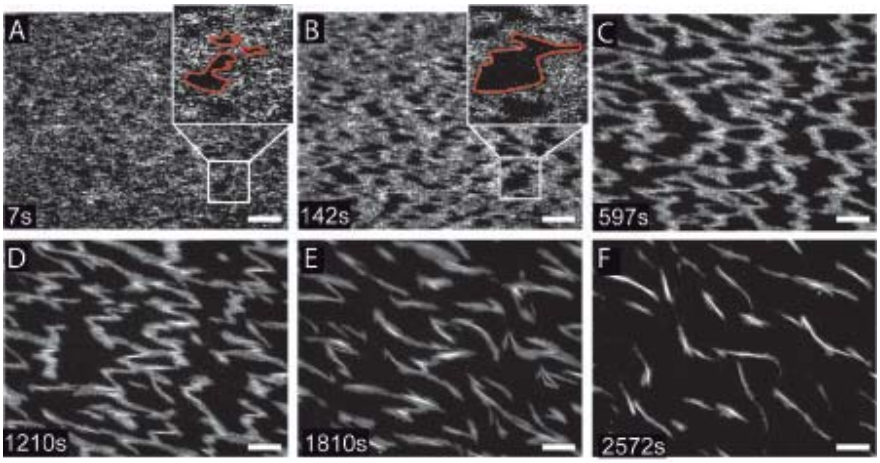


**Figure 4.3: An $\alpha$-actinin/actin network that is set under stress by underlying molecular motors is unstable.** Within several minutes the network is disintegrated and driven into a phase separation between regions densely packed with material and dilute regions, where only a limited number of filaments can be found. These dilute regions appear as holes in the network microstructure (**A**) and (**B**). With time, the holes coarsen as the densely packed patches further compact (**A**) – (**C**). Yet, the dense patches are still interconnected. When the diameter of the holes approximately equals the diameter of the dense patches (**C**), any further compaction requires a rupturing of the dense patches (**D**). This leads to the successive formation of isolated patches (**E**). Now, any further compaction is based on internal reorganizations of these isolated patches (**E**) and (**F**). In the steady state of the pattern forming instability, the system consists of isolated tightly bundled patches (**F**). The actin concentration is $7.6\,\mu$M and the $\alpha$-actinin concentration $c_{cl} = 0.17\,\mu$M. All scalebars are $25\,\mu$m.

variations in the rate of change correspond to the distinct stages of the observed multistage coarsening process. These different stages are: (i) an active shortening of the filaments and the dynamic reorganization of the fragments that triggers the formation of densely packed patches; (ii) the active transport of entire patches; (iii) the disintegration of the dense patches and (iv) their internal compaction.

**(i) Active filament-shortening and reorganization of the fragments**

In the initial stage of the multistage coarsening process, the initially $10\,\mu$m long, isotropically distributed filaments are ruptured into approximately $1\,\mu$m long fragments (Figure 4.5 A and B). This results from the competitive binding of molecular motors and passive crosslinkers to the actin filaments. The active fragmentation is the precondition for the subsequent reorganization of the filaments: only filaments that are short enough can readily detach from the network and can be actively transported, while longer filaments stay firmly crosslinked to the network (Figure 4.5 C). This is reminiscent to observations in cellular systems, where the structure formation also requires predominantly short actin filaments with a highly conserved filament length below $1\,\mu$m. The dynamic reorganization of the filament fragments is the precondition for the observed phase separation of the network into dense and dilute regions. The fragments detach more easily from regions where the material density and thus the number of possible binding partners is low. On the other hand, they are prone to get bound again at regions where the material density is high. This is sufficient to destabilize the $\alpha$-actinin/actin network as local density inhomogeneities are amplified. Successively, this leads to the observed phase separation into dense patches and dilute zones.

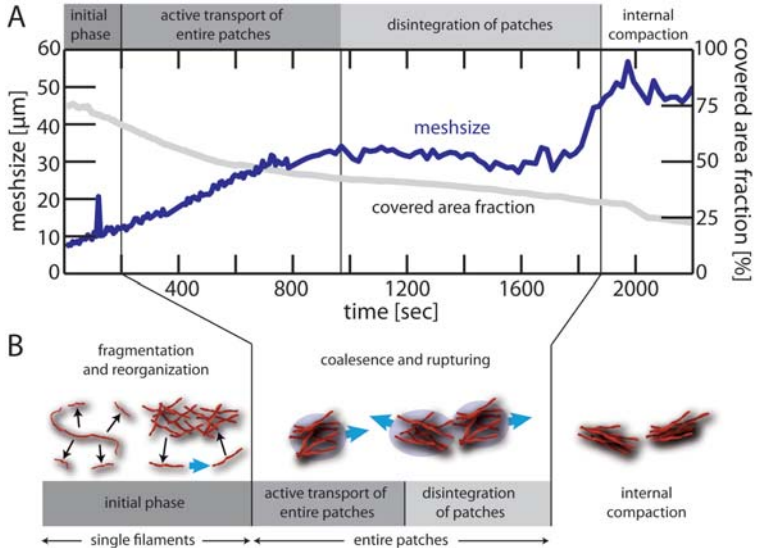


**Figure 4.4: The multiple stages of active compaction.** The active compaction of the $\alpha$-actinin/actin network undergoes distinct stages in a multistage coarsening process. This is visible in the continuous decline of the occupied area fraction and the synchronous increase in the mesh size of the network (**A**). Each phase is characterized by distinct microscopic processes that are schematically depicted in (**B**). In the initial phase, the actin filaments are ruptured into approximately $1\,\mu\mathrm{m}$ long fragments. The fragmentation is the precondition for the subsequent reorganization of the system, as the dynamic relocation of these fragments leads to a phase separation of the network into dilute and densely packed patches. The active transport of entire patches marks the beginning of a phase of rapid compaction, visible in the linear decline in the occupied area fraction and the concomitant decrease in mesh size. This compaction continues until the size of the dilute regions and the dense patches are approximately equal. Now, any further compaction requires a rupturing of the patches. Freely moving patches collide and coalesce leading to tightly interconnected non-moving structures. This is reflected in a decline in the slope of the occupied area fraction and a plateau in the mesh size. This stage continues until the entire network has disintegrated into isolated non-moving structures. Now, any further compaction is mainly based on the internal compaction of these structures, leading to the compact $\alpha$-actinin/actin bundles observed in the steady state. The actin concentration was set to $7.6\,\mu\mathrm{M}$ and the $\alpha$-actinin concentration was set to $c_{cl} = 0.17\,\mu\mathrm{M}$. All scalebars are $25\,\mu\mathrm{m}$.

### (ii) Active transport of entire patches

In the next stage, these patches are transported as a whole by the underlying motor proteins. The patches have a size of the order of $10$ to $100\,\mu\mathrm{m}^2$. Once formed, they are stable and move on straight and persistent trajectories with an average velocity of up to $0.1\,\mu\mathrm{m/sec}$, one order of magnitude slower than the gliding speed of individual filaments (Figure 4.6). The movement of the different patches is uncorrelated in direction and velocity. In the quasi two-dimensional geometry of the motility assay, this leads to a further condensation, as the uncorrelated movements of the patches results in the formation of spots where different patches converge and material gets accumulated (Figure 4.6 B and D). Despite the slow velocity of the moving area fractions, this process results in a comparably rapid compaction that lasts for around $15\,\mathrm{min}$.

### (iii) Disintegration of the dense patches

That followed, in the disintegration phase, the condensation speed starts to decrease because the phase separation into densely packed patches and dilute zones is almost completed. Any further condensation is only possible if the network disintegrates by a rupturing of the dense patches (Figure 4.7). This leads to the formation of isolated patches. Once a rupturing event occurs, patches

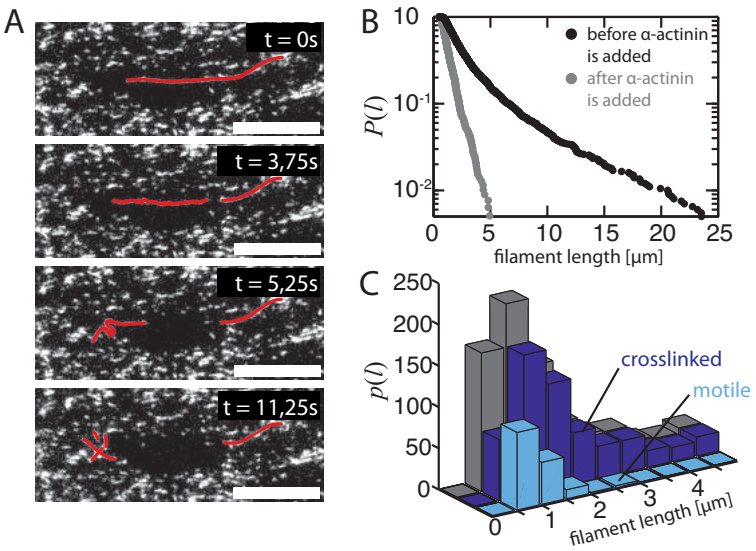


**Figure 4.5: Filament rupturing and filament-lenght distributions.** The competition between active transport and crosslinking leads to a rapid fragmentation of the filaments. The image series in (**A**) shows the motor induced fragmentation of a filament that gets bound to the $\alpha$-actinin/actin network at $t = 0$. Within several seconds the initially $20\,\mu\mathrm{m}$ long filament gets ruptured into fragments not larger than $5\,\mu\mathrm{m}$ in length. The motor-induced rupturing also becomes manifest in the overall cumulative filament length distributions $P(l)$ shown in **B**. Before $\alpha$-actinin is added, the filament lengths are broadly distributed (black curve). After the addition of $\alpha$-actinin the distribution considerably narrows, as the filaments get ruptured (gray curve). The rupturing of individual filaments is the precondition for their subsequent dynamic relocation, as can be seen in the length distributions $p(l)$ shown in (**C**). While long filaments are prone to be firmly crosslinked, shorter filaments can readily detach from the network and are actively transported. The actin concentration was set to $7.6\,\mu\mathrm{M}$ and the $\alpha$-actinin concentration was adjusted to $c_{cl} = 0.17\,\mu\mathrm{M}$. All scale bars are $10\,\mu\mathrm{m}$.

move freely on straight paths until they collide and merge with other patches. The rupturing results in the stagnation of the average mesh size, since the compaction is compensated by the formation of new holes.

The disintegration phase is accompanied by a change in the morphology of the structures: because patches are not firmly interconnected with other patches, they are able to flow past each other, leading to the emergence of zigzag-like patterns (Figure 4.3). Crosslinking of converging patches leads to larger structures. Successively, highly condensed structures form. This comparatively rapid process is recovered in the steep increase in the mesh size at the end of the disintegration phase (Figure 4.4).

### (iv) Internal compaction

After a time period of $30\,\mathrm{min}$, the $\alpha$-actinin/actin network has entirely disintegrated into isolated structures. They are not transported any more and the active transport now fully contributes to their compaction. This marks the beginning of the phase of internal compaction where any further decrease in meshsize is mainly based on the internal compaction finally resulting in highly compact, yet immobile fibres (Figure 4.7 F and G). This is recovered in a slow increase in the average mesh size (Figure 4.4).

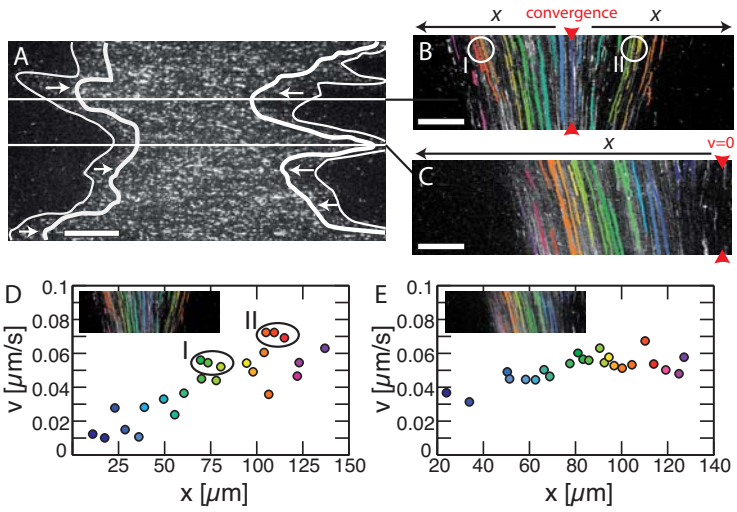


**Figure 4.6: The dynamic compaction of dense patches relies on the convergence of individual patches.** Image (**A**) shows the active compaction of a dense patch over a time period of $0.22\,\mu$M (thin line: initial position; bold line: final position). The compaction of the patch relies on the active transport of subdomains that move independently from one another. This can be seen in the kymographs along two cross-sections of the patch shown in (**B**) and (**C**). While (**B**) shows the homogenous compaction around a zone where several small subdomains converge, (**C**) illustrates the displacement of an entire subdomain. The size of the polar subdomains that drive the compaction can be inferred from the local velocities depicted in (**D**) and (**E**). In (**B**) the compaction is mediated by subdomains that have a diameter of approximately $10\,\mu$m, as exemplified by the regions marked with I and II in (**B**) and (**D**) respectively. In (**C**), the movement is mediated by a subdomain that is $100\,\mu$M in diameter. This is reflected in a constant velocity in the entire field of view (**E**). The actin concentration was set to $16\,\mu$M and the $\alpha$-actinin concentration was adjusted to $c_{cl} = 0.22\,\mu$M. All scalebars are $25\,\mu$m.

### 4.2.3 The active compaction relies on the polarity of the structures

While the dynamics in the initial phase relies on the reorganization of individual filaments, the rapid compaction in the subsequent stages of the coarsening process requires the active transport of entire patches (Figure 4.4). Remarkably, the movement of the patches is highly persistent, both in direction and velocity and, as long as the patches do not interfere with neighboring structures, they move on straight trajectories (Figure 4.6). The active transport of entire patches is likely to rely on a non-vanishing net-polarity of the patches, providing the small but stable directional bias necessary for the observed dynamics. If the patches would have a vanishing net polarity, with filaments that are oriented randomly, any motor induced active transport would result in a displacement in a random direction. Most likely these displacements would cancel out and the patch either would not move at all, or it would show a highly non-persistent motion with frequent directional changes and a varying velocity.

To further explore this aspect, we performed a set of experiments, where we let the system evolve starting from a basic state that is polar on large length scales. In the motility assay such polar basic states can readily be prepared by allowing the system to self-organize into coherently moving structures, before crosslinking proteins are added. In this case the polarity of the basic state is determined by the F-actin concentration: high actin concentrations yield coherently moving structures with a high polarity, while lower actin concentrations result in smaller polar domains (Figure 4.8 A and D). If the dynamics of the patches indeed depended on the net polarity of the patches, a higher initial polarity should have two main consequences: (*i*) an increase of the patch

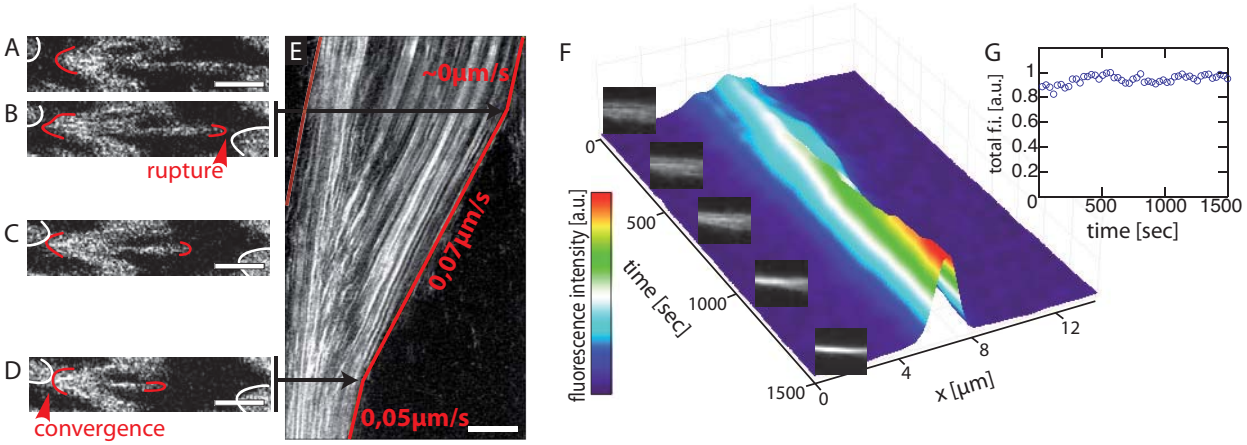


**Figure 4.7: Rupturing and internal compaction of dense patches.** In the disintegration phase of the pattern forming instability, the further compaction of the systems requires the rupturing of dense patches. This is illustrated in the image series shown in (**A**) – (**D**) and the corresponding kymograph (**E**). In image (**A**) the further compaction is hampered by the connectivity of the dense patches. The underlying motor proteins build up tension that finally leads to rupturing of the dense patch at its weakest point (**B**). This is followed by the free retraction of the patch (**C**) with an average retraction speed of $0.07\,\mu\mathrm{m/sec}$ (**E**). The free retraction continues until the tip of the patch hits another patch to form a new zone of convergence (**D**). This is reflected in the subsequent decline in the retraction speed $0.05\,\mu\mathrm{m/sec}$. Once the network has disintegrated into isolated patches, any further contraction relies on the relatively slow internal compaction within the isolated patches (**F**). The figure exemplarily shows the temporal evolution of the cross section of such an isolated patch. Within $1500\,\mathrm{sec}$ it compacts from a thickness of $6\,\mu\mathrm{m}$ to a thickness of $2.5\,\mu\mathrm{m}$. During the compaction the total fluorescence intensity stays approximately constant, indicating that the observed compaction is not based on the loss of material (**G**). The actin concentration was set to $7.6\,\mu\mathrm{M}$ and the $\alpha$-actinin concentration was adjusted to $c_{cl} = 0.17\,\mu\mathrm{M}$. All scalebars are $25\,\mu\mathrm{m}$ and the time period for the kymograph was $375\,\mathrm{sec}$.

size and (*ii*) an increase of the overall structure size in the steady state. As can be seen from the patch dynamics during the pattern formation (Figure 4.8 B and E) and the steady state images (Figure 4.8 C and F), this is exactly the case. The higher the polarity of the initial basic state, the higher is the patch size and the bigger is the size of the $\alpha$-actinin/actin fibres in the steady state. The higher polarity of the patches also becomes manifest in a higher gliding velocity: patches that emerge from a polar basic state move with velocities of up to $0.25\,\mu\mathrm{m/sec}$, significantly higher than observed for apolar starting conditions.

### 4.2.4 Controlling the length scale of the active compaction

The complex dynamics in the present system include the active transport of entire patches, rupturing events and the internal compaction of the emergent structures (Figure 4.4). However, all these processes rely on the preceding reorganization and relocation of individual filaments which triggers the formation of the dense patches. Microscopically, this reorganization is comparatively simple: it is based on the detachment of single filament fragments that are actively transported by the motor proteins before they get bound again. This competition between active transport and passive binding is governed by three microscopic parameters: the effective filament (un-)binding rates $k_{\mathrm{off}}$ and $k_{\mathrm{on}}$ and the motor induced sliding velocity of individual filaments $v$. Together, these parameters set the length scale of the observed phase separation during the initial stages of the pattern forming instability: the length scale is limited by the average distance $\langle x \rangle$ individual filaments can cover after having detached from the network. This average distance is determined by

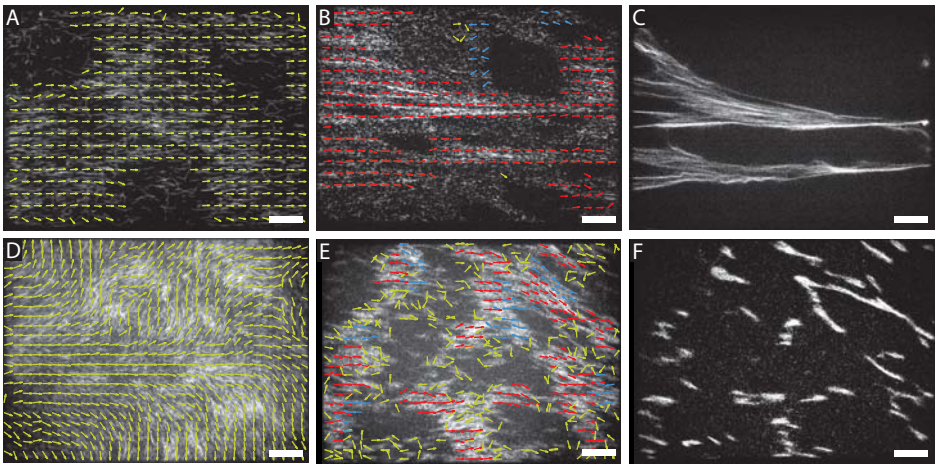


**Figure 4.8: The active compaction relies on the polarity of the structures.** The addition of $\alpha$-actinin to a polar basic state yields larger and faster moving patches. Images (**A**) and (**D**) show microscopy images of collectively moving filaments at different filament densities in the absence of $\alpha$-actinin. High filament densities ($c_a = 10\,\mu$M) lead to the formation of highly ordered collective motion patters (**A**). The yellow arrows denote the velocity profile obtained by particle image velocimetry. The polar order of this basic state is conserved after $\alpha$-actinin is added (**B**). Compared to the case with apolar starting conditions the patches move with a five fold faster velocity of $0.15 - 0.25\,\mu$m/sec and the resulting patches considerably larger. This can be seen in (**B**) where all velocity vectors belonging to coherently moving patches are grouped and colored. Patches that move predominately to the right are coloured in red, patches that move to the left are marked in blue, and velocity vectors that are uncorrelated are colored in yellow. The large patch sizes resulting from polar starting conditions also become manifest in the steady state structure that are shows thicker and larger (**C**). At lower F-actin concentrations ($c_a = 5\,\mu$M) the polarity of the initial basic state is considerably less pronounced (**D**). This leads to smaller patch sizes (**E**), slower moving patches ($0.10 - 0.15\,\mu$m/sec) and smaller structures in the steady state (**F**). The $\alpha$-actinin concentration was $c_{cl} = 0.17\,\mu$M. For (**A**) – (**C**) a ratio of labelled to unlabeled filaments of $1:45$ was used; for (**D**) – (**F**) the labelling ratio was adjusted to $1:20$. In the absence of $\alpha$-actinin the average filament speed is $4.2\,\mu$m/sec. The actin concentration was set to $7.6\,\mu$M and the $\alpha$-actinin concentration was adjusted to $c_{cl} = 0.17\,\mu$M. All scalebars are $25\,\mu$m.

the average detachment time of an individual filament $\propto k_{\text{off}}/(k_{\text{off}} + k_{\text{on}})$ and the gliding speed $v$ according to

$$\langle x \rangle \propto v k_{\text{off}}/(k_{\text{off}} + k_{\text{on}})\,. \tag{4.1}$$

The rates $k_{\text{off}}$ and $k_{\text{on}}$denote the effective on-and off-rates of an entire filament. They depend on the local filament and crosslinker densities and the crosslinker on- and off-rates under load when the system is actively set under stress by motor proteins.

Providing an estimate for the length scale of phase separation during the initial stages of the pattern formation, Equation (4.1) bears two important implications. First, since it directly depends on the filament velocity $v$, any finite filament velocity should result in a phase separation. Second the structure size in general should be controllable by the filament gliding velocity. In the experiment, this can readily be addressed by varying the ATP concentration ($c_{\text{ATP}}$) as it sets the filament speed according to the Michaelis-Menten kinetics: $v \propto c_{\text{ATP}}/(k_{\text{M}} + c_{\text{ATP}})$ with $k_{\text{M}}$ being the enzyme-specific Michaelis-Menten constant. For small ATP concentrations, $v$ rises linearly with $c_{\text{ATP}}$ and approaches a maximal saturation velocity $v_{\text{max}}$ for the freely moving filaments. Moreover, the ATP concentration affects the crossbridge strength of the acto-myosin complex. Lowering the ATP concentration leads to a higher binding affinity of the myosin heads to the actin filaments. Decreasing the effective off rate $k_{\text{off}}$, this effect can be expected to further decrease the length scale $\langle x \rangle$ of the phase separation.

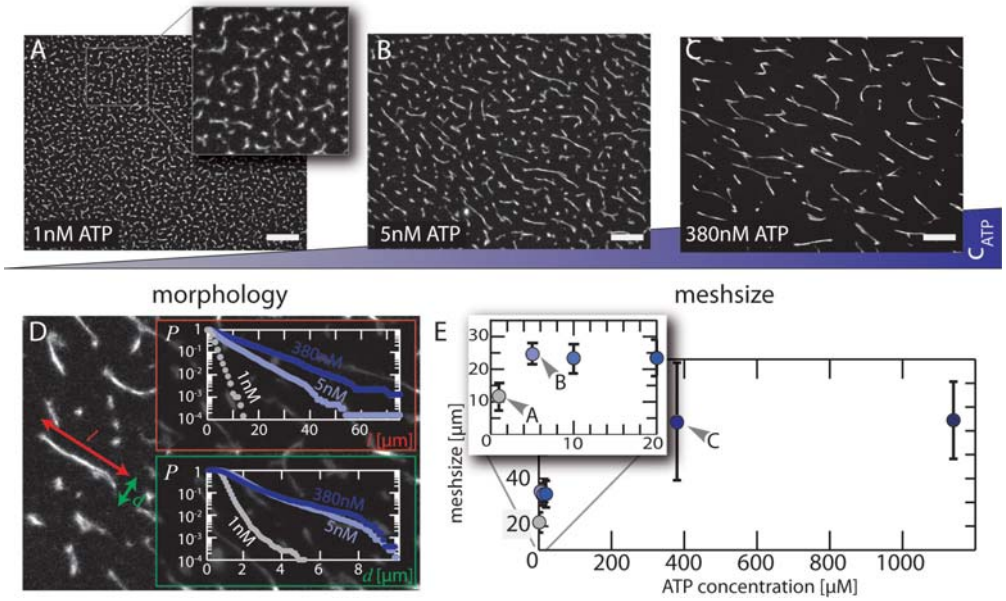


**Figure 4.9: The motor activity controls the morphology and the meshsize of the compact fibres.** Images (**A**) – (**C**) show the steady state of the pattern formation for three different ATP concentrations. For low ATP concentrations, small fibres emerge; they have an average length $l$ of up to $15\,\mu$m and exceed the size of the individual filament by one order of magnitude, as can be seen from the cumulative distributions $P(l)$. The thickness d of these structures is limited to $15\,\mu$m (**A**). Higher ATP concentrations yield considerably bigger structures: with a length of up to several hundreds of micrometers, they exceed the length of the individual filament by two orders of magnitude. The growth in length is accompanied by a slight growth in thickness (**D**). For all ATP concentrations, the fiber lengths are exponentially distributed. Altogether fibers that were formed under high ATP concentrations incorporate considerably more material. The ATP concentration not only determines the morphology but also the spacing between individual fibres. This is retrieved in the average mesh size $|\Phi|$ that increases with increasing ATP concentrations (**E**). Towards high ATP concentrations $|\Phi|$, saturates at an average mesh size of $60\,\mu$m. For any finite ATP concentration, the homogeneous $\alpha$-actinin/actin network is unstable and disintegrates into compact patches. By contrast, the initial network is stable when no ATP is supplied. All scalebars are $25\,\mu$m; the actin concentration was adjusted to $7.6\,\mu$M and the $\alpha$-actinin concentration was set to $c_{cl} = 0.17\,\mu$M.

As can be seen in the steady state images (Figure 4.9 A – C), the structure size is indeed tightly regulated by the ATP concentration. Small ATP concentrations ($1\,\mu$M), corresponding to small gliding velocities, yield small structures with a length of up to $10\,\mu$m and a thickness of up to $5\,\mu$m. For high ATP concentrations, corresponding to the maximal gliding velocity, considerably bigger structures emerge: here, the fibers have a length of up to several hundreds of micrometers and a thickness of up to $10\,\mu$m. The ATP-dependence of the structure size is also reflected in the cumulative length and thickness distributions (Figure 4.9 D). The length distributions are of exponential shape with decreasing decay length for smaller ATP concentrations. Likewise, a decrease of the ATP concentration leads to a narrower thickness distribution. Altogether, the elongated fibers that evolve at high ATP concentrations incorporate up to 100 times more filaments than the ones that form in the presence of low ATP concentrations.

The morphology of the fibres is intimately related to the mesh size $|\Phi|$ observed in the steady state. The higher the level of compaction, the more material is concentrated on fewer but larger fibers. By consequence, the average spacing between the fibres and thus the meshsize $|\Phi|$ increases with increasing ATP concentration. Starting from a minimal mesh size of $|\Phi| = 10\,\mu$m at low

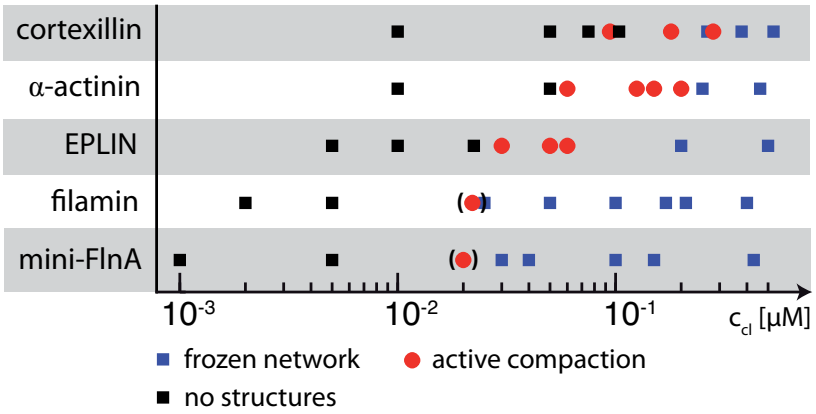


**Figure 4.10: Phase behavior of apolar crosslinking proteins in active systems.** As can be infered from the width and the onset of the concentration regime where the motor-proteins can induce the formation of actively compacting structures, the corsslinking efficiency increases from cortexillin over $\alpha$-actinin and eplin to mini-FlnA and filamin. In the case of filamin and mini-FlnA even low crosslinker concentrations do not result in the formation of isolated structures; the overall connectivity of the network is never compromised. For all data points the actin concentration was set to $c_A = 7.5\,\mu$M of monomeric actin.

ATP, $|\Phi|$ increases with increasing ATP concentration until it saturates at an average mesh size of $|\Phi| = 50\,\mu$m (Figure 4.9 E). The saturation correlates to the saturation of the filament gliding velocity at $v_{\max}$ for high ATP concentrations (Figure 4.9 E). This further confirms the microscopic picture of the balance between active transport and passive binding setting the lengthscale of contraction (Equation 4.1). Remarkably, the structure formation in the system does not require a critical ATP concentration. For any finite ATP concentration or filament gliding velocity, the homogeneous $\alpha$-actinin/actin network is unstable and disintegrates into dense patches – in full agreement with the microscopic picture. By contrast, the initial network is stable when no ATP is supplied.

Accordingly, the motor activity constitutes an effective switch which allows the system to adjust the length scale of the structure formation: a high motor activity yields a pattern formation that is coordinated over a distance of more than $100\,\mu$m, exceeding the size of the individual filament by two orders of magnitude. By contrast, low ATP concentrations result in small patterns with a diameter in the order of the filament length. The ATP concentration also controls the aspect ratio of the structures: while high ATP concentrations lead to highly elongated fibres, low ATP concentrations lead to more rounded structures (Figure 4.9 A – C). This motor-activity-dependent formation of condensed structures is reminiscent to the force dependent aggregation of $\alpha$-actinin/actin networks in rheological experiments [177].

## 4.3 Filamin: Formation of highly resilient networks

According to the microscopic conception of the pattern forming instability established so far, subtle alternations in the properties of the crosslinking protein should become manifest in the pattern forming instability. But does the formation of actively compacting structures only depend on the ability of crosslinking proteins to link actin filaments independent of their orientation? To investigate this question, we added filamin, a crosslinking protein that also connects actin filaments regardless of their orientation. Compared to $\alpha$-actinin, filamin *a priori* forms similar *in vitro* net-

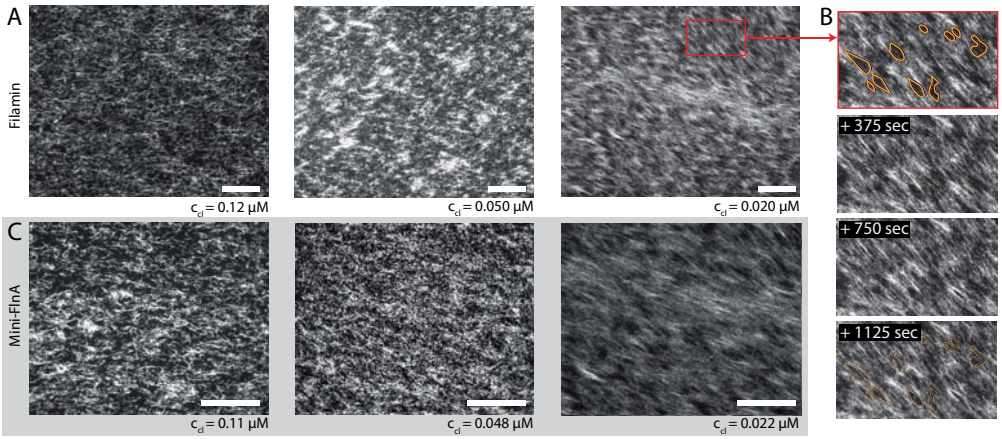


**Figure 4.11: The addition of filamin and mini-FlnA leads to the formation of highly stable networks.** In general, networks crosslinked by filamin or mini-FlnA are considerably more stable than $\alpha$-actinin/actin networks. At a crosslinker concentration around $c_{\mathrm{cl}} = 0.1\,\mu\mathrm{M}$, where in the case of $\alpha$-actinin actively compacting structures emerged filamin/actin and mini-FlnA/actin networks are still stable (**A** and **C**). Only if the crosslinker concentration is diluted five-fold, the motor proteins are able to induce the formation of holes in the network. Even in this concentration regime, however, the overall connectivity of the filamin/actin network is still not affected and the filamin/actin and mini-FlnA networks are even able to close the holes again (**B**). The actin concentration was set to $c_{\mathrm{A}} = 7.6\,\mu\mathrm{M}$. All scale bars are $25\,\mu\mathrm{m}$.

works [176], has a similar binding affinity to actin and also has a spectrin-type binding domain. Despite of these similarities, however, the system behaves entirely different when $\alpha$-actinin is replaced by filamin: in the same concentration regime that in the case of $\alpha$-actinin lead to the dynamic assembly of contractile patches, the homogeneous filamin/actin network is unimpaired by the underlying motor proteins and remains stable (Figures 4.10 and 4.11 A). Only after a ten-fold dilution of the relative filamin concentration, the motor proteins start to reorganize the network, small area fractions begin to move and holes in the network start to emerge – similar to the behaviour of the $\alpha$-actinin/actin network in phase 1 (Figure 4.11 B). However, these holes stay small in diameter and the network is even able to close them again and the overall integrity of the network is never compromised. Moving zones constantly seem to form new connections to the network. This annealing process impedes the further disintegration of the network and leads to a decline in transport and the network remains stable. No concentration regime could be found, where the motor proteins are able to disrupt the filamin/actin network and to compromise its overall connectivity.

This answers the question stated in the beginning of this section: the presence of an apolar crosslinking protein alone is not sufficient to create contractile structures. The high durability of filamin/actin networks is in accordance with observations of *in vitro* networks that identified filamin to be one of the most effective actin-filament crosslinking proteins [195]. On the one hand, this could be ascribed to the structural properties of filamin: the long contour and the high degree of flexibility of the dimeric filamin facilitate an effective actin-filament branching [195], effectively stabilizing the stressed actin network. On the other hand, the invariance of the systems behaviour with respect to alternations of the motor activity could be a hint for a decreased crosslinker off-rate with increasing force as it has already been reported for rigor HMM [75]. Such a "catch-bond"-mechanism would compensate the high motor activity at high ATP concentrations and could contribute to the extraordinary stability of the filamin/actin network.

To further test this assumption, we replaced filamin by mini-FlnA, a synthetic derivative of filamin, that has lost the long repetitive neck regions, but retains the actin binding domains and the domain 23 and 24 [84]. Thus, mini-FlnA has a much shorter contour length than wild-type filamin A. If the durability of filamin/actin networks stems from the highly flexible geometry and not from a possible catch-bond mechanism of wild-type filamin, the motor proteins should readily be able to reorganize the mini-FlnA/actin network. However, this is not the case. The addition of Mini-FlnA, in the same concentration regime as filamin, leaves the phenomenology unchanged. Still, the overall connectivity of the network is never compromised (Figures 4.10 and 4.11). This emphasizes that the behavior of crosslinking proteins in an active environment is mainly determined by the binding affinities under load, and to less extent by the geometry of the crosslinking protein.

While the experiments with Mini-FlnA further substantiate the assumption of a potential catch-bond mechanism involved in the binding of filamin to actin, a molecular understanding of this mechanisms is still at large. The bulk experiments presented here may provide a first idea about the relevant sequence position – for instance, domain 23 or 24 could partially unfold, exposing another binding site for actin – but for a deeper understanding, they have to be complemented by carefully designed single molecule experiments possibly using optical tweezer setups [169].

## 4.4 Comparison to cortexillin, eplin, and anillin

The addition of either $\alpha$-actinin or filamin resulted in a entirely different phenomenology: while the addition of $\alpha$-actinin leads to the active compaction of the network, the presence of filamin leads to highly resilient networks that cannot be reorganized by the underlying motor proteins. These results now provide a benchmark to characterize the behavior of other crosslinking proteins that are also known to crosslink actin filaments regardless of their orientation, namely cortexillin, eplin and anillin.

In principle, the behavior of cortexillin and eplin is similar to the behavior of $\alpha$-actinin. The addition of both crosslinking proteins leads to the formation of actively compacting patches, similar to the ones observed in the case of $\alpha$-actinin. However, the concentration regimes and the time scales for the pattern formation differ considerably, especially for eplin. In the high density motility assay, eplin proves a much more effective crosslinking protein than $\alpha$-actinin, as the concentration regime where eplin can suppress the active compaction is much broader (Figure 4.10). For instance, at an eplin concentration of $0.2\,\mu\mathrm{M}$, where the system in the presence of $\alpha$-actinin already undergoes a transition to compact patches, the network remains static and the initial basic state is frozen in. Only if the eplin concentration is diluted 10-fold, an active compaction can be observed (Figure 4.12 A). Even then, the structure formation is considerably slower and the steady state structures are smaller than in the case of $\alpha$-actinin (Figure 4.12 A). According to the microscopic conception of the pattern formation in the system (Equation 4.1) this is equivalent with the notion that eplin has lower effective unbinding rate $k_{\mathrm{off}}$ or higher effective binding rate $k_{\mathrm{on}}$. This can be interpreted as another hint for the existence of the speculative third actin binding site in the eplin sequence [140].

The addition of cortexillin leads to the formation of actively compacting patches, too (Figure 4.12 B). Compared to eplin, cortexillin is a less effective crosslinker. The concentration regime, in which actively compacting structures are observed, is similar to the one obtained with $\alpha$-actinin (Figure

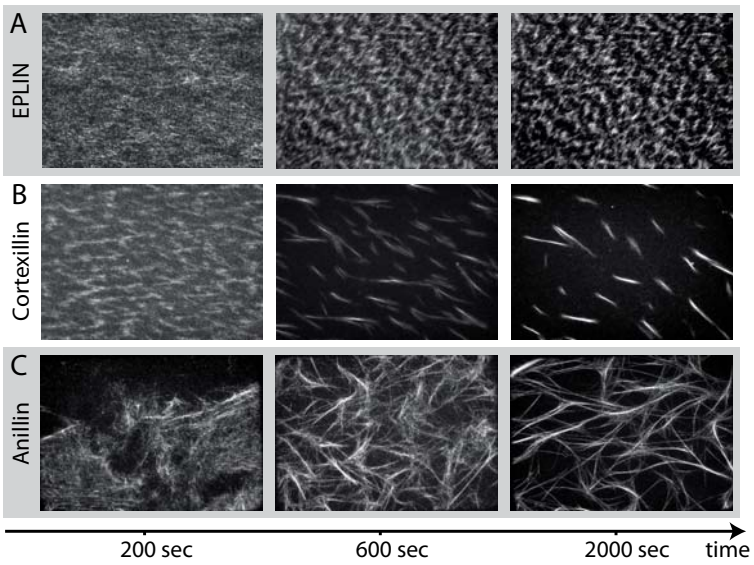


**Figure 4.12: Comparison between eplin, cortexillin, and anillin.** Both, the addition of eplin (**A**) and cortexillin (**B**) results in the formation of actively compacting structures, similar to the ones observed in the presence of $\alpha$-actinin. Albeit, the time scales and structure sizes are slightly different. Compared to $\alpha$-actinin the structure formation in the presence of eplin is considerably slower and the structures in the steady state are smaller, classifying eplin as more effective crosslinking protein in the motility assay. Cortexilin, by contrast, forms larger steady state structures and the structure formation takes place on a considerably shorter time scale, suggesting that cortexillin is a less effective crosslinking protein. The addition of anillin (**C**) does not result in the active compaction of extended patches but to the successive assembly of non-moving fibre-like structures. The actin concentration was adjusted to $7.6\,\mu\mathrm{M}$ and the crosslinker concentration was $0.046\,\mu\mathrm{M}$ in the case of eplin and $0.2\,\mu\mathrm{M}$ in the case of cortexillin and anillin. All scale bars are $25\,\mu\mathrm{m}$.

4.10) and the structures in the steady state are approximately of the same size. Yet, the structure formation runs on a slightly faster time-scale compared to $\alpha$-actinin (Figure 4.12).

In the concert of the crosslinking proteins investigated in this thesis, anillin plays a special role. Not only can it crosslink actin filaments (it forms apolar bundle networks), it is also known to have a binding site for non-muscle myosin [193]. The anillin fragment used here retains this binding site. Thus, one can expect that it also binds to the HMM motor proteins immobilized at the glass slide in the motility assay. The structure formation process that is observed in the presence of anillin indicates that this really is the case. In contrast to the contracting patches observed with $\alpha$-actinin or the polar structures that result from the addition of fascin, anillin forms apolar bundles that are not transported by the underlying motor proteins (Figure 4.12 C).

By comparing $\alpha$-actinin to filamin and mini-FlnA, we already saw that the structure formation in the motility assay does not depend so much on the geometry of the crosslinking protein, but rather on the binding strength and the binding affinity of the crosslinker under load. Even though $\alpha$-actinin and filamin have the same actin binding domains, the addition of filamin leads to the formation of highly stable networks. We attributed this to a potential catch-bond mechanism of filamin under load that is preserved in the truncation mutant mini-FlnA. The fact that the binding affinity under load is decisive for the behavior of crosslinking proteins in active systems, is further underlined by the phase behavior of eplin. Despite eplin is considerably smaller than $\alpha$-actinin, it apparently has a higher ability to stabilize actin networks under stress and to maintain the integrity of the network at considerably lower concentrations.

In summary, the results presented here clearly indicate that the behavior of crosslinking proteins in active systems is not determined by the size of the crosslinking proteins – in contrast to the commonly accepted picture for passive networks.[3] Small crosslinking proteins such as eplin are equally well or even better suited to stabilize active actin networks than the five-fold heavier homodimeric $\alpha$-actinin.

## 4.5 Motility assay experiments: a method to characterize crosslinking proteins in active systems

The cytoskeleton of eukaryotic cells is a highly complex and dynamic scaffold. It consists of filamentous proteins such as F-actin and associated crosslinking proteins and is constantly remodeled by the dynamic (dis-)assembly of filaments and by motor proteins such as myosin-II. While an understanding of the effect of individual actin binding proteins starts to emerge [125], the behavior of crosslinking proteins in an active environment still remains rather unexplored. There is no prediction, what kind of structures or dynamics emerge, once molecular motors and crosslinking molecules interact simultaneously with actin filaments. Yet, the competitive interaction of force exertion and crosslinking is at the heart of the self-organization, which is the basis of the cytoskeleton's unique properties.

To address this challenge, we used high density motility assay experiments, where highly concentrated actin filaments in the presence of crosslinking proteins are propelled by motor proteins that are immobilized on a surface (Figure 4.13 A) [125]. While in the absence of crosslinking molecules, the system self-organizes into collective motion patterns (Figure 4.13 B), the addition of crosslinking molecules leads to a dynamic structure formation that crucially depends on the type of crosslinking protein. If the crosslinking protein fascin is used (compare chapter 3), highly polar structures are assembled on the timescale of seconds (Figure 4.13 C). The assembly of polar structures is the result of an upscaling of the microscopic binding properties of fascin that crosslinks filaments in a parallel or polar orientation only [37]. By contrast, $\alpha$-actinin, filamin, eplin, and cortexillin connect neighbouring filaments regardless of their orientation [37]. Their behavior is determined by the binding affinities of the respective crosslinking protein under load. Eplin, $\alpha$-actinin, and cortexillin, in the right concentration regimes, give way to the hierarchical formation of actively compacting patches (Figure 4.13 D), while the addition of filamin prevents any reorganization within the network (Figure 4.13 E). In contrast to the contracting patches observed with $\alpha$-actinin, eplin, and cortexillin or the polar structures that result from the addition of fascin, actin/anillin assemblies are barely transported by the underlying motor proteins and form tightly bundled non-moving structures (Figure 4.13 F).

The interplay of only three components, F-actin, molecular motors, and crosslinking proteins, is sufficient to drive a complex self-organization process; it results in an extremely rich phase behavior that can comprise large scale contractile and polar structures as well as highly resilient networks. The high variability in the behaviour of different crosslinking proteins in active systems adds a new degree of freedom to the physics of active gels. By varying the specific abundances of crosslinking proteins, active networks can not only tune their mechanical properties,

[3] Recent experimental progress suggests that even in passive systems, the network properties rely on the binding kinetics of the crosslinking proteins to actin and not on the size and geometry of the crosslinker. K.M. Schmoller, private comunication.

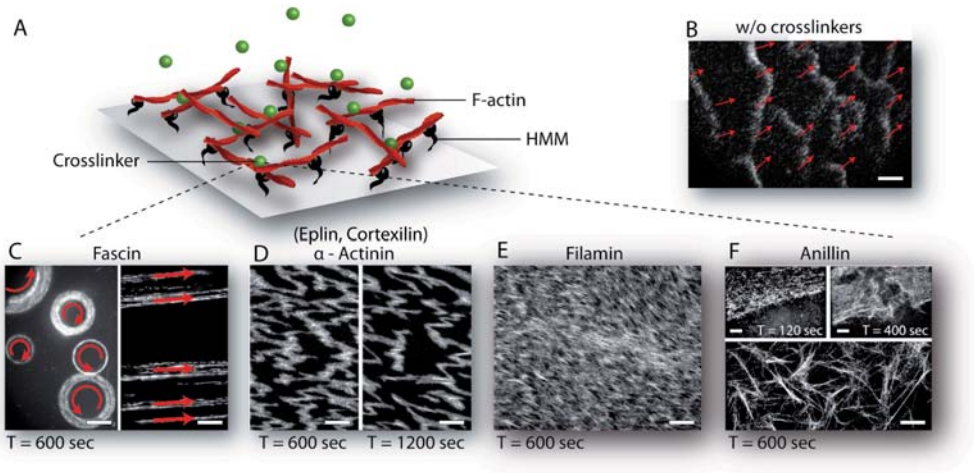


**Figure 4.13: Summary of the main results of this chapter: Crosslinking proteins control the structure formation in active systems.** Schematic representation of the motility assay setup (**A**). In the absence of crosslinkers, density waves of coherently moving actin filaments evolve (**B**). Fascin leads to polar structures, rings and elongated fibres (**C**). While networks fortified by $\alpha$-actinin, eplin, and cortexillin disintegrate to form contractile patches (**D**), filamin/actin networks remain stable (**E**). Anillin forms tightly crosslinked structures that stay immobile (**F**). Parameters: (**B**) actin concentration $c_\mathrm{A} = 10\,\mu\mathrm{M}$ of monomeric actin; (**C**) rings: $c_\mathrm{A} = 3\,\mu\mathrm{M}$, $c_\mathrm{cl} = 0.2\,\mu\mathrm{M}$; fibres: $c_\mathrm{A} = 10\,\mu\mathrm{M}$, $c_\mathrm{cl} = 0.5\,\mu\mathrm{M}$; (**D**) $c_\mathrm{A} = 7.5\,\mu\mathrm{M}$, $c_\mathrm{cl} = 0.2\,\mu\mathrm{M}$; (**E**) $c_\mathrm{A} = 7.5\,\mu\mathrm{M}$, $c_\mathrm{cl} = 0.2\,\mu\mathrm{M}$; (F) $c_\mathrm{A} = 7.5\,\mu\mathrm{M}$, $c_\mathrm{cl} = 1\,\mu\mathrm{M}$. All scale bars are $25\,\mu\mathrm{m}$.

but can also shift gears between different mechanisms and regimes of self-organization – and by that effectively react to changing needs.

The comparison of different crosslinking proteins provides an important insight in the self-organization of active systems: even if crosslinking proteins behave similar in passive systems, they may display a surprisingly different behavior, once they are set under stress in active systems. As the properties of active materials crucially depend on the behavior of the crosslinking proteins, it is thus indispensable to explicitly address their behavior in well defined out-of-equilibrium systems either on the single molecule level or in minimal systems like the one presented here. Altogether, the dynamic properties of systems combining active driving and passive crosslinking are by far more diverse and intricate than what could be expected from experiments on passive reconstituted systems and sensitively rely on the specific out-of-equilibrium properties of the involved components.

# 5 Collective Effects in Active Gels

*In the previous chapters we investigated the self-organization mechanisms that lead to collective motion in motility assay experiments. Subsequently, we assessed how these mechanisms are affected by the presence of cosslinking proteins. In this chapter, we transfer these results to three dimensional active gels.*
*Active gels are minimal model systems consisting of actin filaments, crosslinking proteins and myosin-II filaments. Despite their simplicity, active gels mimic essential aspects of the self-organization processes of the cytoskeleton. In section 5.2, we show that already this minimal system is able to undergo a remarkable self-organization process leading to the hierarchical assembly of clusters of bundled actin filaments.*
*With a minimal agent based simulation that is introduced in section 5.3, we show that most of the experimentally observed phenomena arise from the competitive interaction of crosslinking- and motor-proteins. In the model system as well as in the simulation, this competition results in a characteristic structure size distributions and a complex dynamic behavior of the emerging structures (section 5.4). Further, the structures are constantly transported and move in a succession of runs and stalls, resulting in superdiffusive transport properties (section 5.5). Dependent on the microscopic parameters of the motor-filament interaction and the connectivity within the active gel, this can even lead to long range pulsative collective dynamics (section 5.6).*[1]

## 5.1 Active gels – a model system for the self-organization in the cytoskeleton

The cytoskeleton of eukaryotic cells is a highly flexible and adaptable scaffold that undergoes constant remodeling to meet the cells' changing needs. With its unique static and dynamic properties it facilitates tasks as complex and diverse as cell division or phagocytosis. Cell adhesion, cytokinesis or cell migration are fascinating examples illustrating the power of the cytoskeleton to self-organize locally into complex structures. Often intracellular patterns rely on complex ordering mechanisms, such as large scale collective motion and oscillatory or pulsatile processes. A prominent example for this principle is the apical constriction during Drosophila gastrulation, where the tissue rearrangement is driven by pulsed contractions of the acto-myosin cytoskeleton [137,138]. Moreover such mechanisms are of outmost importance in many aspects of cellular development [66,69,98]. While such processes are tightly controlled by the biochemical activation of the participating proteins, structures need to be formed by a physical self-organization process.

Despite the fundamental importance of self organization processes in such active systems, the microscopic mechanisms and their consequences are poorly understood. To this end, the concept of active gels has been introduced [94,114,121,130,164], with the structure formation in the cytoskeleton being a prime example [64, 95, 119]. Active gel systems rely on pattern forming mechanisms very different from other soft materials: unlike structure formation in passive out-of-equilibrium systems dominated by nucleation and growth processes, the intriguing dynamical properties of active gels are the result of the interplay between active force generation and force dissipation in the (visco-)elastic environment [73].

All these processes rely on the intricate interplay between three major molecular constituents of the actin cytoskeleton: actin filaments, molecular motors and crosslinking proteins. While a poly-

[1] The main results of this chapter are published in References [103] and [104].

mer network consisting of filaments and crosslinkers would result in a viscoelastic physical gel, molecular motors exert local forces and turn it into an active gel [94]. Any structure formation mechanism in active gels is thus based on the interplay between locally produced forces and the stabilization of the filamentous network by crosslinking molecules. From an experimental point of view a minimal *in vitro* system of a dynamic cytoskeletal network thus consists of the combination of only three components: actin filaments, myosin-II motor filaments, and crosslinking proteins [93, 97, 130]. In a parameter regime where still homogenous networks are observed, the effect of molecular motors can directly be detected by the bulk properties of the networks [18,102]. At low actin, but high crosslinker concentrations, local and quasi static structures evolve [10,188]. Yet, cells rely on both highly heterogenous and highly dynamic structures. It is this regime of active gels, where cells are able to constantly reorganize their structure and mechanics to their local needs.

To shed light on the principles underlying the physics of such active gels, to examine their microscopic dynamics, and to classify the resulting dynamic structures, we study a reconstituted actin network that is actively set under stress by molecular motors [103,104]. We identify and quantify the key properties and connect them to the underlying microscopic mechanisms. To this end we combine fluorescence microscopy, digital image analysis including recognition, and tracking of actin structures and phenomenological simulations.

## 5.2 Structure formation in active gels – basic phase behavior

*In vitro*, actin filaments in the presence of the crosslinking molecule fascin at a molar ratio of $1:1$ assemble into a network of stiff and rigid bundles with a well defined bundle thickness of about 20 filaments per bundle and lengths of up to several hundred micrometers (Figure 5.1a) [34]. Thermal excited motions of the bundles are barely visible and the structure remains stable for hours, although permanent unbinding and rebinding of the crosslinking molecules occurs [123].

Once the system is switched from a passive to an active state by the presence of myosin-II filaments and ATP, the network's structure and dynamics are drastically changed. Thereby, it is the concentration ratio between active components and static crosslinkers $\kappa = c_{\mathrm{myosin}} : c_{\mathrm{fascin}}$ that determines the network properties (Fig. 5.1). The actin polymerization triggers a structure formation process that can last for up to 90 minutes resulting in a dynamic steady state. This dynamic steady state shows a characteristic size distribution of the evolved patterns and distinct dynamical properties, both of which crucially depend on the choosen parameter set. Roughly, two different steady state scenarios can be observed: i) a quasi-static regime and ii) a highly dynamic regime. A prevalence of crosslinkers ($\kappa \lessapprox 1:50$) leads to the quasi-static network regime (i) with only minor reorganizations taking place (Figure 5.1b). In this regime, forces of the motor filaments are not sufficient to induce any large scale dynamics in this crosslinker dominated network. Consequently, a single percolated network with heterogenous bundle thicknesses is formed. Only small patches, which are stabilized by few crosslinkers, can be displaced by the relatively small number of motor filaments.

Only in a parameter range where the influence of both components, passive and active crosslinkers is balanced ($\kappa \gtrapprox 1:50$), a highly dynamic regime (ii) of structure formation and constant reorganization can arise. Here, the concentration of molecular motors is high enough to readily disrupt the network (Figure 5.1 C). Instead of well defined bundles, condensed and interconnected

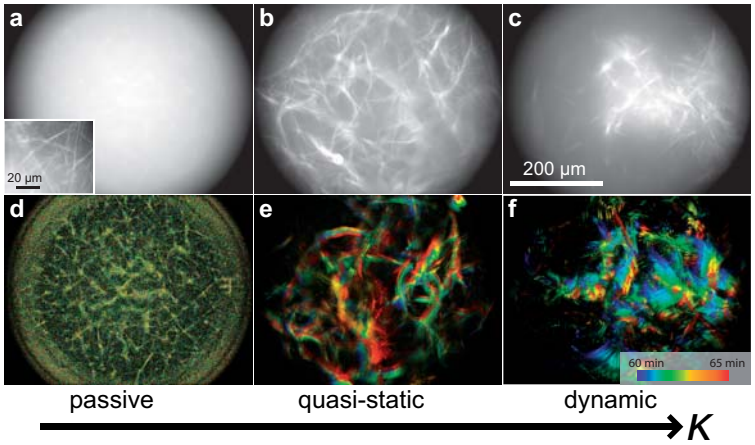


**Figure 5.1: Basic phase behavior in active actin networks.** Images **A – D** show fluorescence micrographs of 1 $\mu$M actin, 1 $\mu$M fascin at different myosin:fascin ratios (images taken 90 min after initiation of polymerization). Images **D – F** are the corresponding color-coded time-overlays of 100 consecutive images ($\approx 5$ min). **A** and **D**: without myosin, a passive actin/fascin network with thin, uniform bundles is observed. **B** and **E**: low myosin concentrations ($\kappa = 1:50$) exhibit quasi-static huge clusters spanning the whole field of view (regime i). **C** and **F**: at high myosin concentrations, large, dense clusters and small clusters coexist in a dynamic steady state ($\kappa = 1:10$; regime ii).

actin-fascin clusters with diameters of up to hundreds of micrometers and variable shapes emerge. Once formed, the clusters are constantly subjected to the action of molecular motors. As a consequence, they are highly mobile and move in a succession of persistent runs with a mean velocity of 0.5 $\mu$m/s (Figure 5.2 ).

From the experimental findings obtained so far, one can already conclude that the complex dynamics occuring in regime (ii) result from the competitive interplay of crosslinking and motor proteins. But is this interplay really sufficient to account for the remarkable structure formation process? Or do the experimentally observed phenomena depend on more complex self-organization principles such as the formation of myosin-II clusters, hydrodynamic effects, or the long-range elastic force percolation inside the active gel? To address this question we devised a minimal agent based simulation that is solely based on short range interactions due the interplay between crosslinker and motor proteins. In the following sections this simulation is introduced, analyzed and systematically compared to the experiment.

## 5.3 Phenomenological simulation for the competition of active and passive crosslinkers

The experimental system consists of interconnected polar fascin bundles that are actively transported and set under stress by myosin-II filaments. The microscopic processes that lead to the observed self organization, arise through the interplay of crosslinking events and active transport. More specifically, the competition between molecular motors and crosslinking proteins gives rise to the active movement, (re-)binding and forced unbinding. These microscopic interactions are the basis for numerical simulations.

In a minimal approach, fascin bundles are modelled as monodisperse and polar rigid rods in a quasi two dimensional geometry. No excluded volume effects are taken into account and the bun-

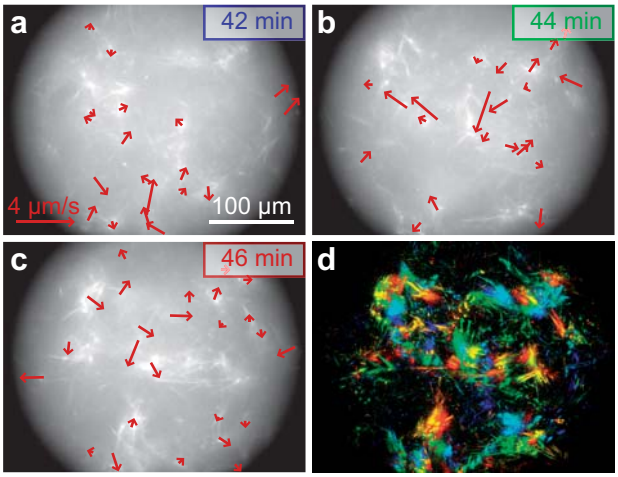


**Figure 5.2: Dynamics of actin/fascin/myosin networks.** Fluorescence micrographs (**A–C**) and the resulting color time overlay (**D**) of active actin networks at indicated times after initiation of polymerization show a drastic structural rearrangement within the network (1 $\mu$M actin, 1 $\mu$Mfascin, 0.1 $\mu$M:myosin, 1 mM ATP). Arrows indicate cluster movement over 3.5 sec. The overlay (**D**) represents 42–46 min after polymerization in blue to red.

dles can readily cross each other. The bundles are actively propelled by motors and crosslinked via passive crosslinkers. Both, active and passive bonds are subjected to forced unbinding events. If two filaments overlap, active or passive binding events occur based on probabilistic interaction rules. In a similar manner unbinding processes are calculated. The displacements that arise due to the action of molecular motors are calculated based on a generic model for a two-filament interaction. Subsequently the details of the simulation are examined.

**Passive and active binding processes.**

If two rods overlap, passive binding events occur with a rate of $p_{\mathrm{on}}$. Within each time step, after all overlaps have been rastered and checked for new passive binding sites, interconnected rods are pooled to clusters. If an overlap between two rods is not already occupied by a passive crosslinker, motor proteins can actively crosslink two intersecting rods with a rate $r_{\mathrm{on}}$.

**Unbinding and forced unbinding.**

Passive crosslinkers are subjected to unbinding events. Without the incorporation of forced unbinding, unbinding events occur at a rate $p_{\mathrm{off}}$. For the phenomenological description of forced unbinding processes in the presence of motor proteins, the number $\epsilon$ of active crosslinks per cluster is determined. Since $\epsilon$ is proportional to the total stress exerted in the interconnected cluster, the averaged unbinding rate $p_{\mathrm{off,forced}}$ should increase with $\epsilon$. Conceptually, the stress increase leads to rupture events within the cluster, whereby especially weakly crosslinked structures with a low actin and/or crosslinker density are prone to disassemble. In a simplified picture, this can be modelled by increasing the off-rate with the number of motor proteins per individual cluster. With this approach an increased off-rate results in the predominant dissociation of weakly crosslinked structures within clustered structures – like it is observed experimentally.

In the simulations, the increase in the off-rate as a function of the number of active crosslinks is

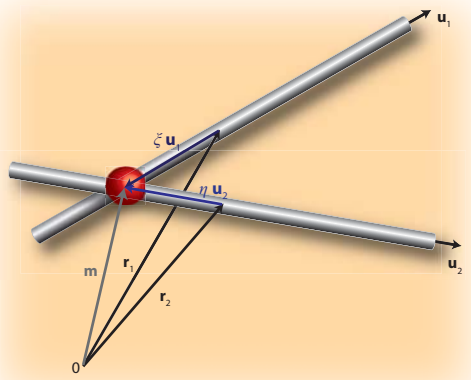


**Figure 5.3: Schematic representation of a motor-mediated two filament interaction.** The two filaments are defined by their length $L$, the position of their centers of mass $\mathbf{r}_{1,2}$ and the unit vectors of their respective orientation $\mathbf{u}_{1,2}$. The motor complex (red) is located at the intersection of the two filaments. For the initial position $\mathbf{m}$ of the motor, the relation $\mathbf{m} = \mathbf{r}_1 + \xi\mathbf{u}_1 = \mathbf{r}_2 + \eta\mathbf{u}_2$ holds, whereby $\xi$ and $\eta$ refer to the Starley coordinates of the interacting filament pair.

described by the relation

$$p_{\text{off,forced}} = p_{\text{off}} + \frac{(p_{\text{off,max}} - p_{\text{off}}) \cdot \epsilon}{\epsilon_{0.5} - \epsilon}\,, \tag{5.1}$$

whereby $p_{\text{off,max}}$ denotes the maximal off-rate due to forced unbinding and $\epsilon_{0.5}$ is the number of crosslinks neccessary to rise the original off-rate by $0.5 \cdot (p_{\text{off,max}} - p_{\text{off}})$.

Noteworthy, an increased crosslinker off-rate does not necessarily compromise the overall stability of large clustered structures. For large structures, it is likely that ruptured fragments rebind in a different conformation, before leaving the structure. Consequently, an increased off-rate also leads to an increased degree of reorganization within large clusters.

### Active transport

If two actin fascin bundles are actively crosslinked, torques and forces are exerted by the bipolar motor filament walking towards the plus ends of the bundles.

The velocities that arise from these active crosslinks can be calculated based on a microscopic force balance of two interacting rods. If $\mathbf{r}_1(t)$ and $\mathbf{r}_2(t)$ are the vectors to the center of mass of two intersecting rods (see Figure 5.3), the position of the motor protein right after the binding event at $t = 0$ is given by the Straley coordinates [196]:

$$\begin{aligned}\mathbf{m}_1(t=0) &= \mathbf{r}_1 + \xi\mathbf{u}_1\,,\\ \mathbf{m}_2(t=0) &= \mathbf{r}_2 + \eta\mathbf{u}_2\,.\end{aligned}$$

If the motor moves with the velocity $v_{\text{m}}$, the motor position after a timestep $\Delta t$ is given by

$$\mathbf{m}_1(t + \Delta t) = \mathbf{r}_1(t) + (\xi + v_{\text{m}}\Delta t)\mathbf{u}_1\,, \tag{5.2}$$

$$\mathbf{m}_2(t + \Delta t) = \mathbf{r}_2(t) + (\eta + v_{\text{m}}\Delta t)\mathbf{u}_2\,. \tag{5.3}$$

Provided that the motor complex acts as a harmonic spring [9, 241], the force $\mathbf{F}_1$ exerted on rod $1$ by the motor is given by

$$\mathbf{F}_1(t + \Delta t) = k \cdot \Delta x = k \cdot (\mathbf{m}_2(t + \Delta t) - \mathbf{m}_1(t + \Delta t)) , \tag{5.4}$$

with $k$ being the spring constant. Accordingly the force $\mathbf{F}_2$ acting on the second rod is given by $\mathbf{F}_2 = -\mathbf{F}_1$. In the overdamped case, these forces are balanced by the frictional force $\gamma \cdot \mathbf{v}$, whereby $\gamma$ denotes an appropiate friction coefficient. For the velocities of the two polar rods $\mathbf{v}_i(t + \Delta t)$ with $i = 1, 2$, this yields

$$\mathbf{v}_i(t + \Delta t) = \gamma^{-1}\mathbf{F}_i(t + \Delta t) . \tag{5.5}$$

Similar expressions can be derived for the angular velocities. The torque exerted by the motor is given by

$$\mathbf{M}_i(t + \Delta t) = \mathbf{F}_i(t + \Delta t) \times \big(\mathbf{m}_i(t + \Delta t) - \mathbf{r}_i(t + \Delta t)\big) , \tag{5.6}$$

with $\mathbf{m}_i(t + \Delta t) - \mathbf{r}_i(t + \Delta t)$ being the lever arm of the motor. With the overdamped equation of motion, $\omega_i = \gamma_{\mathrm{r}}^{-1}\mathbf{M}_i$, expressions for $\omega_{1,2}$ can be derived, whereby $\gamma_{\mathrm{r}}$ denotes the friction coefficient for rotary motion.

For the relative translational velocity $\mathbf{v} = \mathbf{v}_2 - \mathbf{v}_1$ one finally obtains

$$\mathbf{v} = \frac{2kv_{\mathrm{m}}\Delta t}{\gamma}(\mathbf{u}_2 - \mathbf{u}_1) , \tag{5.7}$$

while the relative angular velocity $\omega = \omega_2 - \omega_1$ is given by

$$\omega = \frac{2kv_{\mathrm{m}}\Delta t}{\gamma_{\mathrm{r}}} \left[2v_{\mathrm{m}}\Delta t + \frac{(\mathbf{r}_2 - \mathbf{r}_1) \cdot (\mathbf{u}_1 - \mathbf{u}_2)}{1 - \mathbf{u}_1\mathbf{u}_2}\right] \big(\mathbf{u}_2 \times \mathbf{u}_1\big) . \tag{5.8}$$

At this point it is favourable to compare these expressions to the velocity models derived in Reference [128] starting from generic symmetry arguments. The relative translational velocity $\mathbf{v}$ corresponds to the $\beta$-term in Reference [128], while the first term in expression (5.8) is equivalent to the $\omega_0$-term of Reference [128]. The second term of expression (5.8) was not considered before, but obeys the generic symmetry relations postulated for motor mediated two filament interactions [128].

### 5.3.1 Parameters

For all simulation runs the diffusion constant was adjusted to $D = 10^{-13}\,\mathrm{m}^2/\mathrm{s}$ [51] and the viscosities were set to $\gamma = 10^{-8}\,\mathrm{Ns/m}$ and $\gamma_{\mathrm{r}} = 2 \cdot 10^{-8}\,\mathrm{Ns/m}$ respectively [88]. The motor velocity was set to $v_{\mathrm{m}} = 1\ \mu\mathrm{m/s}$ and the filament length corresponds to $10\ \mu\mathrm{m}$. The simulation time is defined implicitly as the time a motor protein needs to cover a $0.1$ rod-length; one simulation time unit corresponds to $1\,\mathrm{sec}$. Most crosslinking proteins have a comparable affinity to actin with on- and off-rates in the order of $k \approx 1\,\mathrm{sec}^{-1}$ if the concentration is in the order of dissociation constant [125]. With a time step of $0.01$ simulation times, the on- and off-rates of the crosslinking proteins are in the order of $p_{\mathrm{on,off}} \approx 0.01$ per time-step. Since an individual myosin-II filament comprises hundreds of motor head-domains, each with a duty ratio in the order of $1/100\,\mathrm{sec}$ [88], the dynamic on- and off-rates of the motor oligomers was varied in the parameter regime of $r_{\mathrm{on,off}} \approx 0.1 - 0.01$ per time-step.

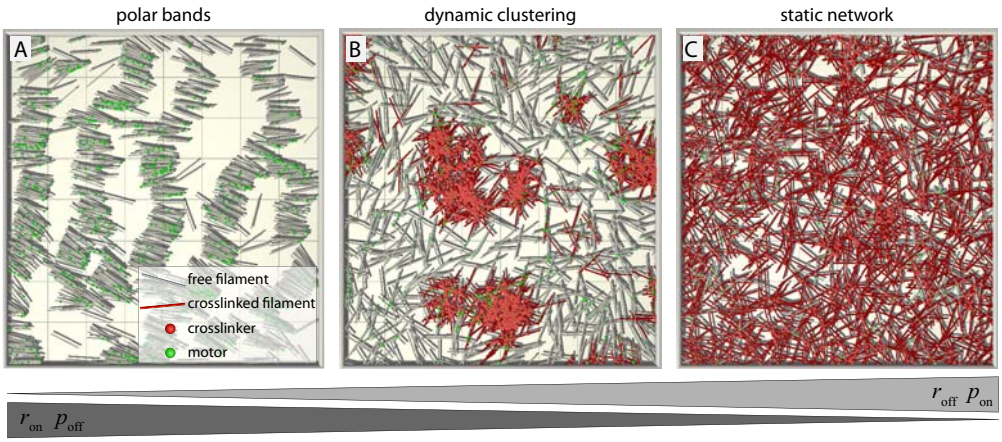


**Figure 5.4: Basic phase behavior in the simulation.** The simulation snapshots **A** – **C** show the behavior of the simulation as a function of the crosslinker binding and un-binding rates ($p_{\mathrm{on}}$, $p_{\mathrm{off}}$) and motor on- and off-rates ($r_{on}$, $r_{\mathrm{off}}$). For low crosslinking binding rates and/or high motor binding rates, the dynamics is dominated by the motor proteins and the steady state is characterized by the emergence of polar bands (**A**). The polar alignment reflects the inherent polar symmetry of the underlying motor-filament interaction. For high-affinity crosslinking proteins and/or a low motor-binding rates a static network evolves (**C**). Only if the influence of the motor- and crosslinking proteins is relatively balanced, a dynamic pattern formation is observed that leads to the assembly of crosslinked actin-fascin-structures (**B**). Parameters: **A**: $r_{\mathrm{off}} = 0.01$, $r_{\mathrm{on}} = 0.1$, $p_{\mathrm{off}} = 0$, $p_{\mathrm{on}} = 0$; **B**: $r_{\mathrm{off}} = 0.01$, $r_{\mathrm{on}} = 0.1$, $p_{\mathrm{off}} = 0.02$, $p_{\mathrm{on}} = 0.01$; **C**: $r_{\mathrm{off}} = 0.01$, $r_{\mathrm{on}} = 0.01$, $p_{\mathrm{off}} = 0.02$, $p_{\mathrm{on}} = 0.1$. For all snapshots the density was set to $\rho = 14$ rods per $L^2$ (with $L$ being the rod length) and the simulation times was $T = 5000$.

### 5.3.2 Basic phase behavior

Like observed in the experiments, the phase behavior is determined by the interplay between motors and crosslinkers (Figure 5.4): An excess amount of passive crosslinkers leads to a quasi-static network structure with only minor reorganizations (Figure 5.4 C). In contrast, a too small amount of crosslinking proteins results in the disintegration of the network and no higher-order structures emerge. In this regime, the dynamics is fully determined by the action of the motor proteins that align the F-actin bundles and drive their polarity sorting [153]. As a result, polar bands of aligned bundles evolve (Figure 5.4 A). These bands are reminiscent to numerical solutions of coarse grained theoretical models that are based on similar interaction rules [128, 240].

A dynamic structure formation is only possible, if the influences of motors and passive crosslinkers are relatively balanced. Here, the interplay of active transport and crosslinking leads to the formation of clusters of aggregated actin/fascin bundles. Starting from a homogeneous initial state, the simulation shows a coarsening behavior, in the course of which small structures like individual bundles or small clusters coalesce and gradually form larger structures (Figure 5.5).

### 5.3.3 Limitations of the simulation

To investigate to what extend the experimentally observed pattern formation results from the local competitive interaction of crosslinking and motor proteins, the simulation is based on local interactions only. It deliberately cannot account for any effects that require a long-range force percolation or hydrodynamic interactions. Further, the simulation does not take the polydispersity of the actin fascin structures into account and the individual rods are not able to fragment. This mainly affects the rupture events within clusters that occur more seldom compared to the

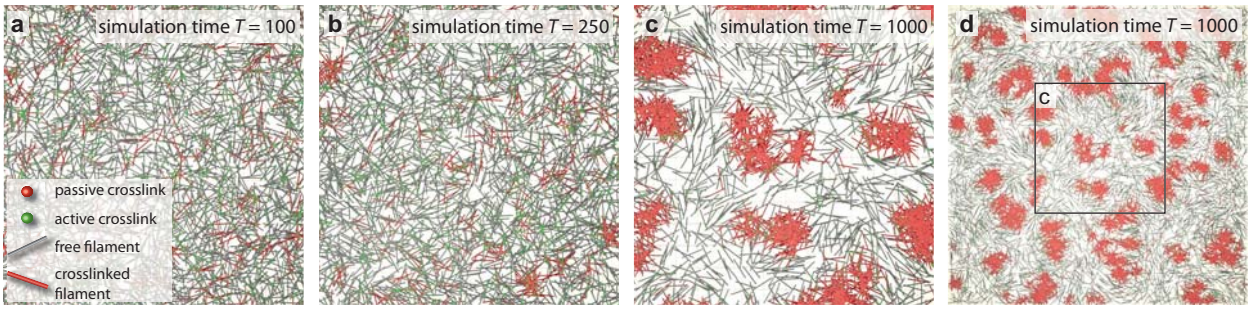


**Figure 5.5: Dynamic structure formation in the simulation.** (**A–C**) show simulation snapshots for a density $\rho$ of 14 rods per $L^2$ (with $L$ being the rod length), a crosslinker unbinding rate $p_{\mathrm{off}} = 0.02$ and a motor binding rate $r_{\mathrm{on}} = 0.1$. The entire simulation box is shown in (**D**). With time, an increasing number of rods is accumulated into clusters and the connectivity concomitantly decreases.

experiment. In general, rupture events very rarely lead to the catastrophic disintegration of entire clusters. More likely individual bonds rupture and single filaments are torn out of the structures. Consequently the simulation cannot account for rupture processes that are based on the fragmentation of individual bundles. In the subsequent chapters the simulation and the experiment are compared in detail.

## 5.4 Dynamics of the structure-formation

The accumulation of material within the clusters during the observed coarsening process in both the experiments and the simulations has profound consequences on the dynamics in the system. The following section focusses on the emergence of the structures and on the resulting transport properties in the active gel. In both the experiments and the simulation, the structure growth is limited by the concomitantly decreasing connectivity within the actin network and the subsequently decreased possibility of active transport.

### 5.4.1 Dynamic structure size distribution

In the regime where the influence of active and passive crosslinkers are balanced, the experimental system evolves into a highly dynamic heterogeneous network that consists of interconnected clusters. The cluster sizes are broadly distributed (Figure 5.6 A). Three characteristic sizes can be identified: small, bundle-like structures (average diameter $d \approx 6\ \mu$m), medium sized clusters ($d \approx 10\ \mu$m), and large clusters ($d \approx 34\ \mu$m).

The time evolution of the cluster size distribution shows that initially predominantly small clusters consisting of several actin/fascin bundles are formed spontaneously (Figure 5.6 A and B). Once formed, these small clusters fuse to form medium sized clusters, yet disruption events of medium and large sized clusters result in their reformation (Figure 5.6 B). At the same time, small clusters are also stable as they are unlikely to be disrupted due to their small contact area. The resulting low probability of motor filaments binding in an appropriate manner to further disrupt the small clusters is limiting their disintegration. Consequently, a large number of small clusters can be found in the active system at all times. Medium sized clusters are formed continuously by fusion of small clusters or disruption of large clusters. At the same time, they can either be annihilated by their adsorption to larger clusters or by disruption into small clusters. All these effects

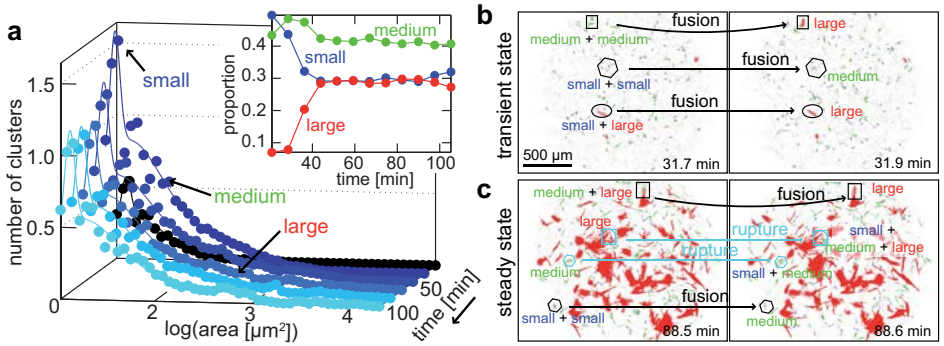


**Figure 5.6: Temporal evolution of the cluster size distribution and cluster dynamics.** (**A**) After polymerization, three types of clusters with distinct sizes emerge. The cluster sizes are calculated for 18.4 min time intervals. The time evolution is robust for all studied actin concentrations. With time, the population of the different cluster sizes changes as seen in their number proportion (inset): Small, homogenously sized clusters (blue) first fuse forming medium sized clusters (green) (**B**). These medium sized clusters further grow forming large and stable clusters (red). A dynamic steady state evolves where medium sized clusters are constantly destroyed and rebuilt (**C**).

contribute to the fact that the total number of medium sized clusters predominates (Figure 5.6 A, inset), although individual medium sized clusters are intrinsically unstable (Figure 5.6 B). The large clusters are stable over time and increase their size by fusing events with clusters of all sizes. Small parts of them are torn out frequently without compromising their structural integrity. Thus, over time a dynamic steady state of cluster size distributions evolves with a frequent exchange of material between the different cluster sizes (Figure 5.6 C).

Like in the experiment, the stability of the clusters in the simulations depends on their size. Large clusters are stable, since they have grown sufficiently large and comprise a sufficiently large number of passive crosslinkers. Motors continuously reorganize even large clusters internally by rupturing individual bonds. They are also able to tear out material from the clusters, yet they are not sufficiently strong and cooperative enough to entirely disintegrate these large structures (Figure 5.7). Medium sized clusters on the contrary can readily be disintegrated by the action of molecular motors. Here motors find a large number of possible binding sites and thus can induce unbinding events of the relatively small number of passive crosslinks within the cluster. For the smallest structures comprising only two to five individual bundles, motor-induced unbinding events only play a minor role: As small clusters do not offer enough binding sites for motors, the cluster disintegration predominantly occurs by stochastic unbinding events not involving motor proteins. Thus – like in the experiment – the stability of the clusters depends on their size, leading to a characteristic cluster size distribution shown in Figure 5.8. Initially, for short simulation times, the cluster size distribution decreases as a power law. As especially large clusters are considerably more stable than smaller clusters, the probability of finding large clusters considerably increases with time. This can be seen in the successive deviation from the power law for longer simulation times (Figure 5.8). Such behavior is reminiscent to cluster size distributions found for systems of self propelled particles with alignment interactions [162, 236].

### 5.4.2 Coarsening dynamics

The dynamic coarsening and the formation of interconnected clusters is a robust feature in both the experimental system and the simulations: For all parameter variations, the system reaches a

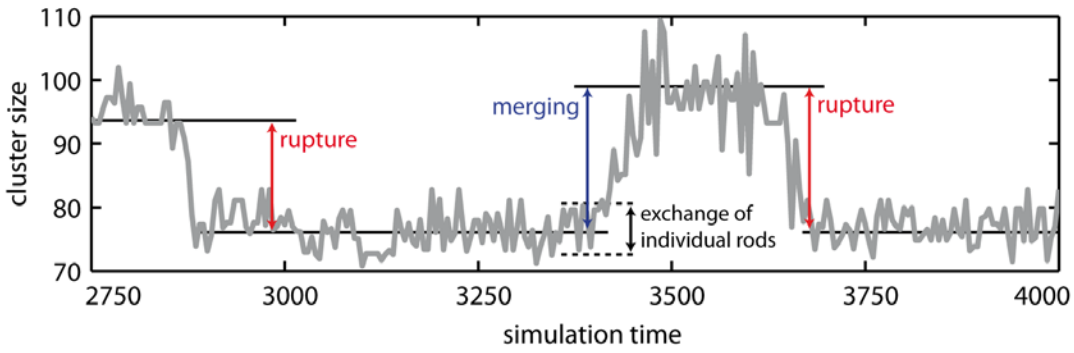


**Figure 5.7: Cluster assembly and disassembly in the simulations.** The curve shows the size of one single cluster as function of time. Individual clusters are subjected to the constant exchange of single filaments that either get crosslinked or are torn out of the cluster by the action of molecular motors. However, the cooperative action of motor filaments can also lead to the fragmentation of entire clusters by rupturing individual bonds. The cluster size is measured in number of rods. The parameters are: $p_{off} = 0.02$, $p_{on} = 0.01$, $r_{off} = 0.01$, $r_{on} = 0.1$, $\rho = 1.4$.

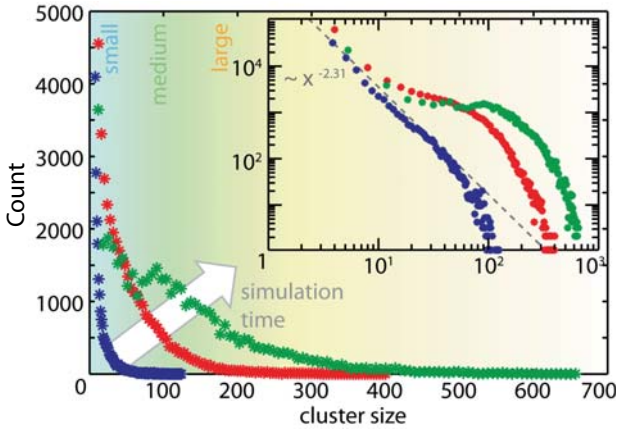


**Figure 5.8: Temporal evolution of the cluster size distributions in the simulation.** Like in the experiment, three different sizes can be defined. Initially, the cluster size distribution decreases as a power law for small clusters and then exponentially for medium sized or larger clusters. With time, in the course of the clustering process, the probability of finding large clusters increases compared to the power law. The cluster size is measured in number of rods.The parameters are: $p_{off} = 0.02$, $p_{on} = 0.01$, $r_{off} = 0.01$, $r_{on} = 0.1$, $\rho = 1.4$.

dynamic steady state, where the cluster size distribution and consequently the mean cluster size remain constant (Fig. 5.9 A and B). The plateau value of the mean cluster size and the time to reach the plateau crucially depend on the actin concentration. Conceptually, a high actin concentration enhances the network connectivity and thus facilitates an effective self organization process. The steady state is reached faster, as an increased actin concentration boosts the initial mobility in the system.

The accumulation of material within the clusters during the observed coarsening process has profound consequences on the dynamics in the system. The more material is accumulated in large clusters, the less material is available to connect the different clusters with each other. Since a weak connectivity hinders the occurrence of persistent runs, large aggregated structures move less and exhibit smaller overall displacements as measured by the mean run length per cluster. In both, the simulations and the experimental system, we observe a generic dependence of the mean run

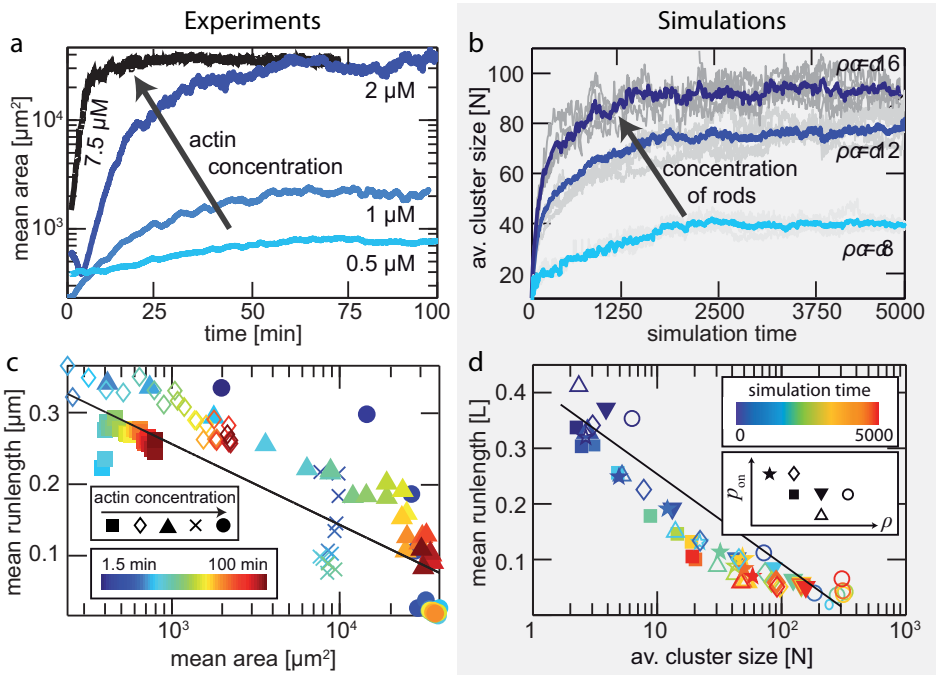


**Figure 5.9: Coarsening dynamics in the active gel and the simulations.** As illustrated in (**A**), the growth of the mean cluster size in the experiments depends on the actin concentration. The higher the actin concentration, the higher the initial connectivity in the system. As a high connectivity is mandatory for an effective self-organization process, high actin concentrations not only result in higher average cluster size in the steady state, but also in shorter lag times until the steady state is reached. As can be seen in (**B**), the simulation shows a similar behavior: higher material concentrations result in larger structure sizes and a faster structure formation process. The structure size is intimately related to the dynamics in the system that can readily be quantified by the mean run length of the clusters shown in (**C**) and (**D**). In the experiment the mean run length monotonically decreases with the cluster size (solid line: logarithmic decrease). This universal finding is found for different actin concentrations ( 7.5 $\mu$M - circles, 5 $\mu$M - crosses, 2 $\mu$M - triangles, 1 $\mu$M - open diamonds, 0.5 $\mu$M - squares) or for different times after initiation of polymerization (**C**). In the simulations a similar behavior can be found: the mean run length monotonically decreases with increasing cluster size (**D**). Like in the experiments, this is robust for a wide range of parameters. For all experiments, the fascin concentration was adjusted to 1 $\mu$M fascin and the ratio of active to passive crosslinks was $\kappa = 1 : 10$. The simulations were performed with a crosslinker unbinding rate of $p_{\text{off}} = 0.02$, a motor binding rate of $r_{\text{on}} = 0.1$ and a motor unbinding rate of $r_{\text{off}} = 0.01$. In (**D**) the concentration of rods was varied from $\rho = 8 - \rho = 16$ and the crosslinker on-rate from $p_{\text{on}} = 0.007 - p_{\text{on}} = 0.013$. The mean run length is averaged over 3 min in the experiments and over a simulation time interval of $\Delta T = 100$ in the simulations respectively.

length on the cluster size and thus the connectivity of the network. Independent of the specific parameter set or the time the system has coarsened, a logarithmic decrease of the mean run length per cluster with increasing cluster size is found (Figure 5.9 C and D).

## 5.5 Superdiffusive transport in active gels

The overall dynamics of the individual structures in the network is best described by the mean squared displacement of the structures. For Brownian diffusion, the mean square displacement, $\langle r^2(\tau)\rangle \propto \tau^\alpha$, is expected to increase with time $\tau$ with a power law exponent $\alpha = 1$ while $0 \leq \alpha < 1$ or $1 < \alpha \leq 2$ are indicative of sub- or superdiffusion, respectively [146,147]. In the presence of ATP, a clear superdiffusive behavior of individual clusters is found: the mean square displacements

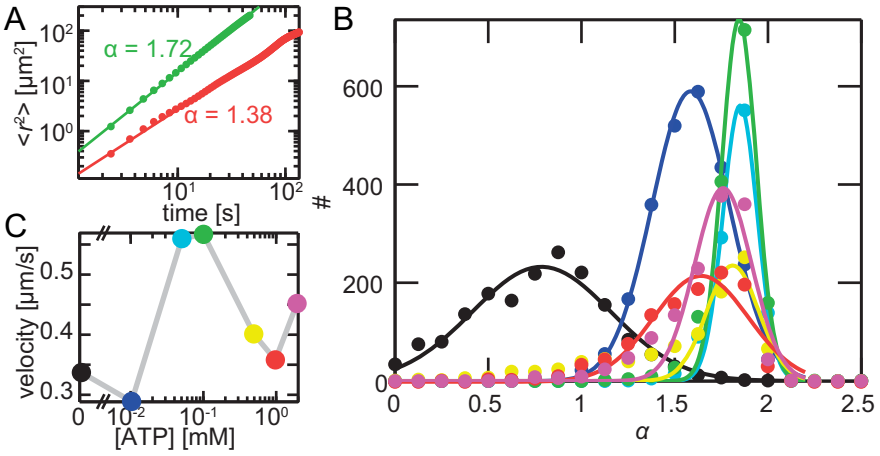


**Figure 5.10: Superdiffusive transport in active gels.** Mean square displacements of two individual structures at 2 mM ATP show superdiffusive power law exponents (**A**). The distributions of the mean squared displacement exponents $\alpha$ show a maximal superdiffusivity at intermediate ATP concentrations (**B**, 50 (cyan) to 100 $\mu$M (green); solid lines show gaussian fits). At low ATP concentrations (10 $\mu$M, blue), the low activity of myosin-II limits the superdiffusive behavior. At high ATP concentrations (0.5 (yellow), 1 (red) or 2 mM (magenta)), myosin-II filaments are not able to exert high enough forces for constant network reorganization resulting in a lower mean superdiffusivity. Similarily, the highest mean run velocities are reached at intermediate ATP concentrations (**C**).

increase in time with $\alpha > 1$ (Figure 5.10 A). This can be traced back to the complex alternation of runs and stalls of the individual network structures.[2].

### 5.5.1 Transport properties as a function of the ATP concentration

Microscopically, stall phases are the direct consequence of the presence of the crosslinking molecules while the runs can be ascribed to the activity of the myosin-II filaments. Accordingly, the dynamics should be set by the motor activity. Indeed, the distribution of the powerlaw exponents depends on the ATP concentration (Figure 5.10 B). Dependent on the ATP concentration four phases are discernible: The passive state (i) without any ATP is characterized by a subdiffusive behavior which can be attributed to the network hindering the diffusion. Already at low ATP concentrations (ii), the dynamics become superdiffusive. This superdiffusivity is even more pronounced at intermediate ATP concentrations (iii). However, at high ATP concentrations (iv), a lower superdiffusivity is observed and the width of the distribution increases again. This width is originated in the highly heterogenous network organization which predominantly occurs in this regime.

Likewise, the maximal velocity of individual structures in run phases of 0.6 $\mu$m/s is observed for intermediate ATP concentrations (regime iii) while higher (regime iv) or lower (regime ii) ATP concentrations result in a decrease of the velocity (Figure 5.10 C). However, in all regimes the velocities in run phases are an order of magnitude lower than the velocity of myosin-II filaments observed in gliding assays at similar ATP concentrations [110]. Thus, in all cases, the speeds are not limited by the maximal speed of the motors, but by the presence of crosslinking bonds.

[2] To extract and quantify the dynamic behavior of the experimentally observed structure formation we used a custom written structure identification and tracking algorithm based on the work of Crocker and Grier [42]. For all data presented here at least 1500 clusters were processed. Details of the algorithm can be found in References [103–105].

The complex ATP dependence is the result of the competition of the motor proteins with the crosslinking molecules. Yet, the variation of the ATP concentration results in a more complex behavior, as the competition of the motors with the crosslinking molecules comes into play. In the absence of ATP (regime i) a passive actin/fascin/myosin network consisting of small, diffusing clusters is observed. At low ATP concentrations (regime ii) the low motor activity is limiting the number of runs and the stalls of the network structures dominate. Consequently, we do observe superdiffusive transport, albeit with small exponents $\alpha$. In the intermediate regime, up to 0.1 mM ATP (regime iii), the highest degree of superdiffusion is observed. Here, the motor proteins dominate the dynamics and allow for an effective transport within the active gel. The decrease in speed and the degree of superdiffusivity that occurs for high ATP-concentrations in regime (iv) can be attributed to the lower affinity of ATP-myosin to actin filaments. This reduced crossbridge strength limits the overall processivity of the myosin-II filaments. Thus the forces myosin-II filaments can exert are lower than at intermediate concentrations of ATP [35, 48]. As a consequence, forced unbinding is less likely at higher ATP concentration. This results in a less effective reorganization within the active gel.

### 5.5.2 Modulating the acto-myosin crossbridge strength by KCl

Alternatively to the variation of the ATP concentration, the crossbridge strength of the myosin-II filaments can be altered independently by the ionic strength [20].[3] Indeed, exceeding a critical KCl concentration of 60 mM prevents any dynamic reorganization within the active gel (Figure 5.11): the structure of an active actin/fascin/myosin network at more than 60 mM KCl cannot be distinguished from a passive actin/fascin network. This critical concentration has also been observed in gliding assays, where salt concentrations higher than 60 mM do not support motility of actin filaments [202]. At this ionic strength the affinity of ATP-myosin does not allow for permanent binding of the myosin-II to the actin filaments throughout its chemomechanical cycle.

Altogether, the results show that, the observed network reorganization critically depends on the strength of the myosin-actin bond: Only a maximal binding strength of the myosin-II filaments to actin at low ionic strength allows exerting high enough forces to disrupt the actin/fascin crosslinking points and to reorganize the network structure. The network reorganization and the observed superdiffusivity not only rely on the competition between active and passive crosslinks, but also on the respective binding strengths and affinities. The lower superdiffusivity at high salt can be attributed to longer stalls due to a decrease in forced unbinding events resulting in less activity and a larger variability.

### 5.5.3 Superdiffusion in the simulation

The implementation of the basic interplay between active and passive crosslinkers in the simulation already suffices to obtain a network dynamics strongly reminiscent to the experimental findings. Due to the concerted action of molecular motors, clusters are constantly transported and the trajectories they perform are characterized by a succession of runs and stalls (Figure 5.12 A). During run phases, the velocity of the fastest clusters does not exceed one tenth of the velocity of the motor proteins; and the larger the clusters are, the lower is their susceptibility to

[3] An increase of the KCl concentration up to 200 mM does not affect the myosin-II filament length [100]. We also do not observe any differences in actin/fascin network structure upon variation of the ionic strength.

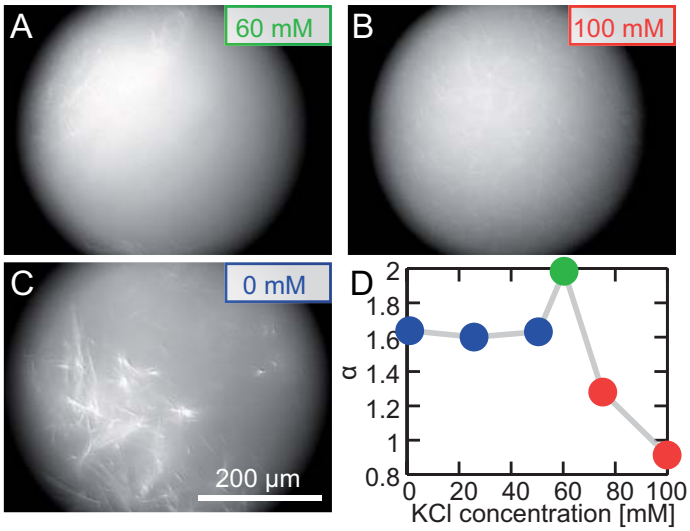


**Figure 5.11: Dependence of the dynamics on the KCl concentration.** Above a critical KCl concentration of 60 mM (**A**), an active actin/fascin/myosin network cannot be distinguished from a passive actin fascin network (100 mM, **B**), while below the critical concentration an active network is formed (**C**). The fluorescence micrographs are taken 90 min after initiation of polymerization. The superdiffusivity as characterized by the mean mean square displacement power exponent $\alpha$ decreases above a critical KCl concentration of 60 mM (**D**).

motor induced displacements and the less they move (Figure 5.12 B). During stall phases clusters essentially exhibit a diffusive motion. In accordance with the experiment, runs and stalls average to a superdiffusive behavior, as can be seen in the distribution of exponents of the mean squared displacement (Figure 5.12 C). While this is in accordance with time dependent ensemble averages [103], the occurence of broad distributions directly relates to the intrinsic degree of heterogeneity in the system. Like in the experiment, the dynamics of individual clusters relies on local influencing factors such as the local network connectivity, the local concentration of active crosslinks, and the individual cluster size.

The exact values of $\alpha$ depend on the details of the actin-fascin and actin-myosin interaction. In the simulation, this is governed by the motor and crosslinker on- and off-rates. An increase in the motor off-rate $r_{\text{off}}$ lowers the crossbridge strength and corresponds to the addition of KCl in the experiment. Similar to the experiment, the increase of the motor off-rate hinders the reorganization in the system and individual structures, single rods, or entire clusters move less. This is reflected in a reduced exponent of the mean square displacement (Figure 5.12 D). If the motor activity drops below a critical value, the dynamics becomes subdiffusive. In this regime, the motor proteins are not strong enough to induce any significant network reorganization and the system essentially consists of one single cluster that only shows diffusive motion. A similar behavior is found if the on-rate of the crosslinking proteins $p_{\text{on}}$ is increased. The higher the on-rate, the more the cluster dynamics is shifted to stall phases and the exponent $\alpha$ decreases concomitantly (Figure 5.12 D).

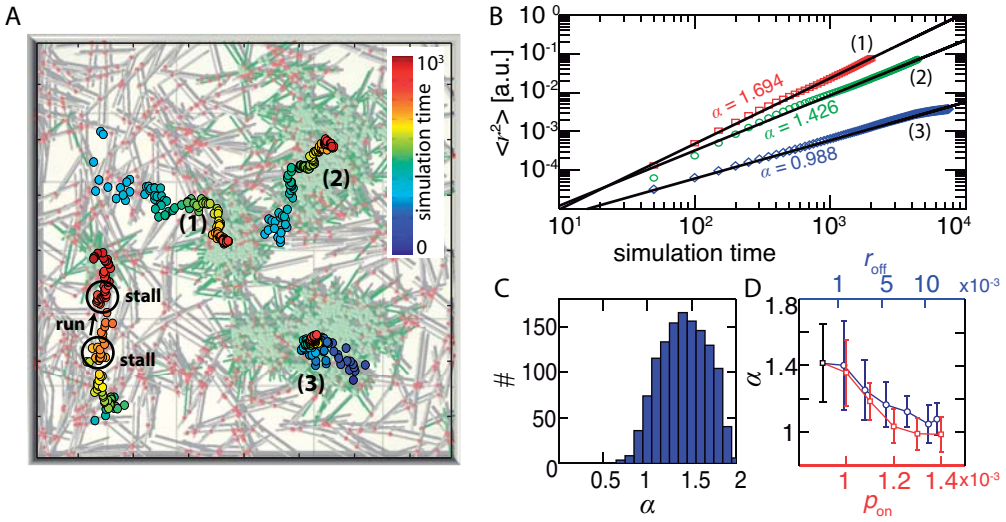


**Figure 5.12: Superdiffusive transport in the simulation.** (**A**) shows a simulation snapshot superimposed with the time-resolved center-off mass positions of the respective clusters. As can be seen from the center-off-mass trajectories, individual clusters move in a succession of runs and stalls. In general they move less, the larger they are. This is reflected in the mean-square displacements depicted in (**B**): while the large cluster shows a diffusive motion (curve 3) the other clusters move in a superdiffusive manner with mean square displacement exponents $\alpha > 1$. The heterogeneity in the system leads to a broad distribution of exponents $\alpha$ with a mean at $\alpha = 1.42 \pm 0.24$ (**C**). The exact value of the mean exponent depends on the details of the motor- and crosslinker (un-)binding kinetics. Increasing the motor off-rate $r_{\mathrm{off}}$ leads to a decreased activity in the system, visible in the decline of the mean square displacement exponent $\alpha$ (**D**, blue curve). Likewise, the activity and hence the exponent $\alpha$ decline, if the crosslinker on-rate $p_{\mathrm{on}}$ is increased (**D**, red curve).

## 5.6 Collective modes in active gels

In general, the individual structures move independently. At the same time, the force exertion inside of crosslinked cytoskeletal networks are expected to induce a force rate dependent rupturing of the crosslinking points [60] and thus the locally induced changes of the elastic environment will also affect and modulate the long-range transport and structure formation dynamics. Thus, it would be conceivable that the connectivity of the filamentous network enables the coordination of the transport and reorganization processes resulting in the appearance of collective modes. In fact, such movements coordinated in time and space as have been observed for the pulsed constrictions during dorsal closure giving rise to a collective behavior *in vivo* [189].

The minimal system investigated here is indeed sufficient to retrieve such collective dynamics: for short time intervals of about 30 s, the self-organized structures can also synchronize their movements. These pulsatile collective modes are characterized by a coordinated movement in time and space of a few or even up to nearly all visible structures of the network (Figure 5.13). Structures which are up to hundreds of microns apart are synchronized in their movement: during run phases their directional motion is coordinated (Figure 5.13 C) and the active movement starts and stops almost simultaneously. This coordinated movement is not altering the steady state of the system and is not linked to a macroscopic contraction, which only occurs at much higher actin concentrations [103].

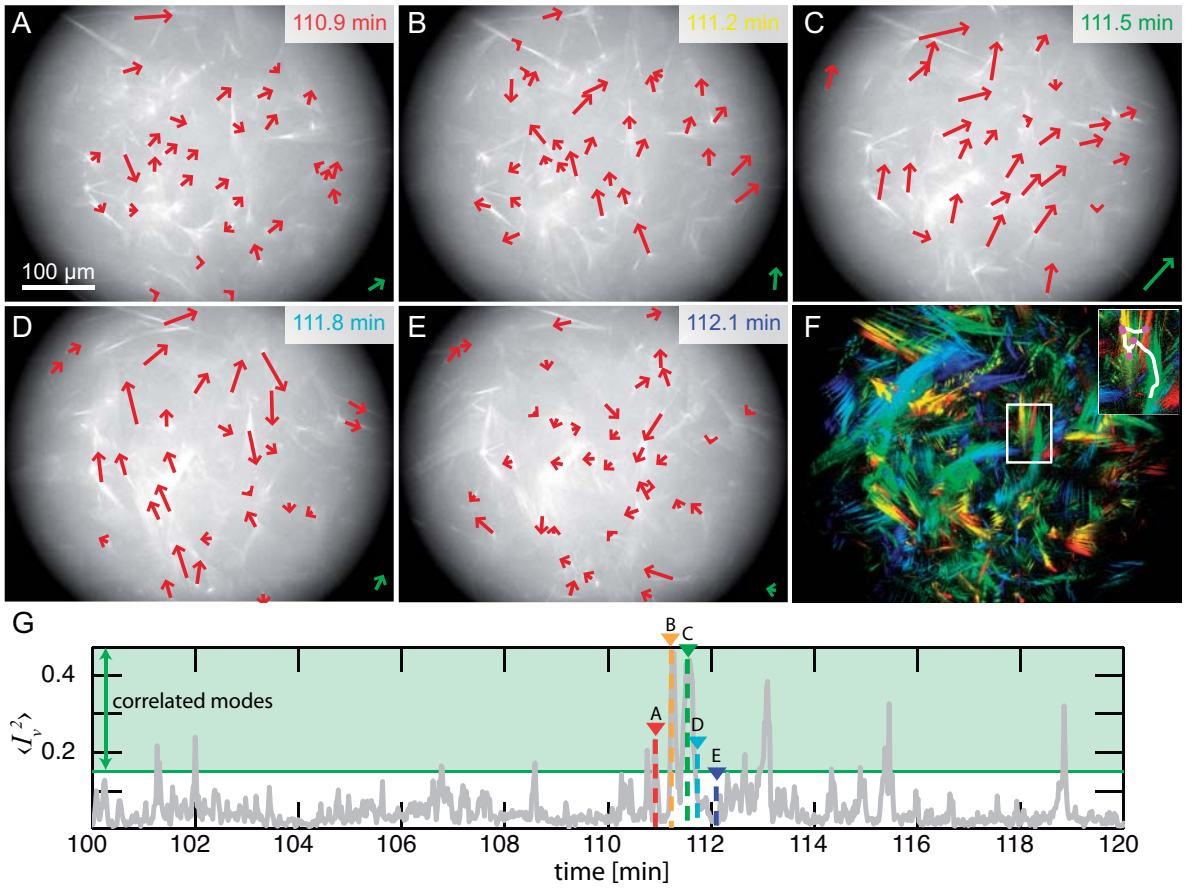


**Figure 5.13: Collective dynamics in active gels.** Fluorescence micrographs (**A–E**) of active actin networks at indicated times after initiation of polymerization show the dynamic reorganization within the network. Red arrows indicate the movement of individual points in the network with lengths 20-fold magnified and a time-average over three frames. Green arrows show the resulting overall movement in the field of view (lengths are 40-fold magnified). These long range reorganization processes are summarized in the colored time overlay (red to blue, **F**). The whole network in the field of view exhibits pulsatile collective dynamics with movements being coordinated in time and direction: Most of the time, individual structures move predominantly for only short periods and in random directions (**A,E**). These quiescent phases are followed by periods with high activity in the entire network. During these active phases, the better part of the network shows long, persistent runs (**B,C**). The degree of coordination of the movement is measured by the average squared velocity cross-correlation function $\langle I_v^2 \rangle$, in which phases of collective movement are reflected as peaks. In such collective phases that last for up to 30 sec, the majority of the identified structures moves in approximately the same direction (**G**).

Introducing the velocity cross-correlation function

$$I_v(\mathbf{r}) = \frac{\left[\langle v(\mathbf{x}+\mathbf{r})v(\mathbf{x})\rangle_\mathbf{x} - \langle v\rangle_\mathbf{x}^2\right]}{\left[\langle v^2\rangle_\mathbf{x} - \langle v\rangle_\mathbf{x}^2\right]}\,, \tag{5.9}$$

the degree of collectivity in the active transport can directly be quantified. For each time point the average of the squared correlation function $\langle I_v(\mathbf{r})^2\rangle_r$ reflects the level of correlation in the system. High values of $\langle I_v(\mathbf{r})^2\rangle_r$ relate to a highly collective movement, while low values close to zero indicate intervals lacking collective modes (Figure 5.13 G). The proportion of time points showing collective modes is evaluated by introducing a correlation cutoff $q$: Averaged squared correlation functions $\langle I_v^2(\mathbf{r})\rangle_r$ above $q$ are defined as collective modes; values below $q$ are defined to relate to

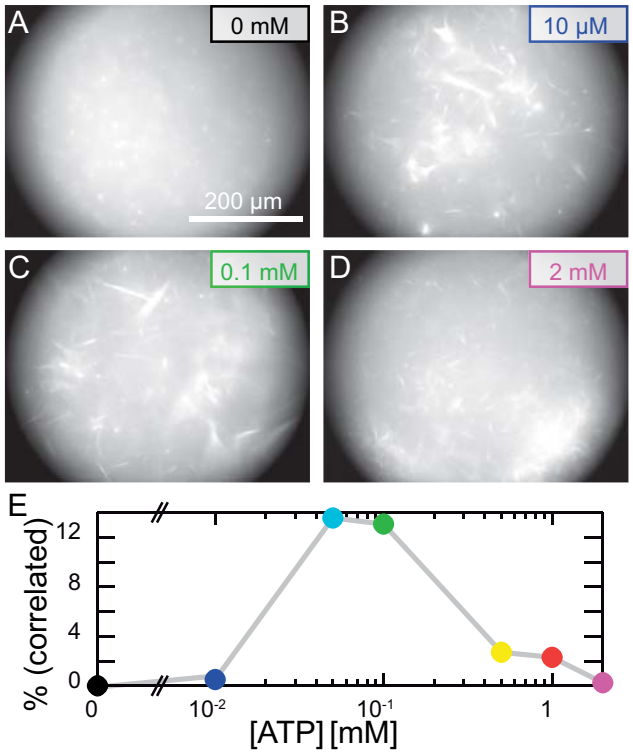


**Figure 5.14: The degree of collectivity depends on the ATP concentration.** In the abscence of ATP, myosin-II filaments act as nucleation seeds, resulting in a multitude of small, well separated clusters as illustrated in the fluorescence micrograph 90 min after polymerization (**A**). In prescence of low (**B**), intermediate (**C**) or high (**D**) ATP concentrations, a highly dynamic network of larger structures is formed. The degree of correlated motion depends on the ATP concentration: Only intermediate ATP concentrations allow for highly correlated movement (**E**).

an uncorrelated movement. The variation of $q$ only affects the absolute values while the relative values and the trend are not affected. At 0.1 mM ATP, for a correlation cutoff of $q = 0.15$ about 9 % of the frames show correlated movement.

Similar to the complex ATP-dependence observed for the superdiffusive transport, the level of collectivity shows four distinct regimes (Figure. 5.14): For passive actin/fascin/myosin networks (regime i) only small, diffusing clusters are observed. Their movement is not correlated (fig. 5.14E). At low ATP concentrations in regime (ii) (10 $\mu$M, Figure. 5.14B), the low motor activity is limiting the number of runs and the stalls of the network structures are dominating the dynamics. Consequently, collective modes barely occur in this crosslinker dominated regime. For intermediate ATP concentrations (up to 0.1 mM, Figure. 5.14C) in regime iii, the highest correlation is observed. At high ATP concentrations (regime iv), correlated motion is again rarely observed. The occurence of four regimes is again attributed to the maximal crossbridge strength of the acto-myosin bond at intermediate ATP-concentrations.

Importantly, the simulation cannot retrieve the pulsatile collective run and stall phases observed in the experiment, where remote structures move in a coordinated manner (Figure 5.13). This indicates that the experimentally observed dynamics not only depend on the identified microscopic interactions but are modulated by a weak but far reaching connectivity within the system. While the incorporation of active transport, crosslinking and forced unbinding suffices to explain the

superdiffusive transport properties, the simulation cannot account for long range force percolation, as the force balance is only local with a typical range of a rodlength. This consistent with the experimental findings, as the lack of connectivity observed for high ATP concentrations leads to a decline in the proportion of collective modes (Figure 5.13 E). The coordinated reorganization is only possible if the structures are connected, which is a prerequisite for the observed long range nature of the interaction. Molecular motors can only transport and exert forces between filaments. Thus, it is the connectivity and discrete nature of the network together with the force exertion mechanism, which enables the collective motion to occur.

In summary, the minimal agent based simulation that is based on local force balances only, can reproduce most of the key experimental findings. The incorporation of the three basic processes, active transport, crosslinking and forced unbinding by means of a simple rate model, is sufficient to retrieve the coarsening process, the superdiffusive behavior and the dependence of the mean run length on the cluster size. Furthermore it helps to identify the phenomena that rely on long range effects, such as the occurrence of collective modes, and helps to pin down which of the conceivable long-raging effects are the most important contributions. This lays the basis for a more complete picture of the pattern formation in active materials.

## 5.7 Discussion

In this chapter we showed that minimal model systems consisting of actin filaments, crosslinking molecules and myosin-II motor filaments can undergo an astonishing self-organization process. In the course of this self-organization process the initially homogeneous system phase-separates into an interconnected network of clusters that are densely packed with material. Compared to other phase separation processes in soft materials like nucleation and growth of crystals [233], phase separation in binary mixtures [118] or diffusion limited aggregation [221], active gels in the parameter regime studied here show a remarkable dynamic behavior.

As demonstrated by the simulation results, this highly dynamic behavior is attributed to the competitive interaction of molecular motors and passive crosslinkers: while crosslinking proteins are required for the mechanical stability of the actin network, molecular motors introduce an active component to the networks [89,102,150,188]. The presence of only motor filaments and ATP does not suffice to induce any reorganization or structure formation in an actin solution. Only the combination of motors and crosslinking molecules can result in structure formation [10] and even can induce a macroscopic contraction of cytoskeletal *in vitro* networks [18,93,97].

The incessant local input of mechanical energy at the smallest scales via myosin-II filaments then drives a constant reorganization of the actin/fascin network through forced unbinding and rebinding events. In the course of this constant network reorganization, a highly dynamic steady state of aggregated clusters emerges whose characteristic properties crucially depend on the systems key parameters: the actin, motor and crosslinker concentrations and the binding affinity of the myosin-II filaments to actin-fascin structures that directly regulates the maximal force the myosin-II filaments can exert. The activity of the highly heterogenous system depends on its connectivity, as molecular motors need tracks to exert forces. This dependence of the activity on the connectivity of the networks opens up the possibility that already small perturbations can result in a large structural response by the identified self organization mechanisms of the active gel – visible in the emergence of collective modes that propagate through the active network. Biochemical

signaling as well as a mechanical stimulus would result in a shift in the phase diagram enabling a rapid, local and highly robust mechanosensing mechanism as observed in cytokinesis or upon mechanical stimulation [59].

Importantly, the transport dynamics recovered in the reconstituted system is in excellent agreement with the dynamics inside the cytoplasm of cells. Here too, a superdiffusive behavior is observable with exponents between 1.5 and 1.7 [66, 86, 119]. While in cells the mechanism can only be linked to the energy consumption, presumably through the activity of molecular motors, the model system presented here allows the identification of the underlying microscopic mechanisms, which is the competition between binding and rupturing events evoked by crosslinking molecules and molecular motors.

With a simple phenomenological simulation the main experimental features can be retrieved: The incorporation of the three basic processes, active transport, crosslinking and forced unbinding is sufficient qualitatively reproduce several key results of the experiment. This includes the cluster formation and the coarsening process, the superdiffusive behavior and the dependence of the mean run length on the cluster size. However, a more systematic approach based on first principles proves difficult: While individual patterns like asters of cytoskeletal filaments have been successfully described both by mesoscopic models in the dilute regime [3, 128] and macroscopic models [96, 114], the explicit modelling of the nonlinear dynamics of extended patterns and coarsening processes is still at large. This is attributed to the inherent heterogeneity in many model systems which comprise a polymorphism of many coexisting patterns. Especially for generic approaches that are based on linear irreversible thermodynamics with geometric nonlinearities, it is therefore challenging to narrow down the parameter space and to decide which additional nonlinearities are important [96].

The combination of simplified *in vitro* model systems with simulations based on simple interaction rules opens up the perspective of addressing the governing principles of the cytoskeletal structure formation processes. By extending the experimental system to include other physiological cross-linkers, such as $\alpha$-actinin or filamin or external stimuli, reconstituted systems like the one presented here will become an ideal tool to accompany theoretical efforts to obtain a sound physical understanding of the self-organization in cytoskeletal systems.

# 6 Conclusions and Outlook

## 6.1 Summary of the main results

In this thesis, I used reconstituted systems consisting of actin filaments, the motor protein myosin-II, and crosslinking proteins to elucidate the self-organization processes in active materials. The design and analysis of these systems was motivated by several key problems in the field of active soft materials that served as the road map for the work presented here. In the introductory chapter of the thesis, these key problems where outlined in the form of several key questions – that we are now, with the results obtained in this thesis, able to answer. The first set of questions encircled the pattern formation in the high density motility assay:

1. *Is it possible to induce a transition to collective motion by increasing the filament density in motility assay experiments? If so: What are the statistical properties of this ordered state and how do they compare to theoretic predictions? Is it possible to map the transition to collective motion by a simple simulation that is solely based on short range interactions?*

By increasing the filament density, it was indeed possible to trigger a transition to collective motion. The patterns comprised the theoretically predicted clusters, swirls and density waves formed by collectively moving filaments. The minimal nature of the system enabled the quantification of the statistical properties found in collective motion: the fluctuations in the particle density are anomalously large, the correlations of the order parameter are anisotropic with respect to the mean direction of motion, and individual filaments, though being part of a collectively moving structure, perform a superdiffusive motion perpendicular to the mean direction of motion. All these experimental findings are in precise agreement with theoretical predictions. With an agent-based simulation, it was possible to relate the emergence of collective motion in the motility assay to weak and local alignment interactions. At the same time the simulation indicated that the pattern formation also relies on long-range hydrodynamic interactions – an assumption that could be substantiated by motility assay experiments in confinement.

2. *What happens if the active transport in the motility assay is complemented by a defined growth process induced by crosslinking proteins? How do the mechanical properties of the emergent structures affect the pattern formation?*

The addition of the crosslinking protein fascin fundamentally altered the pattern formation and the steady state properties of the system. Complementing the active transport in the system by the defined growth induced by fascin lead to the formation of elongated fibres and rings of crosslinked actin filaments that reflect the binding properties of fascin. The properties of these structures arise from the interplay of active transport and the mechanical properties of the emergent structures: the random curvature fluctuations that characterize the active transport are successively eliminated as the emergent structures gradually get stiffer during the growth process. Hence, the steady state structure could be identified as „frozen-in“structures where fluctuations on the single filament level are successively eliminated while the system is kept in an active state.

3. *How do different crosslinking proteins behave in active systems? Can the motility assay be used as a tool to selectively investigate and pinpoint the non-equlibrium properties of crosslinking proteins?*

The structure formation in the high density motility assay depends sensitively on the crosslinking protein that is added. The addition of different crosslinking proteins not only lead to a polymorphism of different steady state structures like actively compacting networks or highly symmetric assemblies, but also to a self-organization dynamics that is highly specific for the individual crosslinking protein. Thereby, I could show that motility assay experiments can indeed provide a first benchmark for the behavior of crosslinkers in an active environment. Moreover, it turned out that the behavior of crosslinking proteins in active systems depends mainly on the binding strength to actin under load rather than on other parameters like the geometry of the crosslinker.

4. *What are the dynamic properties of an active actin network that is set under stress by molecular motors? Can these properties be retrieved in a simple simulation that models the interplay between passive crosslinking and active driving based on interaction rates? Do active gels also display collective modes?*

Active gels consisting of actin, fascin and myosin-II filaments undergo a highly dynamic pattern formation in the course of which the gel phase separates to form dense clusters of crosslinked filaments. The clusters have a characteristic structure size distribution and show superdiffusive transport properties. By using a simple phenomenological simulation that is based on binding and unbinding dynamics of motors and crosslinkers, it is shown that most of this remarkable structure formation processes can be explained by the competitive interaction of molecular motors and crosslinking proteins. The emergence of collective modes, however, relies on the long-range connectivity in the active gel.

## 6.2 Outlook

The results of this thesis were obtained by conceiving, performing and analyzing reconstituted systems consisting of a minimal set of purified components. The major advantage of this class of experiments is the excellent accessibility of all relevant system parameters. This allowed to systematically accompany the experimental efforts by tailored agent based simulations and enabled a detailed comparison to theoretical predictions. Thus, the results presented in this thesis provide an excellent starting point to address further questions that encircle the structure formation in active systems.

Towards a more complete and unifying physical picture about the dynamic processes in motility assay experiments, a more detailed theoretic framework is desired. This becomes evident when the results obtained in this thesis with the actin-based motility assay are compared to recent experiments on microtubuli-based assays where microtubuli filaments are propelled by dynein motor proteins [197]. Coarse grained theoretic approaches would suggest that both systems belong to the same universality class and thus should show similar self-organization phenomena. However, albeit both systems generically show a density dependent transition to collective motion, the patterns in the ordered state are qualitatively different in nature: while the actin-based setup is characterized by highly polar, large scale density inhomogeneities, the microtubuli-based gliding assay self-organizes in arrays of swirling microtubules, where the polarity is less developed. The major differences between the two assays lie in the microscopic properties and processes that are

barely taken into account in existing theoretical frameworks. More specifically, both experiments differ in (*i*) the mechanical properties of the filaments and (*ii*) in the motor-filament interaction. With a ten-fold higher persistence length, microtubuli are much stiffer than the semiflexible actin filaments. Moreover, the microtubuli-associated motor dynein is processive [167], while HMM or Myosin-II respectively, used in most actin-based assays, are non-processive [87, 166].

The biomechanical differences between microtubuli- and actin-based assays most prominentely become manifest during collisions of two interacting filaments: while collisions between microtubules almost always lead to directional rearrangements and to a local increase of order [197], colliding actin filaments can readily cross each other; only very rarely and only between already sufficiently aligned filaments, a significant directional rearrangement is observable. While these differences in principle are straight forward to understand, their impact on the structure formation process is less clear, as a general microscopic framework for the pattern formation in gliding assays is still elusive. However, from a theoretical physics perspective it is already clear that any differences in the microscopic collision rules bear a number of interesting implications. The strict excluded volume interaction observed for gliding microtubules could explain why the amount of microtubules moving in opposition to the mean direction of motion is much higher in microtubuli-based experiments than in actin-based experiments. Moreover, following mesoscopic models that are based on coarse grained microscopic processes [13,14,111,128,240], this difference in the microscopic interactions should have direct consequences to the macroscopic properties of the ordered state. Thus the shift from weak excluded volume in the case of actin to a strict excluded volume in the case of microtubuli could switch the nature of the phase transition from a long-wavelength to a finite wavelength instability [17, 164]. This would explain why the patterns in the two motility assays based on actin and microtubules look qualitatively different.

On the way to a unifying microscopic framework for the pattern formation in the motility assay, a detailed quantification of the interaction of two colliding filaments is needed. This will require to record the intersection angles and velocities of an ensemble of interacting filaments before and after the collision. In the next step, this data could then be compared to microscopic simulations, where the relevant parameters like the stiffness of the filaments and the processivity of the motor proteins can readily be varied. This will lead to a set of interaction rules that can be used either in agent based simulations or as a starting point to derive coarse grained equations that then can be solved numerically or by means of a linear or weakly non-linear analysis. In any case, these results will allow to systematically study the impact of microscopic interaction parameters on the pattern formation. These findings can then be tested by varying the mechanochemical properties in the experiment. In the case of the actin-based gliding assay, this can for instance be done by placing a network of non-absorbing polymers on top of the motor-coated surface that, by preventing filaments from leaving the surface, limits crossing events in the actin-based motility assay. Alternatively, one could use extremely short actin filaments that are closer to the stiff rod limit. The usage of motor proteins different from myosin-II is another promising route to modify the mechanochemical interactions directly. For instance, by replacing the myosin-II motors by myosin-V, a processive actin-based motor protein [145], one can study how the processivity of the filament transport affects the pattern formation in the system.

The development of a unifying mechanistic picture for the pattern formation in gliding assays also raises the fundamental question about the nature of the phase transition to collective motion itself. However, the exact characterization of the phase transition is a delicate problem and even for simulations that are precisely quantifiable, the investigation of the phase transition turned out

to be problematic. Recent work on the Vicsek model showed that the characteristics of the phase transition may be masked by finite size effects that arise from too small simulation boxes [29]. Only by a careful analysis of the fluctuations that arise around the critical density in large enough systems, it was possible to find evidence that the transition is in fact of second order in this class of simulations [29, 30]. In experimental systems, the detailed analysis of the nature of the phase transition is even more problematic. Here, the detailed investigation of the phase transition is not only hampered by the limited system size but also by higher order effects that arise in many experimental systems studied to date. Yet again, the motility assay at high filament densities could provide the ideal tool to pinpoint the nature of the phase transition to collective motion; it provides sufficiently large system sizes in a rotational invariant environment. Interestingly, the persistent density modulations that arise in the density wave regime and in the cluster phase can be already interpreted as a sign of a second order transition [30]. Yet, the experimental verification still requires the precise measurement of the fluctuations of the order parameter and its derivatives around the critical density.

Apart from fundamental theoretical questions, the work presented here may also stimulate new experiments for a better understanding of the self-organization phenomena inside living cells in a bottom-up approach [15]. The conditions for the acto-myosin interaction in motility assay experiments are not dissimilar to the conditions found in the lamellipodium of migrating cells [24]; for instance, the average motor density applied here resembles the myosin concentration in platelets [21] and like the active networks investigated in this study, the lamellipodium is densely packed with actin filaments [195]. Thus, the mechanisms identified in this study will also contribute to the self-organization in migrating cells. In the lamellipodium, however, actin filaments themselves are subjected to dynamic assembly and disassembly [62]. The extension of the model system to include F-actin (de-)polymerization dynamics together with various crosslinking proteins offers a promising route for *in vitro* studies of the active turnover of the self-organized structures. This would require to substitute the pre-polymerized filaments stabilized by phalloidin by a solution containing actin monomers. Similar to experiments on active gels, the actin polymerization can then be initiated by providing appropriate salt concentrations in the assay buffer [103, 104]. Alternatively, the active turnover of crosslinked structures can be induced by adding the drug latrunculin that has been shown to promote the deploymerization of crosslinked actin structures [178]. The local addition of latrunculin either by using a diffusion chamber [178] or by using micropipettes [106] might even offer the possibility to generate a local symmetry breaking in the interplay between the assembly and disassembly of the patterns and to steer the pattern formation in the system.

The results of this thesis also indicate that the structure formation depends sensitively on the properties of the respective crosslinking protein. Transferred to the structure formation in the cytoskeleton, this indicates that by varying the relative concentrations of crosslinking proteins, the cell can not only tune the mechanic properties of the network, but can also shift gears between different mechanisms and regimes of self-organization. By that, the cell can effectively react to changing needs: while an abundance of $\alpha$-actinin can drive the formation of local contractile elements, an excess amount of fascin results in the formation of large scale polar structures. Yet, the deployment of filamin leads to the formation of a highly sustainable scaffold that is insensitive to force exertion. In this context, it is an interesting question if a combination of different crosslinking proteins would give rise to new structural elements that are not observed so far. Similar to passive crosslinked actin networks, the interplay of different crosslinkers could be competitive or

synergetic [175, 212]. For example, the combination of $\alpha$-actinin and fascin in the right concentration regime could lead to the formation of large scale contractile arrays, whereas trace amounts of filamin might always suppress any structure formation in the system. The precise type of the evolving structures may well depend on both the binding properties of the combined crosslinkers and their relative concentrations. In any case, the well characterized influence of individual crosslinking proteins on the structure formation as discussed in this thesis, provides an excellent starting point for the analysis of active systems with multiple crosslinking proteins.

The next step toward a sound physical understanding of the self-organization phenomena inside the active cytoskeleton involves the question of how the self-organization processes are triggered and regulated. In living organisms cells are constantly subjected to mechanical distortions that may either be induced by external forces or internal stresses which are actively generated by the concerted action of an ensemble of cells [59, 142, 210]. Cells posses the remarkable property to actively sense and react to these mechanical stresses. For instance, forces exerted locally on focal adhesion sites lead to a structural fortification and an increased stiffness of the entire cell [16, 32, 77, 229] and directly affect the nucleus and the spatial organization of the chromosomes [135]. Similar observations have been made in recent experiments where either single cells [63, 149] or model tissues [74] are subjected to uniform pressures or stretching and shearing forces. Another striking manifestation of the mechanosensing ability of cells is the synchronization of the cell beating in model tissues on length scales considerably exceeding the individual cell size [155,204]. Remarkably, the reaction of the cells to these external constraints is highly coordinated throughout the cell and takes place on the time scale of seconds or even fractions of seconds [135, 149].

The mechanisms that lead to this rapid and highly concerted response are only partly understood. On the molecular level, it has been shown that local forces can induce conformational changes of cytoskelstal proteins that may expose binding sites for other proteins or substrates [58, 67, 169]. Further, forces may trigger the opening of ion channels and thereby stimulate ion flux through the cell membrane [91,139]. While all these processes are very local and specific, they may serve as the starting point for a concerted response of the cell by triggering downstream signaling processes. For instance, such signaling processes can regulate the transcriptional activity within the cell and lead to the synthesis of actin binding proteins [230] – what, in the framework of this thesis, has been shown to crucially modify the self-organization of active systems. However, the synthesis of proteins not only is very expensive, but also a very slow way to react to external forces, and certainly does not suffice to explain the rapid reaction times observed *in vivo*. Another possible explanation for the remarkable ability of cells to react to external stimuli involves the aforementioned opening of ion channels. This may lead to a change in pH or salt concentrations that recently have been shown to crucially affect both the properties of reconstituted cytoskeletal networks [101,180] and the contractile activity of *in vitro* active actin networks and cell-extracts [106]. Yet, the amount of time it takes to build up a pH or salt gradient is still limited by diffusion. A small chemical such as magnesium, with a diffusion constant in the order of $100\,\mu\mathrm{m}^2/\mathrm{sec}$, takes a time interval in the order of $20\,\mathrm{sec}$ to cover a distance of $50\,\mu\mathrm{m}$ – and this is most probably only one step of multiple diffusional steps. So, apparently, the signal propagation due to diffusion would also not suffice to explain the rapid response of living cells to mechanical constraints.

The results presented in this thesis could provide another explanation for the remarkable mechanosensing ability of living matter. From the physics perspective, the cytoskeleton is an active gel that is constantly held under tension by molecular forces. Thus, while all the aforementioned processes are certainly important, they will be complemented by the unique material properties of

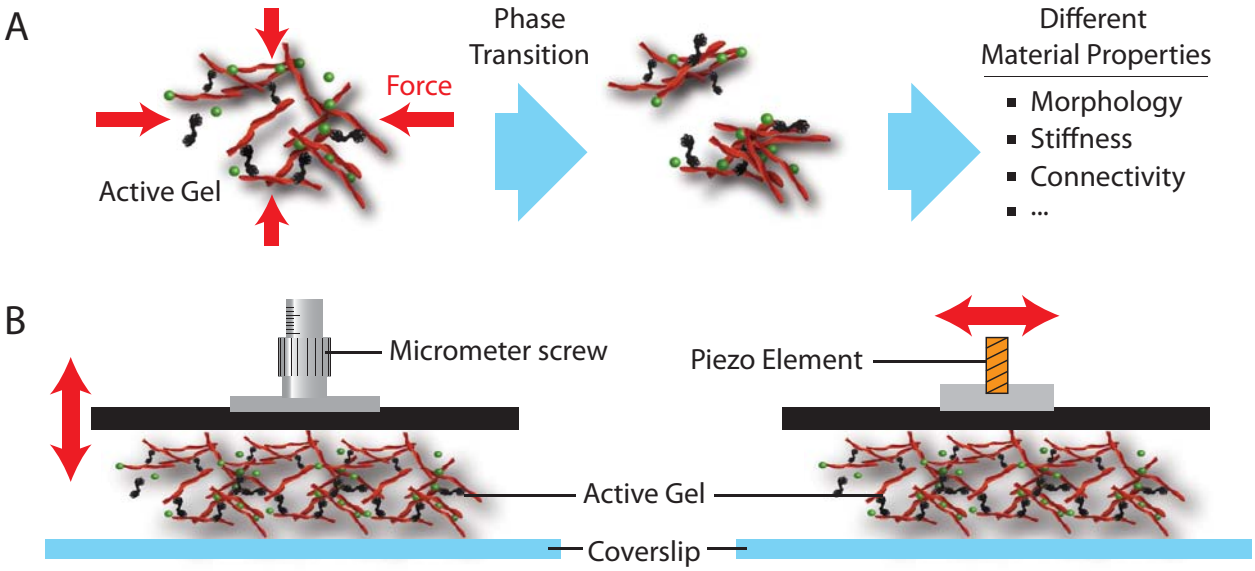


**Figure 6.1: Exploring the inherent mechanosensitivity of active gels.** Image **A** illustrates the principle of the inherent mechanosensing ability of active gels. Every external force will change the local conformation of the gel. This affects the local material concentrations as well as the morphology and the connectivity in the gel. As these parameters tightly regulate the phase behavior of active gels, these changes are likely to trigger a phase transition inside the active gel. In turn, this results in globally different material properties. The schematics shown in **B** illustrate how the mechanosensing ability of active gels can systematically be explored. By placing the gel in squeezing (left) or shearing (right) chambers, one can exert forces in a controlled manner and simultaneously monitor the resultant reorganization inside the gel.

active gels. On the one hand, the pre-stressed structures in network allow for a swift information transfer in the order of $\mu$sec [25,91,230]. On the other hand – as demonstrated in this thesis – active systems can undergo a succession of instabilities and phase transitions. These phase transitions in turn would provide a highly effective and rapid way to react to external constraints and would provide the cytoskeleton with an inherent mechanosensing ability (Figure 6.1 A).

The reconstituted systems introduced in this thesis are ideally suited to investigate the mechanosensing ability of active systems. As a first approach, one could for instance place a minimal active gel consisting of F-actin, Myosin-II filaments and one type of crosslinking protein inside shear- or squeezing-chambers (Figure 6.1 B). Such minimal approach would not only help to pin down the most interesting parameter regime, it would also provide information which of the various actin binding proteins is best suited to either promote or impede the mechanosensing ability: It is clear *a priori* that not all crosslinking proteins are equally well suited to support the reorganization of active gels responding to external forces. From the results obtained in this thesis, one could for instance speculate that filamin might suppress any reorganization while this is readily possible in the case of fascin. For a more quantitative characterization of the mechanosensing ability of active gels, one could use a confocal rheometer [177], with which one can exert shear forces and at the same time record the elastic response and follow the reorganization inside the active gel.

After having established the parameter regime that allows for a mechanosensitive response, the next steps should aim for a stepwise increase of complexity in the system. This can be achieved by adding mixtures of different actin binding proteins. Another promising route may be to complement the actin based active gel with other scaffold proteins of the cytoskeleton like microtubuli and intermediate filaments and to investigate cell-extracts. The results can then be compared to

experiments on single cells or cell ensembles [63, 74, 149]. By that, it can be revealed whether the reconstituted systems retrieve the *in vivo* behavior – at least on the qualitative level. For a more quantitative comparison, it will be necessary to identify and characterize parameters that can be varied simultaneously *in vitro* and *in vivo*. *In vivo*, this can be done by using knock-down mutants where particular actin binding proteins are inactivated or by applying drugs like the myosin-II inhibiting blebbistatin [8,194]. Local parameter changes can also be induced by using microinjection techniques, as has been demonstrated in experiments on active gels [106] and *in vivo* [28].

Reconstituted model systems have proven a versatile tool to selectively investigate the complex self-organization phenomena in living matter. The bottom-up approach with only few purified components allows to bridge between the overwhelming complexity of *in vivo* systems and theoretic approaches that aim for a general formalism for this material class. While most experimental studies to date mainly seek to qualitatively rebuild the functionality of *in vivo* systems, the results of this thesis demonstrate that the comparison with theoretical concepts provides a very promising perspective as well. This will not only promote our physical understanding of self-organization processes in active systems, it will also shed new light on the functionality of living matter. Thus, future studies will benefit from an integrated approach that combines carefully designed reconstituted experimental systems with *in vivo* studies and theoretic approaches.

# A Materials and Methods

*In this chapter, the materials and methods used in this thesis are outlined. It starts with a detailed description of the experimental procedures (section A.1), including the protein preparation, the protocols for the motility assay, the microcontact imprinting technique, and the generation of external flow fields. The second part (section A.2) contains a detailed description of the image processing and data analysis tools developed in this thesis. It particularly focuses on the identification and quantification of the particle fluctuations and the density and velocity correlations in motility assay experiments. In the last section of the materials and methods chapter (section A.3), the numerical methods used in the agent based simulations are outlined.*

## A.1 Experimental procedures

### A.1.1 Protein preparation

#### Actin

Fresh G-actin was obtained from rabbit skeletal muscle (purchased at *Hasenhof Weh*, Albertshofen, Germany) following a standardized protocol [133,190]. G-actin is kept in G-buffer ($2\,\mathrm{mM}$ Tris/HCl ( pH 8), $0.2\,\mathrm{mM}$ ATP, $0.2\,\mathrm{mM}$ $CaCl_2$, $0.2\,\mathrm{mM}$ DTT and 0.005 % $NaN_3$) at $4\,^\circ\mathrm{C}$ and used within seven days. Actin polymerization was initiated by adding one-tenth of the sample volume of a tenfold concentrated F-buffer ($20\,\mathrm{mM}$ Tris/HCl (pH 7.4), $20\,\mathrm{mM}$ $MgCl_2$, $2\,\mathrm{mM}$ $CaCl_2$, $2\,\mathrm{mM}$ DTT and $1\,\mathrm{M}$ KCl). For fluorescence microscopy, fluorescently labelled reporter filaments are used at a ratio of labelled to unlabeled filaments ranging from 1:2 to 1:50. They were stabilized with Alexa-Fluor-488 ($\rightarrow$)phalloidin (Invitrogen) at a ratio of 1:2. Unlabeled filaments are stabilized with phalloidin (Sigma), likewise at a ratio of 1:2. Once polymerized, actin was used within 2 days. To ensure that the density inhomogeneities observed in the high density motility assay are not the result of a de-mixing of labeled and unlabeled filaments, control experiments with an isotropic labeling were performed. The density inhomogeneities as well as the clusters and density waves persisted.

While individual filaments can reach lengths of up to $100\,\mu\mathrm{m}$ under optimal conditions, the overall filament-length distribution is exponential (Figure A.1). The filament length is either adjusted by using the capping/severing protein ($\rightarrow$) gelsolin, or by mechanically shearing the filaments by repeated pipetting steps using a syringe needle (Eppendorf) [24]. The latter method proved to be very convenient to achieve filament length distributions with small average filament lengths ranging from $1\,\mu\mathrm{m}$ to approximately $3\,\mu\mathrm{m}$. The filament length distribution stayed exponential (Figure A.1), implying a constant probability of filament-breaking per unit length. For filament length distributions with an aver length bigger than $3\,\mu\mathrm{m}$, gelsolin was used.

#### Gelsolin

Gelsolin belongs to a family of actin cutting/capping proteins. By nucleation, filament capping and severing gelsolin regulates the length distribution of actin filaments [92]. It can be used to control the average length of actin filaments – as long as this length is shorter than the average length of pure actin, which is in the order of $5\,\mu\mathrm{m}$ [179]. Gelsolin is prepared from bovine plasma serum following [117]. For the motility assay experiments performed in chapter 2, small amounts

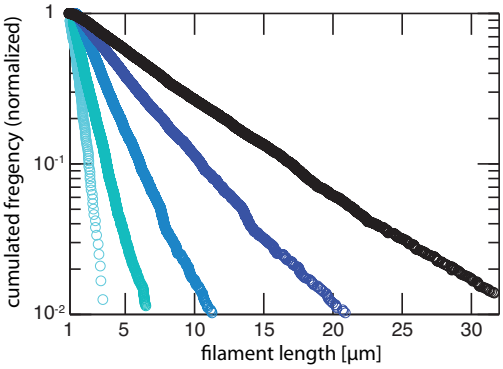


**Figure A.1: Filament length distributions.** The image shows the cumulated filament length distributions obtained by repeated shearing cycles of a $5\,\mu\mathrm{M}$ pure actin solution (black curve). All distributions can be described by exponentials, indicating a constant probability of filament-breaking per unit length, if shear forces are applied. From cyan to blue approximately $35$, $25$, $10$, and $5$ shearing cycles were carried out.

of gelsolin (1 gelsolin per 1110 actin molecules) have been added. To ensure that the observed phenomena are not affected by the use of gelsolin, control assays without gelolin have been performed; no change in the behavior was observed.

### Phalloidin

Phalloidin is an F-actin stabilizing molecule, which binds between two neighboring actin monomers and suppresses the actin depolymerization. Phalloidin is isolated from the poisonous amanita phalloides mushrooms and purchased from Sigma. It is a cyclic peptide with a molecular weight of $789\,\mathrm{Da}$ and can be used to attach a fluorophor to the actin filament. For the fluorescence micrographs shown in this thesis, Alexa-488-labelled phalloidin was used (purchased from Invitrogen). To ensure that the self-organization processes are not affected by the usage of this particular fluorophor, control assays with Rhodamine- and Atto-phalloidin were performed; no difference in the pattern formation was detected.

### Myosin-II, HMM and NEM-HMM

Sekletal muscle **myosin-II** is purified from rabbit skeletal muscle as reported in [215] and stored at $-80\,^{\circ}\mathrm{C}$ in $10\,\mathrm{mM}\,\mathrm{KH_2PO_4}$ (pH $6.5$), $0.6\,\mathrm{M}$ KCl, $25\,\mathrm{mM}$ $\mathrm{MgCl_2}$, $2\,\mathrm{mM}$ DTT, 3% $\mathrm{NaN_3}$ and 35% sucrose. At low to intermediate ionic strengths, myosin-II polymerizes to form filaments with a mean length of $0.7\,\mu\mathrm{m}$, corresponding to approximately 200-300 single motor heads [104].

To obtain the myosin-II fragment **HMM**, the molecular motor myosin II is enzymatically cleaved by chymotrypsine as described in [215]. The larger of the two resulting fragments, heavy meromyosin (HMM), has a molecular weight of 350 kDa [132] and retains the two actin binding domains of myosin II as well as the ATP binding site. However, it has lost its tail region. Thus, it is still working as molecular motor, but does not assemble into filaments.

N-ethylmaleimide-modified HMM (**NEM-HMM**) is prepared as described in [26]. Inhibiting the ATP-ase activity of HMM, this modification induces HMM-ADP rigor complexes, which bind tightly to actin filaments.

**Actin crosslinking proteins**

In this thesis a number of crosslinking proteins was used. Recombinant human **fascin** is purified from E.coli BL21-CodonPlus-RP and stored at $-80\,^{\circ}\mathrm{C}$ in $20\,\mathrm{mM}$ Tris/HCl (pH$\approx 7.4$), $150\,\mathrm{mM}$, following Ref. [224]. **$\alpha$-actinin** is isolated from turkey gizzard smooth muscle following [40], dialyzed against G-buffer and stored at $4\,^{\circ}\mathrm{C}$ for several weeks. Muscle **filamin** was isolated from chicken gizzard and further purified as reported in [184]. The sequence for the filamin-fragment **Mini-FlnA** was obtained from D. Fürst (Universität Bonn, Germany). It is purfied from E.coli BL21using a GST-tag and stored at $-80\,^{\circ}\mathrm{C}$ in $50\,\mathrm{mM}$ Tris/HCl (pH$\approx 8.0$), $5\,\mathrm{mM}$ GSH) similar to [84]. Recombinant Dictyostelium discoideum **cortexillin**-I (obtained from G. Gerisch, Max Planck Institute of Biochemistry, Germany) is purified from E. coli BL21using a C-terminal $\mathrm{His}_6$-Tag and stored at $-80\,^{\circ}\mathrm{C}$ in $20\,\mathrm{mM}$ Tris/HCl (pH$\approx 8.0$), $100\,\mathrm{mM}$ NaCl, $4\,\mathrm{mM}$ $\mathrm{CaCl}_2$ and $2\,\mathrm{mM}$ DTT [61]. The fragment of *Xenopus laevis* **anillin** spanning amino acids $1-428$, was cloned into pET-28a and purified from E.coli BL21-CodonPlus-RP using His-Tags on both termini. Anillin 1-428 is stored in $25\,\mathrm{mM}$ Imidazol (pH$\approx 6.0$), $25\,\mathrm{mM}$ KCl, $4\,\mathrm{mM}$ $\mathrm{CaCl}_2$, $4\,\mathrm{mM}$ $\mathrm{MgCl}_2$, $1\,\mathrm{mM}$ EGTA, and $2\,\mathrm{mM}$ DTT at $-80\,^{\circ}\mathrm{C}$. The **EPLIN**-$\alpha$ isoform (obtained from R. Fässler, Max Planck Institute of Biochemistry, Germany) is purified from E.coli BL21 using a FLAG-tag. It is stored at $-80\,^{\circ}\mathrm{C}$ in $50\,\mathrm{mM}$ Tris/HCl (pH$\approx 7.4$), $150\,\mathrm{mM}$ NaCl.

### A.1.2 Motility assay experiments

**Sample preparation**

Flow chambers were prepared with pre-cleaned microscope slides (Carl Roth, Germany) and coverslips (Carl Roth, Germany, $20\mathrm{x}20\,\mathrm{mm}$, No. 1). Coverslips were coated with a $0.1\%$ nitrocellulose solution diluted from a $2\%$ stock-solution (Electron Microscopy Sciences, USA) in amyl acetate (Carl Roth, Germany). The coverslips were fixed to the microscope slides using parafilm, yielding an overall chamber volume of $\approx 30\,\mu\mathrm{l}$. Prior to each experiment, a $30\,\mu\mathrm{l}$ actin dilution ($1-25\,\mu\mathrm{M}$ monomeric actin) was prepared by gently mixing labelled and unlabeled actin filaments with Assay Buffer ($25\,\mu\mathrm{M}$ Imidazol (pH 7.4), $25\,\mu\mathrm{M}$ KCl, $4\,\mu\mathrm{M}$ $\mathrm{MgCl}_2$, $1\,\mu\mathrm{M}$ EGTA, $1\,\mu\mathrm{M}$ DTT). The flow chamber was incubated with HMM diluted in Assay Buffer. Prior to the insertion of the respective actin dilutions, surfaces are passified with a BSA solution ($1\,\mathrm{mg/ml}$ BSA (Sigma) dissolved in Assay Buffer). To start the experiment, $2\,\mu\mathrm{M}$ of ATP together with the respective crosslinker concentration dissolved in Assay Buffer is flushed into the flow chamber. Oxidation of the fluorophore was prevented by adding a standard antioxidant buffer supplement GOC ($2\,\mathrm{mg}$ Glucose-Oxidase, Sigma; $0.5\,\mathrm{mg}$ Catalase, Fluka). To verify that the observed patterns are not affected by the use of GOC, control assays without the antioxidant supplement were performed. After addition of ATP, flow chambers were sealed with vacuum grease (Bayer Silicones).

**Actin and HMM concentrations**

The numbers for the actin concentration denote the monomeric actin concentration inserted into the flow chamber. This concentration is slightly lowered by up to $20\%$ by the subsequent rinse with the ATP-crosslinker dilution, as can be inferred from the decline in the bulk fluorescence intensity. The HMM concentrations $\sigma_m$ given in the thesis denote the concentration with which the flow chamber was incubated. The relation between $\sigma_m$ and the motor density at the surface $\Phi$ was determined to increase linearly in a wide concentration range with a ratio of $\sigma_m/\Phi = 0.04\,\mathrm{nM}\mu\mathrm{m}^2$

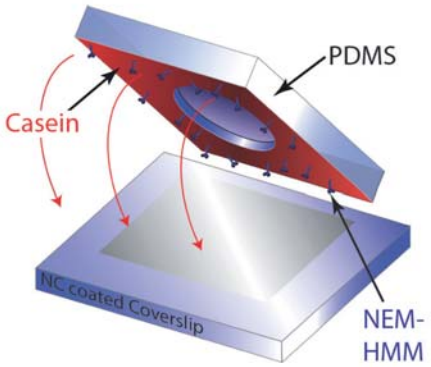


**Figure A.2: Microcontact imprinting technque.** The image shows a schematic representation of the used microcontact imprinting technique, with the help of which arbitrary boundaries with a diameter down to $50\,\mu\mathrm{m}$ can be designed. To passivate distinct regions selectively, a PDMS stamp treated with Casein and HMM motor proteins in the rigor state (NEM-HMM) is placed on the coverslip.

[209]. Above a HMM concentration of $\sigma_m = 200\,\mathrm{nM}$, the motor density at the surface saturates at a value of $\Phi \approx 6000\,\mu\mathrm{m}^{-2}$ [198]. If not indicated otherwise all experiments were performed at a HMM concentration of $\sigma_m = 90\,\mathrm{nM}$.

### A.1.3 Micro-contact imprinting

To functionalize the surface on the $\mu$m scale, a microcontact imprinting technique based on poly-(dimethylsiloxane) (PDMS) stamps was used (Figure A.2). The fabrication of the stamps follows the procedure for rapid prototyping of microfluidic devices [143]. More specifically, the design of the desired structure is printed in high resolution (3,000 dpi) on a transparency which is used as a mask to expose SU-8 50 positive photoresist (Microchem). After developing, the SU-8 structure serves as a master for the casting of PDMS, which is poured onto the master as a liquid. PDMS was cured for over night at $70\,^{\circ}\mathrm{C}$.

After being removed from the master, the PDMS replica of the structure is cleaned with Isopropanol (Roth) and plasma oxidized. To selectively passivate distinct regions of the coverslip, the stamp is wetted for $3\,\mathrm{min}$ with a mixture of NEM-HMM and $1\,\mathrm{mg/ml}$ Casein diluted in Assay Buffer and then surface dried for $30\,\mathrm{sec}$. Subsequently it is placed on the coverslip. After an incubation time of $3\,\mathrm{min}$ it is removed and the motility assay is prepared as described above.

### A.1.4 Generation of external flow fields

The flow fields were generated by attaching a syringe loaded with ABSA and $2\,\mu\mathrm{M}$ ATP to the flow chamber. During flow pulses, the flow rate was $6 \pm 2\,\mu\mathrm{l/sec}$. The area cross-section of the chamber was $2\,\mathrm{mm}^2$ with a height of $0.5\,\mathrm{mm}$ and a width of $4\,\mathrm{mm}$. The velocity of the flow fields was checked by evaluating the velocity of confluent particles close to the surface. Rarely, the flow lead to an unbinding of the filaments.

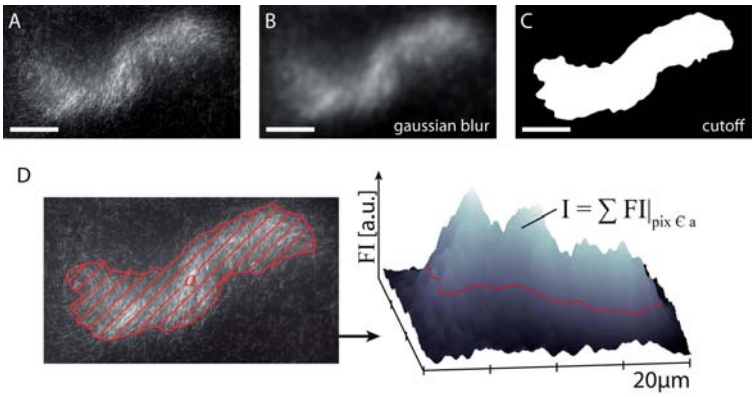


**Figure A.3: Cluster identification and calculation of the cluster sizes.** First, the raw images (**A**) are treated with a Gaussian blur filter (radius: 2 pixels, result shown in **B**). This smoothes the fluorescence signal of the cluster and simplifies the identification of the cluster as coherent area fraction that is based on applying a cutoff in the fluorescence intensity (**C**). Thus the cutoff defines the margin of the cluster; for all clusters the same cutoff was applied. To calculate the cluster size distribution two observables are evaluated: the area $a$ of the cluster and the sum of the fluorescence signal $I$ within the margin of the clusters (**D**). All scale bars are $20\,\mu$m.

### A.1.5 Image acquisition

All data are acquired on a Leica DMI 2000 inverted microscope or a Zeiss Axiovert 200 inverted microscope that were equipped with either a x100 oil objective (numerical aperture: 1.4), a x63 oil objective (numerical aperture: 1.4), or a x40 oil objective (numerical aperture: 1.35). Images (resolution: 1344 x 1024 pixels) were captured with a charge-coupled device camera (C4880-80, Hamamatsu) attached via a 0.35, a 0.4, or a 1.0 camera mount. Image acquisition and storage are carried out with the image processing software *OpenBox* [181].

## A.2 Data analysis

### A.2.1 Cluster size distributions

To quantify the morphology of the clusters and to extract the cluster size distributions from the microscope images (Figure A.3 A), we first smooth the raw images by using a Gaussian blur filter (radius: 2 pixels; algorithm: ImageJ). We then apply a cut off in the fluorescence intensity that defines the margin of the cluster (Figure A.3 D). Subsequently, the surface area of the cluster and the cumulated fluorescence intensity are calculated. For all clusters the same cutoff is used.

### A.2.2 Quantification of particle fluctuations

The fluctuations in the filament density were calculated by recording and evaluating the fluorescence intensity of 2500 consecutive images (corresponding to $4.88\,\mathrm{min}$) for five different spots per sample. To quantify the intensity fluctuations, the raw images are first subjected to a background subtraction. Background images where recorded separately with homogeneous samples that contain the same amount of fluorophores as the actual experiments. The subtraction of these homogeneous background images proved to be the best way to correct for the slight but inevitable inhomogeneities in the fluorescence illumination that are particularly pronounced at the margins

of the field of view. To further correct for these inhomogeneities, a region of interest was defined that leaves out the boundary regions of the field of view. It contains only 60% (1024 x 768) of the original image. To rule out systematic intensity fluctuations that occur due to bleaching of the sample, the averaged decay (gliding average over 25 frames) in the temporal evolution of the fluorescence intensity per pixel $i$ was fitted with a single exponential according to $\exp(-t/t_i)$ with a characteristic decay time of $t_i$ for each pixel. This factor was used to correct the image sequence for bleaching by multiplying each pixel by $\exp(t/t_i)$. The temporal intensity fluctuations $\Delta I$ are then evaluated for rectangular subsystems of varying size and plotted against the mean intensity $I$ in the subsystem, following the approach introduced in Ref. [154].

With the image processing described here, the fluorescence intensity provides a good measure for the particle density in the field of view. To illustrate this, we performed experiments at a lower labeling ratio of one labelled filament to 200 unlabeled filaments and observed the collectively moving filaments at a higher magnification with a x100 objective and using 1.0 camera mount. The sparse labeling at high magnifications allows us to simultaneously record the fluorescence intensity and to track individual filaments. As can be seen from Figure A.4, the number of filaments $N$ is indeed directly proportional to the fluorescence intensity $I$. As a consequence the temporal fluctuations of both quantities are highly correlated and coincide in magnitude and duration (Figure A.4 A and B). These temporal fluctuations average up to anomalously large fluctuations with comparable exponents for both quantities (Figure A.4 C and D): the particle fluctuations $\Delta N$ scale with $0.73 \pm 0.03$ and the fluctuations in the fluorescence intensity $\Delta I$ scale with $0.76 \pm 0.05$ for the given image sequence. This exemplifies that the evaluation of the density fluctuations can readily be calculated via the fluorescence intensity. However, using the fluorescence intensity as readout has the advantage that much larger regions of interest that comprise millions of individual filaments can be analyzed which is mandatory for any comparison with macroscopic theories. Moreover, the usage of the fluorescence intensity to quantify the density fluctuations, allows for higher labeling ratios which minimizes labeling artifacts and at the same time enables the precise evaluation of the corresponding macroscopic velocity profiles with PIV.

### A.2.3 Calculation of filament length distributions

Following the approach described in [178], we used the MATLAB function "regionprops" to identify the interconnected objects with an area of $> 10$ pixels. Subsequently, the objects are fitted with an ellipse that has the same normalized second central moments as the region, and the major axis length is used as a measure for filament length. The usage of the "regionsprops" library requires the conversion of the microscopy images into binary images. This was carried out in ImageJ with a threshold adjusted globally for all images. The distributions shown in Figure A.1 are obtained from a minimum of 10 images.

### A.2.4 Particle Image Velocimetry

The velocity profiles were calculated with a Particle Image Velocity (PIV) algorithm written in MATLAB. The PIV code estimates the most probable displacement of small quadratic blocks by evaluating the cross-correlation function of two consecutive images [39]. The block size was adjusted to roughly match the average filament length: for images taken with the x40 objective, a block-size of 25 pixels was used; for the x100 objective, the block-size was adjusted to 40 pixels. This turned out to be the ideal choice for an accurate determination of the velocity fields.

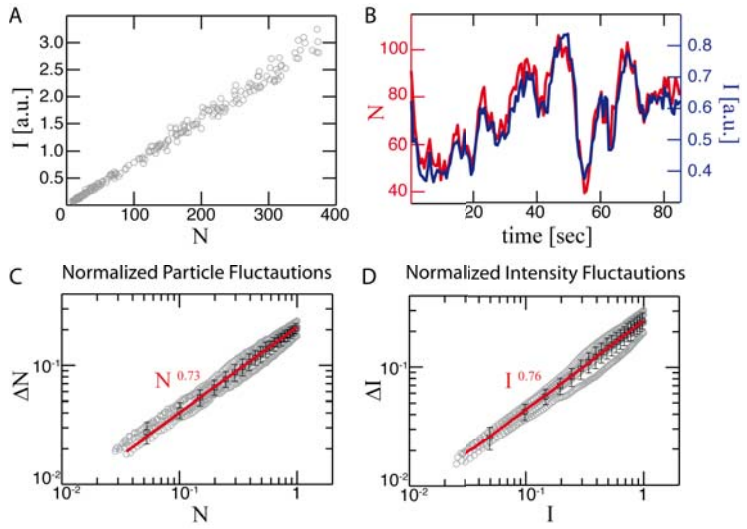


**Figure A.4: Comparison of fluctuations in the fluorescence intensity and in the number of particles.** (**A**) shows the fluorescence intensity $I$ as a function of the number of labeled filaments $N$ in the field of view for coherently moving structures in the motility assay. In the investigated parameter regime, the fluorescence intensity is directly proportional to the number of particles. Likewise, the temporal fluctuations of both quantities are similar in magnitude and duration (**B**). As a consequence the fluctuations scale with roughly the same exponent as shown in (**C** and **D**). The filament density was adjusted to $\rho = 12 \pm 2\,\mu\mathrm{m}^{-2}$ and the average filament length was $1.1\,\mu\mathrm{m}$.

### A.2.5 Velocity correlations in active fluids

The experimental system is characterized by a highly coherent collective movement of millions of filaments. The statistical properties of this collective motion patterns can be quantified by calculating the spatial and temporal correlations of the velocity field. In this thesis, this is done starting from the velocity field $\mathbf{v}$ that is calculated from the PIV scheme described in section A.2.4. To achieve a higher accuracy for the velocity correlation functions shown in section 2.4, a 25% overlap between adjacent blocks was used. The temporal correlations can then simply be calculated using the standard expression

$$\begin{aligned} G_v(T) &= \langle g_v(\mathbf{r},T)\rangle_r\,, \text{ with} \\ g_v(\mathbf{r},T) &= \frac{\langle \mathbf{v}(\mathbf{r},t+T)\cdot\mathbf{v}(\mathbf{r},t)\rangle - \langle \mathbf{v}(\mathbf{r},t)\rangle^2}{\langle \mathbf{v}(\mathbf{r},t)^2\rangle - \langle \mathbf{v}(\mathbf{r},t)\rangle^2}\,, \end{aligned} \tag{A.1}$$

whereby $\langle\cdot\rangle_r$ denotes a spatial average over all blocks of the PIV-grid ($\approx 500\,\mathrm{blocks}$) [53].

The full characterization of the spatial velocity correlations is more involved. As the polar ordered state that evolves above a critical filament density, is a broken-symmetry state, the correlations can be expected to be anisotropic with respect to the direction of motion [206,207,213]. With the naive implementation of a standard correlation function one average over all directions, and thereby loose the information about the anisotropy. To overcome this problem, we calculated the angle-resolved correlation function

$$\begin{aligned} P_{\mathbf{v}}(\mathbf{r},\alpha) &= \langle p_{\mathbf{v}}(\mathbf{r},\alpha,t)\rangle_t\,, \text{ with} \\ p_{\mathbf{v}}(\mathbf{r},\alpha,t) &= \frac{\langle \mathbf{v}(\mathbf{R}+\mathbf{r},\alpha,t)\cdot v(\mathbf{R},t)\rangle - \langle \mathbf{v}(\mathbf{R},t)\rangle^2}{\langle \mathbf{v}(\mathbf{R},t)^2\rangle - \langle \mathbf{v}(\mathbf{R},t)\rangle^2}\,, \end{aligned} \tag{A.2}$$

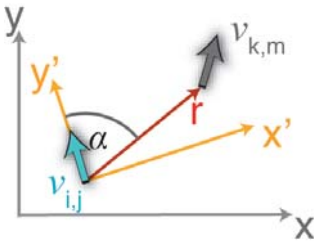


**Figure A.5: Calculation of angle-resolved correlation functions.** The correlation function is evaluated in a coordinate system that co-rotates with the local direction of motion. This allows to calculate the correlation in any given direction relative to the local velocity vector $\mathbf{v}_{i,j}$. The angle $\alpha$ denotes the angle between the local velocity vector $\mathbf{v}_{i,j}$ and the distance vector $\mathbf{r}$ of two PIV-blocks $(i,j)$ and $(k,l)$.

whereby $\langle\cdot\rangle_t$ is a temporal average over $2500\,\mathrm{frames}$ corresponding to $\approx 5\,\mathrm{min}$. The angle $\alpha$ is the angle between the local direction of motion and the vector $\mathbf{r}$ connecting the two PIV-blocks (Figure A.5). Mathematically, this can be conceived as a transformation of the velocity field into a coordinate system that co-rotates with the local direction of motion. The output of the correlation function defined in equation A.2 is a fully angle-resolved correlation map that allows to extract the correlation in any given direction relative to the local polarity.

### A.2.6 Density correlations in active fluids

To quantify the long range density correlations on length scales much larger than the average filament length of $5\,\mu\mathrm{m}$, the density first has to be coarse grained. To this end, we calculate the average fluorescence intensity $I$ in small quadratic blocks with a block-size corresponding to the PIV-grid (described in section A.2.4). Thereby, each block is assigned a local average intensity $I_i$ with $i = 1..N$. The image processing prior to the calculation of the coarse grained intensity map follows the procedure outlined in section A.2.2. Using this procedure, the fluorescence intensity $I$ is directly proportional to the filament density $\rho$ (Figure A.4) and the calculation of the locally coarse grained fluorescence intensities $I_i$ provides a good measure for the coarse grained filament density $\rho_i$. Subsequently the temporal and spatial correlations of the intensities can be calculated following the expressions

$$\begin{aligned} G_I(t) &= \langle g_I(\mathbf{r},t)\rangle_r\,, \text{ with} \\ g_I(\mathbf{r},t) &= \frac{\langle I(T+t,\mathbf{r})\cdot I(T,\mathbf{r})\rangle - \langle I(T,\mathbf{r})\rangle^2}{\langle I(T,\mathbf{r})^2\rangle - \langle I(T,\mathbf{r})\rangle^2}\,, \end{aligned} \tag{A.3}$$

for temporal correlations, and

$$\begin{aligned} P_I(\mathbf{r},\alpha) &= \langle p_I(\mathbf{r},\alpha,t)\rangle_t\,, \text{ with} \\ p_I(\mathbf{r},\alpha,t) &= \frac{\langle I(\mathbf{R}+\mathbf{r},\alpha,t)\cdot I(\mathbf{R},t)\rangle - \langle I(\mathbf{R},t)\rangle^2}{\langle I(\mathbf{R},t)^2\rangle - \langle I(\mathbf{R},t)\rangle^2} \end{aligned} \tag{A.4}$$

for spatial correlations. $\langle\cdot\rangle_t$ denotes a temporal average over all frames (if not indicated otherwise $2500\,\mathrm{frames}$ corresponding to $\approx 5\,\mathrm{min}$) and $\langle\cdot\rangle_r$ denotes a spatial average over all blocks in the field of view ($\approx 500\,\mathrm{blocks}$). The angle $\alpha$ in the expression for the spatial correlations again denotes the angular difference between local mean directions of motion of the two intensities $I(\mathbf{R})$ and $I(\mathbf{R}+\mathbf{r})$ (*c.f.* section A.2.5).

To calculate the correlations in the density *fluctuations* $\delta\rho$, the average intensity in the entire field of view $\bar{I} = \langle N^{-1} \sum_{i=1}^{N} I_i \rangle_T$, averaged over the entire period of observation T, is subtracted from the the local densities $\rho_i$. The spatial and temporal correlations of the density fluctuations $\delta\rho$ are then evaluated with the same formalism introduced in Equations (A.3) and (A.4).

The calculations of the density correlations depends sensitively on the block-size. A too small block size, of the order of several pixels, does not allow to quantify the long-range correlations in the system, as any long range correlations would be masked by correlations on the single filament level, *i.e.* by correlations in the mean distance between labelled filaments. The usage of a too big block size, on the other hand, would smoothen the large-scale density inhomogeneities that extend over several tens of filament lengths, impeding their accurate measurement. For all calculations presented in this thesis, the block size was adjusted to be of the order of the average filament length. This proved to be the optimal compromise to accurately calculate the local coarse grained density correlation, without loosing the long-range and long-term correlations stemming from large-scale density inhomogeneities.

### A.2.7 Characterization of filament transport in active fluids

Despite the collectively moving phase is characterized by the highly coherent motion of millions of filaments, individual filaments can deviate considerably form the mean direction of motion. To quantify this phenomenon, we first tracked the trajectories $\mathbf{x}_i(t)$ of $n$ individual filaments in a given field of view and subsequently calculated the mean trajectory $\bar{\mathbf{r}}(t) = \sum_{i=1}^{n} \mathbf{x}_i(t)$ of all traced filaments. The relative separation $\Delta\mathbf{d}_i(t)$ of the individual filaments from mean trajectory is then given by $\Delta\mathbf{d}_i(t) = \mathbf{x}_i(t) - \bar{\mathbf{r}}(t)$. To characterize the filament transport relative to the mean direction of motion, we calculate the mean-squared displacement (msd) of the relative separations

$$\mathrm{msd}[\Delta\mathbf{d}_i(\tau)] \;=\; \langle \Delta\mathbf{d}_i(\tau + t) \Delta\mathbf{d}_i(\tau) \rangle_t \,, \tag{A.5}$$

whereby $\langle \cdot \rangle_t$ denotes the time average. The time average is limited by the field of view and the tracking accuracy of the used tracking algorithm. Only the first 10% of the resulting mean squared displacement are used. The mean-squared displacement exponents are fitted logarithmically to trajectories with more than 50 time points, corresponding to $5.85\,\mathrm{sec}$.

The tracking algorithm that was used to identify the trajectories of the individual filaments is written in MATLAB and based on the built function "regionprops". It first identifies all filaments in the field of view and subsequently tracks them from frame to frame. The frame-to-frame recognition of the identified objects follows three criteria: (*i*) the distance covered from frame to frame, (*ii*) the object size, and (*iii*) the direction of movement. In its current stage the algorithm has difficulties in resolving filament crossovers which limits the trajectory lengths. To avoid excessive crossing events, the experiments were performed with predominately short filaments ($\approx 1\,\mu\mathrm{m}$) with a low ratio of labeled to unlabeled filaments ($\approx 1 : 400$).

### A.2.8 Ring size distributions

The frozen steady state observed in the presence of fascin (chapter 3), is characterized by the emergence of constantly rotating rings. Generically, these rings occur in two configurations: in a closed and in an open conformation. To characterize the frozen steady state and the mechanism that lead to the formation of the rings, the ring curvatures had to be quantified.

To this end, the ring curvature statistics for hundreds of individual rings are evaluated by using an automated ring recognition and analysis tool. Once the system reached its steady state, between 15 and 20 regions of interest were randomly chosen and imaged for around one minute. For each region, we first subtracted the background with ImageJ (rolling ball radius of $250\,\mathrm{pixels}$). The ring-radius distributions for open and closed rings are calculated in two steps: first, the distribution for all rings is measured and then separately the distribution for closed rings, only. Subsequently, the ring-radius distribution for open rings is obtained by subtracting the distribution for closed rings from the radii-distribution of all rings.

The ring recognition is carried out in MATLAB using an ellipsoid fit to the outer radius. Signatures which are not approximately of circular shape (ratio of semi-minor to semi-major axis $< 0.7$) are rejected. Closed rings can be directly analyzed without further processing steps. To calculate the distribution of open rings an average intensity projection in time is performed. This leads to closed objects also for the open rings that can be analyzed using the method described above.

For the characterization of the mechanisms leading to the frozen steady state, the inner radius of the rotating structures is more relevant. As material uptake after the curvature is already frozen, leads predominantly to a growth of the outer radius, the inner radius more accurately reflects the initial frozen-in radius. The inner ring radius is calculated via the area of the ring (obtained by the intensity projection) and the outer radius by using simple trigonometry.

### A.2.9 Meshsize evaluation

For the calculation of the meshsize of the actively compacting structures that form in the presence of $\alpha$-actinin, eplin and cortexilin, microdscopy images are converted into binary images with the same threshold for all images. Subsequently, the discrete derivative in x- in y-direction is calculated. For each direction, the distance between rising flanks is measured. A cumulative histogram over all distances is generated and fitted using a single exponential $\exp(-x/\lambda)$. To avoid errors, only the histogram entries between 20% and 80% of the maximal value are considered. The mean over $\lambda$ for the x- and y-direction is the average mesh size [7].

### A.2.10 Calculation of collective modes in active gels

The complex dynamics inside active gels includes the emergence of collective modes, where all structures in the field of view coherently move in one direction. These collective modes are characterized by velocities that are highly correlated both in magnitude and direction. To systematically quantify these collective modes, we first traced the individual structures in the field of view and subsequently calculated the cross-correlation function of the resulting velocity field.

To trace individual actin structures, images are background subtracted in ImageJ. To identify individual actin structures of the network, an intensity threshold value is applied in ImageJ to generate a binary image. Individual structures are identified as connected bright pixels using a cutoff of ten pixels. The structures are traced over time by means of their intensity weighted centroid positions using MATLAB, largely following the method developed by John C. Crocker [42] . To minimize tracking artifacts, the trajectories are subjected to a gliding average over 4 frames. Individual structures are traced for up to $6\,\mathrm{min}$ in the highly dynamic state, or over $2.5\,\mathrm{h}$ in the passive state until they fuse with a different structures, they are disintegrated, or move out of focus. To deter-

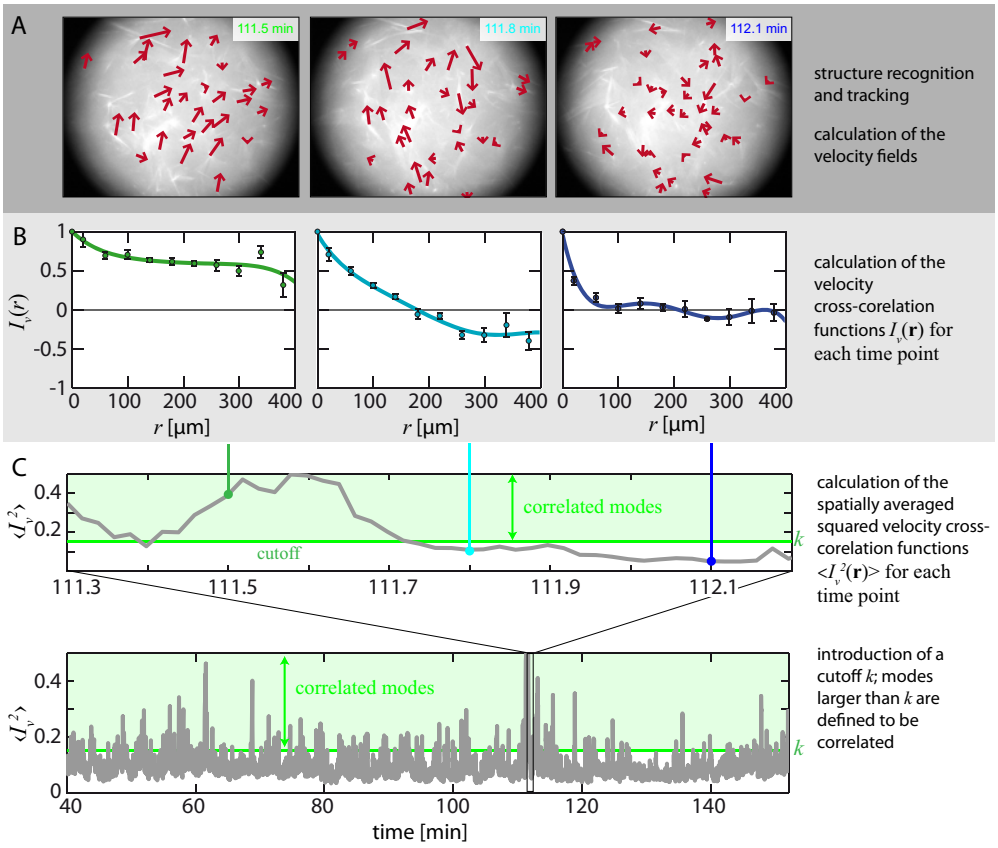


**Figure A.6: Identification and quantification of correlated modes.** First, the velocity field for the identified structures is calculated for each time point (**A**). Second, the velocity cross-correlation function $I_v(\mathbf{r})$ is evaluated for each frame. In (**B**) individual velocity cross-correlations averaged over 3 successive frames are shown. Correlation functions close to 1 indicate highly correlated or collective movements, whereas non-correlated movements average to correlation functions close to zero. If structures move in the opposite direction, they are anti-correlated with negative correlation functions. Therefore, the squared correlation function, averaged over all distances $\mathbf{r}$, $\langle I_v^2(\mathbf{r}) \rangle_r(t)$ is a measure for the level of correlation at each point in time $t$. (**C**) shows the time course of $\langle I_v^2(\mathbf{r}) \rangle_r(t)$, in which time points with highly correlated movements appear as peaks. To quantify the level of correlation, we introduce a global cutoff $k$. Modes with $\langle I_v^2(\mathbf{r}) \rangle_r > k$ are defined as collective or correlated modes and modes with $\langle I_v^2(\mathbf{r}) \rangle_r < k$ are not-correlated.

mine phases of correlated movement, the velocity cross-correlation function of moving structures

$$I_v(r,t) = \frac{\langle \mathbf{v}(\mathbf{x}+\mathbf{r},t) \cdot \mathbf{v}(\mathbf{x},t) \rangle_x - \langle \mathbf{v}(\mathbf{x},t) \rangle_x^2}{\langle \mathbf{v}(\mathbf{x},t)^2 \rangle_x - \langle \mathbf{v}(\mathbf{x},t) \rangle_x^2} \tag{A.6}$$

is evaluated. The degree of correlation at each time point $t$ is proportional to the average of the squared correlation function $\langle I_v(r)^2 \rangle_r(t)$ (Figure A.6).

The proportion of time points showing collective modes is evaluated by introducing a correlation cutoff $k$: Averaged squared correlation functions $\langle I_v(r)^2 \rangle_r(t)$ above $k$ are defined as collective modes; values below $k$ are defined to relate to an uncorrelated movement. For the data displayed in (Figure A.6) $k$ was set to $0.15$. The variation of $k$ only affects the absolute values while the relative values and the trend are not affected.

## A.3 Numerical methods

The agent based simulations that complemented the experimental results achieved with the motility assay setup (chapters 2 and 3) were developed together with C. A. Weber and E. Frey (Ludwig Maximilians Universität, München). The implementation of the interaction rules in C++ was carried out by C. A. Weber. Details of the algorithms can be found in References [171, 173, 232].

The minimal agent based simulation that models the pattern formation in active actin networks (chapter 5) was implemented in C++, using the *ANN*-library (*www.cs.umd.edu/ mount/ANN*), the *DISLIN*-library (*www.dislin.de*), and the *BOOST*-library (*www.boost.org*). If not indicated otherwise, the simulation runs were performed with $10000 - 25000$ unit-length rods, embedded in a quadratic arena with a side-length of 10 rod-lengths and periodic boundary conditions. To integrate the equations of motion that result from rate-based multiple interactions of crosslinkers and motor-proteins, a random sequential updating scheme was used. The time-step of the updating was set to $0.01$ simulation times, whereby the simulation time is defined implicitly as the time a motor filament needs to cover $0.1$ rod-length. The simulation snapshots were visualized using the 3D ray tracer tool *PovRay* (*www.povray.org*).

The mean squared displacements shown in chapter 5, are calculated for entire trajectories individually and the first 10% of the resulting mean square displacements are used. The power law exponent is fitted logarithmically to mean square displacements longer than 5000 time steps. Average values of the exponent are obtained by fitting a Gaussian to the distribution of $> 500$ power exponents.

# Bibliography


[1] Angelini, T. E.; Hannezo, E.; Trepat, X.; Fredberg, J. J.; Weitz, D. A.:
*Cell migration driven by cooperative substrate deformation patterns.*
PHYS. REV. LETT., **104** (2010), 168104.

[2] Angelini, T. E.; Hannezo, E.; Trepat, X.; Marquez, M.; Fredberg, J. J.; Weitz, D. A.:
*Glass-like dynamics of collective cell migration.*
PROC. NATL. ACAD. SCI. U. S. A., **108** (2011), 4714.

[3] Aranson, I. S.; Tsimring, L. S.:
*Pattern Formation of microtubules and motors: Inelastic interaction of polar rods.*
PHYS. REV. E, **71** (2005), 050901.

[4] Aranson, I. S.; Tsimring, L. S.:
*Patterns and collective behavior in granular media: Theoretical concepts.*
REV. MOD. PHYS., **78** (2006), 641.

[5] Aranson, I. S.; Sokolov, A.; Kessler, J. O.; Goldstein, R. E.:
*Model for dynamical coherence in thin films of self-propelled microorganisms.*
PHYS. REV. E, **75** (2007), 040901.

[6] Aranson, I. S.; Snezhko, A.; Olafsen, J. S.; Urbach, J. S.:
*Comment on: "Long-Lived Giant Number Fluctuations in a Swarming Granular Nematic".*
SIENCE, **320** (2008), 612c.

[7] Arevalo, R. C.; Urbach, J. S.; Blair, D. L.:
*Size-dependent rheology of type-I collagen networks.*
BIOPHYS. J., **99** (2010), L65.

[8] Aratyn-Schaus, Y.; Gardel, M. L.:
*Transient frictional slip between integrin and the ECM in focal adhesions under myosin II tension.*
CURR. BIOL., **20** (2010), 1145.

[9] Åström J. A.; Kumar P. B. S.; Karttunen M.:
*Aster formation and rupture transition in semi-flexible fiber networks with mobile cross-linkers.*
SOFT MATTER, **5** (2009), 2869–2874.

[10] Backouche, F.; Haviv, L.; Groswasser, D.; Bernheim-Groswasser, A.:
*Active gels: dynamics of patterning and self-organization.*
PHYS. BIOL., **3** (2006), 264 – 273.

[11] Ballerini, M.; Calbibbo, N.; Candeleir, R.; Cavagna, A.; Cisbani, E.; Giardina, I.; Lecomte, V.; Orlandi, A.; Parisi, G.; Procaccini, A.; Viale, M.; Zdravkovic, V.:
*Interaction ruling animal collective behavior depends on topological rather than metric distance: Evidence from a field study.*
PROC. NATL. ACAD. SCI. U. S. A., **105** (2008), 1232.

[12] Basan, M.; Risler, T.; Joanny, J. F.; Sastre-Garau, X.; Prost, J.:
*Homeostatic competition drives tumor growth and metastasis nucleation.*
HFSP J., **3** (2009), 265.

[13] Baskaran, A.; Marchetti, M. C.:
*Hydrodynamics of self-propelled hard rods.*
PHYS. REV. E, **77** (2008), 011920.

[14] Baskaran, A.; Marchetti, M. C.:
*Statistical mechanics and hydrodynamics of bacterial suspensions.*
PROC. NATL. ACAD. SCI. U. S. A., **106** (2009), 15567.

[15] Bausch, A.; Kroy, K.:
*A bottom-up approach to cell mechanics.*
NATURE MATERIALS, **2** (2006), 231.

[16] Bershadsky, A. D.; Balaban, N. Q.; Geiger, B.:
*Adhesion-Dependent Cell Mechanosensivity.*
ANNU. REV. CELL DEV. BIOL., **19** (2003), 677.

[17] Bertin, E.; Droz, M.; Gregoire, G.:
*Boltzmann and hydrodynamic description for self-propelled particles.*
PHYS. REV. E, **74** (2006), 022101.

[18] Bendix, P.M.; Koenderink, G. H.; Cuvelier, D.; Dogic, Z.; Koeleman, B. N.; Brieher, W. M.; Field, C. M.; Mahadevan, L.; Weitz, D.A.:
*A quantitative analysis of contractility in active cytoskeletal protein networks.*
BIOPHYS. J., **94** (2008), 3126.

[19] Besser, A.; Schwarz, U. S.:
*Coupling biochemistry and mechanics in cell adhesion: a model for inhomogeneous stress fibre contraction.*
NEW J. PHYS., **9** (2007), 425.

[20] Brenner B.; Schoenberg M.; Chalovich J. M.; Greene L. E.; Eisenberg E.:
*Evidence for cross-bridge attachment in relaxed muscle at low ionic strength.*
PROC. NATL. ACAD. SCI. U.S.A., **79** (1982), 7288.

[21] Brensnick A. R.:
*Molecular mechanisms of nonmuscle myosin-II regulation.*
CURR. OPIN. CELL BIOL., **26** (1999), 11.

[22] Burgis, M.; Schaller, V.; Gläßl, M.; Kaiser, B.; Köhler, W.; Krekhov, A.; Zimmermann, W.:
*Anomalous diffusion in viscosity landscapes.*
NEW J. PHYS., **10** (2011), 043031.

[23] Bussemaker, H.; Deutsch, A.; Geigant, E.:
*Mean-field analysis of a dynamical phase transition in a cellular automaton model for collective motion.*
PHYS. REV. LETT., **78** (1996), 5018.

[24] Butt, T.; Mufti, T.; Humayun, A.; Rosenthal, P. B.; Khan, S.; Molloy, J. E.:
*Myosin Motors Drive Long Range Alignment of Actin Filaments.*
J. BIOL. CHEM., **285** (2009), 4964.

[25] Canadas, P.; Laurent, V. M.; Oddou, C.; Isabey, D.; Wendling, S.:
*A cellular tensegrity model to analyse the structural viscoelasticity of the cytoskeleton.*
J. THEOR. BIOL., **218** (2002), 155.

[26] Cande, W.Z.:
*Preparation of N-ethylmaleimide-modified heavy meromyosin and its use as a functional probe of actomyosin-based motility.*
METH. ENZYMOL., **134** (1986), 473.

[27] Cates, M. E.; Fielding, S. M.; Marenduzzo, D.; Orlandini, E.; Yeomans, J. M.:
*Shearing Active Gels Close to the Isotropic-Nematic Transition.*
PHYS. REV. LETT., **101** (2008), 068102.

[28] Charras, G. T.; Hu, C.-K.; Coughlin, M.; Mitchison, T. J.:
*Reassembly of contractile actin cortex in cell blebs.*
J. BIOL. CHEM., **175** (2006), 477.

[29] Chate, H.; Ginelli, F.; Montagne, R.:
*Simple model for active nematics: quasi-long-range order and giant fluctuations.*
PHYS. REV. LETT., **96** (2006), 180602.

[30] Chate, H.; Ginelli, F.; Gregoire, G.; Raynaud, F.:
*Collective motion of self-propelled particles interacting without cohesion.*
PHYS. REV. E, **77** (2008), 046113.

[31] Chen, X.; Xu, D.; Avraham, B.; Swinney, H. L.; Zhang, H. P.:
*Scale-Invariant Correlations in Dynamic Bacterial Clusters.*
PHYS. REV. LETT., **108** (2012), 148101.

[32] Chicurel, M. E.; Chen, C. S.; Ingber, D. E.:
*Cellular control lies in the balance of forces.*
CURR. OPIN. CELL BIOL., **10** (1998), 232.

[33] Cisneros, L. H.; Cortez, R.; Dombrowski, C.; Goldstein, R. E.; Kessler, J. O.:
*Fluid dynamics of self-propelled microorganisms, from individuals to concentrated populations.*
EXP. FLUIDS, **43** (2007), 737.

[34] Claessens M. M. A. E.; Semmrich C.; Ramos L.; Bausch A. R.:
*Helical twist controls the thickness of F-actin bundles.*
PROC. NATL. ACAD. SCI. U.S.A., **105** (2008), 8819.

[35] Cooke R.; Bialek W.:
*Contraction of glycerinated muscle fibers as a function of the ATP concentration.*
BIOPHYS. J., **28** (1979), 241.

[36] Corte, L.; Chaikin, P. M.; Gollub, J. P.; Pine, D. J.:
*Random organization in periodically driven systems.*
NATURE PHYSICS, **4** (2008), 420.

[37] Courson, D.S.; Rock, R.S.:
*Actin Cross-link Assembly and Disassembly Mechanics for alpha-Actinin and Fascin.*
J. BIOL. CHEM., **285** (2010), 26350.

[38] Couzin, I.D.; Krause, J.; Franks, N. R.; Levin, S. A.:
*Effective leadership and decision-making in animal groups on the move.*
NATURE, **433** (2005), 513.

[39] Cowen, E. A.; Sveen, J. K.:
*in PIV and Water Waves, edited by J. Grue, P. L. F. Liu, and G. K. Pedersen.*
World Scientific Publishing, Singapore, 2003.

[40] Craig, S. W.; Lancashire, C. L.; Cooper, J. A.:
*Preparation of Smooth-muscle-$\alpha$-actinin.*
METHODS ENZYMOL., **85** (1982), 316.

[41] Cramer, L. P.; Siebert, M.; Mitchison, T. J.:
*Identification of novel graded polarity actin filament bundles in locomoting heart fibroblasts: implications for the generation of motile force.*
J. CELL BIOL., **136** (1997), 1287.

[42] Crocker, J. C.; Grier, D. G.:
*Methods of digital video microscopy for colloidal studies.*
J. COLLOID. INTERFACE SCI., **179** (1996), 298.

[43] Cross, M. C.; Hohenberg, P. C.:
*Pattern formation outside of equilibrium.*
REV. MOD. PHYS., **65** (1993), 851.

[44] Csirók, A.; Ben-Jacob, E.; Cohen, I.; Vicsek, T.:
*Formation of complex bacterial colonies via self-generated vortices.*
PHYS. REV. E, **54** (1996), 1791.

[45] Dalhaimer, P.; Discher, E. D.; Lubensky, T. C.:
*Crosslinked actin networks show liquid crystal elastomer behaviour, including soft-mode elasticity.*
NATURE, **3** (2007), 354.

[46] Davis, M. J.; Hill, M. A.:
*Signaling mechanisms underlying the vascular myogenic response.*
PHYSIOL. REV., **79** (1999), 387.

[47] DeBiasio, R.; LaRocca, G.; Post, P.; Taylor, D.:
*Myosin II transport, organization and phosphorylation: evidence for cortical flow/solation-contraction coupling during cytokinesis and cell locomotion.*
MOL. BIOL. CELL, **10** (1996), 1259.

[48] Debold E. P.; Patlak J. B.; Warshaw D. M.:
*Slip sliding away: load-dependence of velocity generated by skeletal muscle myosin molecules in the laser trap.*
BIOPHYS J., **89** (2005), L34.

[49] Deseigne, J.; Dauchot, O.; Chaté, H.:
*Collective motion of vibrated polar disks.*
PHYS. REV. LETT., **105** (2010), 098001.

[50] Deseigne, J.; Léonard, S.; Dauchot, O.; Chaté, H.:
*Vibrated polar disks: spontaneous motion, binary collisions, and collective dynamics.*
SOFT MATTER, **8** (2012), 5629.

[51] Doi, M.; Edwards, S. F.:
*The Theory of Polymer Dynamics.*
Oxford Science Publications, 1998.

[52] Döbereiner, H.; Dublin-Thaler, B.; Giannone, G.; Xenias, H.; Sheetz, M.:
*Dynamic phase transitions in cell spreading.*
PHYS. REV. LETT., **93** (2004), 108105.

[53] Dombrowski, C.; Cisneros, L.; Chatkaew, S.; Goldstein, R. E.; Kessler, J. O.:
*Self-concentration and large-scale coherence in bacterial dynamics.*
PHYS. REV. LETT., **93** (2004), 098103.

[54] Drescher, K.; Goldstein, R. E.; Michel, N.; Polin, M.; Tuval, I.:
*Direct measurement of the flow field around swimming microorganisms.*
PHYS. REV. LETT., **105** (2010), 168101.

[55] Duke, T.; Holy, T.; Leibler, S.:
*"Gliding Assays" for Motor Proteins: A Theoretical Analysis.*
PHYS. REV. LETT., **74** (1995), 330.

[56] Ebashi, S.; Ebashi, F.:
*$\alpha$-actinin, a new structural protein from striated muscle.*
J. BIOCHEM., **58** (1965), 7.

[57] Edlund, M.; Lotano, M. A.; Otey, C. A.:
*Dynamics of $\alpha$-actininin focal adhesions and stress fibers visualized with $\alpha$-actinin-green fluorescent protein.*
CELL MOT. AND THE CYTOSKELETON, **48** (2001), 190.

[58] Ehrlicher, A. J.; Nakamura, F.; Hartwig, J. H.; Weitz, D. A.; Stossel, T. P.:
*Mechanical strain in actin networks regulates FilGAP and integrin binding to filamin A.*
NATURE, **478** (2011), 260.

[59] Effler J. C.; Kee Y.-S.; Berk J. M.; Tran M. N.; Iglesias P. A.; Robinson D. N.:
*Mitosis-specific mechanosensing and contractile-protein redistribution control cell shape.*
CURR. BIOL., **16** (2006), 1962.

[60] Evans E, Ritchie K.:
*Dynamic strength of molecular adhesion bonds.*
BIOPHYS. J., **72** (1997), 1541.

[61] Faix, J.; Steinmetz, M.; Boves, H.; Kammerer, R. A.; Lottspeich, F.; Mintert, U.; Murphy, J.; Stock, A.; Aebi, U.; Gerisch, G.:
*Cortexillins, major determinants of cell shape and size, are actin-bundling proteins with a parallel coiled-coil tail.*
CELL, **86** (1996), 631.

[62] Feng, Y. Y.; Walsh, C. A.:
*The many faces of filamin: a versatile molecular scaffold for cell motility and signalling.*
NATURE CELL BIOL., **6** (2004), 1034.

[63] Fernandez, P.; Maier, M.; Lindauer, M.; Kuffer, C.; Storchova, Z.; Bausch, A. R.:
*Mitotic Spindle Orients Perpendicular to the Forces Imposed by Dynamic Shear.*
PLOS ONE, **6** (2011), e28965.

[64] Fletcher, D. A.; Geissler, P. L.:
*Active biological materials.*
ANN. REV. PHYS. CHEM., **60** (2009), 469.

[65] Galbraith, C. G.; Sheetz, M.:
*Forces on adhesive contacts affect cell function.*
CURR. OPIN. CELL BIOL., **10** (1998), 566.

[66] Gallet, F.; Arcizet, D.; Bohec, P.; Richert, A.:
*Power spectrum of out-of-equilibrium forces in living cells: amplitude and frequency dependence.*
SOFT MATTER, **5** (2009), 2947.

[67] Geiger, B.; Spatz, J. P.; Bershadsky, A. D.:
*Environmental sensing through focal adhesions.*
NAT. REV. MOL. CELL BIOL., **10** (2009), 21.

[68] Gentry, B.; Smith, D.; Käs, J.:
*Buckling-induced zebra stripe patterns in nematic F-actin.*
PHYS. REV. E, **79** (2009), 031916.

[69] Giannone, G; Dublin-Thaler, B.; Döbereiner, H.; Kieffer, N.; Bresnick, A., Sheetz, M.:
*Periodic lamellipodial contractions correlate with reaward actin waves.*
CELL, **116** (2004), 431.

[70] Goldman, A. J.; Cox, R. G.; Brenner, H.:
*Slow viscous motion of a sphere parallel to a plane wall–I Motion through a quiescent fluid.*
CHEM. ENG. SCI., **22** (1967), 653.

[71] Gregoire, G.; Chaté, H.: *Onset of Collective and Cohesive Motion.*
PHYS. REV. LETT., **92** (2004), 025702.

[72] Grossman, D.; Aranson, I. S.; Ben Jacob, E.:
*Emergence of agent swarm migration and vortex formation through inelastic collisions.*
NEW J. PHYS., **10** (2008), 023036.

[73] Guerin T.; Prost J.; Martin P.; JoannyJ.-F.:
*Coordination and collective properties of molecular motors: Theory.*
CURR. OPIN. CELL BIOL., **22** (2010), 14.

[74] Guevorkian K.; Gonzales-Rodriguez D.; Carlier C.; Dufourb, S.; Brochard-Wyarta, F.:
*Mechanosensitive shivering of model tissues under controlled aspiration.*
PROC. NATL. ACAD. SCI. U.S.A., **108** (2011), 13387.

[75] Guo, B.; Guilford, W. H.:
*Mechanics of actomyosin bonds in different nucleotide states are tuned to muscle contraction.*
PROC. NATL. ACAD. SCI. U.S.A., **103** (2006), 9844.

[76] Hallatschek, O.; Nelson, D. R.:
*Life at the front of an expanding population .*
EVOLUTION, **64**, (2009), 193.

[77] Harris, A. K.; Stopak, D.; Wild, P.:
*Fibroblast traction as mechanism for collagen morphogenesis.*
NATURE, **290** (1981), 249.

[78] Hatwalne, Y.; Ramaswamy, S.; Rao, M.; Simha, R. A.:
*Rheology of active-particle suspensions.*
PHYS. REV. LETT., **92** (2004), 118101.

[79] Head, D. A.; Levine, A. J.; MacKintosh, F. C.:
*Mechanical response of semiflexible networks to localized perturbations.*
PHYS. REF. LETT., **91** (2003), 703.

[80] Henkel, M.; Hinrichsen, H.; Lubeck, S.:
*Non-Equilibrium Phase Transitions: Volume 1: Absorbing Phase Transitions.*
Springer, Netherlands, 2009.

[81] Hess, H.; Clemmens, J.; Brunner, C.; Doot, R.; Luna, S.; Ernst, K. H.; Vogel, V.:
*Molecular self-assembly of nnanowiresänd nnanospoolsüsing active transport.*
NANO LETTERS, **5** (2005), 629.

[82] Heusinger, C.; Frey, E.:
*Floppy modes and Non affine Deformations in Random Fibre Networks.*
PHYS. REF. LETT., **97** (2003), 105501.

[83] Heussinger, C.; Bathe, M.; Frey, E.:
*Statistical mechanics of semiflexible bundles of wormlike polymer chains.*
PHYS. REF. LETT. **99** (2007), 048101.

[84] Himmel, M.; van der Ven, P. F. M.; Stöcklein, W.; Fürst, D. O.:
*The limits of promiscuity: Isoform-specific dimerization of filamins.*
BIOCHEMISTRY **42** (2003), 430.

[85] Hinrichsen, H.:
*Non-equilibrium critical phenomena and phase transitions into absorbing states.*
ADV. PHYS., **49** (2000), 815.

[86] Hoffman B. D.; Massiera G.; Van Citters K. M.; Crocker J. C.:
*The consensus mechanics of cultured mammalian cells.*
PROC. NATL. ACAD. SCI. U.S.A., **103** (2006), 10259.

[87] Howard, J.:
*Molecular motors: Structural adaptations to cellular functions.*
NATURE, **389** (1997), 561.

[88] Howard, J.:
Mechanics of Motor Proteins and the Cytoskeleton.
Sinauer, Sunderland, 2001.

[89] Humphrey D.; Duggan C.; Saha D.; Smith D.; Käs J.A.:
*Active fluidization of polymer networks through molecular motors.*
NATURE, **416** (2002), 413.

[90] Hunt, A. J.; Gittes, F.; Howard, J.:
*The force exerted by a single kinesin molecule against a viscous load.*
BIOPHYS. J., **67** (1994), 766.

[91] Ingber, D. E.:
*Cellular mechanotransduction: putting all the pieces together again.*
FASEB J., **20** (2006), 811.

[92] Janmey, P. A.; Peetermans, J.; Zaner, K. S.; Stossel, P. S.; Tanaka, T.:
*Structure and Mobility of Actin Filaments as Measured by Quasielastic Light Scattering, Viscometry, and Electron Microscopy.*
J. BIOL CHEM., **261** (1986), 8357.

[93] Janson L. W.; Kolega J.; Taylor D. L.:
*Modulation of contraction by gelation/solation in a reconstituted motile model.*
J. CELL BIOL., **114** (1991), 1005.

[94] Joanny, J.-F.; Jülicher F.; Kruse, K. Prost, J.:
*Hydrodynamic theory for multicomponent active polar gels.*
NEW J. PHYS., **9** (2007), 422.

[95] Joanny, J.-F.; Prost, J.:
*Active gels as a description of the actin-myosin cytoskeleton.*
HFSP J., **3** (2009), 94.

[96] Jülicher, F.; Kruse, K.; Prost, J.; Joanny, J. F.:
*Active behavior of the cytoskeleton.*
PHYS. REP., **449** (2007), 3.

[97] Kane R. E.:
*Interconversion of structural and contractile actin gels by insertion of myosin during assembly.*
J. CELL BIOL., **97** (1983), 1745.

[98] Karsenti, E.:
*Self-organization in cell biology: A brief history.*
Nat. Rev. Mol. Cell. Biol., **9** (2008), 255.

[99] Katoh, K.; Yumiko, K.; Michitaka, M.; Hirofumi, O.; Fujiwara, K.:
*Isolation and Contraction of the Stress Fiber.*
MOL. BIOL. CELL, **9** (1997), 1919 – 1938.

[100] Katsura, I.; Noda, H.:
*Studies on the formation and physical chemical properties of synthetic myosin filaments.*
JOURNAL OF BIOCHEMISTRY, **69** (1971), 219.

[101] Kayser, J.; Grabmayr, H.; Herrmann, H.; Bausch, A. R.:
*Assembly kinetics determine the structure of keratin networks.*
SOFT MATTER, (2012) doi:10.1039/C2SM26032H.

[102] Koenderink, G. H.; Dogic, Z.; Nakamura, F.; Bendix, P. M.; MacKintosh, F. C.; Hartwig, J. H.; Stossel,T. P.; Weitz, D. A.:
*Liquids and structural glasses special feature: An active biopolymer network controlled by molecular motors.*
PROC. NATL. ACAD. SCI. U.S.A., **106** (2009), 15192.

[103] Köhler, S.; Schaller, V.; Bausch, A. R.:
*Structure formation in active networks.*
NATURE MATERIALS, **10** (2011), 462.

[104] Köhler, S.; Schaller, V.; Bausch, A. R.:
*Collective motion in active networks.*
PLOS ONE, **6** (2011), e23798.

[105] Köhler, S.:
*Dynamics and structure formation in active actin networks.*
PhD Thesis, Technische Universität München, 2012.

[106] Köhler, S.; Schmoller, K. M.; Crevenna, A.H.; Bausch, A R.:
*Regulating contractility of the acto-myosin cytoskeleton by pH.*
CELL REPORTS, in press (2012).

[107] Köhler, S.; Bausch, A R.:
*Contraction mechanisms in composite active actin networks.*
PLOS ONE, **7** (2012), e39869.

[108] Kraikivski, P.; Lipowsky, P.:
*Enhanced ordering of interactin filaments by molecular motors.*
PHYS. REV. LETT., **96** (2006), 258103.

[109] Kreis, T. E.; Birchmeier, W.:
*Stress Fibre Sarcomeres of Fibroblasts are Contractile.*
CELL, **22** (1980), 555 – 561.

[110] Kron S. J.; Spudich J. A.:
*Fluorescent actin filaments move on myosin fixed to a glass surface.*
PROC. NATL. ACAD. SCI. U.S.A., **83** (1986), 6272–6276.

[111] Kruse, K.; F.; Jülicher:
*Actively Contracting Bundles of Polar Filaments.*
PHYS. REV. LETT., **85** (2000), 1778.

[112] Kruse, K.; Camalet, S.; Jülicher, F.:
*Self-Propagating Patterns in Active Filament Bundles.*
PHYS. REV. LETT., **87** (2001), 138101.

[113] Kruse, K.; Jülicher, F.:
*Self-organization and mechanical properties of active filament bundles.*
PHYS. REV. E, **67** (2003), 051913.

[114] Kruse, K.; Joanny, J. F.; Jülicher, F.; Prost, J.; Sekimoto, K.:
*Asters, Vortices, and Rotating Spirals in Active Gels of Polar Filaments.*
PHYS. REV. LETT., **92** (2004), 078101.

[115] Kudrolli, A.; Lumay, G.; Volfson, D.; Tsimring, L. S.:
*Swarming and swirling in self-propelled polar granular rods.*
PHYS. REV. LETT., **100** (2008), 058001.

[116] Kumar, S.; Maxwell, I. Z.; Heisterkamp, A.; Polte, T. R.; Lele, T. P.; Salanga, M.; Mazur, E.; Ingber, D. E.:
*Viscoelastic Retraction of Single Living Stress Fibres and Its Impact on Cell Shape, Cytoskeletal Organization, and Extracellular Matrix Mechanics.*
BIOPHYSICAL J., **90** (2006), 3762.

[117] Kurokawa, H.; Fujii, W.; Ohmi, K.; Sakurai, T.; Nonomura, Y.:
*Simple and Rapid Purification of Brevin.*
BIOPH. RES. CO., **168** (1990), 451.

[118] Langer, J.:
*Theory of Spinodal Decomposition in Alloys.*
ANN. PHYS., **65** (1971), 53.

[119] Lau A. W. C.; Hoffman B. D.; Davies A.; Crocker J. C.; Lubensky T. C.:
*Microrheology, stress fluctuations, and active behavior of living cells.*
PHYS. REV. LETT., **91** (2003), 198101.

[120] Lau A. W. C.; Prasad, A.; Dogic, Z.:
*Condensation of isolated semi-flexible filaments driven by depletion interactions.*
EPL, **87** (2009), 48006.

[121] LeGoff, L.; Amblard, F.; Furst, E. M.:
*Motor-driven dynamics in actin-myosin networks.*
PHYS. REV. LETT., **88** (2002), 018101.

[122] Lenart, P.; Bacher, C. P.; Daigle, N.; Hand, A. R.; Eils, R.; Terasaki, M.; Ellenberg, J.:
*A contractile nuclear actin network drives chromosome congression in oocytes.*
NATURE, **436** (2005), 812.

[123] Lieleg, O.; Claessens, M. M. A. E.; Luan, Y.; Bausch, A. R.:
*Transient binding and dissipation in cross-linked actin networks.*
PHYS. REV. LETT., **101** (2008), 108101.

[124] Lieleg, O.; Schmoller, K. M.; Cyron, C J.; Luan, Y.; Wall, W. A.; Bausch, A. R.:
*Structural Polymorphism in Heterogeneous Cytoskeletal Networks.*
SOFT MATTER, **5** (2009), 1796.

[125] Lieleg, O.; Claessens, M. M. A. E.; Bausch, A. R.:
*Structure and Dynamics of Cross-linked Actin Networks.*
SOFT MATTER, **10** (2010), 218.

[126] Liu, C.-H.; Pine, D. J.:
*Shear-Induced Gelation and Fracture in Micellar Solutions.*
PHYS. REV. LETT., **77** (1996), 2121.

[127] Liu, H. Q.; Spoerke, E. D.; Bachand, M.; Koch, S. J.; Bunker, B. C.; Bachand, G. D.:
*Biomolecular Motor-Powered Self-Assembly of Dissipative Nanocomposite Rings.*
ADV. MATER., **20** (2008), 4476.

[128] Liverpool, T. B.; Marchetti, M. C.:
*Instabilities of Isotropic Solutions of Active Polar Filaments.*
PHYS. REV. LETT., **90** (2003), 138102.

[129] Liverpool, T. B.; Marchetti, M. C.:
*Rheology of active filament solutions.*
PHYS. REV. LETT., **97** (2006), 268101.

[130] Liverpool, T. B.; Marchetti, M. C.; Joanny, J. F.; Prost, J.:
*Mechanical response of active gels.*
EUROPHYS. LETT., **85** (2009), 18007.

[131] Loose, M.; Fischer-Friedrich, E.; Ries, J.; Kruse, K.; Schwille, P.:
*Spatial Regulators for Bacterial Cell Division Self-Organize into Surface Waves in Vitro.*
SCIENCE, **320** (2008), 789.

[132] Lowey, S.; Slayter, H. S.; Weeds, A. G.; Baker, H.:
*Substructure of the Myosin Molecule.*
J. MOL. BIOL., **42** (1969), 1.

[133] MacLean-Fletcher, S.; Pollard, T. D.:
*Identification of a factor in conventional muscle actin preparations which inhibits actin filament self-association.*
BIOCHEM. BIOPHYS. RES. COMMUN., **96** (1980), 18.

[134] Maddox, A. S.; Lewellyn, L.; Desai, A.; Oegema, K.:
*Anillin and the septins promote asymmetric ingression of the cytokinetic furrow.*
DEVELOPMENTAL CELL, **12** (2007), 827.

[135] Maniotis, A. J.; Chen, C. S.; Ingber, D. E.:
*Demonstration of mechanical connections between integrins, cytoskeletal filaments, and nucleoplasm that stabilize nuclear?structure.*
PROC. NATL. ACAD. SCI. U. S. A., **94** (1997), 849.

[136] Margossian, S. S.; Lowey, S.:
*Preparation of myosin and its subfragments from rabbit skeletal muscle.*
METH. ENZYMOL., **85** (1982), 55.

[137] Martin, A. C.; Kaschube, M.; Wieschaus, E. F.:
*Pulsed contractions of an actin-myosin network drive apical constriction.*
NATURE, **457** (2009), 495.

[138] Martin, A. C.; Gelbart, M.; Fernandez-Gonzalez, R.; Kaschube, M.; Wieschaus, E. F.:
*Integration of contractile forces during tissue invagination.*
J. CELL BIOL., **188** (2010), 735.

[139] Martinac, B.:
*Mechanosensitive ion channels: molecules of mechanotransduction.*
J. CELL SCI., **117** (2004), 2449.

[140] Maul, R. S.; Song, Y.; Amann, K. J.; Gerbin, S. C.; Pollard, T. D.; Chang D. D.:
*EPLIN regulates actin dynamics by cross-linking and stabilizing filaments.*
J. CELL BIOL, **160** (2003), 399.

[141] Mayer, M.; Depken, M.; Bois, J.; Jülicher, F.; Grill, S. W.:
*Anisotropies in cortical tension reveal the physical basis of polarizing cortical flows.*
NATURE, **467** (2010), 617.

[142] McCain, M. L.; Hyungsuk, L.; Aratyn-Schausa, Y.; Kléber, A. G.; Parkera, K. K.:
*Cooperative coupling of cell-matrix and cell-cell adhesions in cardiac muscle.*
PROC. NATL. ACAD. SCI. U.S.A., **109** (2012), 9881.

[143] McDonald, J. C.; Whitesides, G. M.:
*Poly(dimethylsiloxane) as a Material for Fabricating Microfluidic Devices.*
ACC. CHEM. RES., **35** (2002), 491.

[144] Medeiros, N. A.; Burnette, D. T.; Forscher, P.:
*Myosin II functions in actin-bundle turnover in neuronal growth cones.*
NATURE CELL BIOL., **8** (2006), 215.

[145] Mehta, A. D.; Rock, R. S.; Rief, M.; Spudich, J. A.; Mooseker, M. S.; Cheney, R. E.:
*Myosin-V is a processive actin-based motor.*
NATURE, **400** (1999), 590.

[146] Metzler R.; Klafter J.:
*The random walk's guide to anomalous diffusion: a fractional dynamics approach.*
PHYSICS REPORTS, **339** (2000), 1.

[147] Metzler R.; Klafter J.:
*Accelerating brownian motion: A fractional dynamics approach to fast diffusion.*
EUROPHYS. LETT., **51** (2000), 492.

[148] Mishra, S.; Baskaran, A.; Marchetti, M. C.:
*Fluctuations and pattern formation in self-propelled particles.*
PHYS. REV. E, **81** (2010), 061916.

[149] Mitrossilis, D.; Fouchard, J.; Pereira, D.; Postic, F.; Richert, A.; Saint-Jean,M.; Asnacios, A.:
*Real-time single-cell response to stiffness.*
PROC. NATL. ACAD. SCI. U.S.A., **107** (2010), 16518.

[150] Mizuno, D.; Tardin, C; Schmidt, C. F.; MacKintosh, F. C.:
*Nonequilibrium mechanics of active cytoskeletal networks.*
SCIENCE, **315** (2007), 370.

[151] Mori, M.; Monnier, N.; Daigle, N.; Bathe, M.; Ellenberg, J.; Lénárt, P.:
*A novel mechanism of intracellular transport: sieving by an anchored homogeneously contracting F-actin meshwork.*
CURR. BIOL., **21** (2011), 606.

[152] Nakamura, F.; Osborn, T. M.; Hartemink, C. A.; Hartwig, J. H.; Stossel, T. P.:
*Structural basis of filamin A functions.*
J. CELL BIOL., **179** (2007), 1011.

[153] Nakazawa, H.; Sekimoto, K.:
*Polarity sorting in a bundle of actin filaments by two-headed myosins.*
J. PHYS. SOC. JPN., **65** (1996), 2404.

[154] Narayan, V.; Ramaswamy, S.; Menon, N.:
*Long-lived giant number fluctuations in a swarming granular nematic.*
SCIENCE, **317** (2007), 105.

[155] Nawroth, J. C.; Lee, H.; Feinberg, A. W.; Ripplinger, C. M.; McCain, M. L.; Grosberg, A.; Dabiri, J. O.; Parker, K. K.:
*A tissue-engineered jellyfish with biomimetic propulsion.*
NATURE BIOTECH. (2012), doi:10.1038/nbt.2269.

[156] Nédélec, F. J.; Surrey, T.; Maggs, A. C.; Leibler, S.:
*Self-organization of microtubules and motors.*
NATURE, **389** (1997), 305.

[157] Nédélec, F. J.:
*Computer simulations reveal motor properties generating stable antiparallel microtubule interactions.*
J. CELL BIOL., **158** (2002), 1005.

[158] Olafsen, J. S.; Urbach, J. S.:
*Clustering, Order, and Collapse in a Driven Granular Monolayer.*
PHYS. REV. LETT., **81** (1998), 4369.

[159] Onsager, L.:
*Reciprocal relations in irreversible processes. I.*
PHYS. REV., **37** (1931), 405.

[160] Paluch, E.; Piel, M.; Prost, J.; Bornens, M.; Sykes, C.:
*Cortical Actomyosin Breakage Triggers Shape Oscillations in Cells and Cell Fragments.*
BIOPHYS. J., **89** (2005), 724.

[161] Pelletier, O.; Pokidysheva, E.; Hirst, L. S.; Bouxsein, N.; Li, Y.; Safinya, C. R.:
*Structure of actin cross-linked with $\alpha$-actinin: A network of bundles.*
PHYS. REV. LETT., **91** (2003), 148102.

[162] Peruani F.; Deutsch A.; Bär M.:
*Nonequilibrium clustering of self-propelled rods.*
PHYS. REV. E, **74** (2006), 030904.

[163] Peruani, F.; Klauss, T.; Deutsch, A.; Voss-Boehme, A.:
*Traffic jams, gliders, and bands in the quest for collective motion of self-propelled particles.*
PHYS. REV. LETT., **106** (2011), 128101.

[164] Peter, R.; Schaller, V.; Ziebert, F.; Zimmermann, W.:
*Pattern formation in active cytoskeletal networks.*
NEW J. PHYS., **10** (2008), 035002.

[165] Quaas, J.; Wylie, C.:
*Surface Contraction Waves (SCWs) in the Xenopus Egg Are Required for the Localization of Germ Plasm and Are Dependent upon Material Stores of Kinesin-like Protein Xklp1.*
DEVELOPMENTAL BIOLOGY, **243** (2002), 272.

[166] Rayment, I.; Holden, H. M.; Whittaker, M.; Yohn, C. B.; Lorenz, M.; Holmes, K. C.; Milligan, R. A.:
*Structure of the actin-myosin complex and its implications for muscle contraction.*
SCIENCE, **261** (1993), 58.

[167] Reck-Peterson, S. L.; Yildiz, A.; Carter, A. P.; Gennerich, A.; Zhang, N.; Vale, R. D.:
*Single-Molecule Analysis of DyneinProcessivity and Stepping Behavior.*
CELL, **126** (2006), 335.

[168] Riedel, I. H.; Kruse, K.; Howard, J.:
*A self-organized vortex array of hydrodynamically entrained sperm cells.*
SCIENCE, **309** (2005), 300.

[169] Rognioni, L.; Stigler, J.; Pelz, B.; Ylänne, J.; Rief, M.:
*Dynamic force sensing of filamin in single molecule experiments.*
submitted 2012.

[170] Sanger, J. M.; Mittal, B.; Pochapin, M. B.; Sanger, J. W.:
*Stress fiber and cleavage furrow formation in living cells microinjected with fluorescently labeled $\alpha$-actinin.*
MOTILITY AND THE CYTOSKELETON, **7** (1987), 209.

[171] Schaller, V.; Weber, Ch.; Semmrich, Ch.; Frey, E.; Bausch, A.R.:
*Polar patterns of driven filaments.*
NATURE, **467** (2010), 73.

[172] Schaller, V.; Weber, Ch.; Frey, E.; Bausch, A.R.:
*Polar pattern formation: hydrodynamic coupling of driven filaments.*
SOFT MATTER, **7** (2011), 3213.

[173] Schaller, V.; Weber, Ch.; Hammerich, B.; Frey, E.; Bausch, A.R.:
*Frozen steady states in active systems.*
PROC. NATL. ACAD. SCI. U.S.A., **108** (2011), 19183.

[174] Schaller, V.; Hammerich, B.; Bausch, A.R.:
*Active compaction of driven filaments.*
EUROP. PHYS. J. E, **35** (2012), 9758.

[175] Schmoller K. M.; Lieleg O.; Bausch A. R.:
*Cross-linking Molecules Modify Composite Actin Networks Independently.*
PHYS. REV. LETT., **101** (2008), 118102.

[176] Schmoller K. M.; Lieleg O.; Bausch A. R.:
*Structural and viscoelastic properties of actin/filamin networks: cross-linked versus bundled networks.*
BIOPHYS J, **97** (2009), 83.

[177] Schmoller, K. M.; Fernandez, P.; Arevalo, R. C.; Blair, D.L.; Bausch, A. R.:
*Cyclic hardening in bundled actin networks.*
NATURE COMMUN., **1** (2010), 134.

[178] Schmoller, K. M.; Semmrich, C.; Bausch, A. R.:
*Slow down of actin depolymerization by cross-linking molecules.*
J. STRUCT. BIOL., **173** (2010), 350.

[179] Schmoller, K. M.; Niedermayer, T.; Zensen, C.; Wurm, C.; Bausch, A. R.:
*Fragmentation Is Crucial for the Steady-State Dynamics of Actin Filaments.*
BIOPHYS. J., **101** (2011), 803.

[180] Schmoller, K. M.; Koehler, S.; Crevenna, A. H.; Wedlich-Söldner, R.; Bausch, A R.:
*Modulation of cross-linked actin networks by pH.*
SOFT MATTER, in print (2012).

[181] Schilling, J.; Sackmann, E.; Bausch, A.R.:
*Digital imaging processing for biophysical applications.*
REV. SCI. INSTRUM., **75** (2004), 2822.

[182] Schwarz, U. S.; Bischofs, I. B.:
*Physical determinants of cell organization in soft media.*
MEDICAL ENGINEERING & PHYSICS, **27** (2005), 763.

[183] Sheetz, M. P.; Chasan, R.; Spudich, J. A.:
*ATP-dependent movement of myosin in vitro: characterization of a quantitative assay.*
J. CELL BIOL., **99** (1984), 1867.

[184] Shizuta, Y.; Shizuta, H.; Gallo, M.; Davies, P.; Pastan. I.:
*Purification and properties of filamin, and actin binding protein from chicken gizzard.*
J. BIOL. CHEM., **251** (1976), 6562.

[185] Silva, M. S. E.; Depkenb, M.; Stuhrmanna, B.; Korstena, M.; MacKintosh, F. C.; Koenderink, G. H.:
*Active multistage coarsening of actin networks driven by myosin motors.*
PROC. NATL. ACAD. SCI. U. S. A., **108** (2011), 9408.

[186] Simha, R.A.; Ramaswamy, S.:
*Hydrodynamic fluctuations and instabilities in ordered suspensions of self-propelled particles.*
PHYS. REV. LETT., **89** (2002), 058101.

[187] Sjöblom, B.; Salmazo, A.; Djinovic-Carugo, K.:
*$\alpha$-actininStructure and Regulation.*
CELL. MOL. LIFE SCI., **65** (2008), 2688.

[188] Smith, D. M.; Ziebert, F.; Humphrey, D.; Duggan, C.; Steinbeck, M.; Zimmermann, W.; Käs, J. A.:
*Molecular motor-induced instabilities and crosslinkers determine biopolymer organization.*
BIOPHYSICAL JOURNAL, **93** (2007), 4445.

[189] Solon J.; Kaya-Copur A.; Colombelli J.; Brunner D.:
*Pulsed forces timed by a ratchet-like mechanism drive directed tissue movement during dorsal closure.*
CELL **137** (2009), 1331.

[190] Spudich J. A.; Watt S.:
*The regulation of rabbit skeletal muscle contraction. i. biochemical studies of the interaction of the tropomyosin-troponin complex with actin and the proteolytic fragments of myosin.*
J BIOL CHEM, **246** (1971), 4866.

[191] Stock, A.; Steinmetz, M. O.; Janmey, P. A.; Aebi. U.; Gerisch G.; Kammerer, R. A.; Weber, I.; Faix. J.:
*Domain analysis of cortexillin I: actin-bundling, PIP(2)-binding and the rescue of cytokinesis*
EMBO J., **18** (1999), 5274.

[192] Storm, C.; Pastore, J. J.; MacKintosh, F. C.; Lubensky, T. C.; Janmey, P. A.:
*Nonlinear elasticity in biological gels.*
NATURE, **435** (2005), 191.

[193] Straight, A. F.; Field, C. M.; Mitchison, T. J.:
*Anillin binds non-muscle myosin II and regulates the contractile ring.*
MOLECULAR BIOLOGY OF THE CELL, **16** (2005), 193.

[194] Stricker, J.; Aratyn-Schaus, Y.; Oakes, P. W.; Gardel, M. L.:
*Spatiotemporal constraints on the force-dependent growth of focal adhesions.*
BIOPHYS. J., **100** (2011), 2883.

[195] Stossel, T. P.; Condeelis, J.; Cooley, L.; Hartwig, J. H.; Noegel||, A.; Schleicher, M.; Shapiro, S. S.:
*Filamins as integrators of cell mechanics and signalling.*
NATURE REV. MOLEC. CELL BIOL., **2** (2001), 138.

[196] Straley J. P.:
*Frank elastic-constants of hard-rod liquid crystals.*
PHYS. REV. A, **8** (1973), 2181.

[197] Sumino, Y.; Nagai, K. H.; Shitaka, Y.; Tanaka, D.; Yoshikawa, K.; Chaté, H.; Oiwa. K.:
*Large-scale vortex lattice emerging from collectively moving microtubules.*
NATURE, **483** (2012), 448.

[198] Sundberg, M.; Balaz, M.; Bunk, R.; Rosengren-Holmberg, J. P.; Montelius, L.; Nicholls, I. A.; Omling, P.; Tagerud, S.; Mansson, A.:
*Selective spatial localization of actomyosin motor function by chemical surface patterning.*
LANGMUIR, **22** (1973), 7302.

[199] Surrey, T.; Nédélec, F. J.; Leibler, S.; Karsenti, E.:
*Physical properties determining self-organization of motors and microtubules.*
SCIENCE, **292** (2001), 1167.

[200] Taguchi, K.; Ishiuchi, T.; Takeichi. M.:
*Mechanosensitive EPLIN-dependent remodeling of adherens junctions regulates epithelial reshaping.*
J. CELL BIOL., **194** (2011), 643.

[201] Takeuchi, K. A.; Kuroda, M.; Chate, H.; Sano, M.:
*Directed Percolation Criticality in Turbulent Liquid Crystals.*
PHYS. REV. LETT., **99** (2007), 234503.

[202] Takiguchi K.; Hayashi H.; Kurimoto E.; Higashi-Fujime S.:
*In vitro motility of skeletal muscle myosin and its proteolytic fragments.*
*Journal of Biochemistry*, **107** (1990), 671.

[203] Takiguchi, K.:
*Heavy Meromyosin Induces Sliding Movements between Antiparallel Actin filaments.*
J. BIOCHEM., **109** (1991), 520.

[204] Tang, X.; Bajaj, P.; Bashir, R.; Saif, T. A.:
*How far cardiac cells can see each other mechanically.*
SOFT MATTER, **7** (2011), 6151.

[205] Thoresen, T.; Lenz, M.; Gardel, M. L.:
*Reconstitution of contractile actomyosin bundles.*
BIOPHYS. J., **100** (2011), 2698.

[206] Toner, J.; Tu, Y. H.:
*Long-range order in a two-dimensional dynamical XY model: how birds fly together.*
PHYS. REV. LETT., **75** (1995), 4326.

[207] Toner, J.; Tu, Y. H.:
*Flocks, herds, and schools: A quantitative theory of flocking.*
PHYS. REV. E, **58** (1998), 4828.

[208] Toner, J.; Tu, Y. H.; Ramaswamy, S.:
*Hydrodynamics and phases of flocks.*
ANN. PHYS., **318** (2005), 170.

[209] Toyoshima, Y. Y.; Kron, S. J.; Spudich, J. A.:
*The Myosin step-size - measurement of the unit displacement per ATP hydrolyzed in an in vitro assay.*
PROC. NATL. ACAD. SCI. U.S.A., **87** (1990), 7130.

[210] Trepat, X.; Wassermann, M. R.; Angelini, T. E.; Millet, E.; Weitz, D. A.; Butler, J. P.; Fredberg, J. J.:
*Physical forces during collective cell migration.*
NATURE PHYSICS, **5** (2009), 426.

[211] Tsai, J. C.; Ye, F.; Rodriguez, J.; Gollub, J. P.; Lubensky, T. C.:
*Physical forces during collective cell migration.*
PHYS. REV. LETT., **94** (2005), 214301.

[212] Tseng, Y.; Kole, T. P.; Lee, J. S. H.; Fedorov, E.; Almo, S. C. ; Schafer, B. W.; Wirtz, D.: (2005).
*How Actin Crosslinking and Bundling Proteins Cooperate to Generate an Enhanced Cell Mechanical Response.*
BIOCHEM. BIOPH. RES. CO. **334** (2005), 183.

[213] Tu, Y. H.; Toner, J.; Ulm, M.:
*Sound Waves and the Absence of Galilean Invariance in Flocks.*
PHYS. REV. LETT., **80** (1998), 4819.

[214] Turing, A. M.:
*The Chemical Basis of Morphogenesis.*
PHIL. TRANS. R. SOC. LOND. B, **237** (1952), 37.

[215] Uhde, J.; Keller, M.; Sackmann, E.:
*Internal Motility in Stiffening Actin-Myosin Networks.*
PHYS. REV. LETT., **93** (2004), 268101.

[216] Umbanhowar, P. B.; Melo, F.; Swinney, H. L.:
*Localized excitations in a vertically vibrated granular layer.*
NATURE, **382** (1996), 793.

[217] Uyeda, T. Q.; Kron, S. J.; Spudich, J. A.:
*Myosin step size: Estimation from slow sliding movement of actin over low densities of heavy meromyosin.*
J. MOL. BIOL., **214** (1990), 699.

[218] Valentine, M. T.; Perlman, Z. E.; Mitchison, T. J.; Weitz, D. A.:
*Mechanical Properties of Xenopus Egg Cytoplasmic Extracts.*
BIOPHYS. J., **88** (2005), 680.

[219] van den Heuvel, M. G. L.; Dekker, C.:
*Motor Proteins at Work for Nanotechnology.*
SCIENCE, **317** (2007), 333.

[220] Verkhovsky, A. B.; Borisy, G. G.:
*Non-sarcomeric mode of myosin II organization in the fibroblast lamellum.*
J. CELL BIOL., **123** (1993), 637.

[221] Vicsek T.; Family F.:
*Dynamic Scaling for Aggregation of Clusters.*
PHYS. REV. LETT., **52** (1984), 1669.

[222] Vicsek, T.; Czirók, A.; Ben-Jacob, E.; Cohen, I.; Shochet, O.:
*Novel type of phase transition in a system of self-driven particles.*
PHYS. REV. LETT., **75** (1995), 1226.

[223] Vignjevic, D.; Yarar, D.; Kojima, S.; Aratyn, O.; Danciu, T.; Svitkina, T.; Borisy, G. G.:
*Formation of filopodia-like bundles in vitro from a dendritic network.*
J. CELL. BIOL., **160** (2003), 951.

[224] Vignjevic D.; Yarar D.; Welch M. D.; Peloquin J.; Svitkina T.; Borisy G. G.:
*Role of Fascin Filopodial Protrusions.*
J. CELL. BIOL., **174** (2006), 863.

[225] Vikhorev, P.G.; Vikhoreva, N. N.; Sundberg, M.; Balaz, M.; Albet-Torres, N.; Bunk, R.; Kvennefors, A.; Liljesson, K.; Nicholls, I. A.; Nilsson, L.; Omling, P.; Tagerud, S.; Montelius, L.; Mansson, A.:
*Diffusion dynamics of motordriven transport: Gradient production and self-organization of surfaces.*
LANGMUIR, **24** (2008), 13509.

[226] Wachsstock, D.; Schwarz, W.; Pollard, T.:
*Affinity of alpha-actinin for actin determines the structure and mechanical properties of actin filament gels.*
BIOPHYS. J., **65** (1993), 205.

[227] Wachsstock, D.; Schwarz, W.; Pollard, T.:
*Cross-linker dynamics determine the mechanical properties of actin gels.*
BIOPHYS. J., **66** (1994), 801.

[228] Wagner, B.; Tharmann, R.; Haase, I.; Fischer, M.; Bausch, A. R.:
*Cytoskeletal polymer networks: molecular structure of crosslinkers determine macroscopic properties.*
PROC. NATL., ACAD. SCI. U.S.A., **103** (2006), 13974.

[229] Wang, N.; Butler, J. P.; Ingber, D. E.:
*Mechanotransduction across the cell surface and through the cytoskeleton.*
SCIENCE, **260** (1993), 1124.

[230] Wang, N.; Tytell, J. D.; Ingber, D. E.:
*Mechanotransduction at a distance: mechanically coupling the extracellular matrix with the nucleus.*
NAT. REV. MOL. CELL BIOL., **10** (2009), 75.

[231] Ward, A. J. W.; Sumpter, D. J. T.; Couzin, L.D.; Hart, P. J. B.; Krause, J.:
*Quorum decision-making facilitates information transfer in fish shoals.*
PROC. NATL., ACAD. SCI. U.S.A., **105** (2008), 6948.

[232] Weber, Ch.; Schaller, V.; Bausch, A.R.; Frey, E.:
*Nucleation-induced transition to collective motion in active systems.*
submitted 2012.

[233] Weitz D. A.; Oliveria M.:
*Fractal Structures Formed By Kinetic Aggregation Of Aqueous Gold Colloids.*
PHYS. REV. LETT., **52** (1984),1433.

[234] Wilhelm, J.; Frey, E.:
*Elasticity of Stiff Polymer Networks.*
PHYS. REV. LETT., **91** (2003), 108103.

[235] Xu, J.; Tseng, Y.; Wirtz, D.:
*Strain hardening of actin filament networks.*
J. BIOL. CHEM., **46** (2000), 35886.

[236] Peruani F.; Deutsch A.; Bär M.:
*Swarm behavior of self-propelled rods and swimming flagella.*
PHYS. REV. E, **82** (2010), 031904.

[237] Yamashiro-Matsumura, S.; Matsumura, F.:
*Purification and Characterization of an F-actin-bundling 55-Kilodalton Protein from HeLa Cells.*
J. BIOL. CHEM., **280** (1985), 5087.

[238] Yamashiro-Matsumura, S.; Matsumura, F.:
*Intracellular Localization of the 55-kD Actinbinding Protein in Cultured Cells: Spatial Relationships with Actin, $\alpha$-actinin,Tropomyosin, and Fimbrin.*
J. BIOL. CHEM., **103** (1986), 631.

[239] Zhang, H. P.; Be'er A.; Florin E.-L.; Swinney H. L.:
*Collective motion and density fluctuations in bacterial colonies.*
PROC. NATL. ACAD. SCI. U.S.A., **107** (2010), 13626.

[240] Ziebert, F.; Zimmermann, W.:
*Nonlinear competition between asters and stripes in filament-motor systems.*
EUR. PHYS. J. E, **18** (2005), 41.

[241] Ziebert, F.; Aranson, I. S.:
*Rheological and structural properties of dilute active filament solutions.*
PHYS. REV. E, **18** (2008), 011918.

[242] Zumdieck, A.; Lagomarsino, M. C.; Tanase, C.; Kruse, K.; Mulder, B.; Dogterom, M.; Jülicher, F.:
*Continuum Description of the Cytoskeleton: Ring Formation in the Cell Cortex.*
PHYS. REV. LETT., **95** (2005), 258103.

# List of Publications

1. Peter, R.; **Schaller, V.**; Ziebert, F.; Zimmermann, W.:
   *Pattern formation in active cytoskeletal networks.*
   NEW J. PHYS., **10** (2008), 035002.

2. **Schaller, V.**; Weber, Ch.; Semmrich, Ch.; Frey, E.; Bausch, A.R.:
   *Polar patterns of driven filaments.*
   NATURE, **467** (2010), 73-77.

3. Köhler, S.; **Schaller, V.**; Bausch, A.R.:
   *Structure formation in active networks.*
   NATURE MATERIALS, **10** (2011), 462–468.

4. Burgis, M.; **Schaller, V.**; Gläßl, M.; Kaiser, B.; Köhler, W.; Krekhov, A.; Zimmermann, W.:
   *Anomalous diffusion in viscosity landscapes.*
   NEW J. PHYS., **10** (2011), 043031.

5. **Schaller, V.**; Weber, Ch.; Frey, E.; Bausch, A.R.:
   *Polar pattern formation: hydrodynamic coupling of driven filaments.*
   SOFT MATTER, **7** (2011), 3213–3218.

6. Köhler, S.; **Schaller, V.**; Bausch, A.R.:
   *Collective Dynamics of Active Cytoskeletal Networks.*
   PLOS ONE, **6**(8) (2011), e23798.

7. **Schaller, V.**; Weber, Ch.; Hammerich, B.; Frey, E.; Bausch, A.R.:
   *Frozen steady states in active systems.*
   PROC. NATL. ACAD. SCI. U.S.A., **108** (2011), 19183-19188.

8. **Schaller, V.**; Bausch, A.R.:
   *A fresh twist for self assembly.*
   NATURE (news&views), **481** (2012), 268-269.

9. **Schaller, V.***; Hammerich, B.*; Bausch, A.R.:
   *Active compaction of driven filaments.*
   EUROP. PHYS. J. E, **35** (2012), 9758.
   *equal contributions

10. Weber, Ch.; **Schaller, V.**; Bausch, A.R.; Frey, E.:
    *Nucleation-induced transition to collective motion in active systems.*
    submitted.

11. **Schaller, V.**; Bausch, A.R.:
*Collective motion: giant fluctuations and anisotropic correlations.*
submitted.

12. **Schaller, V.**; Schmoller, K.M.; Hammerich, B.; Bausch, A.R.:
*Crosslinker sensitive structure formation of driven filaments.*
in preparation.

# Acknowledgements

Mit der Danksagung kommt nun nicht nur das wichtigste Kapitel der Arbeit, sondern auch das Kapitel, das wohl am meisten gelesen werden wird. An dieser Stelle möchte ich allen danken, die zum Gelingen der Arbeit bei getragen haben.

Meinem Doktorvater Prof. Andreas Bausch möchte ich zuallererst dafür danken, dass er mich, quasi als humanitären Akt (Zitat!) und trotz aller Risiken (sooo viel ging auch gar nicht kaputt), als Theoretiker in seine Gruppe aufgenommen hat. Auch die vielen gemeinsamen Paper-schreib-Sitzungen werden mir wohl in dauerhafter Erinnerung beleiben (-"Der Satz ist ja mal richtig gut!" - "Den hast du gestern geschrieben." -"Ah, wusst' ich's doch..."). Dann natürlich für die hervorragende Betreuung, die fast immer offen stehende Bürotür und die vielen Diskussionen zusammen mit "unseren" Theoretikern (s.u.).

Prof. Erwin Frey und Christoph Weber, "unseren" Theoretikern, möchte ich dafür danken, dass sie es irgendwie geschafft haben im Theorie-Dschungel, der da heißt "active soft matter", den Überblick zu behalten. Das hat nicht nur zu vielen tollen Ergebnissen geführt, sondern das ein oder andere Projekt erst in die richtige Richtung gelenkt.

Simone Köhler danke ich dafür, dass ich ihre spannenden Experimente mit einer langweiligen Simulation bereichern durfte. Außerdem natürlich für das tägliche Biochemie-Grundpraktikum, dass ich bei ihr absolvieren... naja... durfte und für die tolle Zeit im Büro.

Kurt Schmoller, meinem Biochemie-Grundpraktikums-Leidensgenossen, danke ich dafür, dass er es nach der Halbfinal-Niederlage Deutschlands gegen Spanien, die wir während einer Konferenz in Granada (das liegt in Spanien!) erlebten, seine Schadenfreude sehr taktvoll hinter einem breiten Grinsen zu verbergen wusste (obwohl er Österreicher ist). Außerdem für diverse Kaffee-Pausen und Beach-Volleyball-Einlagen.

Bei meiner Bürokollegin Christine Wurm bedanke ich mich dafür, dass sie die kollektive Phase, die sie – so will es die Legende – eines schönen Freitag-Nachmittags vor meiner Zeit entdeckt hat, nicht gleich zu Ende gemessen hat und für die vielen Kaugummis und die Schokolade zur Frust-Therapie.

Jona Kayser, meinem direkten Platznachbarn, danke ich dafür, dass er das Chaos auf meiner Seite der Demarkations-Linie mit viel Gleichmut ertragen hat ("Ist der Tacker vielleicht irgendwo unter dem linken Haufen?"). Außerdem für die vielen Diskussionen während diverser Kaffee-Pausen.

Bei meinen Diplomanden, Bachelor- und Werks-Studenten, Benjamin Hammerich, Simone Ferstl und Timo Kaldeway, möchte ich mich für die gute Zusammenarbeit und die vielen gemeinsam erzielten Ergebnisse bedanken. Bei allen TAs, Gabi Chmel, Monika Rusp, Daniela Scheikl und Karin Vogt möchte ich mich besonders bedanken. Ihnen ist es zu verdanken, dass nicht alle Labore

im völligen Chaos versinken und dass wir immer so hervorragende Protein-Präparationen zur Verfügung haben. Bei Anja Gieseke, Simone Köhler Matthias Maier und Kurt Schmoller bedanke ich mich dafür, dass sie mir ihre Vernetzer-Proteine zum Spielen gegeben haben.

Dank gilt natürlich auch den Korrekturlesern: Ryo Suzuki, Kurt Schmoller, Börn Meier, Svenja Lippok und Jona Kayser.

Bei den Sekretärinnen, Elke Fehsenfeld, Katherina Girgensohn, Iris König-Decker, Nicole Mitermüller und Katharina Scholz bedanke ich mich dafür, dass sich der tägliche Papierkrieg für die Doktoranden in erträglichem Umfang hält und für die unkomplizierte Abwicklung von Material-Bestellungen und Dienstreise-Anträgen.

Bei allen Mitgliedern von E22 und E27 bedanke ich mich für das super Arbeitsklima und die hervorragende Atmosphäre am Lehrstuhl... was die Beach-Volleyball Pausen ausdrücklich mit einschließt.

Bei der Studienstiftung des deutschen Volkes bedanke ich mich für die Finanzierung meiner Promotion durch ein Promotionsstipendium und beim Graduierten-Kolleg CompInt für die Finanzierung der vielen Konferenzen und Auslandsaufenthalte.

Bei meinen Eltern möchte ich mich für all die andauernde und langjährige Unterstützung bedanken, die weit über die bloße Finanzierung meines Studiums hinaus ging.

Bei Svenja bedanke ich mich dafür, dass sie bei mir geblieben ist nachdem sie erfahren hat, dass ich eigentlich Theoretiker bin, dass sie mich beständig zum Schreiben gezwungen hat und für alles andere.